

Syracuse University

## SURFACE at Syracuse University

---

Dissertations - ALL

SURFACE at Syracuse University

---

8-26-2022

### Geometry of discrete and continuous bounded surfaces

Kyung Eun Kim

Syracuse University, ke03kim@gmail.com

Follow this and additional works at: <https://surface.syr.edu/etd>



Part of the [Condensed Matter Physics Commons](#)

---

#### Recommended Citation

Kim, Kyung Eun, "Geometry of discrete and continuous bounded surfaces" (2022). *Dissertations - ALL*. 1656.

<https://surface.syr.edu/etd/1656>

This Dissertation is brought to you for free and open access by the SURFACE at Syracuse University at SURFACE at Syracuse University. It has been accepted for inclusion in Dissertations - ALL by an authorized administrator of SURFACE at Syracuse University. For more information, please contact [surface@syr.edu](mailto:surface@syr.edu).

# Abstract

We work on reconstructing discrete and continuous surfaces with boundaries using length constraints. First, for a bounded discrete surface, we discuss the rigidity and number of embeddings in  $\mathbb{R}^3$ , modulo rigid transformations, for given real edge lengths. Our work mainly considers the maximal number of embeddings of rigid graphs in  $\mathbb{R}^3$  for specific geometries (annulus, strip). We modify a commonly used semi-algebraic, geometrical formulation using Bézout's theorem, from Euclidean distances corresponding to edge lengths. We suggest a simple way to construct a rigid graph having a finite upper bound. We also implement a generalization of counting embeddings for graphs by segmenting multiple rigid graphs in  $\mathbb{R}^d$ . Our computational methodology uses vector and matrix operations and can work best with a relatively small number of points ( $< 1000$ ). Second, we also generalize the shapes of surfaces made from multiple materials. We present continuous surfaces with length constraints to achieve maximum volume or minimum energy. The solution from the Euler-Lagrange equation can be unique or have a finite number of solutions, depending on boundary conditions. Next, we develop an  $n$ -dimensional extension using a constitutive relation. Because these solutions are in integral form, we show a method based on a binomial approximation to estimate curvature and derivatives for analytical purposes. The binomial approach shows good agreement  $n \geq 10$  for derivatives and  $n \geq 100$  for the original equation if we exclude results near the boundary.

# Geometry of Discrete and Continuous Bounded Surfaces

by

Kyung Eun Kim

B. Eng., HONGIK UNIVERSITY, 2004

M.S., HANYANG UNIVERSITY, 2010

DISSERTATION

Submitted in partial fulfillment of the requirements for the degree of

Doctor of Philosophy in Physics

Syracuse University

August 2022

Copyright © Kyung Eun Kim, August 2022  
All Rights Reserved

# Acknowledgements

First, I would like to thank advisor Professor Christian D. Santangelo for his guidance and support during the phase of my academic career and during the COVID-19 pandemic. Additionally, I would like to express gratitude to my committee members, Professors Wanliang Shan, Jennifer Ross, Jack Laiho, Jennifer Schwartz, and Alison Patteson. I appreciate the Physics Department staff, including Professor Mitchell Soderberg, for their help during these years. I acknowledge funding through NSF EFRI 1935294. My appreciation also goes to the material geometry group members: Michelle, Mary Elizabeth, Manu, Sourav, Samay, Gentian, and Alexia. I also thank Graduate School people (Gabrielle Chapman, Glenn Wright, and Daniel Olson-Bang). I would like to thank all my friends for all their encouragement, including Sung and Emma. Last, I would like to express my profound appreciation to Sook-Lim Kang for her love and support.

# Contents

<b>List of Figures</b>	<b>ix</b>
<b>List of Tables</b>	<b>xv</b>
<b>1 Introduction</b>	<b>1</b>
<b>2 Conditions, upper and lower bounds for a pinned rigid graph</b>	<b>11</b>
2.1 Generic upper and lower bounds for a rigid graph . . . . .	13
2.1.1 Dimension 2 . . . . .	13
2.1.2 Dimension 3 . . . . .	22
2.2 Conditions for a graph to have a finite number of embeddings . . . . .	25
2.2.1 Discrete annulus . . . . .	26
2.2.2 Strips and general graphs . . . . .	38
2.2.3 Upper and lower bounds . . . . .	40
<b>3 Explicit construction for a pinned graph to have a finite number of embeddings</b>	<b>41</b>
3.1 Explicit construction for a pinned graph . . . . .	41
3.1.1 Annulus and Strips . . . . .	43
3.1.2 General Graphs . . . . .	47
3.2 Computational Methods . . . . .	49
3.2.1 Methods to compute system of polynomials . . . . .	49

3.2.1.1	Resultants . . . . .	50
3.2.1.2	Homotopy continuation . . . . .	52
3.2.1.3	Euclidean distance matrix . . . . .	53
3.2.2	Trilateration and Linear Matrix . . . . .	55
3.2.2.1	Trilateration . . . . .	55
3.2.2.2	Linear matrix . . . . .	57
3.2.3	Optimization . . . . .	58
3.2.4	Adding more constraints . . . . .	59
3.3	Discussions for computational methods . . . . .	60
3.3.1	Trilateration . . . . .	61
3.3.2	Linear matrix . . . . .	64
3.3.3	Optimization . . . . .	68
3.3.4	Merging different methods . . . . .	70
<b>4</b>	<b><i>n</i>-dimensional extension of Euler’s elastica with constitutive relations</b>	<b>74</b>
4.1	Mylar balloon and Euler’s elastica . . . . .	74
4.1.1	History of Euler’s elastica . . . . .	74
4.1.2	Formation of Mylar balloon . . . . .	76
4.1.3	Mylar balloon with point mass . . . . .	82
4.1.4	Mylar balloon with cylindrical mass . . . . .	85
4.1.5	Mylar ballon with perpendicular forces . . . . .	88
4.1.6	Mylar balloon with applied force . . . . .	91
4.2	Euler’s elastica for <i>n</i> -dimensional implementation . . . . .	95
4.2.1	Spherical balloon with perpendicular forces . . . . .	96
4.2.2	<i>n</i> -dimensional implementation . . . . .	100
4.2.3	Generalized implementation . . . . .	105
4.2.4	Generalized case with multiple boundary conditions . . . . .	111
4.2.5	Application for non axis-symmetric surface . . . . .	118

4.3	Analytical approximation of $n$ -dimensional Euler's elastica . . . . .	126
4.3.1	Parametrization method . . . . .	127
4.3.2	Curvature estimation of Mylar and spherical balloon . . . . .	127
4.3.3	Curvature estimation of $n$ -dimensional Euler's elastica . . . . .	133
4.3.4	Curvature estimation of a surface with multiple functions . . . . .	135
4.3.5	Curvature estimation of generalized case . . . . .	138
<b>5</b>	<b>Conclusion</b>	<b>148</b>
5.1	Conditions and constructions of a pinned rigid graph . . . . .	148
5.2	$n$ -dimensional extension of Euler's elastica with constitutive relations . . . . .	151
	<b>Appendices</b>	<b>157</b>
<b>A</b>	<b>Mathematical backgrounds for isometric embeddings</b>	<b>157</b>
A.1	Properties of isometric mappings . . . . .	157
A.2	$C^k$ isometric embeddings . . . . .	157
A.3	Isoperimetric problems . . . . .	158
<b>B</b>	<b>Mathematical backgrounds for rigidity theory</b>	<b>160</b>
B.1	Rings and matrices . . . . .	160
B.2	Matroid and ring theory . . . . .	164
B.3	Algebraic geometry and distance geometry . . . . .	173
<b>C</b>	<b>Mathematical backgrounds for Euler's elastica and binomial expansion</b>	<b>176</b>
C.1	Elements of the calculus of variations . . . . .	176
C.2	Original proof of Euler's elastica . . . . .	178
C.3	Elliptic integrals and functions . . . . .	182
C.4	Coefficients of first and second fundamental forms . . . . .	184
C.5	Fractional binomial theorem . . . . .	185

<b>D Willmore energy and Willmore surfaces</b>	<b>187</b>
D.1 Willmore conjectures . . . . .	188
D.2 Willmore surfaces and Willmore flow . . . . .	189
D.3 Hopf tori and Willmore Hopf tori . . . . .	191
<b>Bibliography</b>	<b>192</b>
<b>Vita</b>	<b>206</b>

# List of Figures

1.1	A cube can be made from the Latin cross. . . . .	2
1.2	A tetrahedron can be made from the Latin cross. . . . .	3
1.3	A triangulated strip can be folded in multiple ways. . . . .	3
1.4	An example of a graph embedding problem. . . . .	4
1.5	Four embeddings from Euclidean distance equations of figure 1.4 (b). . . . .	5
1.6	Eliminating folded cases of figure 1.5 by adding one more edge. . . . .	5
1.7	Counting can be done by segmenting a graph into sub-graphs. . . . .	7
1.8	Gluing two sub-graphs into one. . . . .	8
1.9	Four embeddings from Euclidean distance equations of figure 1.8 (a). . . . .	8
1.10	Experimental constant mean curvature surface of genus 2 by GeometrieWerkstatt in [94] under License CC BY-NC-SA 3.0. . . . .	9
2.1	A flat triangulated sheet can have multiple embeddings. . . . .	11
2.2	Illustrations of properly intersected 2-spheres from [113]. . . . .	12
2.3	Henneberg sequence for (a) graph $G_i$ (b) graph $G_{i+1}$ adding vertex (blue dot) using type I (c) graph $G_{i+1}$ adding vertex (blue dot) using type II (dashed line represents edge will be removed). . . . .	15
2.4	Planar triangulation for $n = 4$ . . . . .	15
2.5	Graph (b) can be obtained by folding a sub-graph of (a). . . . .	16
2.6	Edge length set having 6 embeddings for Desargues framework $G$ . . . . .	17
2.7	Edge length set having 8 embeddings for Desargues framework $G$ . . . . .	18

2.8	Maximum embeddings for Desargues framework $G$ [16]. . . . .	19
2.9	Examples of (a) caterpillar and (b) fan construction [30]. . . . .	20
2.10	Some realizations for Laman graphs $ V  = 5, 6$ embedded in $\mathbb{R}^2$ [16][117]. . .	20
2.11	Henneberg sequence (a) graph $G_i$ (b) graph $G_{i+1}$ adding vertex (blue dot) using type I (c) graph $G_{i+1}$ adding vertex (blue dot) using type II (dashed line represents edge will be removed). . . . .	23
2.12	Geiringer graphs (a) $ V  = 6$ , (b) $ V  = 7$ , and (c) $ V  = 8$ [30]. . . . .	24
2.13	Examples of (a) annulus and (b) discrete annulus. . . . .	26
2.14	(a) $ I  =  P  = 3$ , (b) $ I  =  P  = 4$ , (c) $ I  =  P  = 5$ , (d) nested two annuli with each of them have $ I  =  P  = 3$ , and (e) (d) with triangular cone. . . .	34
2.15	(a) $3d$ graph fixed on a plane with 8 pinned vertices, (b) projected map of graph (a), (c) projected map of modified version for graph (a) . . . . .	35
2.16	(a) a pinned graph projected on a plane with 7 pinned vertices, (b) sub-graph $H$ generated by each $i \in I$ , and the number of local symmetry is 2. . . . .	36
2.17	(a), (b), and (c) $3d$ graph fixed on a plane with pinned vertices, (d), (e), and (f) projected map of graph (a), (b), and (c) respectively. . . . .	37
2.18	Examples of (a) strip and (b) discrete strip. . . . .	38
3.1	Examples of connecting pinned rigid graphs. . . . .	41
3.2	Examples of gluing rigid graphs. . . . .	42
3.3	Double banana graph. . . . .	42
3.4	A method of constructing strips with finite embeddings. . . . .	45
3.5	(a) Constructing graph for sequential computation, (b) and (c) show possible representation for annulus type surfaces. . . . .	46
3.6	New point can be added not to generate additional embeddings by choosing $d$ -linear connections. . . . .	47
3.7	A case with $N_G \leq N_{G_1} \cdot N_{G_2} = 2^5$ : (a) a graph $G_1$ with $N_{G_1} \leq 2^4$ , (b) top view of (a), and (c) $N_{G_2} = 2$ (d) adding $G_2$ to $G_1$ . . . . .	48

3.8	Intersection points of two circles. . . . .	56
3.9	Trilateration demonstration in [105] under License CC BY-NC-SA 3.0. . . .	57
3.10	An example of error inflation. . . . .	63
3.11	An example of discrete annulus. . . . .	65
3.12	(a) Structure of test surface and (b) scatter plots of reconstructed surface. .	66
3.13	(a) circular type and (b) zigzag type of boundaries. . . . .	66
3.14	Test structure for error inflation inspired by an exhaust pipe. . . . .	67
3.15	An example of (a) discrete annuli, (b) taking multiple starting points, and (c) computing solutions using two directions. . . . .	68
3.16	An example of the optimization method. . . . .	69
3.17	Error depends on geometrical structures. . . . .	70
3.18	(a) Scatter plot, (b) triangulated plot, and (c) structure of the surface. . . .	71
3.19	Comparison between different computational methods. . . . .	71
3.20	Demonstrations of different layer constructions. . . . .	72
3.21	3-dimensional (a) triangulated plot and (b) scatter plot of figure 3.20 (c) . .	72
3.22	(a) reconstructed surface for 3.21 (b) reprocessed fifth layer using optimization methods. . . . .	73
4.1	A problem posed by James Bernoulli. . . . .	75
4.2	Geometry of the Mylar balloon. . . . .	77
4.3	Top profile of Mylar balloon. The blue line represents the initial radius, the red dashed line shows wrinkles caused by the non-stretchable property, and the black line represents the final mean radius. . . . .	81
4.4	A geometry of Mylar balloon with point mass. . . . .	83
4.5	Profiles from different ratio of pressure and point mass defined by $\eta = \frac{mg}{2\pi p}$ . .	85
4.6	A geometry of Mylar balloon with cylindrical mass. . . . .	85
4.7	Profiles from different radius $d$ of masses and $\eta = \frac{mg}{2\pi p}$ . . . . .	88
4.8	Profiles from different $\alpha, \beta, \gamma$ where $\alpha = \frac{1}{\lambda}, \beta = \frac{F}{2\pi p \lambda}$ , and $\gamma = \frac{f}{\lambda 2\pi p}$ . . . . .	89

4.9	Different values of $\alpha$ with a same ratio of $\frac{\alpha}{\beta} = 0.7, \frac{\alpha}{\gamma} = 0.35$ show identical profile. . . . .	90
4.10	Profile comparison of forces with different directions for $\gamma \neq 0$ . . . . .	90
4.11	Profile comparison of forces with different directions for $\gamma = 0$ . . . . .	91
4.12	Comparison of numerical and symbolic integration results for equation 4.13. . . . .	94
4.13	Various profiles of equation 4.14 for $0.3 \leq \lambda \leq 10$ . . . . .	95
4.14	Geometry of spherical balloon. . . . .	96
4.15	Profiles of spherical balloon with different $b, c$ values (where $a = \frac{R-bR-c}{R^2}$ ). . . . .	99
4.16	Profile comparison of a spherical balloon for positive and negative $b$ values (where $c = 0$ ). . . . .	99
4.17	Profile of a spherical balloon with higher forces for $\alpha = 1$ . . . . .	100
4.18	Profiles of figure 4.17 for $x \leq 0.6, z(x) \in \mathbb{C}$ . . . . .	102
4.19	An example of coordinate settings for $z(x) \in \mathbb{C}$ . . . . .	103
4.20	Profiles of $f(x) = mt^n + \lambda$ for various $m, n$ . . . . .	104
4.21	Profile changes from different slope $z'(R_-)$ . . . . .	105
4.22	A surface constructed with high and low stiffness regions. . . . .	109
4.23	A surface having a fixed volume region for $x \leq 2$ . . . . .	110
4.24	Profile differences of high and low stiffness surfaces from different gluing methods. . . . .	112
4.25	Glued type of surface can be composed by adding two different surfaces. . . . .	113
4.26	Geometry for the multiple volume method . . . . .	114
4.27	One way to simulate non-uniform perpendicular force can be done by adding extra volume to the surface. . . . .	115
4.28	An example to show a difference between gluing and summing method. . . . .	116
4.29	Vertical profiles of figure 4.28. . . . .	116
4.30	Graph of $b(\theta) = \cos(4\theta)$ . . . . .	119
4.31	Profiles of $b(\theta) = -1, 1$ for $z(5_-) = -\infty$ . . . . .	120

4.32	Equation 4.30 with different aligning methods. . . . .	120
4.33	3-dimensional plot of equation 4.31. . . . .	121
4.34	Top view of a surface. . . . .	122
4.35	Vertical slices of a surface. . . . .	122
4.36	three-dimensional representation of a joint surface for eq. 4.32. . . . .	123
4.37	three-dimensional representation of a smooth surface for eq. 4.32. . . . .	123
4.38	Profiles of eq. 4.33 for $\theta = 0, \pi$ . . . . .	124
4.39	Examples of $R(\theta) = 5 + \cos(n\theta)$ for $n = 2, 5$ . . . . .	125
4.40	An example of a surface with genus 1. . . . .	126
4.41	Profiles of Mylar balloon from numerical integration and binomial expansion for $n \sim 10$ . . . . .	128
4.42	Gaussian curvature of Mylar balloon from different parametrization methods. . . . .	130
4.43	Mean curvature of Mylar balloon from different parametrization methods. . . . .	131
4.44	Profiles of Mylar balloon for various $n$ . . . . .	131
4.45	Gaussian curvature of Mylar balloon for various $n$ . . . . .	132
4.46	Profiles of a spherical balloon for $n \sim 10$ . . . . .	133
4.47	Gaussian and mean curvatures of a spherical balloon for $n \sim 10$ . . . . .	133
4.48	Profiles of eq. 4.41 from the binomial approximation for $n \sim 10, 40$ . . . . .	134
4.49	Gaussian and mean curvatures of eq. 4.41 from the binomial approximation for $n \sim 10$ . . . . .	135
4.50	Profiles of $z_1(x)$ , $z_2(x)$ , and a surface $z(x)$ constructed using $z_1(x)$ and $z_2(x)$ . . . . .	136
4.51	Gaussian curvatures of $z_1(x)$ and $z_2(x)$ from the binomial approximation $n \sim 10$ . . . . .	137
4.52	Mean curvatures of $z_1(x)$ and $z_2(x)$ from the binomial approximation $n \sim 10$ . . . . .	137
4.53	Approximated Gaussian curvature of $z(x)$ . . . . .	138
4.54	Approximated mean curvature of $z(x)$ . . . . .	138
4.55	Profiles of Mylar balloon from binomial approximation for $n \sim 10, 120$ . . . . .	141
4.56	Profiles of excess term $c(t)$ for $n \sim 10, 50$ . . . . .	142

4.57	Profiles of $\frac{\partial}{\partial x}z(x)$ (partial derivative of Mylar balloon along $x$ ) from binomial approximation for $n \sim 2, 10$ . . . . .	142
4.58	Profiles of a spherical balloon from binomial approximation for $n \sim 10$ . . . . .	143
4.59	Profiles of figure 4.18 approximated from binomial expansion for $n \sim 10, 50$ . . . . .	145
4.60	Profiles of eq. 4.42 at $\theta = 0$ approximated from binomial expansion for $n \sim 20$ . . . . .	147
4.61	Profiles of eq. 4.42 at $\theta = \pi$ approximated from binomial expansion for $n \sim 20$ . . . . .	147
5.1	A graph with $N_G = 2$ . . . . .	149
5.2	Plots drawn using $n$ -dimensional Euler's elastica similar to nature structures. . . . .	152
5.3	Image of red blood cell [108]. . . . .	152
5.4	Image of apple [109]. . . . .	153
5.5	Hopf torus plotted using R with codes in [102]. . . . .	154
5.6	Constrained Willmore Hopf torus by GeometrieWerkstatt in [94] under License CC BY-NC-SA 3.0. . . . .	155

# List of Tables

2.1	Number of Laman graphs with $ V $ vertices computed in [16]. . . . .	20
2.2	Minimal and maximal Laman number among all Laman graphs with $ V $ vertices [16] for $6 \leq  V  \leq 9$ and Lemma 2.0.1 was used for $3 \leq  V  \leq 5$ (all graphs are constructed with triangles). . . . .	21
2.3	Maximal Laman number and upper bound among all Laman graphs with $ V  = n$ vertices for $3 \leq  V  \leq 9$ [16]. . . . .	22
2.4	Maximal number and upper bounds among all Geiringer graphs with $ V  = n$ vertices for $6 \leq  V  \leq 10$ [30]. . . . .	25
2.5	$M_3(n)$ and upper bounds among all Geiringer graphs with $ V $ vertices for $6 \leq  V  \leq 10$ and lower and upper bounds for pinned discrete annulus for $6 \leq  V  \leq 10$ with $ P  = 3$ . . . . .	40
3.1	Accumulated error for each layer. . . . .	67
3.2	Accumulated error for each layer. . . . .	73

# Chapter 1

## Introduction

Isometric embedding problems arise in mechanics when one attempts to reconstruct shapes in  $\mathbb{R}^n$  from a set of length constraints. A recent example comes from the emerging field of 4D printing. 4D printing allows one to fabricate 3D objects from patterned, 2D sheets of locally grown materials. For example, a flat disk is programmed to have a particular metric and submerged in a hot bath to transform the designated shape [45]. This thin sheet is designed to have a non-uniform shrinkage, and the sheet can buckle to achieve that metric with strictly zero strain. The theoretical formulation is established by using non-Euclidean metric [19] [20] (though [40] points out there is a technical error related to their works). Generically, many such shapes may have a given metric, just as over one realization corresponds to a given sheet. Similar problems arise in discrete analogs of 4D printing, for example, when continuum elastic sheets are patterned with dots to represent different stiffness. It is observed that when two same hybrid Enneper's surfaces deswell and recover, they show different pathways [44]. Some of them utilize triangular faces to represent continuum elastic sheets. Thus, the metric constraint on an elastic sheet translates to constraints on the edge lengths of the faces. In that case, the isometric embedding problem can arise by states generated from the folding and unfolding of a triangulated sheet. In the [49], the authors presented a way to solve an inverse problem of finding surfaces compatible with a given metric. They obtained a surface (without re-optimization) that is not smooth

and not unique. Moreover, a singularity is observed when they find a minimum energy function, and they assume it is caused by the uncertainty that the surface can grow from its initial conditions. They implemented a typical triangulation method (six nearest neighboring points) instead of a standard cloth model [86]. For this reason, some papers used additional information. [37] uses Gaussian curvature and edge length as constraints for a discrete metric to prevent this issue. [26] used discrete grid structures to study hierarchical buckling patterns. They used Gaussian curvatures associated with the branch points. Mathematically, for  $C^1$ -differentiable function (it can be viewed as a graph without a loop), Nash (weak condition  $N \geq m + 2$ ) and Kuiper showed  $N \geq m + 1$  for a short smooth embedding for a surface  $M$ ,  $M \subset \mathbb{R}^m \rightarrow \mathbb{E}^N$  (see appendix A.2). It tells a smooth surface can be embedded in a higher dimensional space than itself to preserve distances between points. Moreover, this is related to a local isometry. If we consider a global isometry, there is no naturally bijective or a countable number of maps for any graph  $G$  such that  $f : G \subset \mathbb{R}^n \rightarrow \mathbb{R}^n$  using only (Euclidian) distances between vertices as constraints. One of the widespread problems in mathematics and mechanics is the folding and unfolding problem. It usually deals with a planar sheet that can be folded into three-dimensional objects. The following example shows Latin cross can be folded into two different objects out of 21 distinct polytopes (in three-dimension) [85][63].

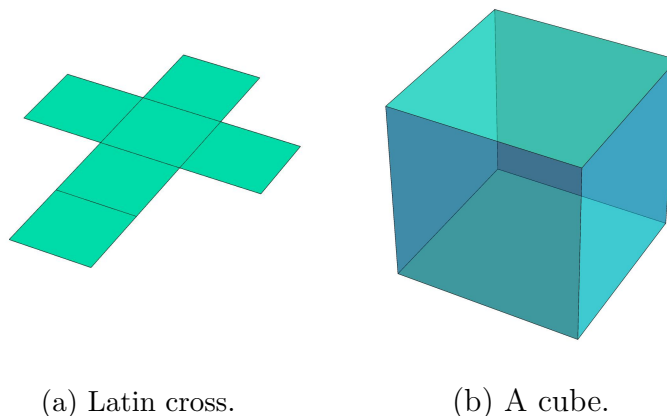
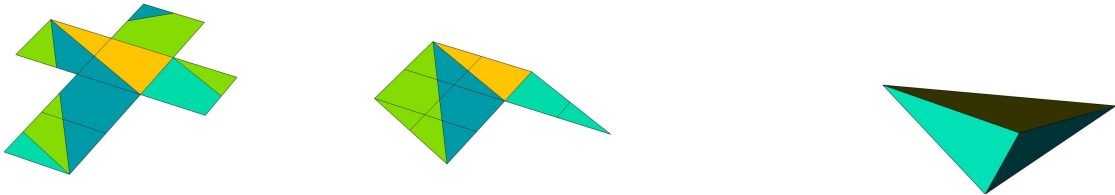


Figure 1.1: A cube can be made from the Latin cross.

Figure 1.2 shows a tetrahedron that can be folded from a Latin cross. (a) represents a colored Latin cross corresponded to the face of the tetrahedron. (b) is the rearranged pieces of squares related to each face of the tetrahedron. (c) presents the tetrahedron folded from (b).



(a) Latin cross. (b) Rearranged Latin cross. (c) A tetrahedron can be folded from (b).

Figure 1.2: A tetrahedron can be made from the Latin cross.

Generally, triangulation on a plane can generate multiple realizations with no additional constraints.

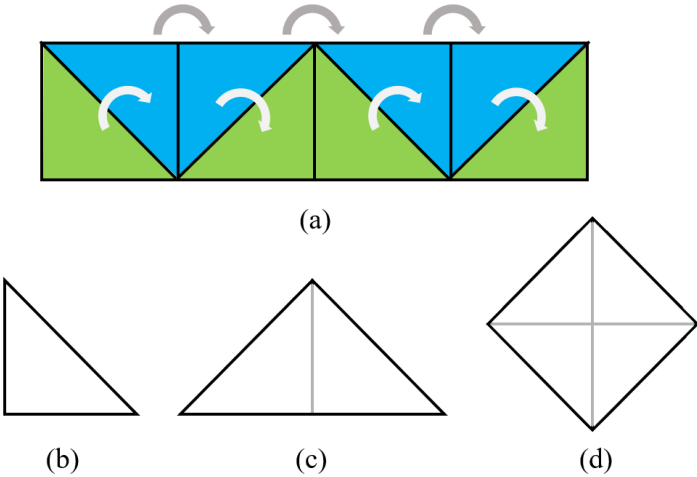


Figure 1.3: A triangulated strip can be folded in multiple ways.

For example, (b),(c),(d) in figure 1.3 are convex polygons can be folded from (a). Moreover, the number of embeddings will be increased as we increase the number of triangles.

This folding and unfolding problem can be extended to a graph embedding problem for  $n$ -dimensional space where graph  $G$  consists of labeled vertices in  $n$ -dimensional space. For example, it is a problem finding a number of embeddings from a set of edges and vertices, as shown below.

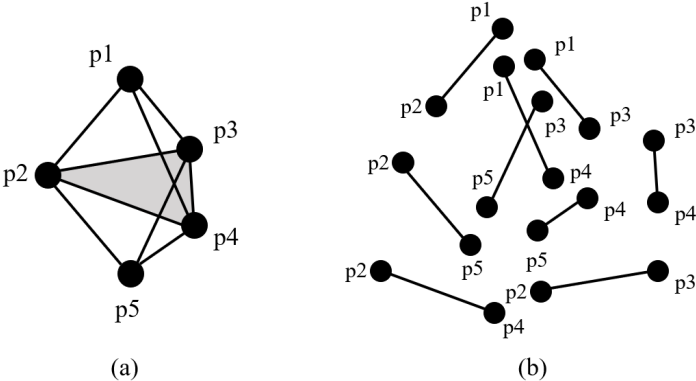


Figure 1.4: An example of a graph embedding problem.

Figure 1.4 (a) presents a graph with two tetrahedrons. If we disassemble (a) into a set of edges and labeled vertices (or technically 1-simplices), we can get (b). A graph embedding problem is finding all realizations from (b). If we reconstruct a graph from (b) using length equations between points, we can get figure 1.5. Notice that a tetrahedron can be positioned to “up” or “down”, so we get four embeddings.

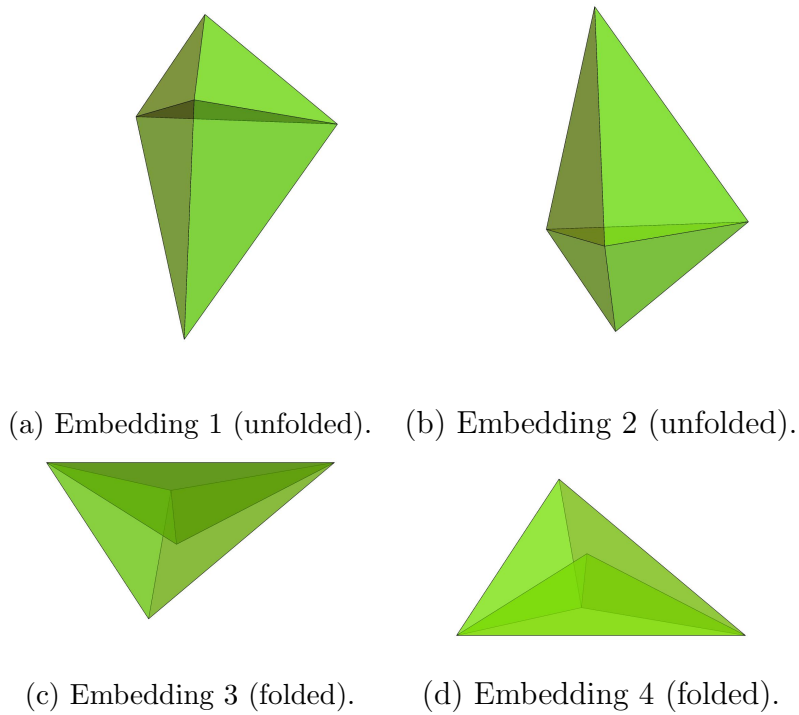


Figure 1.5: Four embeddings from Euclidean distance equations of figure 1.4 (b).

However, there exist maps  $f : G \subset \mathbb{R}^n \rightarrow \mathbb{R}^n$  for some  $G$  based on their networks (shape of graphs).

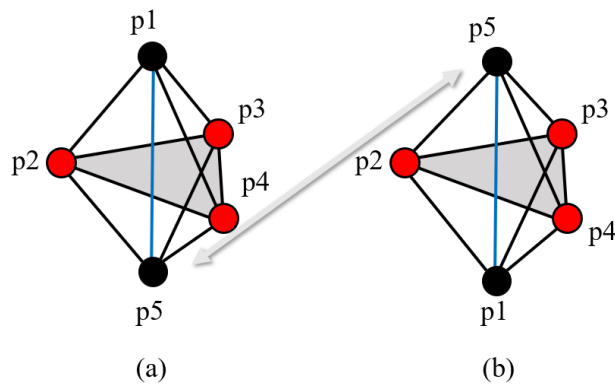


Figure 1.6: Eliminating folded cases of figure 1.5 by adding one more edge.

For example, we can eliminate folded cases by adding an edge  $(p_1, p_5)$  (blue line). Then, we have left two embeddings which is symmetric on the plane  $(p_2, p_3, p_4)$ . This graph can be unique up to reflection. Moreover, if we pin three vertices  $p_2, p_3, p_4$  such that their coordinates

are fixed, we can easily identify the position of  $p_1$  and  $p_5$  by using the length of each edge. In that sense, our works are related to designing controllable surfaces such that they can be uniquely (if not, at least there are finite copies that we can recognize) identified from given Euclidean lengths on the bounded (pinned) geometry. If the surface varies over time, it can be reconstructed by given information when it is bounded (or with given position vectors of boundary vertices over time) and when we know changes in Euclidean lengths. One can utilize more information in addition to the edge length as shown in [37]. More discussions can be found in section 3.2.4.

Chapter 2 deals with methods of counting the number of embedding of a graph. Since it is difficult to measure the exact number of embeddings for a particular graph, knowing the range (upper and lower bounds) helps estimate the number of realizations. Previous methods, which will be introduced in section 2.1 require intensive mathematical backgrounds. We have implemented and developed simple algebraic methods to count the number of embeddings in section 2.2 readers can apply. The chapter is written such that the approach can be applied in  $n$ -dimensional space. However, the main idea of counting is simple. We can count the number from ungrouping (or segmenting) a graph into smaller structures. The number of embedding of a graph will be less and equal to the multiplication of embedding for all rigid sub-graphs if a graph is rigid. The following figure presents a general idea in three-dimensional space.

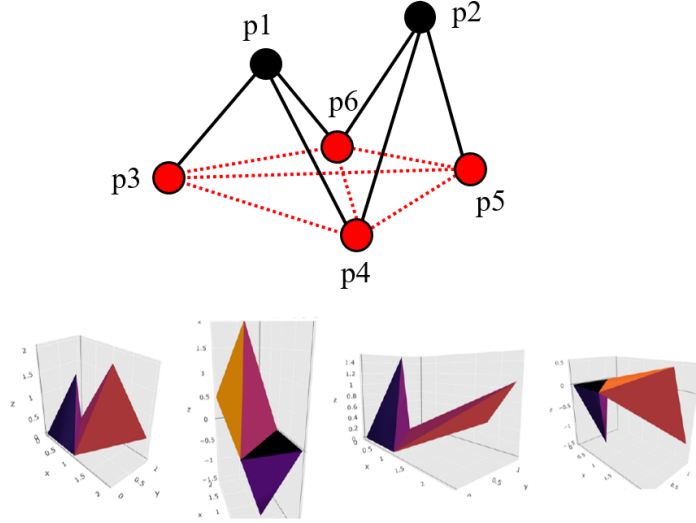


Figure 1.7: Counting can be done by segmenting a graph into sub-graphs.

Figure 1.7 illustrates counting methods. We can ungroup a graph to two tetrahedrons  $((p_1, p_3, p_4, p_6)$  and  $(p_2, p_4, p_5, p_6))$ . Each tetrahedron will have two realizations, so we get four as a total number of embeddings.

Chapter 3 illustrates the explicit construction of a graph to have a finite number of embeddings and corresponding upper (and lower) bounds. The main idea of this approach is to take sub-graphs with finite embeddings and glue them into a graph. Using this result, one can easily design a graph, and this explicit construction automatically defines the upper bound. The chapter is mainly focused on three-dimensional space. However, we can quickly expand this concept to the  $d$ -dimensional space. Intuitively, each sub-graph is at least  $d$ -simplex in  $d$ -dimensional space or more constrained (additional edges) structures such that it can be interpreted as a union of  $d$ -simplices with additional edges. Therefore, a minimally rigid graph in  $(d+1)$ -dimension can have a unique realization in  $d$ -dimension (up to reflection) if there exists a map  $\mathbb{R}^{d+1} \rightarrow \mathbb{R}^d$  such that each point satisfies to be in the general position between its neighboring points. For example, we need at least three edges for each vertex to be stable in the three-dimensional space. A flattened tetrahedron will have a unique realization in two-dimensional space (up to reflection) based on the choice of edge lengths.

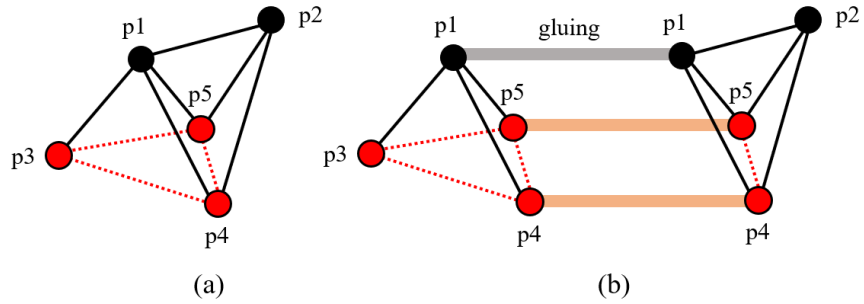


Figure 1.8: Gluing two sub-graphs into one.

Figure 1.8 represents how to glue two sub-graphs. In this case, two sub-graphs can be merged via a face. Since each sub-graph is a tetrahedron, we can easily expect the number of embeddings to be four, as shown below.

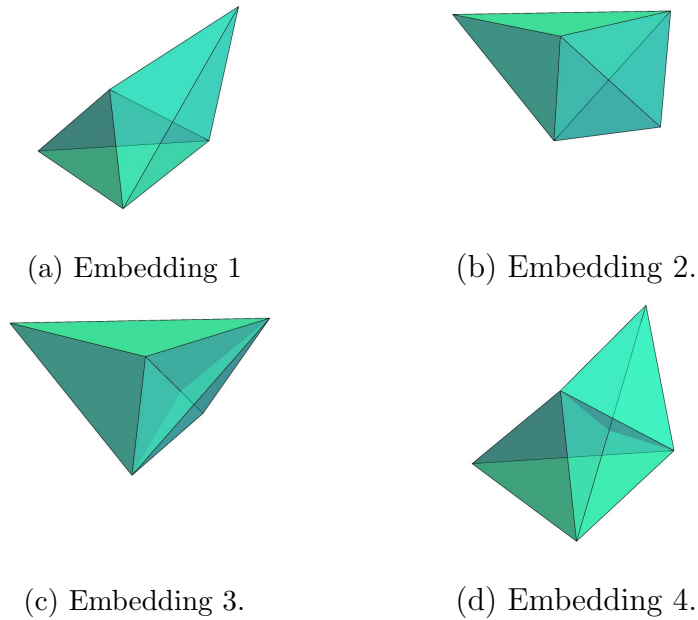


Figure 1.9: Four embeddings from Euclidean distance equations of figure 1.8 (a).

Moreover, we have applied two computational methods related to sub-graphs structures. The first method is trilateration, adapted from the method used in a satellite system. The second one is what we have developed using the linearity of intersecting circles. Linearity means that a linear equation can be obtained by subtracting one circle equation from another. We will also briefly introduce a few existing methods, including optimization. Our methods work

with a relatively larger number of points compared to the resultants, homotopy continuations, and Euclidean distance matrix without high performance computing resources. However, it has an error inflation problem caused by the sequential computation.

In chapter 4, we are working on continuous surfaces related to this setting. We still work with bounded surfaces using the Euler-Lagrange equation. However, instead of Euclidean length, we have applied constraints related to the perimeter. These can be viewed as isoperimetric problems using a constitutive relation (see appendix A.3 for isoperimetric problems). The physical interpretation of these can be used in describing a membrane with applied forces. The result is also related to Euler’s elastica, which is associated with thin inextensible material. Several studies and experiments connected to Euler’s elastica can be found in [6][28][54][70][46]. Intuitively, this can be related to the Willmore energy and Willmore surfaces studied in computational geometry. For example, Willmore Hopf tori can be generated by stereographic projection of  $S^3$  (3-sphere) from a closed constrained elastic curve [100] (see appendix D.2). Moreover, Willmore energy states bending energy in n-dimensional space, and the lower bound of this is related to minimal surfaces. Minimal surfaces are a subset of the constant-mean-curvature surfaces. The following figure 1.10 shows an example of a constant mean curvature surface of genus two, which will be of interest to some readers.



Figure 1.10: Experimental constant mean curvature surface of genus 2 by GeometrieWerkstatt in [94] under License CC BY-NC-SA 3.0.

Next, we show the  $n$ -dimensional extension using a constitutive relation. These solutions

are in integral form; some do not have known answers. Therefore, we offer a method based on a binomial approximation to estimate these integrals for analytical purposes.

We close this thesis in Chapter 5 with conclusions, including further studies.

# Chapter 2

## Conditions, upper and lower bounds for a pinned rigid graph

As discussed in the introduction, we can have multiple results if we fold a flat sheet from a given Euclidean length (pattern).

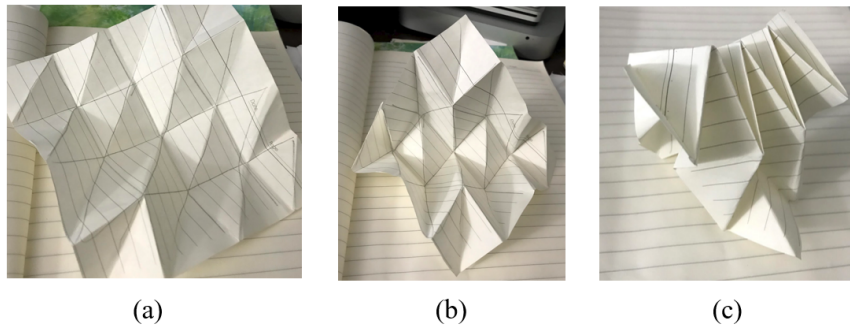


Figure 2.1: A flat triangulated sheet can have multiple embeddings.

Checking whether a graph is rigid will help determine whether the number of solutions is finite. Sometimes, knowing the maximum number of embeddings a graph can have is convenient. One case will be a bar and joint structure. Once we know about maximal embeddings, even if the bar length has changed, we can estimate all shapes of these networks. Although these structures are rigid, they can have an infinite number of position vectors from rigid transformation if we do not have any prior position information. Therefore, we have focused on the bounded surface; pinned rigid graphs to reconstruct position vectors from

given Euclidean lengths. In this chapter, we will discuss conditions and bounds for a pinned rigid graph. Section 2.1 introduces previous works for the number of embeddings in  $\mathbb{R}^2$  and  $\mathbb{R}^3$ . With a mixed volume method, we can predict almost the exact number of solutions [98] for a system of polynomials by Newton polytope. However, these approaches need algebraic computation. Therefore, in section 2.2, we introduce our approach to estimating embeddings employing simple counting criteria using a concept called “properly intersected  $n$ -spheres” with Bézout’s Theorem (Theorem B.3.2). Figure 2.2 presents a graphical illustration, and we are considering case (a) as our estimation.



(a) Properly intersected 2-spheres.      (b) Not properly intersected 2-spheres.

Figure 2.2: Illustrations of properly intersected 2-spheres from [113].

We can deduce all the Euclidean distance functions related to unknown vertex  $v_i$  to several circles, and we have defined embeddings based on the number of intersection points. We know that properly intersected two circles have 2 points up to multiplicity. However, we have assumed that a circle projected  $xy$ -plane in  $\mathbb{R}^3$  will become an ellipse with the same number of solutions. Thus, we set an upper bound as 4 (which is analogous to the maximal number of solutions for a system of two second-order polynomials). Therefore, we have estimated

that the maximal number of embeddings  $N_G$  for a graph  $G$  will vary  $2^m \leq N_G \leq 4^m$  for  $m$  unknown vertices ( $N_G$  is the number of embeddings of  $G$  from the given edge set. See Definition B.2.4 for details). In our context, the graph is  $C^1$ -differentiable and does not contain a loop.

**Definition 2.1.** A graph  $G(V, E)$  is a discrete network constructed to  $n$  vertices  $V = \{v_1, \dots, v_n\}$  and  $m$  edges  $E = \{e_1, \dots, e_m\}$ .

We can find more detailed definitions in Appendix B.2. We will use cardinality  $|V| = n$ ,  $|E| = m$  to notate the number of elements for convenience. Next, we will define a generic rigid framework and minimally rigid graph for Chapter 2.1.

**Definition 2.2** ([41]). A framework is said to be generic if the set containing the coordinates of all its points is algebraically independent.

We can also write generic configuration as shown below.

**Definition 2.3.** Generic configuration means a configuration for which the set of the  $d|V|$  coordinates of the points is algebraically independent over the rationals [29].

**Definition 2.4** ([4]). A rigid graph is (generically) minimally rigid if any edge removal breaks the rigidity.

## 2.1 Generic upper and lower bounds for a rigid graph

We will cover previous studies and results for the upper bound of rigid graphs in dimensions 2 and 3. However, we will slightly change from a rigid graph to a pinned rigid graph.

### 2.1.1 Dimension 2

**Definition 2.5** (Definition 1.7[16]). A Laman graph is a graph  $G(V; E)$  such that  $|E| = 2|V| - 3$ , and for every sub-graph  $H(V'; E') \subset G$  it holds  $|E'| \leq 2|V'| - 3$ .

**Definition 2.6** (Definition 2[30]). For a Laman graph  $G = (V, E)$  we define  $Lam_2(G)$ , called the Laman number of  $G$ , to be the number of (complex) planar embeddings that a generic labeling  $\lambda : E \rightarrow \mathbb{C}$  (the “edge lengths” of  $G$ ) admits. We define  $M_2(n)$  to be the largest Laman number that is achieved among all Laman graphs with  $n$  vertices.

Next, we will illustrate how to construct a rigid graph referred to as Henneberg sequences.

**Definition 2.7** ([10][16][30]). Henneberg sequences are used to construct Laman graph inductively such that, for a graph  $G$ , there is a sequence  $G_3, G_4, \dots, G_n$  of Laman graphs on  $3, 4, \dots, n$  vertices.  $G_3$  is a triangle,  $G_n = G$  and each graph  $G_{i+1}$  is obtained from the previous one  $G_i$  via one of two types of steps

1. Type I : adds a new vertex and two new edges connecting this vertex to two arbitrary vertices of  $G_i$  (increase Laman number by a factor of 2)
2. Type II : adds a new vertex and three new edges, and removes an old edge. The three new edges must connect the new vertex to three old vertices, such that at least two of them are joined via an edge which will be removed (no concrete relations with Laman number).

Figure 2.3 shows Henneberg sequence (b) type I and (c) type II.

**Lemma 2.0.1** (Lemma 5.1 [10]). Any realizable Henneberg I graph obtained by “adding triangles” has exactly  $2^{n-2}$  embeddings.

This implies any triangulation with non-crossing edges in  $\mathbb{R}^2$  has  $2^{n-2}$  embeddings. The following figure 2.4 demonstrates an example for  $n = 4$  which is  $N_G = 2^2 = 4$ .

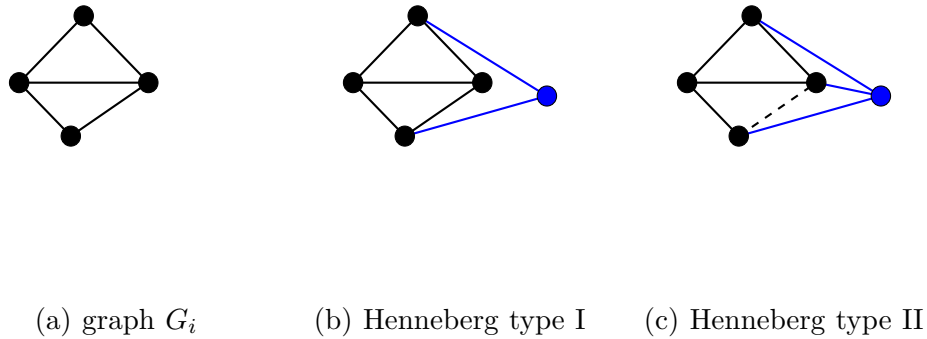


Figure 2.3: Henneberg sequence for (a) graph  $G_i$  (b) graph  $G_{i+1}$  adding vertex (blue dot) using type I (c) graph  $G_{i+1}$  adding vertex (blue dot) using type II (dashed line represents edge will be removed).

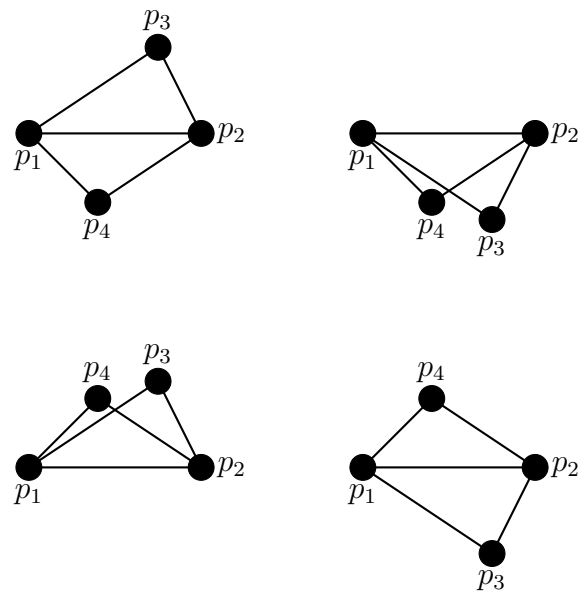


Figure 2.4: Planar triangulation for  $n = 4$ .

We can apply this similarly for a pinned rigid graph if the number of pinned vertices is 2. Figure 2.4 shows that embeddings can be counted from the number of flipping (or folding) sub-graphs of  $G$ . Figure 2.5 depicts one example. The number of realizations will

be remained as same if we pin  $p_1, p_2$  of figure 2.4. (The other two realizations are reflected graph along the line  $(p_1, p_2)$ .)

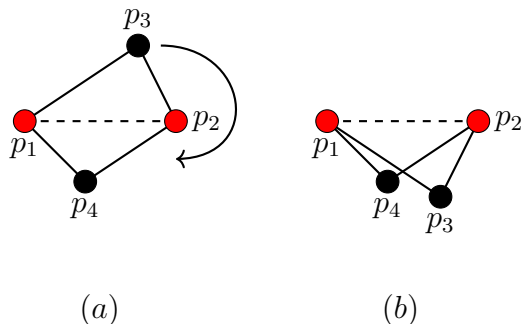
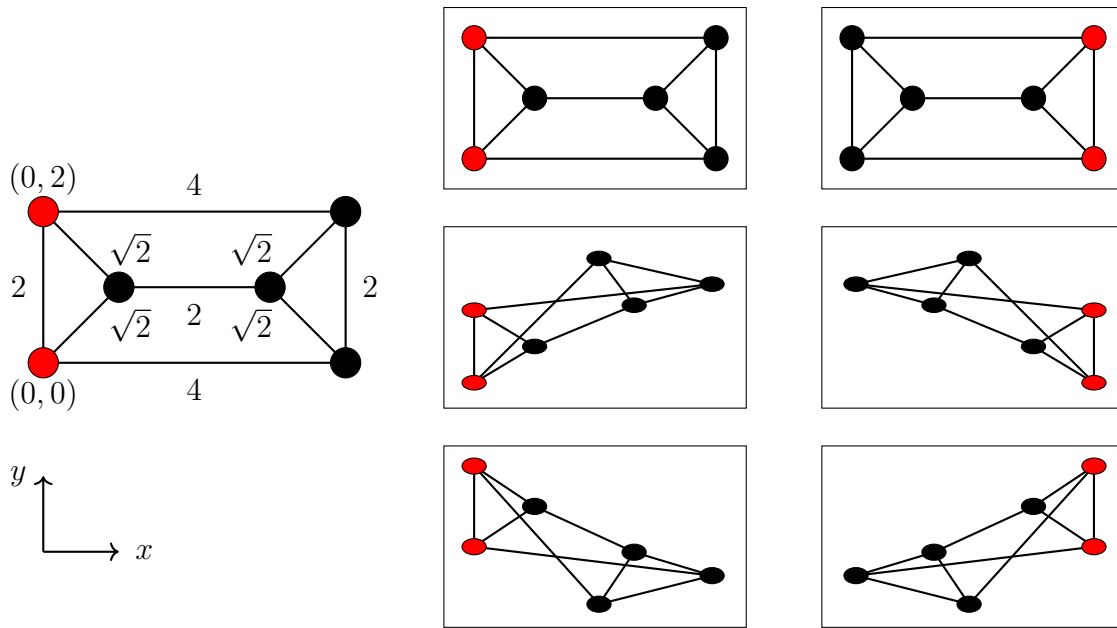


Figure 2.5: Graph (b) can be obtained by folding a sub-graph of (a).

**Definition 2.8.** A Desargues framework is an infinitesimally rigid graph constructed from 9 edges and two triangles. Note that it is different from a general Desargues framework in Graph theory. Details can be found in [10][30].

Figure 2.6 shows one of Desargues frameworks. (a) Red dots represent pinned points with fixed  $(x, y) \in \mathbb{R}^2$ , and the number on each edge implies edge length. Black dots are unpinned points. (b) a number of embeddings in  $\mathbb{R}^2$  with given information. Notice that  $N_G = 6$  for this configuration (a set of edge lengths).

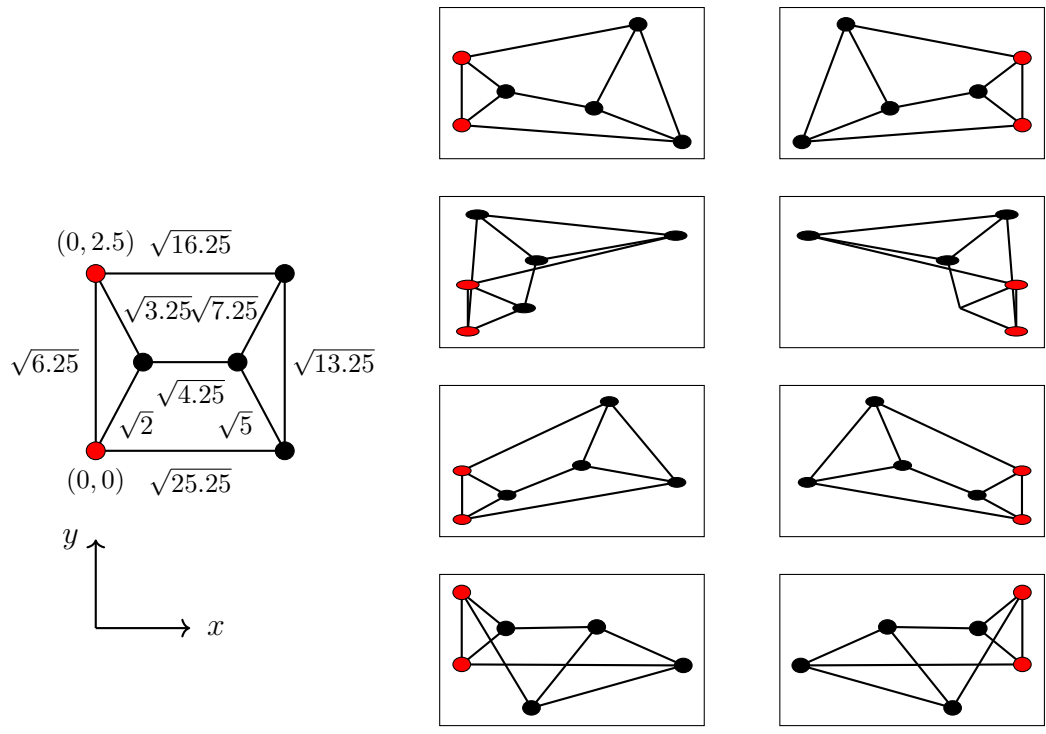


(a) Pinned points and edge lengths

(b) number of embeddings

Figure 2.6: Edge length set having 6 embeddings for Desargues framework  $G$ .

Figure 2.7 shows the same graph with different configuration compared to figure 2.6. We have  $N_G = 8$  in this case.



(a) Pinned points and edge lengths

(b) number of embeddings

Figure 2.7: Edge length set having 8 embeddings for Desargues framework  $G$ .

**Lemma 2.0.2** (Lemma 5.3[10]). There exist edge lengths for the Desargues framework, which induce 24 embeddings.

Proof of lemma is included in [10]. One can also use  $CM$  matrix (Cayley-Menger matrix) and use mixed volume technique to get 24 embeddings. Details can be found in [23][78]. Figure 2.8 shows Desargues framework with  $N_G = 24$ . Note that compared to figure 2.6 and 2.7, figure 2.8 has different pinned vertices.

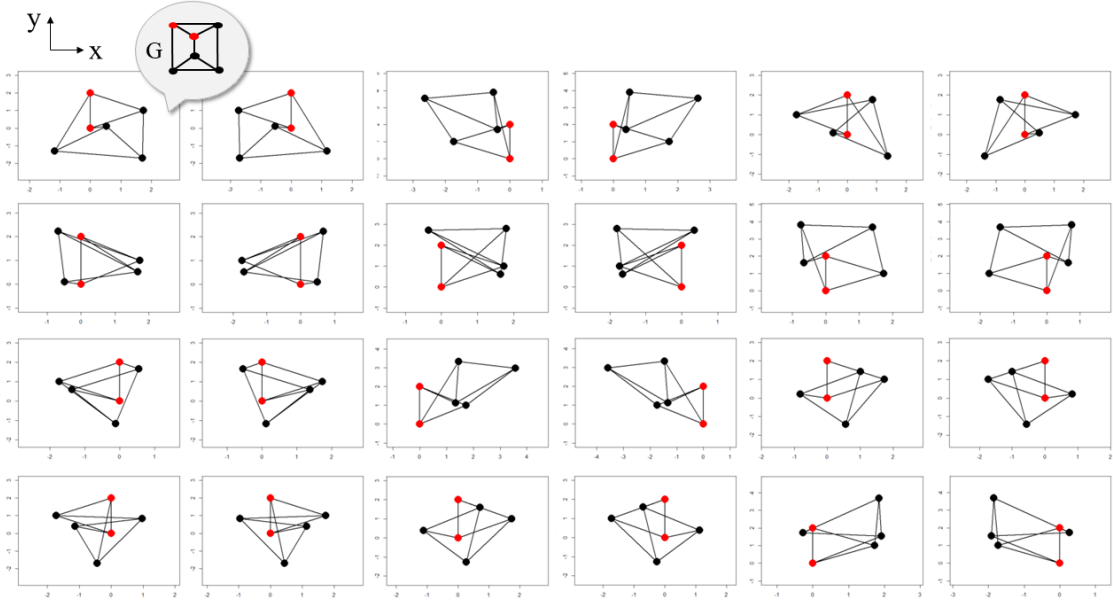


Figure 2.8: Maximum embeddings for Desargues framework  $G$  [16].

Recall that  $Lam_2(G)$  is the maximum possible realization of graph  $G(V; E)$ .  $Lam_2(G)$  for the Desargues framework is 24 [16]. As we observed for figure 2.6, figure 2.7, and figure 2.8,  $N_G \leq Lam_2(G)$  for the graph  $G$ .

**Lemma 2.0.3** (Lemma 5.4[10]). There exist edge lengths for which the number of embeddings of the iterated “caterpillar” Desargues framework is of the order of  $24^{n/4} \simeq (2.21)^n$ .

**Lemma 2.0.4** (Proposition 5.6[10]). There exist edge lengths for which the number of embeddings of the iterated “fan” Desargues framework is of the order of  $24^{n/3} \simeq (2.88)^n$ .

Figure 2.9 (a) shows an example of caterpillar construction and (b) is an example of fan construction. The red circled graph represents each construction’s unit (Desargues framework).

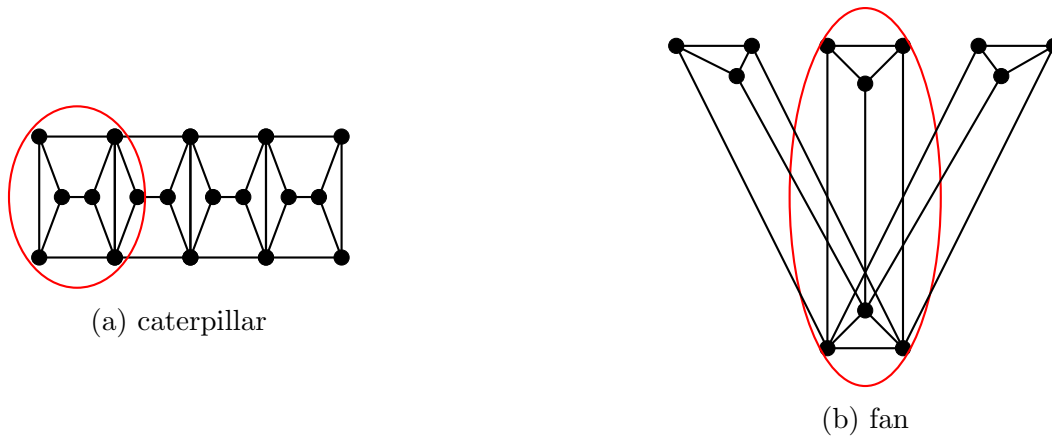


Figure 2.9: Examples of (a) caterpillar and (b) fan construction [30].

Now we will discuss the realization of all Laman graphs with a fixed number of vertices. The following table shows the number of Laman graphs with different numbers of vertices. Figure 2.10 shows all realization for Laman graph  $|V| = 5$  and some realizations for Laman

$ V $	2	3	4	5	6	7	8	9
#	1	1	1	3	13	70	608	7222

Table 2.1: Number of Laman graphs with  $|V|$  vertices computed in [16].

graph  $|V| = 6$ .

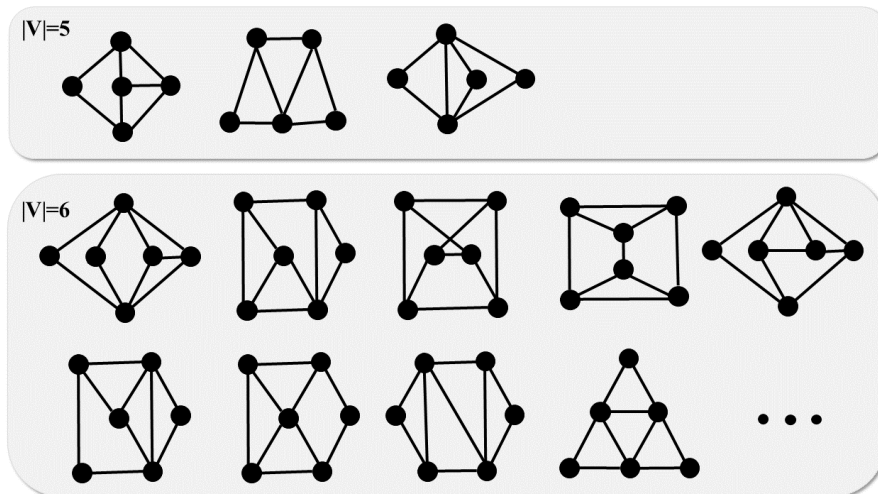


Figure 2.10: Some realizations for Laman graphs  $|V| = 5, 6$  embedded in  $\mathbb{R}^2$  [16][117].

Notice that for fixed  $|V|$ , all graphs have the same number of edges,  $|E|$ . However, these

graphs have a different number of embeddings. The below table shows maximal and minimal values of  $Lam_2(G)$  for the same number of vertices. By definition, we have  $Lam_2(G) \leq M_2(n)$

$ V $	3	4	5	6	7	8	9
min	2	4	8	16	32	64	128
max	2	4	8	24	56	136	344

Table 2.2: Minimal and maximal Laman number among all Laman graphs with  $|V|$  vertices [16] for  $6 \leq |V| \leq 9$  and Lemma 2.0.1 was used for  $3 \leq |V| \leq 5$  (all graphs are constructed with triangles).

for  $G(V; E)$  and  $|V| = n$ . There are several ways to get these numbers. For small  $|V|$ , the mixed volume technique can be used for  $|V| \geq 6$ . It can also be counted using computer software by assigning different edge lengths. From the table 2.2, we can see  $M_2(6) = 24$  and  $M_2(7) = 56$ . Next, we will consider lower bounds of  $M_2(n)$  for some  $n$  introduced in [30]. The following equations are lower bounds of  $M_2(n)$  using the caterpillar and fan construction as represented in figure 2.9 [30].

1. Caterpillar:  $M_2(n) \geq 2^{(n-2) \bmod (|V|-2)} \cdot Lam_2(G)^{\lfloor (n-2)/(|V|-2) \rfloor}$  for  $n \geq 2$
2. Fan:  $M_2(n) \geq 2^{(n-3) \bmod (|V|-3)} \cdot 2 \cdot (Lam_2(G)/2)^{\lfloor (n-3)/(|V|-3) \rfloor}$  for  $n \geq 3$

We can evaluate the maximal Laman number through these constructions, as shown below. Details can be found in reference [30].

**Theorem 2.1** (Theorem 5[30]). The maximal Laman number  $M_2(n)$  satisfies

$$M_2(n) \geq 2 \cdot 2^{(n-3) \bmod 15} \cdot 976908^{\lfloor (n-3)/15 \rfloor}$$

We will introduce the upper bound from [10] using Theorem B.3.4.

**Theorem 2.2** (Theorem 4.3[10]). Given a generic choice of edge lengths, a Laman graph with  $n$  vertices has at most  $2 \deg(CM^{2,n}(\mathbb{C})) = \binom{2n-4}{n-2}$  planar embeddings, up to rigid motions.

$ V $	3	4	5	6	7	8	9
$M_2(n)$	2	4	8	24	56	136	344
lower (Theorem 2.1) [30]	2	4	8	16	32	64	128
upper (Theorem 2.2) [10]	2	6	20	70	252	924	3432

Table 2.3: Maximal Laman number and upper bound among all Laman graphs with  $|V| = n$  vertices for  $3 \leq |V| \leq 9$  [16].

Table 2.3 shows a comparison between the maximal Laman number derived from [30], the upper bound from [10] using Cayley–Menger variety  $CM^{d,n}(\mathbb{C})$  (Theorem 2.2), and lower bound from [30]. (Notice that the value of the upper bound increases drastically for larger  $n$ .) Recall that Laman graphs are minimally rigid. Thus, Laman graphs do not include complete, globally rigid, or redundantly rigid graphs. However, these graphs are over-constrained compared to Laman graphs, so it is easy to conclude  $N_G \leq Lam_2(G')$  where  $G'$  is a minimally rigid graph having the same number of vertices with  $G$  such that  $E(G') \subseteq E(G)$ .

### 2.1.2 Dimension 3

In this subsection, we will compare the upper and lower bounds of a minimally rigid graph in  $\mathbb{R}^3$ . Like the Laman graph in  $\mathbb{R}^2$ , a minimally rigid graph can be constructed using Henneberg sequences. Since the Laman graph usually refers to a minimally rigid graph in  $\mathbb{R}^2$ , for  $\mathbb{R}^3$ , we will use the definition from [4].

**Definition 2.9** ([4]). A Geiringer graph refers minimally rigid graph in  $\mathbb{R}^3$ .

**Definition 2.10** ([4][30][10]). Henneberg sequences are used to construct the Geiringer graph inductively, such that for a graph,  $G$  is a sequence  $G_3, G_4, \dots, G_n$  of Geiringer graphs on  $3, 4, \dots, n$  vertices.  $G_3$  is a triangle,  $G_n = G$  and each graph  $G_{i+1}$  is obtained from the previous one  $G_i$  via one of two steps.

1. Type I : adds a new vertex and three new edges connecting this vertex to three arbitrary vertices of  $G_i$

2. Type II : adds a new vertex and four new edges and removes an old edge. The four new edges must connect the new vertex to four old vertices, so at least three of them are joined via an edge that will be removed.
  
3. Type III : adds a new vertex and five new edges and removes two old edges.

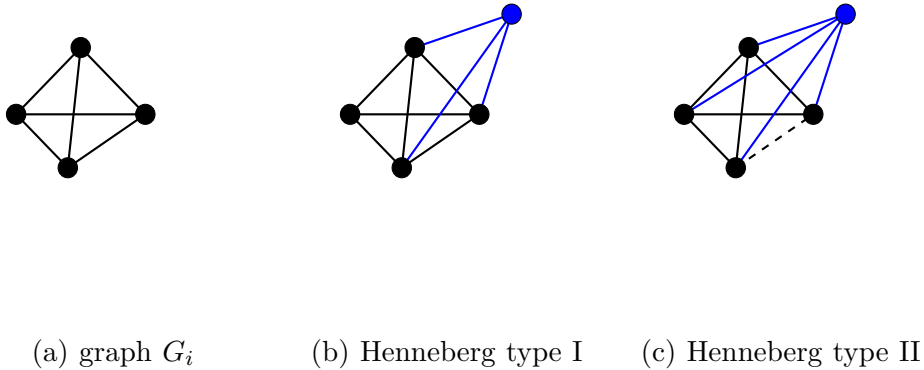


Figure 2.11: Henneberg sequence (a) graph  $G_i$  (b) graph  $G_{i+1}$  adding vertex (blue dot) using type I (c) graph  $G_{i+1}$  adding vertex (blue dot) using type II (dashed line represents edge will be removed).

**Definition 2.11** (Definition 6[30]). For a Geiringer graph  $G = (V, E)$  we define  $Lam_3(G)$ , called the  $3D$ -Laman number of  $G$ , to be the number of (complex) spatial embeddings in  $\mathbb{C}^3$  that a generic labeling  $\lambda : E \rightarrow \mathbb{C}$  (the 'edge lengths' of  $G$ ) admits. We define  $M_3(n)$  as the largest  $3D$ -Laman number achieved among all Geiringer graphs with  $n$  vertices.

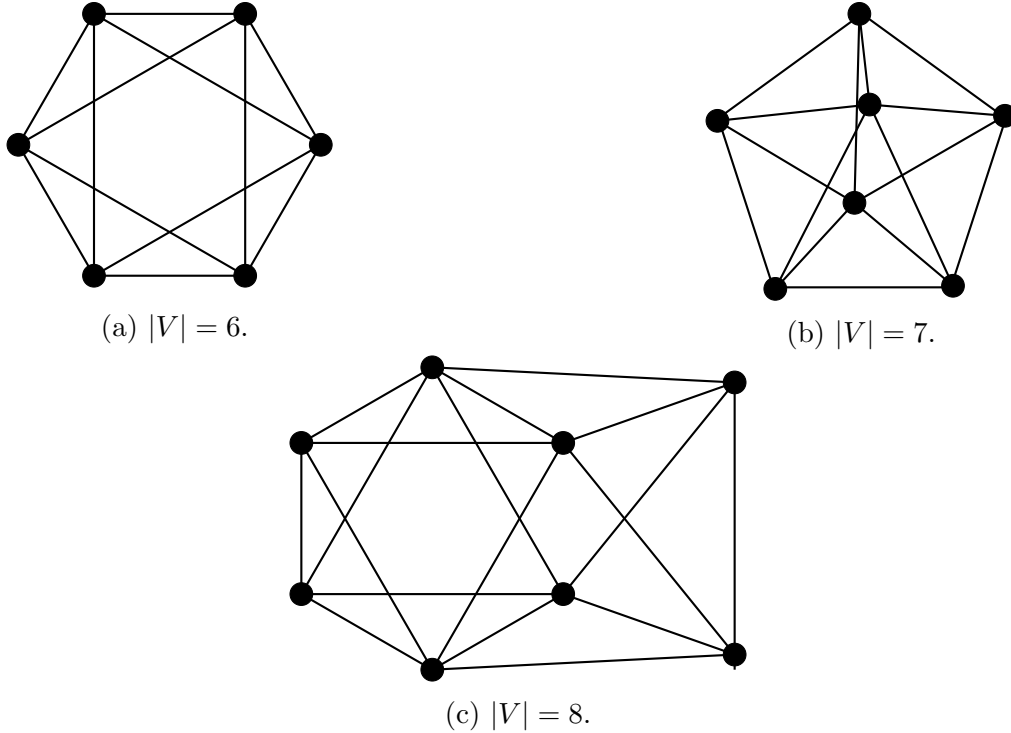


Figure 2.12: Geiringer graphs (a)  $|V| = 6$ , (b)  $|V| = 7$ , and (c)  $|V| = 8$  [30].

Figure 2.12 shows examples of Geiringer graphs  $6 \leq n \leq 8$  [30]. Lower bounds, as in dimension two, can be estimated by a caterpillar and fan construction. Following theorem 2.3 represents estimated bounds from [30] using these methods.

**Theorem 2.3** (Theorem 7[30]). The maximal number  $M_3(n)$  satisfies

$$M_3(n) \geq 2^{(n-3) \bmod 7} \cdot 2560^{\lfloor (n-3)/7 \rfloor}$$

$M_3(n)$  grows approximately  $3.06825^n$ .

Meanwhile, we can get the upper bounds from Cayley–Menger variety  $CM^{d,n}(\mathbb{C})$  as dimension 2. The following theorem shows upper bounds from [10].

**Theorem 2.4** (Theorem 4.4[10]). Given a generic choice of edge lengths, the 1-skeleton of a simplicial convex polyhedron with  $n$  vertices has at most  $2 \deg(CM^{3,n}(\mathbb{C})) = (2^{n-3}/(n-2)) \binom{n-6}{n-3}$  embeddings in  $\mathbb{R}^3$ , up to rigid motions.

Note that The 1-skeleton of a polyhedral surface is the set of edges and vertices of the surface [88]. We can approximate  $D^{d,n} = \deg(CM^{d,n}(\mathbb{C}))$  bound to  $2^{nd}$  for sufficiently large  $n$  in  $d$ -dimensional space (Theorem B.3.4). Table 2.4 shows computed  $M_3(n)$  from [30], upper bounds, and lower bounds among vertices for  $6 \leq |V| \leq 10$ . Like dimension 2, Geiringer

$ V $	6	7	8	9	10
$M_3(n)$ [30]	16	48	160	640	2560
lower (Theorem 2.3)	8	16	32	64	2560
upper (Theorem 2.4)	40	224	1344	8448	54912

Table 2.4: Maximal number and upper bounds among all Geiringer graphs with  $|V| = n$  vertices for  $6 \leq |V| \leq 10$  [30].

graphs do not include complete, globally rigid, or redundantly rigid graphs so that we can conclude  $N_G \leq Lam_3(G')$ .  $G'$  is a minimally rigid graph having the same number of vertices with  $G$  such that  $E(G') \subseteq E(G)$ .

## 2.2 Conditions for a graph to have a finite number of embeddings

We will introduce our work for the bounded graph using a simple algebraic approach to count the number of embeddings.

## 2.2.1 Discrete annulus

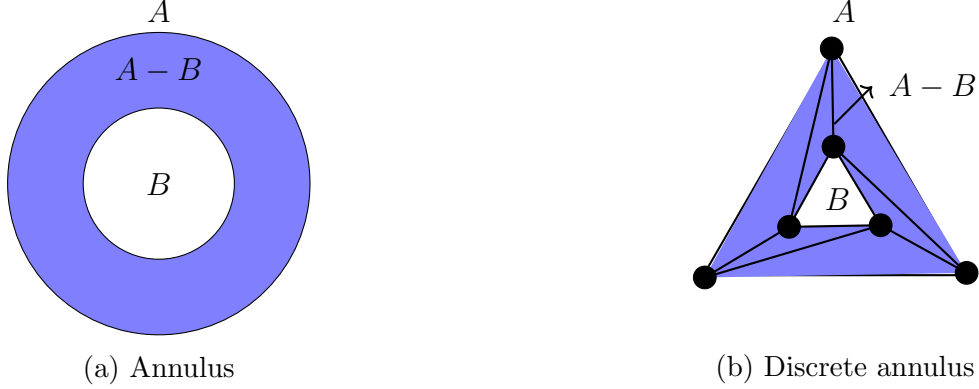


Figure 2.13: Examples of (a) annulus and (b) discrete annulus.

**Definition 2.12.** Discrete annulus is a graph constructed to inner polygon ( $B$  in figure 2.13 (b)), outer polygon ( $A$  in figure 2.13 (b)), and edges connecting these two ( $A-B$  in figure 2.13 (b)).

**Definition 2.13.** For a pinned framework  $\tilde{G} = G(I, P; E')$  (Definition B.2.13),  $B$  is defined as a set of edges connecting  $p \in P$  and  $i \in I$ .

**Definition 2.14.** Properly intersected  $d$ -spheres are any pair of  $d$ -spheres where the overlapped area will form  $S^{d-1}$  (See figure 2.2 for  $S^1$ ).

**Definition 2.15.**  $n$ -properly intersected  $d$ -spheres implies any pair of  $d$ -spheres where overlapped area of two  $S^d$  will form  $S^{d-1}$  and intersection region of two  $S^{d-1}$  will form  $S^{d-2}$  such that common intersection of  $n$  number of  $d$ -spheres will form  $S^{d-n+1}$  such that  $S^{d-n+1}$  is contained in intersection of two  $S^{d-n+2}$ 's.

**Proposition 2.4.1.** Let  $f_1, \dots, f_k \in k[X] = k[x_1, \dots, x_n]$  be Euclidean distance function between  $x$  and point  $q_i \in \mathbb{A}^n$  for  $1 \leq i \leq k$  with real values such that  $f_1 = d(x, q_1) - l_1, \dots, f_k = d(x, q_k) - l_k$  where  $l_i \in \mathbb{R} \setminus \{0\}$ , then for solution space  $T$  which satisfies  $f_i(T) = 0$  for  $1 \leq i \leq k$ , we have  $T \subseteq \mathbb{A}^m$  where  $m = n - \text{dimension of vectors } \{q_1 - q_2, \dots, q_1 - q_k\}$  ( $\dim T \leq m$ ).

*Proof.* Suppose  $f_1, f_2 \in I$ , then  $f_1 - f_2 \in I$  by Definition B.1.5. Because  $q_i$  is a point with real value, we get  $f_1 - f_2 = d(x, q_1) - d(x, q_2) = (l_1 - l_2 - (q_1^1)^2 + (q_2^1)^2 - \dots - (q_1^n)^2 + (q_2^n)^2) + 2 \cdot (q_1^1 - q_2^1)x_1 + \dots + 2(q_1^n - q_2^n) \cdot x_n = b_{1,2} + \sum_{i=1}^n a_i \cdot x_i$  where  $b_{1,2} = l_1 - l_2 - (q_1^1)^2 + (q_2^1)^2 - \dots - (q_1^n)^2 + (q_2^n)^2$ ,  $a_i = 2(q_1^i - q_2^i)$ . We also know that from Definition B.1.5 if  $f_1 - f_2, f_1 - f_3 \in I$ ,  $f_1 - f_2, f_2 - f_3 \in I$ . Without loss of generality, we take a set  $I = \{f_1, f_1 - f_2, \dots, f_1 - f_k\}$ , by B.3.0.1 (ii),  $Z(I) = Z(f_1 + f_1 - f_2 + \dots + f_1 - f_k) = Z(f_1) \cap Z(\sum f_1 - f_i)$ . Since  $f_1 - f_j$ 's are a linear combination of  $x_i$ 's, thus the ideal  $I$  is minimally generated by a minimal basis of  $f_1 - f_j$ 's and  $f_1$ . If we assume a minimal basis of  $f_1 - f_j$ 's has dimension  $r$ , the dimension of  $I$  will be  $n - r$ . Moreover, if dimension of polynomials  $(f_1 - f_2, \dots, f_1 - f_k)$  is  $r$ , then  $k[x_1, \dots, x_n]/(f_1, f_1 - f_2, \dots, f_1 - f_k) \cong k[x_1, \dots, x_m]/(f'_1)$  for  $m = n - r$  where  $f'_1$  is new equations with dimension at most  $m$  obtained from  $f_1$  using linear relations of  $(q_1 - q_i)$ 's.  $\square$

**Definition 2.16.** All sub-graph  $H \subset G$  defined as  $H = \{p_1, \dots, p_n, v_i\}$  for  $v_i \in I, p_j \in P$  of pinned graph  $G(I, P; E')$  is  $(n - 1)$ -linear in  $\mathbb{R}^d$  for the  $d \times (n - 1)$  matrix  $C(G)$  defined by

$$C(G) = \begin{bmatrix} (p_1^1 - p_2^1) & \cdots & (p_1^d - p_2^d) \\ & \vdots & \\ (p_1^1 - p_n^1) & \cdots & (p_1^d - p_n^d) \end{bmatrix}$$

and  $d \times n$  matrix  $C_v(G)$

$$C_v(G) = \begin{bmatrix} (v_i^1 - p_1^1) & \cdots & (v_i^d - p_1^d) \\ & \vdots & \\ (v_i^1 - p_n^1) & \cdots & (v_i^d - p_n^d) \end{bmatrix}$$

such that  $\text{rank } C(G) = n - 1$  and  $\text{rank } C_v(G) = \min(n, d)$  for  $n \leq d + 1$ .

The above definition implies a set  $H$  is in the general position (Definition A.1.3).

**Proposition 2.4.2.** For a pinned graph  $G(I, P; E')$ , vectors  $(p_j - p_k)$ 's are linearly independent for  $v_i \in I$  and  $p_j, p_k \in P$  ( $1 \leq j \neq k \leq d$ ) in a vector space  $\mathbb{R}^d$  if

- (i)  $\text{rank } C_v(M) = d$  where a graph  $M$  is defined by pinned vertices  $V_M = \{v_i, p_1, \dots, p_d\}$  with edges connecting these points.
- (ii)  $d$ -properly intersected  $(d - 1)$ -spheres defined by non-zero Euclidean distance function between  $v_i$  ( $i$  is fixed) and  $d$  number of distinct  $p_j = (p_j^1, \dots, p_j^d)$ 's.

*Proof.* (i) If  $\text{rank } C_v(M) = d$ , then we can obtain  $\text{rank } C(M) = d - 1$ . We can obtain a relation of  $p_j - p_k$  by subtracting  $k$ -th row from  $j$ -row. The rank of the matrix will be the same by row operation. This implies  $(p_j - p_k)$ 's are linearly independent.

- (ii)  $d$ -properly intersected  $(d - 1)$ -spheres will have a finite number of intersection points ( $S^0$ ) by definition 2.15. Because we can interpret the Euclidean distance function as  $(d - 1)$ -spheres, we have  $d$  number of Euclidean distance functions with  $d$  unknowns such that  $f_j = d(p_j, v_i)$ . From Proposition 2.4.1,  $Z(f'_1)$  will be a set of solutions and the dimension of  $Z(f'_1)$  will be less than and equal to  $m$ . These  $(d - 1)$ -spheres are not  $d$ -properly intersected if  $m \neq 0$  (if solution exists). Therefore,  $(p_j - p_k)$ 's are linearly independent.

For example, if  $d = 3$ , we have

$$\begin{aligned} f_1: (v_i^1 - p_1^1)^2 + (v_i^2 - p_1^2)^2 + (v_i^3 - p_1^3)^2 &= l_1^2 \\ f_2: (v_i^1 - p_2^1)^2 + (v_i^2 - p_2^2)^2 + (v_i^3 - p_2^3)^2 &= l_2^2 \\ f_3: (v_i^1 - p_3^1)^2 + (v_i^2 - p_3^2)^2 + (v_i^3 - p_3^3)^2 &= l_3^2 \end{aligned}$$

That will become

$$\begin{aligned}
f_1 &: (v_i^1 - p_1^1)^2 + (v_i^2 - p_1^2)^2 + (v_i^3 - p_1^3)^2 = l_1^2 \\
f_2 - f_1 &: 2v_i^1(p_1^1 - p_2^1) + 2v_i^2(p_1^2 - p_2^2) + 2v_i^3(p_1^3 - p_2^3) = m^2 \\
f_3 - f_1 &: 2v_i^1(p_1^1 - p_3^1) + 2v_i^2(p_1^2 - p_3^2) + 2v_i^3(p_1^3 - p_3^3) = n^2
\end{aligned}$$

where  $m^2 = l_2^2 - l_1^2 + (p_1^1)^2 - (p_2^1)^2 + (p_1^2)^2 - (p_2^2)^2 + (p_1^3)^2 - (p_2^3)^2$  and  $n^2 = l_3^2 - l_1^2 + (p_1^1)^2 - (p_3^1)^2 + (p_1^2)^2 - (p_3^2)^2 + (p_1^3)^2 - (p_3^3)^2$ . Therefore, we get

$$2 \begin{bmatrix} (p_1^1 - p_2^1) & (p_1^2 - p_2^2) & (p_1^3 - p_2^3) \\ (p_1^1 - p_3^1) & (p_1^2 - p_3^2) & (p_1^3 - p_3^3) \end{bmatrix} \begin{bmatrix} v_i^1 \\ v_i^2 \\ v_i^3 \end{bmatrix} = \begin{bmatrix} m^2 \\ n^2 \end{bmatrix}$$

If vectors  $p_2 - p_1$  and  $p_3 - p_1$  are not linearly independent, the leftmost matrix will have  $rank < 2$  and we can reduce  $f_1, f_2, f_3$  to one or two equations which implies dimension of solution space  $> 0$ . However, by our assumption, each overlapped  $S^2$  will form  $S^1$ , and three  $S^1$  will intersect as points (dimension 0). We require  $rank C(M) = 2 = d - 1$ . Thus, we get the desired result.  $\square$

Note that above Proposition implies for graph  $G = \{p_1, \dots, p_n, v_i\}$  in  $\mathbb{R}^d$ , there exists convex polyhedra containing vertices in  $G$  (locally convex at  $v_i$ ).

**Proposition 2.4.3.** If pinned graph  $G(I, P; E')$  is  $(d - 1)$ -linear, then edges connected to  $v_i$  will have at least  $d$ -properly intersected  $(d - 1)$ -spheres.

*Proof.* Use Definition 2.16 and Proposition 2.4.2.  $\square$

**Theorem 2.5.** There exists a countable number of solutions for  $m$  number of vertices in the inner polygon ( $m > 2$  and  $|I| = m$ ) of a pinned  $d$ -rigid graph (for rigid polytope). If every vertex in the inner polygon has at least  $(d - 1)$  number of connected edges in  $B$  which

is  $(d - 2)$ -linear in  $\mathbb{R}^d$ , and there is a vector  $v_i - v_j$  in an inner polygon which is linearly independent with edges  $b \in B$  connected to  $v_i$  ( $v_j$  is one of the nearest neighbors), then

- (i) Weak condition : we need  $2m = 2|I| = |B|$  and  $3 \leq |P| \leq 2|I|$  to get a countable number of solutions in  $\mathbb{R}^3$ . Generally, we need  $(d - 1)m = (d - 1)|I| = |B|$  for  $\mathbb{R}^d$ . ( $N_G \leq 4^m$  in  $\mathbb{C}$ )
- (ii) Intermediate condition : we need  $2m + 1 = 2|I| + 1 = |B|$  and  $d \leq |P|$  to get upper bound of  $N_G \leq 2^{|I|}$  in  $\mathbb{R}$ .
- (iii) Strong condition : we need  $3m = 3|I| = |B|$  and  $d \leq |P|$  to get two solutions ( $N_G = 2$ ) in  $\mathbb{R}^3$  if every vertex in inner polygon has at least  $d$  number of connected edges in  $B$  and  $(d - 1)$ -linear in  $\mathbb{R}^d$ . We require  $dm = d|I| = |B|$  for  $\mathbb{R}^d$ .

*Proof.* (i) Let's start with  $d = 3$ . For example, we have

$$\begin{aligned} (p_1^1 - x_1)^2 + (p_1^2 - y_1)^2 + (p_1^3 - z_1)^2 &= l_{p_1,1} \\ (p_2^1 - x_1)^2 + (p_2^2 - y_1)^2 + (p_2^3 - z_1)^2 &= l_{p_2,1} \\ (x_1 - x_2)^2 + (y_1 - y_2)^2 + (z_1 - z_2)^2 &= l_{1,2} \end{aligned}$$

where  $p_i = (p_i^1, p_i^2, p_i^3)$ ,  $p_1, p_2 \in P$  are pinned points and  $i_j = (x_j, y_j, z_j)$  for  $i_1, i_2 \in I$ . Let's consider one possible value for  $i_2 \in \mathbb{R}^3$ , then from Lemma B.3.1. The above equation will have a finite number of solutions; thus, none of  $i_j \in I$  can be continuous in some interval. Also, by assumption, the graph is pinned rigid, and by Lemma B.2.3 (consider pinned points as a rigid graph), it is rigid. Therefore, the dimension of infinitesimal motion is zero by Theorem B.2.2, and there exists a finite number of embeddings. Moreover, we can manipulate the given equation and get one relation as

$$\begin{aligned} 2x_1 \cdot (p_1^1 - p_2^1) + 2y_1 \cdot (p_1^2 - p_2^2) + 2z_1(p_1^3 - p_2^3) &= l_{p_2,1} \\ -l_{p_1,1} + (p_1^1)^2 - (p_2^1)^2 + (p_1^2)^2 - (p_2^2)^2 + (p_1^3)^2 - (p_2^3)^2 & \end{aligned}$$

We can rewrite this as  $z_1 = a \cdot x_1 + b \cdot y_1$  because all of  $p_j^i$ 's are constant. Using the previous relation, we can deduce three equations into two circle equations (equivalently, a circle and a line passing two intersection points). We know that the degree of a circle equation in a projective plane is 2. Therefore, by Bézout's Theorem B.3.2 and considering  $i_2$  as a constant by taking one possible solution, the number of intersection points for two properly intersected circle  $X$  and  $Y$  for  $X, Y \in k[x_1, y_1]$  is at most  $\deg X \cdot \deg Y = 4$ . Thus, the maximum number of solutions for each point  $i \in I$  is 4, and we get the upper bound as  $4^{|I|}$ . We know that  $m$ -gon has  $m$  edges. Using our assumption and Proposition 2.4.3, we can consider neighboring edges in the inner polygon, and the polygon is convex. Therefore, for the general  $d$  dimension, we can assume every vertex  $v_i \in I$  will have at least  $d$ -properly intersected  $(d - 1)$ -spheres. Therefore, we can reduce  $d$  number of Euclidean distance equations in  $d$  dimension to 2 circle equations.

- (ii) From (i), if we start with  $d$  pinned points for  $i_1$ , we get two circle equations. By considering the real space solution for circles counting multiplicity, we can get the maximum number of possible solutions as  $2^{|I|}$ .
- (iii) We have  $n + 1$  number of quadratic equations from the Euclidean distance function in  $n$ -dimensional object. Moreover, we know  $n$  positions and one of the unknown points. For example, if we consider 3d case and by (ii), we know that if  $m = 1$ , we get  $N_G = 2$ . Suppose we know  $v_1 = (x_1, y_1, z_1), p_2 = (x_2, y_2, z_2), p_3 = (x_3, y_3, z_3), p_4 = (x_4, y_4, z_4), v_2 = (x_5, y_5, z_5)$ ,  $v_1$  is a neighboring vertex for  $v_2$  in  $I$ , and  $p_2, p_3, p_4$  are

connected to  $v_2$  where  $p_2, p_3, p_4 \in P$ , then we have

$$(x_1 - x_5)^2 + (y_1 - y_5)^2 + (z_1 - z_5)^2 = l_{1,5}$$

$$(x_2 - x_5)^2 + (y_2 - y_5)^2 + (z_2 - z_5)^2 = l_{2,5}$$

$$(x_3 - x_5)^2 + (y_3 - y_5)^2 + (z_3 - z_5)^2 = l_{3,5}$$

$$(x_4 - x_5)^2 + (y_4 - y_5)^2 + (z_4 - z_5)^2 = l_{4,5}$$

Subtracting the last equation to the first three and write as a matrix, then we get

$$\begin{aligned} & \begin{bmatrix} x_4 - x_1 & y_4 - y_1 & z_4 - z_1 \\ x_4 - x_2 & y_4 - y_2 & z_4 - z_2 \\ x_4 - x_3 & y_4 - y_3 & z_4 - z_3 \end{bmatrix} \begin{bmatrix} x_5 \\ y_5 \\ z_5 \end{bmatrix} \\ = & \begin{bmatrix} l_{1,5}^2 - l_{4,5}^2 - x_1^2 + x_4^2 - y_1^2 + y_4^2 - z_1^2 + z_4^2 \\ l_{2,5}^2 - l_{4,5}^2 - x_2^2 + x_4^2 - y_2^2 + y_4^2 - z_2^2 + z_4^2 \\ l_{3,5}^2 - l_{4,5}^2 - x_3^2 + x_4^2 - y_3^2 + y_4^2 - z_3^2 + z_4^2 \end{bmatrix} \end{aligned}$$

If we define

$$\begin{aligned} A &= \begin{bmatrix} x_4 - x_1 & y_4 - y_1 & z_4 - z_1 \\ x_4 - x_2 & y_4 - y_2 & z_4 - z_2 \\ x_4 - x_3 & y_4 - y_3 & z_4 - z_3 \end{bmatrix}, \mathbf{x} = \begin{bmatrix} x_5 \\ y_5 \\ z_5 \end{bmatrix}, \text{ and} \\ b &= \begin{bmatrix} l_{1,5}^2 - l_{4,5}^2 - x_1^2 + x_4^2 - y_1^2 + y_4^2 - z_1^2 + z_4^2 \\ l_{2,5}^2 - l_{4,5}^2 - x_2^2 + x_4^2 - y_2^2 + y_4^2 - z_2^2 + z_4^2 \\ l_{3,5}^2 - l_{4,5}^2 - x_3^2 + x_4^2 - y_3^2 + y_4^2 - z_3^2 + z_4^2 \end{bmatrix} \end{aligned}$$

Because  $A$  has a full rank (by  $(d-1)$ -linear and convexity of  $m$ -gon, it is  $d$ -linear), by inverse matrix theorem, there exists an inverse of  $A$ . Thus, we can compute  $\mathbf{x} = A^{-1}b$ .

We can easily expand the previous equation to the  $d$ -dimensional case since we have

$d+1$  number of Euclidean distance ( $(d-1)$ -spheres) equations. We can compute points sequentially and get a single solution for each point except for the first one. Thus, we have two solutions because the only first point is  $(d-1)$  linear. (If a graph of all pinned points is  $d$ -linear, we get a single solution.)

□

If we consider real embeddings in  $\mathbb{R}^d$ , we get  $2^m$  from the intersection points of overlapping circles.

**Remark 2.5.1.** Considering real solutions (up to rigid motions) of all possible discrete annulus graphs satisfy pinned  $d$ -rigidity and for fixed  $|I| = m$ , the maximum number of embeddings in  $\mathbb{R}^3$  is greater than  $2^m$  (see Definition B.2.15 for pinned  $d$ -rigid).  $M_{3,\text{annulus}}(m) \geq 2^m$ .

Geometrically, we can contain reflection in  $2^m$  real solutions. Thus, we can estimate the existence of a graph having solutions  $2 \cdot 2^m$  up to multiplicity. Note that a pinned  $d$ -rigid graph refers to a  $d$ -dimensional version of a pinned rigid graph (usually for two or three-dimensional space).

**Remark 2.5.2.** For a pinned graph having one or multiple annuli, which satisfies Theorem 2.5 (i), there exists vertex and edge sets having  $2^r \cdot 2^{\sum |I|}$  solutions up to multiplicity for Euclidean distance function.  $r$  is the number of annuli and  $\sum |I|$  is sum of all inner vertices where  $\sum |I| \geq 3$ .

Remark 2.5.1 and 2.5.2 can be explained with following figure.

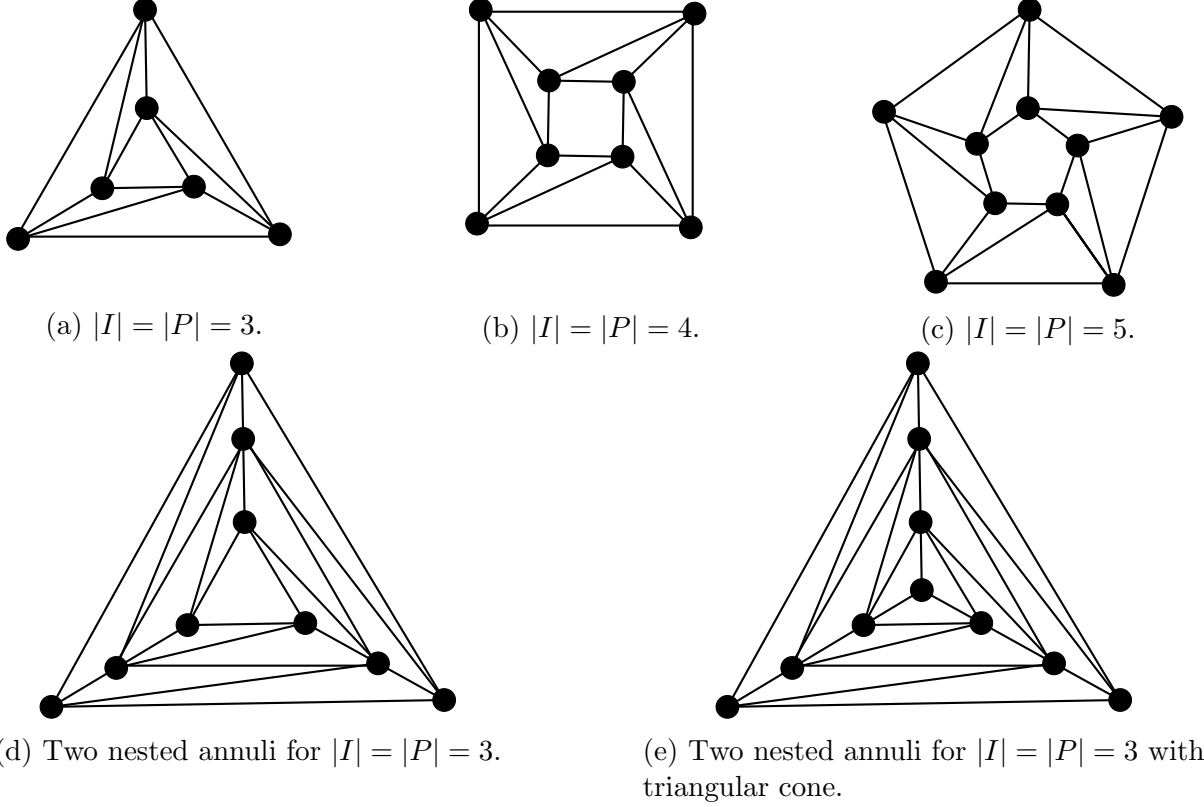
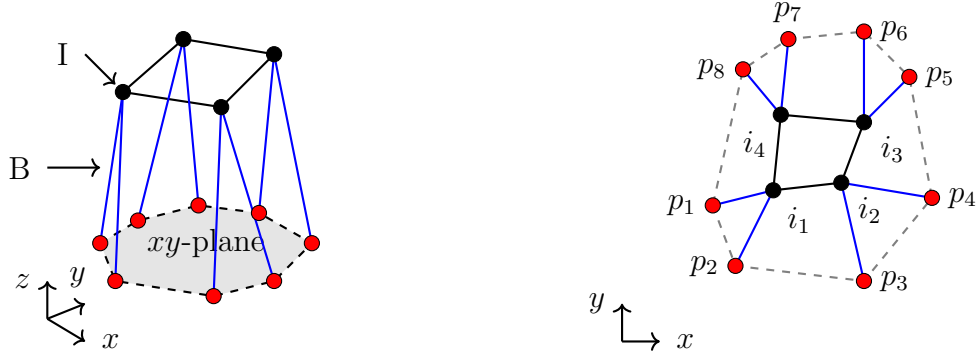


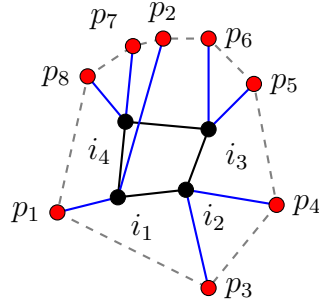
Figure 2.14: (a)  $|I| = |P| = 3$ , (b)  $|I| = |P| = 4$ , (c)  $|I| = |P| = 5$ , (d) nested two annuli with each of them have  $|I| = |P| = 3$ , and (e) (d) with triangular cone.

Figure 2.14 (a) represents the annulus with  $|I| = |P| = 3$ . For some length set satisfies Theorem 2.5 (i), one can get  $2^3$  distinct real solutions and  $2^4$  solutions up to multiplicity. (b) has  $2^4$  distinct real solutions and  $2^5$  solutions up to multiplicity, and (c) has  $2^5$  and  $2^6$  respectively.

**Remark 2.5.3.** Let  $\tilde{G}$  be a pinned graph  $\tilde{G} = G(I, P; E')$  which satisfies  $B = (d - 1)|I|$ ,  $E' = d|I|$ , and  $\text{rank } \mathcal{R}(\tilde{G}) = d|I|$  (see Definition B.2.5 for  $\text{rank } \mathcal{R}(G)$ ) and  $\text{rank } \mathcal{R}(\tilde{G}, q) = d|I| - 1$  (Definition B.2.14). There exists configuration (arrangement) of pinned vertices with different positions  $q'$  satisfies  $\text{rank } \mathcal{R}(\tilde{G}, q') = d|I|$  without changing connection of edges, position of inner vertices, or labels of vertices.



(a) A graph with 8 pinned vertices on  $xy$ -plane. (b) A graph projected on  $xy$ -plane (top view).



(c) Graph (a) with different pinned vertices.

Figure 2.15: (a) 3d graph fixed on a plane with 8 pinned vertices, (b) projected map of graph (a), (c) projected map of modified version for graph (a)

Figure 2.15 shows an example of Remark 2.5.3. (a) shows 3–dimensional graph pinned on a plane. (b) and (c) represent the projected graph on the plane. Consider pinned rigidity matroid  $\mathcal{R}(\tilde{G})$  of  $G$  where pinned points are defined by  $p_1 = (-1, 0, 0), p_2 = (0, -1, 0), p_3 = (1, -1, 0), p_4 = (2, 0, 0), p_5 = (2, 1, 0), p_6 = (1, 2, 0), p_7 = (0, 2, 0), p_8 = (-1, 1, 0)$ . Both (b) and (c) will have  $\text{rank } \mathcal{R}(\tilde{G}) = 12$ . However, if we take a set of inner vertices  $v_1 = (0, 0, 2), v_2 = (1, 0, 2), v_3 = (1, 1, 2), v_4 = (0, 1, 2)$ , rigidity matrix of (a) will be  $\text{rank } \mathcal{R}(\tilde{G}, q) = 11$  and  $\text{rank } \mathcal{R}(\tilde{G}, q) = 12$  for (b). Transitioning (b) to (c) can be simply done by moving  $p_2$  to the combinatorially different position, which increases the linear independence of edges (bases for rigidity matrix). Note that although (b) and (c) have the same labels, they are different graphs for  $G(P; E_P)$ , which is constructed only with pinned points ( $P$ ) and edges connecting them ( $E_P$ ).

**Conjecture 2.16.1.** Let  $G$  be a pinned  $d$ -rigid graph  $|E| = d|I|, |P| = |I|$ . Let the number

of solution from the Euclidean length equation in real space is  $N_G$ . If we define  $G'$  by swapping  $P$  and  $I$ , the number of solutions from the Euclidean length equation in real space is  $N_{G'}$ , which is the same as  $N_G$  unless the length of edges is changed.

**Definition 2.17.** Let sub-graph  $H \subset G$  of the pinned  $d$ -rigid graph be the structure defined by one element  $v \in I$  and corresponding  $b \in B$ . (recall that  $B$  refers to edges connecting one inner vertex and pinned points). We define the number of local symmetry (Definition B.2.16) as the maximum number of possible covering from each  $H$ .  $H$  is a sub-graph generated by each  $v \in I$  (based on the distinct label, sharing vertices do not count).

Figure 2.16 shows an example of counting local symmetry. Notice that this definition allows small variation in edge lengths for covering, so it takes geometrical symmetry related to the number of solutions.

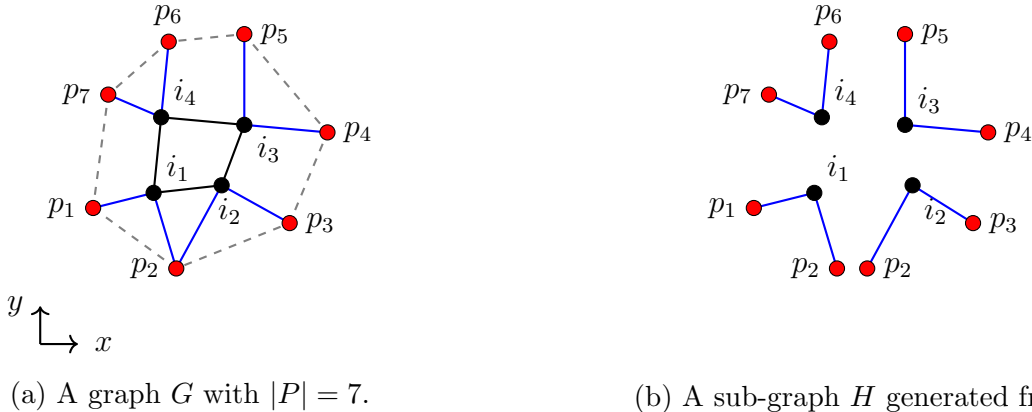


Figure 2.16: (a) a pinned graph projected on a plane with 7 pinned vertices, (b) sub-graph  $H$  generated by each  $i \in I$ , and the number of local symmetry is 2.

**Conjecture 2.17.1.** Let  $G$  be a pinned  $d$ -rigid graph  $|E| = d|I|, |P| = |I|, |I| \geq d$ , and  $(d - 1)|I| = |B|$  with  $N_G$  embedded in  $\mathbb{R}^d$ . Let  $G'$  be a new graph obtained by removing some pinned points with related edges, adding some pinned points  $p$ , and adding edges  $e$  which satisfies  $G' = H \cup e \cup p$  and  $H \subset G$ . For  $G'$  is embedded in  $\mathbb{R}^d$ , there are following properties for  $|P| \geq d$ .

- (i) If  $G'$  satisfies  $|E| = d|I|, |P| < |I|$ , and  $(d - 1)|I| = |B|$ ,  $N_{G'}$  can be estimated to

smaller than or equal to  $N_G$  if the number of local symmetry is smaller than or equal to  $G$ .

(ii) If  $G'$  satisfies  $|E| = d|I|, |P| > |I|$ , and  $(d - 1)|I| = |B|$ ,  $N_{G'}$  can be estimated to greater than or equal to  $N_G$  if the number of local symmetry is greater than or equal to  $G$ .

(iii) If  $G'$  satisfies  $|E| = d|I|, |P| > d$ , and  $|I| = 1 : N_G = 2$

(iv) If  $G'$  satisfies  $|E| = d|I| + 1$  and  $(d - 1)|I| + 1 = |B| : N_G$  can be estimated to smaller than or equal to  $2^{|I|}$  up to multiplicity. (Theorem 2.5 intermediate condition)

This conjecture tells a number of realizations can be decreased if we reduce symmetric vertices. Note that the above property is related to the range of angles for edges and the number of crossing edges. Also,  $N_G$  strongly depends on the choice of edge lengths. As seen

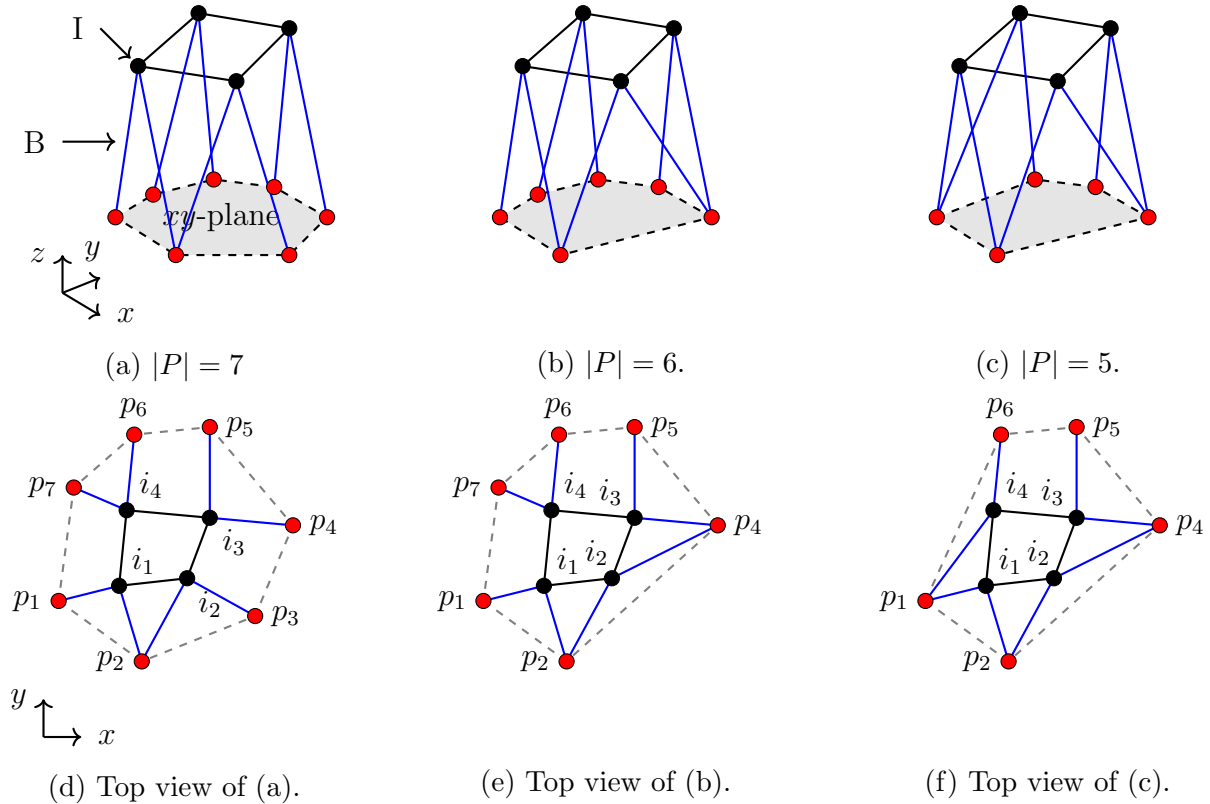


Figure 2.17: (a), (b), and (c) 3d graph fixed on a plane with pinned vertices, (d), (e), and (f) projected map of graph (a), (b), and (c) respectively.

in figure 2.17,

**Conjecture 2.17.2.** A graph satisfies the condition in Theorem 2.5 (iii) is globally rigid but may not be universally rigid.

This is straightforward since a graph satisfies condition (iii) in  $d$  will satisfy condition (i) assuming all of pinned vertices satisfy  $(d - 1)$ -linear condition ( $((d + 1) - 2)$ -linear condition) in  $\mathbb{R}^{d+1}$ .

### 2.2.2 Strips and general graphs

In this subsection, we will define a number of embeddings for a strip-type graph. Note that strip implies a graphical object in  $d$  dimension, so inner vertices do not form a polygon or circle.



Figure 2.18: Examples of (a) strip and (b) discrete strip.

**Definition 2.18.** A discrete strip is a graph constructed to two separate consecutive lines (A and B in figure 2.18 (b)) and edges connecting them.

**Definition 2.19.** Suppose we define a sub-graph  $H \subset G$  as  $v$  in  $\mathbb{R}^d$  and its neighboring points. Edges between these points are said to be locally linearly independent if a sub-graph  $H' \subseteq H \setminus \{v\}$  from  $d$  vertices of  $H$  and  $v$  is in the general position ( $(d - 1)$ -linear).

**Theorem 2.6.** For a graph  $G(V; E)$  with redefined  $G(I, P; E')$  for  $|P| = p$ ,  $|V| = n$ , and  $|I| = m$  from sub-graph structure  $G(P; E_p)$  where all edges connecting to vertex  $v \in V$  are locally linearly independent, we can define the upper bounds for each case as follows.

- (i) Weak condition : if  $|E(v)| \geq d + 1$  for every  $v \in I$ , then  $N_G \leq 2^m$  in  $\mathbb{R}^3$

(ii) Strong condition : if  $|E(v)| \geq d + 2$  for every  $v \in I$ , then  $N_G = 1$  in  $\mathbb{R}^3$

*Proof.* Same as Theorem 2.5 (ii), (iii). □

Note that  $2^m$  is for the generic case. Thus, if there are some algebraic relations between inner vertices (for example, some inner vertices construct a straight line), the number of embedding will be decreased. Next, we will define the same thing for the general graph.

**Theorem 2.7.** For a graph  $G(V; E)$  with redefined  $G(I, P; E')$  for  $|P| = p$ ,  $|V| = n$ , and  $|I| = m$  from sub-graph structure  $G(P; E_p)$  where all edges connecting to vertex  $v \in V$  are locally linearly independent and  $G(P; E_p)$  is rigid, we can define the upper bounds for each case as follows.

- (i)  $G(V; E)$  is rigid and  $d$ -independent (See Definition B.2.12) or locally linearly independent at each  $v \in V$ ,  $G(I, P; E') = G'$  is pinned  $d$ -rigid which satisfies  $|E'| \geq d|I|$ , and  $\text{rank } \mathcal{R}(\tilde{G}, q) = d|I| : N_G \leq k \cdot 4^m$  up to rigid motions where  $k$  is  $N_H$  for  $H = G(P; E_p)$  (see Definition B.2.15 for pinned  $d$ -rigid).
- (ii)  $G(V; E)$  is rigid and  $d$ -independent or locally linearly independent at each  $v \in V$ ,  $G(P; E_p)$  is globally rigid,  $G(I, P; E')$  is pinned  $d$ -rigid which satisfies  $|E'| \geq d|I|$ , and  $\text{rank } \mathcal{R}(\tilde{G}, q) = d|I| : N_G \leq 4^m$  up to rigid motions.
- (iii) A graph is globally rigid :  $N_G = 1$  up to congruence (up to reflection).

*Proof.* (i) Since  $G$  is rigid, at least  $d$  edges for each  $v_i \in I$  are independent of each other. If the dimension of solution space of  $G$  is equal to or greater 1, then it will infinitesimally flex, which violates our assumption. We know that  $d$  independent edges will satisfy  $(d-1)$ -linear which implies every vertex  $v_i \in I$  will have at least  $d$ -properly intersected  $(d-1)$ -spheres. Therefore, we can apply the same argument with Theorem 2.5 and estimate  $G$  will have  $d$  number of Euclidean distance equations in  $d$  dimension, which we will reduce to 2 circle equations. By Bézout's Theorem, we get  $4^{|I|}$ , which will

be bound for a pinned  $d$ -rigid graph. Thus, the total possible realization will be a multiplication of pinned  $d$ -rigid graph  $G(I, P; E')$  and graph  $G(P; E_p)$ .

(ii) Same as above.

(iii) See definition B.2.18.

□

### 2.2.3 Upper and lower bounds

This section will briefly discuss upper and lower bounds. Note that we have considered graphs satisfies Theorem 2.5 condition (i) since (ii) and (iii) are not minimally rigid. Table

$ V $	6	7	8	9	10
lower (annulus)	8	16	32	64	128
upper (annulus)	64	256	1024	4096	16384
$M_3(n)$ [30]	16	48	160	640	2560
upper (Theorem 2.4)	40	224	1344	8448	54912

Table 2.5:  $M_3(n)$  and upper bounds among all Geiringer graphs with  $|V|$  vertices for  $6 \leq |V| \leq 10$  and lower and upper bounds for pinned discrete annulus for  $6 \leq |V| \leq 10$  with  $|P| = 3$ .

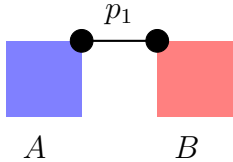
2.5 shows a comparison between upper and lower bounds of discrete annulus for  $|P| = 3$ , the upper bound of the minimally rigid graph from Theorem 2.4, and the maximum number of realization ( $M_3(n)$ ) computed from all minimally rigid graph for  $|V|$  [30]. Note that  $|P| = 3$  is the lowest number for 3-dimensional pinned rigid graph. Thus, if  $|P| > 3$ , lower and upper bounds will be smaller or equal to the number shown in Table 2.5.

# Chapter 3

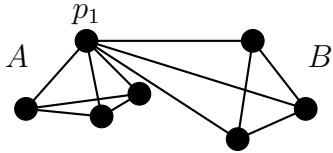
## Explicit construction for a pinned graph to have a finite number of embeddings

### 3.1 Explicit construction for a pinned graph

This section will introduce a sequential method to construct a (pinned) graph with  $2^m$  or  $4^m$  upper bound. Our approach employs adding a patch of a graph composed of one inner vertex and related pinned vertices. The basic idea is simple. First, we can make a graph (one inner vertex and 2-3 pinned points in  $\mathbb{R}^3$ ) to satisfy to be in the general position (see Definition A.1.3) or convex polyhedrons. Next, two pinned rigid graphs can be connected so we can do the computation to reconstruct position vectors from given Euclidean lengths.



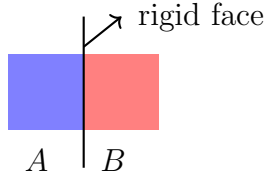
(a) Two graphs A and B are connected via vertex  $p_1$ .



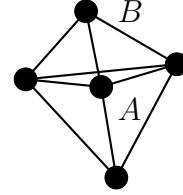
(b) Two tetrahedrons are connected via  $p_1$ .

Figure 3.1: Examples of connecting pinned rigid graphs.

Similarly, we can merge several rigid graphs via rigid faces to construct a union of multiple rigid graphs.



(a) Two graphs, A and B, are glued to a rigid face.



(b) Two tetrahedrons are glued to the triangle.

Figure 3.2: Examples of gluing rigid graphs.

If the face is not rigid, the structure becomes flexible. Figure 3.3 illustrates an example. Each banana (two tetrahedrons) is rigid, but the whole graph is flexible because they are glued to the line.

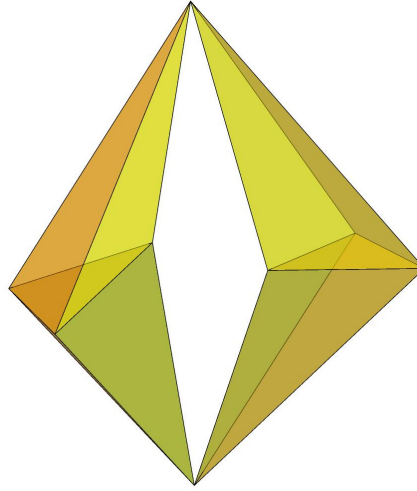


Figure 3.3: Double banana graph.

Note that the first method only works for a pinned rigid graph because the merged graph will not be rigid if there are no pinned vertices. One can compute a rigidity matroid  $\mathcal{R}(G)$  to check if the whole graph can be rigid. In this section, we will talk about  $(d-1)m = (d-1)|I| < |B|$  cases which are related next section (One can easily construct  $(d-1)m = (d-1)|I| = |B|$  case same way).

### 3.1.1 Annulus and Strips

Before we start, we will redefine the definition 2.16 for more general cases.

**Definition 3.1.** Let sub-graph  $H \subset G$  is defined by all vertices connected to  $v_i$  as  $H = \{p_1, \dots, p_j, \dots, p_n, v_i, v_1, \dots, v_k, \dots, v_m\}$  for  $v_i \in I, v_k \in I, p_j \in P$  of pinned graph  $G(I, P; E')$ .  $v_i$  has a  $d$ -linear neighborhood points in  $\mathbb{R}^d$  if  $H \setminus \{v_k\}$  for some  $v_k \neq v_i$  satisfies  $rank C(G) = d$  of matrix  $C(G)$  where  $C(G)$  is defined by

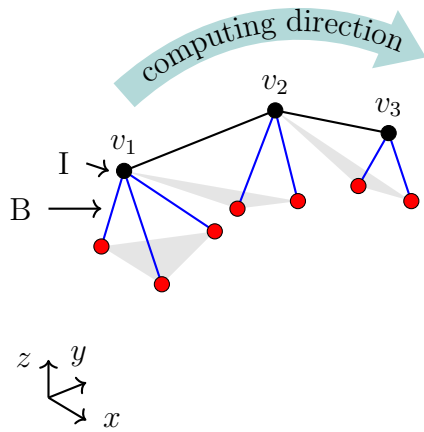
$$C(G) = \begin{bmatrix} (p_1^1 - p_2^1) & \cdots & (p_1^d - p_2^d) \\ & \vdots & \\ (p_1^1 - p_n^1) & \cdots & (p_1^d - p_n^d) \\ (v_1^1 - v_2^1) & \cdots & (v_1^d - v_2^d) \\ & \vdots & \\ (v_1^1 - v_m^1) & \cdots & (v_1^d - v_m^d) \\ (v_1^1 - p_2^1) & \cdots & (v_1^d - p_2^d) \\ & \vdots & \\ (v_m^1 - p_n^1) & \cdots & (v_m^d - p_n^d) \end{bmatrix}$$

Next, we will define a sequence of graphs constructed with a set defined as one inner vertex and corresponding pinned vertices for  $(d-1)m = (d-1)|I| < |B|$  and  $d \leq |P|$ .

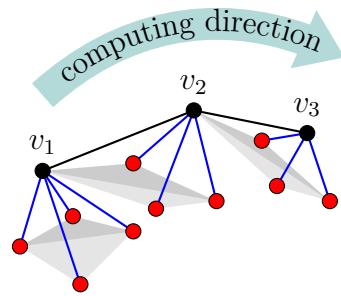
- (i) Diverging : for each  $v_i \in I$ , there exists  $d$  (pinned) neighboring vertices satisfy  $(d-1)$ -linear.
- (ii) Converging : for each  $v_i \in I$ , there exists  $d+1$  (pinned) neighboring vertices satisfy  $d$ -linear (general position).

As shown in Theorem 2.5, for the case (i), two possible solutions exist in real space. Thus, the upper bound for  $N_G$  will be increased by a power of 2 based on  $|I|$ . If we use the above sequence straightly, we get  $d$  dimensional strip. One can easily construct an annulus structure

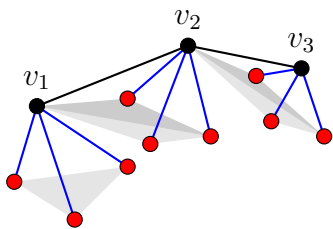
by gluing the first point  $v_i \in I$  in the sequence to the last end  $v_j \in I$  with an additional edge. Notice that pinned vertices could be shared (which may cause crossing edges). These points do not have to be accumulated or located closed to each other. For example, figure 3.4 (a) shows the method with trilateration, which has  $2^n$  number of solutions. Red dots represent locally linearly independent pinned points such that a gray shade shows a plane generated between three pinned points. Thus, two different gray shade implies four pinned points construct 3-dimensional space in  $\mathbb{R}^3$ . (b) The case can be computed using the linear matrix (or trilateration method twice), which has a single solution. (c) is an example of the mixture of (a) and (b), with two solutions for  $v_1$  and one for other points. (d) shows an example of gluing. We can glue two sequences at one vertex point, and this point can be computationally solvable if it is connected to more than  $d - 2$  pinned vertices. Notice that these pinned points can be shared as shown in figure 2.16 if they are locally linearly independent at each point.



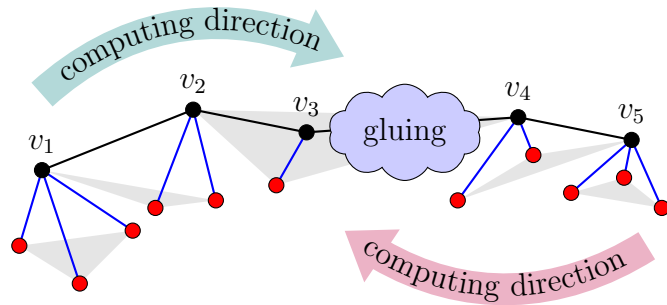
(a) 3 pinned points at a starting point and 2 for others (diverging case).



(b) 4 pinned points at a starting point and 3 for others (converging case).



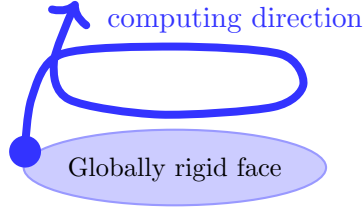
(c) 3 pinned points for each point (2 embeddings).



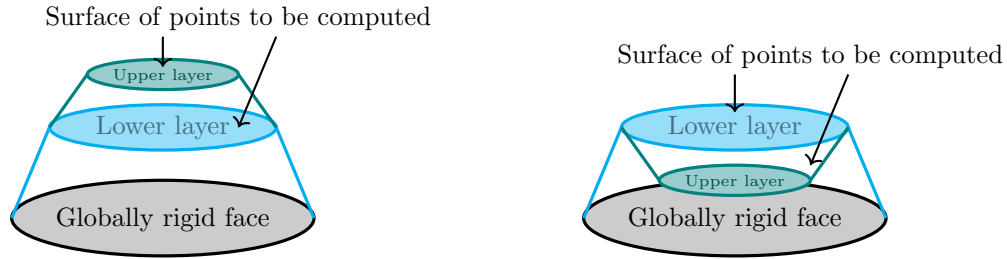
(d) An example of gluing.  $v_1, v_5$  are starting points and  $v_3$  is the endpoint.

Figure 3.4: A method of constructing strips with finite embeddings.

Figure 3.5 shows an example of constructing a graph for sequential computation.



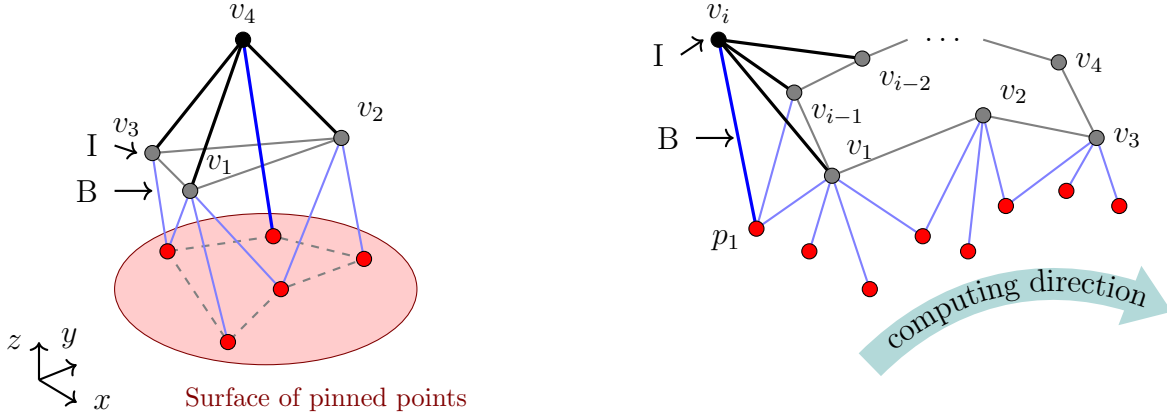
(a) Constructing a graph for sequential computation.



(b) Layering annulus type surfaces (unfolded). (c) Layering annulus type surfaces (folded).

Figure 3.5: (a) Constructing graph for sequential computation, (b) and (c) show possible representation for annulus type surfaces.

The blue arrow in figure 3.5 (a) shows the direction of computation, and the blue shaded area represents a globally rigid face or a face with fixed points where we can start the computation. If one uses multiple layers of annulus-type surfaces, then there could be 2 possible representation for each additional layer, as shown in 3.5 (b) and (c). Thus, we can assume  $2^n$  possible embeddings for  $n$  number of layers. These structures can be glued as explained in figure 3.4 (d).



(a) Adding a point  $v_4$  to prevent folded case.

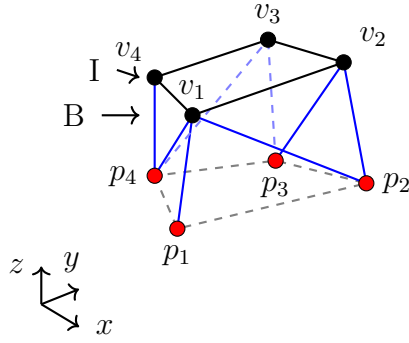
(b) Adding  $v_i$  using  $\{v_1, v_{i-2}, v_{i-1}, p_1\}$ .

Figure 3.6: New point can be added not to generate additional embeddings by choosing  $d$ -linear connections.

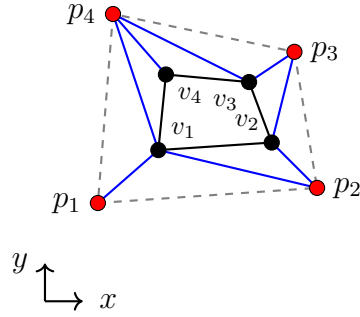
One can use an overlapped surface to prevent  $2^n$  possible representation generated from each layer, as shown in 3.6. For (a), there are  $N_G \leq 2^3$  embeddings from  $v_1, v_2, v_3$ , however,  $v_4$  cannot have a folded case. If  $\{v_1, \dots, v_{i-1}\}$  are all 3-linear and choose  $v_i$  to be 3-linear, (b) will have a single answer.

### 3.1.2 General Graphs

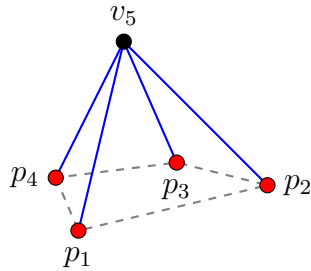
We can use Lemma B.2.3 for constructing a general graph with upper bound  $N_G$ . If we have two graphs  $G_1(V_1; E_1)$  and  $G_2(I_2, P_2; E_2)$ , we can estimate the upper bound of  $N_G$  by  $N_G \leq N_{G_1} \cdot N_{G_2}$ . Notice that since we count reflected cases separately,  $N_{G_i} = 1$  implies every point has 3-linear neighboring points. Figure 3.7 shows an example of  $N_G \leq N_{G_1} \cdot N_{G_2}$ .



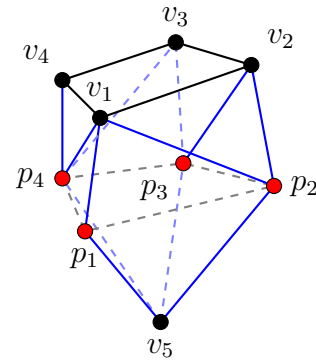
(a) A graph  $G_1$  with  $N_{G_1} \leq 2^4$ .



(b) Top view of (a).



(c) A graph  $G_2$  with  $N_{G_2} = 2$ .



(d) Forming a graph  $G$  by gluing  $G_1$  and  $G_2$ .

Figure 3.7: A case with  $N_G \leq N_{G_1} \cdot N_{G_2} = 2^5$ : (a) a graph  $G_1$  with  $N_{G_1} \leq 2^4$ , (b) top view of (a), and (c)  $N_{G_2} = 2$  (d) adding  $G_2$  to  $G_1$ .

A pinned rigid graph  $G_1$  in figure 3.7(a) shows a discrete annulus shape with  $2^4 = 16$  solutions. Upper bound can be obtained from counting each vertex with 3 pinned points (starting from  $v_1$  with  $p_1, p_2, p_4$ ). (c) represents a rigid graph of discrete cone shape with 2 embeddings, and (d) shows a graph obtained by gluing these two graphs. We can expect solutions less than or equal to  $2^5 = 32$ .

## 3.2 Computational Methods

In Definition B.2.4, we have defined labeled, undirected graph  $G$ , algebraic space  $X$  from Euclidean distance function, and labeled points such that the following diagram commutes.

$$\begin{array}{ccc} G & \xrightarrow{g_p} & X \\ & \searrow f_p & \downarrow h_p \\ & & \mathbb{R}^d / J \end{array}$$

Since we assume we do not have position information of vertices (or inner vertices for pinned graph) along the time, we do not have a way to map  $G$  to  $\mathbb{R}^d$  without using length relations. Thus, in this section, we are mainly focusing on constructing  $h_p$  using  $g_p$  to get  $f_p = h_p \cdot g_p$ . Once we have a set of equations and unknowns, there are various ways to compute solutions. The most common method will be methods based on Algebraic Geometry (Notice that  $X$  is algebraic space). However, these methods may require specific software or high computing powers. In this section, we will introduce two methods for  $(d-1)|I|+1 = |B|$  and  $d|I| = |B|$ , which can be easily computed via vector computation and simple linear algebra. We will also show that we can use the second case with the optimization method, commonly used in machine learning which is also easy to implement. From now, we will focus on solutions for  $\mathbb{R}^3$ .

### 3.2.1 Methods to compute system of polynomials

There are various ways (algebraically, statistically, geometrically, ...) to solve a system of polynomials. We will briefly introduce a few methods in this section.

### 3.2.1.1 Resultants

**Definition 3.2** (Section 1 [13]). Let  $P(z)$  and  $Q(z)$  be a univariate polynomial of degree  $d_1, d_2 \in \mathbb{N}$  and coefficients in a field  $k$ :

$$P(z) = \sum_{i=0}^{d_1} a_i z^i \quad Q(z) = \sum_{i=0}^{d_2} b_i z^i$$

The system  $P(z) = Q(z) = 0$ .

**Theorem 3.1** (Theorem 1.3.1 [13]).  $\text{Res}_{d_1, d_2}(P, Q) = \text{Res}_{d_1, d_2}(a_0, \dots, a_{d_1}, b_0, \dots, b_{d_2}) \in \mathbb{Z}[a_0, \dots, a_{d_1}, b_0, \dots, b_{d_2}]$ , called the resultant of  $P$  and  $Q$ , which verifies that for any specialization of the coefficients  $a_i, b_i$  in  $\mathbf{k}$  with  $a_{d_1} \neq 0$  and  $b_{d_2} \neq 0$ . The resultant vanishes if and only if the polynomials  $P$  and  $Q$  have a common root in any algebraically closed field  $\mathbb{K}$  containing  $\mathbf{k}$ .

It has a property  $\text{Res}_{d_1, d_2}(P, Q) = \pm \det(M_{d_1, d_2})$  and  $M_{d_1, d_2}$  denotes a Sylvester matrix.  $\det(M_{d_1, d_2})$  has a structure with  $d_2$  columns of  $a_i$  and  $d_1$  columns of  $b_i$  as shown below [124][13].

$$\begin{vmatrix} a_0 & 0 & \cdots & 0 & b_0 & 0 & \cdots & 0 \\ a_1 & a_0 & \cdots & 0 & b_1 & b_0 & \cdots & 0 \\ a_2 & a_1 & \ddots & 0 & b_2 & b_1 & \ddots & 0 \\ \vdots & \vdots & \ddots & a_0 & \vdots & \vdots & \ddots & b_0 \\ \vdots & \vdots & \ddots & a_1 & \vdots & \vdots & \ddots & b_1 \\ a_{d_1} & a_{d_1-1} & \cdots & \vdots & b_{d_2} & b_{d_2-1} & \cdots & \vdots \\ 0 & a_{d_1} & \ddots & \vdots & 0 & b_{d_2} & \ddots & \vdots \\ \vdots & \vdots & \ddots & a_{d_1-1} & \vdots & \vdots & \ddots & b_{d_2-1} \\ 0 & 0 & \cdots & a_{d_1} & 0 & 0 & \cdots & b_{d_2} \end{vmatrix}$$

It has roots  $\lambda_i, \mu_j$  when the coefficients of the polynomials belong to an integral domain

[124].

$$\begin{aligned}
\text{Res}_{d_1, d_2}(P, Q) &= a_0^{d_1} b_0^{d_2} \prod_{i,j} (\lambda_i - \mu_j) \quad (1 \leq i \leq d_1, 1 \leq j \leq d_2) \\
&= a_0^{d_1} \prod_{i=1}^{d_2} Q(\lambda_i) \\
&= (-1)^{d_1 d_2} b_0^{d_2} \prod_{j=1}^{d_1} P(\mu_j)
\end{aligned}$$

**Example 3.2.1** (Example 3.6 [127]). Let  $P(z) = yz^2 + z^2 + 3z - 1$ ,  $Q(z) = zy^2 + y - 5$ .

Since  $a_0 = -1$ ,  $a_1 = 3$ ,  $a_2 = (y + 1)$  and  $b_0 = y - 5$ ,  $b_1 = y^2$ , we get

$$\begin{aligned}
\text{Res}_{2,1}(P, Q) &= \begin{vmatrix} -1 & y-5 & 0 \\ 3 & y^2 & y-5 \\ y+1 & 0 & y^2 \end{vmatrix} \\
&= -y^4 - (y-5)(3y^2 - (y+1)(y-5)) \\
&= (y+1)(y-5)^2 - 3y^2(y-5) - y^4.
\end{aligned}$$

We can easily check by putting  $P(z) = 0$ ,  $Q(z) = 0$ . Using  $Q(z) = 0$ , we have  $zy^2 + y - 5 = 0 \rightarrow z = \frac{-(y-5)}{y^2}$  and this equation can be plugged into  $P(z) = 0$  as

$$\begin{aligned}
&yz^2 + z^2 + 3z - 1 \\
&= z^2(y+1) + 3z - 1 \\
&= \frac{(y-5)^2}{y^4}(y+1) - 3\frac{(y-5)}{y^2} - 1 \\
&= (y+1)(y-5)^2 - 3y^2(y-5) - y^4 = 0.
\end{aligned}$$

Notice that  $y \neq 0$  from  $Q(z) = 0$ .

We can generalize to a system of equations for  $f_1, \dots, f_m = 0$  with  $n$  variables of degree

$d_1, \dots, d_m$  ( $m > n$ ) [22].

$$\begin{aligned} \mathcal{S}: \mathcal{V}_1 \times \dots \times \mathcal{V}_m &\rightarrow V \\ (q_1, \dots, q_m) &\mapsto \sum_{i=1}^m f_i q_i \end{aligned}$$

where  $\mathcal{V}_i = \langle x^{E_i} \rangle$  is a vector space generated by monomials, where  $E_i$  denotes the set of exponents of these monomials. The matrix  $S$  is a rectangular matrix and can be divided into blocks.

---

**Algorithm 1:** Resultant matrix with over-constrained system [13]

---

**Result:**  $\xi = (\frac{w_{x_1}}{w_1}, \dots, \frac{w_{x_n}}{w_1})$

Input : A system  $f_1, \dots, f_m \in k[x_1, \dots, x_n]$  ( $m > n$ );

Compute the resultant matrix  $S$ ;

Compute the kernel of  $S$  and check that it is generated by one vector

$w = (w_w, w_{x_1}, \dots, w_{x_n}, \dots)$ ;

---

$S$  can be computed using Mathematica or Maple functions.

### 3.2.1.2 Homotopy continuation

We will introduce homotopy continuation based on [13]. This method uses homotopy, defined as

$$h(x, t) = \gamma(1 - t)g(x) + tf(x) = 0, t \in [0, 1]$$

where  $\gamma \in \mathbb{C}$  is a random number.  $g(x)$  is generated that are easy to compute [125]. While  $t$  moves from 0 to 1, it traces the path of solutions. This method has three nice properties based on a homotopy, as shown below [13].

- The solutions for  $t = 0$  are trivial to find.
- Because of  $\gamma$ , no singularities can occur along the solution paths.

- An isolated solution of multiplicity  $m$  is reached by exactly  $m$  paths.

**Example 3.2.2** (Section 8.2.1 [13]). Let  $f(x, y) = \begin{pmatrix} x^2+4y^2-4 \\ 2y^2-x \end{pmatrix}$ . We can take  $g(x, y)$  to be solved easily as  $g(x, y) = \begin{pmatrix} x^2-1 \\ y^2-1 \end{pmatrix}$ . Now we have

$$h(x, y, t) = \gamma \begin{pmatrix} x^2 - 1 \\ y^2 - 1 \end{pmatrix} (1 - t) + \begin{pmatrix} x^2 + 4y^2 - 4 \\ 2y^2 - x \end{pmatrix} t$$

where  $\gamma$  is a random constant defined by  $\gamma = e^{\theta\sqrt{-1}}$  for some random angle  $\theta$ . Since we need the solution paths  $t \in [0, 1]$  to be free of singularities, it can be checked by computing Jacobian matrix  $J_h$  of  $h(x, y, t) = 0$ .

### 3.2.1.3 Euclidean distance matrix

We will briefly introduce a method to get position vectors from a given Euclidean distance matrix. Before we talk about the Euclidean distance matrix, we will define the Gram matrix first.

**Definition 3.3** ([120]). Gram matrix (or Gramian) of a set of vectors  $X = (x_1, \dots, x_n)$  in an inner product space is the Hermitian matrix (positive semi-definite matrix) of inner products defined by  $G_{ij} = \langle x_i, x_j \rangle$ .

Gram matrix can be represented as [18]

$$G = X^T X = \begin{bmatrix} x_1^T \\ \vdots \\ x_n^T \end{bmatrix} \begin{bmatrix} x_1 & \cdots & x_n \end{bmatrix} = \begin{bmatrix} |x_1|^2 & x_1^T x_2 & \cdots & x_1^T x_n \\ x_2^T x_1 & |x_2|^2 & \cdots & x_2^T x_n \\ \vdots & \vdots & \ddots & \vdots \\ x_n^T x_1 & x_n^T x_2 & \cdots & |x_n|^2 \end{bmatrix}$$

**Definition 3.4** ([18]). Let  $x_l \in \mathbb{R}^n$  and  $1 \leq l \leq N$  to be the columns of a matrix  $X = [x_1 \cdots x_n] \in \mathbb{R}^{n \times N}$ . A Euclidean distance matrix, an EDM in is an exhaustive table of

distance-square  $d_{ij}$  defined by a square of  $l^2$  norm

$$d_{ij}^2 = \|x_i - x_j\|_2^2 = \langle x_i - x_j, x_i - x_j \rangle.$$

If we use standard basis vectors  $e_i \in \mathbb{R}^N$  for  $i = 1 \dots N$ , we can represent  $d_{ij}$  as  $d_{ij}^2 = \|x_i - x_j\|_2^2 = \langle \Phi_{ij}, X^T X \rangle$  where  $\Phi_{ij} = (e_i - e_j)(e_i - e_j)^T$ . The distance matrix can also be obtained from the Cayley-Menger matrix (or Cayley-Menger determinants) in definition B.3.4. There is a relationship between the distance matrix and the Gram matrix.

$$d_{ij}^2 = g_{ii} + g_{jj} - 2g_{ij}$$

where  $d_{ij}^2$  and  $g_{ij}$  represent entries of distance matrix and Gram matrix, respectively. Similarly, we can compute the Gram matrix using the distance matrix.

**Theorem 3.2** (Theorem 1 [76]). A necessary and sufficient condition that the matrix  $D = \{d_{ij}^2\}$  represents the distances of a system of  $N + 1$  points  $P_0, P_1, \dots, P_n$  in Euclidean space  $E^M$  but not in  $E^{M-1}$  is that the quadratic form

$$\begin{aligned} F(x_1, x_2, \dots, x_N) &= \frac{1}{2} \sum_{i,j=1}^N (d_{0i}^2 + d_{0j}^2 - d_{ij}^2) x_i x_j \\ &= \sum_{i,j=1}^N v_{ij} x_i x_j = x^T V x \end{aligned}$$

where  $V = \{v_{ij}\}$  and  $v_{ij} = (d_{0i}^2 + d_{0j}^2 - d_{ij}^2)/2$ .

If  $F$  is positive and has a rank  $M$ , the actual construction of the coordinates of the  $N + 1$  points is equivalent to reducing  $F$  to [76]

$$F(x_1, x_2, \dots, x_N) = \sum_{k=1}^M y_k^2$$

where  $C$  is a matrix of  $M \times N$  and the elements of matrix  $y = Cx$  represent  $P_1, \dots, P_N$  and

$P_i = (c_{1i}, \dots, c_{1M})$  for  $c_{ij} \in C$ . Thus, we can set the following algorithm as shown below [101].

---

**Algorithm 2:** Compute  $G$  from given distance matrix [101]

---

**Result:**  $-2G$

Input distance matrix  $D$ ;

Subtract the first row of  $D$  from each row.;

Subtract the first column from each column.;

Delete the first row and column.;

---

Once  $G$  is obtained, we can find position vectors  $X$  from  $G = X^T X = V E V^T$  using normal matrix  $V$  satisfies  $V^T V = I$ , and a diagonal matrix  $E$ . Then, we can get  $X = \sqrt{E} V^T$ .

## 3.2.2 Trilateration and Linear Matrix

### 3.2.2.1 Trilateration

Let us consider the following in  $\mathbb{R}^2$ .

- (i) We know the length of two edges and the angle between these two edges.
- (ii) We know the length of three edges.
- (iii) We know the length of two edges and know vertex position for each end.

Considering case (i), we can use the law of cosines and find the length of other edges, but we cannot know the positions of each vertex. This triangle can be located anywhere in  $\mathbb{R}^2$ . Case (ii) will be similar. We know what a triangle looks like using the law of cosines, but we will not be able to position the triangle in the exact place. For case (iii), if we assume we know two vertex positions and look for the third one using the information  $l_1, l_2$ , the easiest way is to draw circles by setting the origin from each vertex center and finding the crossing point. If the length of edges is within the range to form a triangle, we will have two solutions “up” and “down” (the name implies relative position from the line formed by two other vertices) if they are linearly independent.

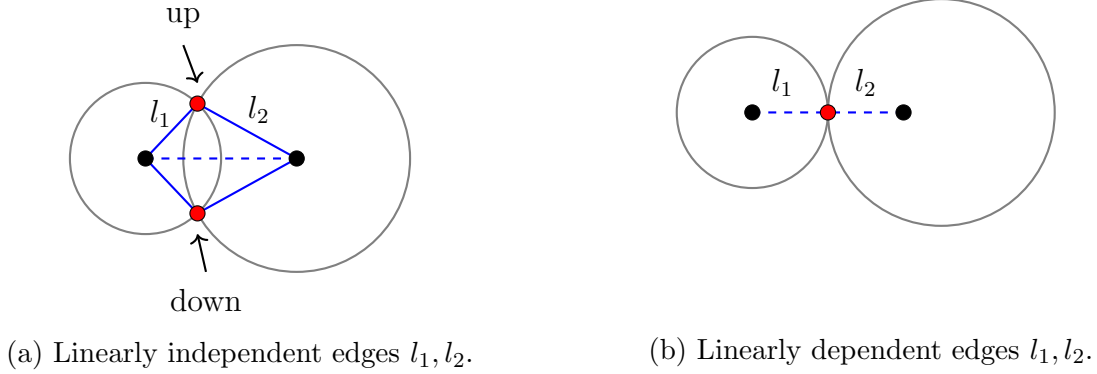


Figure 3.8: Intersection points of two circles.

The three-dimensional case will be similar to the previous one. We can consider a tetrahedron, and we have the following information:

- (i) We know the length of three edges connected to the peak vertex and the angle between these two edges.
- (ii) We know the length of six edges.
- (iii) We know the length of three edges and know the vertex position for each end.

For (i) and (ii), using given information, we will be able to find out the shape of a tetrahedron by figuring out each side (triangles), but we do not know the exact positions. The third case will be similar to the two-dimensional case. We can use a sphere in  $\mathbb{R}^3$  instead of a circle in  $\mathbb{R}^2$ . We get a circle if we calculate the intersection points of two spheres. When we have three points in  $\mathbb{R}^3$ , we can also consider the intersection of three circles. However, three circles in  $\mathbb{R}^3$  are different from  $\mathbb{R}^2$  because we will get two solutions in  $\mathbb{R}^3$  instead of one solution. (Because the third circle depends on the other two circles, it does not help to reduce the number of answers.) This method is known as a trilateration method and is frequently used in the navigation system. As shown below, we always have two solutions (red dots) up to multiplicity (for any angles between edges  $> 0$ ). Therefore, considering pinned  $d$ -rigid graph  $G(I, P; E')$  with  $(d-1)$ -linear edges satisfies  $(d-1)m = (d-1)|I| < |B|$ , we get  $2^{|I|}$  solutions by trilateration method in three-dimensional space.

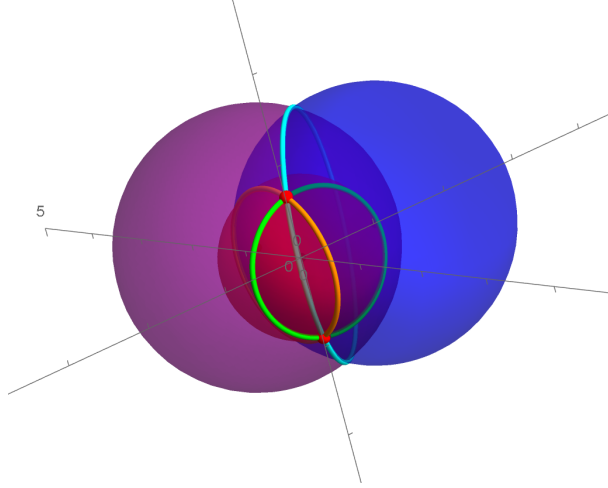


Figure 3.9: Trilateration demonstration in [105] under License CC BY-NC-SA 3.0.

### 3.2.2.2 Linear matrix

If we assume  $v_1$  has two solutions by trilateration method ( $v_1 \in I$ ),  $v_2, v_3, v_4 \in P$ ,  $v_5 \in I$ , and  $v_i = (x_i, y_i, z_i)$ , we can construct a matrix as follows from Euclidean distance function.

$$\begin{aligned}
 & \begin{bmatrix} x_4 - x_1 & y_4 - y_1 & z_4 - z_1 \\ x_4 - x_2 & y_4 - y_2 & z_4 - z_2 \\ x_4 - x_3 & y_4 - y_3 & z_4 - z_3 \end{bmatrix} \begin{bmatrix} x_5 \\ y_5 \\ z_5 \end{bmatrix} \\
 = & \begin{bmatrix} l_{1,5}^2 - l_{4,5}^2 - x_1^2 + x_4^2 - y_1^2 + y_4^2 - z_1^2 + z_4^2 \\ l_{2,5}^2 - l_{4,5}^2 - x_2^2 + x_4^2 - y_2^2 + y_4^2 - z_2^2 + z_4^2 \\ l_{3,5}^2 - l_{4,5}^2 - x_3^2 + x_4^2 - y_3^2 + y_4^2 - z_3^2 + z_4^2 \end{bmatrix}
 \end{aligned}$$

where  $l_{i,j}$  is Euclidean length between  $v_i$  and  $v_j$ . Thus, if we define  $A, x$ , and  $b$  as:

$$A = \begin{bmatrix} x_4 - x_1 & y_4 - y_1 & z_4 - z_1 \\ x_4 - x_2 & y_4 - y_2 & z_4 - z_2 \\ x_4 - x_3 & y_4 - y_3 & z_4 - z_3 \end{bmatrix}, \mathbf{x} = \begin{bmatrix} x_5 \\ y_5 \\ z_5 \end{bmatrix}, \text{ and}$$

$$b = \begin{bmatrix} l_{1,5}^2 - l_{4,5}^2 - x_1^2 + x_4^2 - y_1^2 + y_4^2 - z_1^2 + z_4^2 \\ l_{2,5}^2 - l_{4,5}^2 - x_2^2 + x_4^2 - y_2^2 + y_4^2 - z_2^2 + z_4^2 \\ l_{3,5}^2 - l_{4,5}^2 - x_3^2 + x_4^2 - y_3^2 + y_4^2 - z_3^2 + z_4^2 \end{bmatrix}$$

If edges are  $d$ -linear (first point is  $(d-1)$ -linear),  $A$  is full rank and invertible. Thus, we can easily compute a solution by  $x = A^{-1}b$ . For  $3m = 2|I| \geq |B|$ , we can compute the first point using the trilateration method, then other points can be obtained using the linear matrix method. If all points are  $d$ -linear, the solution will be one.

### 3.2.3 Optimization

Previously, we have focused on finding  $h_p$  algebraically. However, we could also use the optimization method to find solutions. Since this method is frequently used in data science and other computational fields, we would not explain details. For example, if we define function  $g$  as  $g = f(x) - y$  where  $x \in X$  and  $y \in Y$ , then finding a minimum of  $g$  will get the closest solution for  $x$ . Notice that  $Z(g) = Z(f(x)^2 - y^2) \subset Z(g^2) = Z((f(x)^2 - y^2)^2)$ , so one can also use a different combination of polynomials for  $g$  instead of nonlinear square function of  $g$ . We will focus on using energy minimization (or the nonlinear least-squares method) by finding the minimum value of  $(f(x)^2 - y^2)^2$ . There are several ways to find the minimum, for example, conjugate gradients and the quasi-Newton method, but we would not include explanations about these methods here. Detailed can be found in [62][12]. This method can be computed at once rather than sequentially.

### 3.2.4 Adding more constraints

So far, we have not considered a graph is having constraints other than Euclidean distance between vertices. However, in this subsection, we will briefly introduce how to compute  $f_p$  by adding more constraints. Suppose graph  $G$  is time-varying graph, and we know initial position of  $G$   $q_i(0)$  with a Euclidean distance of each time such that  $l_{i,j}(t)$  for  $q_i(t)$  and  $q_j(t)$ . We have  $d(q_i(t), q_j(t)) = l_{i,j}(t)$  and  $\sum_k (q_i^k(t) - q_j^k(t))^2 = l_{i,j}(t)^2$ . If we take time derivatives, we get  $\frac{d}{dt} \sum_{i,j} (\sum_k (q_i^k(t) - q_j^k(t))^2 - l_{i,j}(t)^2) = 2 \sum_{i,j} \sum_k (q_i^k(t) - q_j^k(t)) (\dot{q}_i^k(t) - \dot{q}_j^k(t)) - 2 \sum_{i,j} l_{i,j}(t) \dot{l}_{i,j}(t) = 0$ . Since  $\sum_{i,j} \sum_k (q_i^k(t) - q_j^k(t))$  can be written as  $\mathcal{R}(G, q)$

(see Definition B.2.6 for  $\mathcal{R}(G, q)$ ), we can get  $\mathcal{R}(G, q)\dot{q} = L(t)$  where  $\dot{q} = \begin{bmatrix} \dot{q}_1^1 \\ \dot{q}_1^2 \\ \vdots \\ \dot{q}_n^d \end{bmatrix}$ ,  $L(t) =$

$\begin{bmatrix} \sum_{i,j} l_{1,i}(t) \dot{l}_{1,i}(t) \\ \vdots \\ \sum_{i,j} l_{n,j}(t) \dot{l}_{n,j}(t) \end{bmatrix}$ , and  $|V| = n$ . Note that  $i, j$ 's are corresponding vertices connected to

$q_1, \dots, q_n$ , respectively. Since  $\mathcal{R}(G, q)$  has a maximum rank of  $nd - \binom{d+1}{2}$  and it is not a square matrix. Thus it is not invertible. Generally we have  $nd > |E|$ , if we have more constraints and  $(nd - |E|) \times nd$  matrix satisfies  $C\dot{q} = d$ , then we can construct a matrix equation as:

$\begin{bmatrix} \mathcal{R}(G, q) \\ C \end{bmatrix} \dot{q} = \begin{bmatrix} L(t) \\ d \end{bmatrix}$ . If a square matrix  $C' = \begin{bmatrix} \mathcal{R}(G, q) \\ C \end{bmatrix}$  is invertible, we will have  $\dot{q}$  from

$C'^{-1} \begin{bmatrix} L(t) \\ d \end{bmatrix}$ . This approach can be found in [81]. For pinned graph  $G$ , if  $\dot{p}_i = 0$  for  $p \in P$

and  $\dot{q}_i \neq 0$  for  $q \in I$ , then we have  $\mathcal{R}(\tilde{G}, q)\dot{q} = L(t)$  (see Definition B.2.15 for  $\mathcal{R}(\tilde{G}, q)$ )

where  $\dot{q} = \begin{bmatrix} \dot{q}_1^1 \\ \dot{q}_1^2 \\ \vdots \\ \dot{q}_n^d \end{bmatrix}$ ,  $L(t) = \begin{bmatrix} \sum_{i,j} l_{1,i}(t) \dot{l}_{1,i}(t) \\ \vdots \\ \sum_{i,j} l_{n,j}(t) \dot{l}_{n,j}(t) \end{bmatrix}$  for  $i, j$  are indices of  $V = P \cup I$  and  $|I| = n$

which comes from  $\frac{d}{dt} \sum_{i,j} (\sum_k (q_i^k(t) - p_j^k(t))^2 - l_{i,j}(t)^2) = 2 \sum_{i,j} \sum_k (q_i^k(t) - p_j^k(t)) \dot{q}_i^k(t) - 2 \sum_{i,j} l_{i,j}(t) \dot{l}_{i,j}(t) = 0$ . If pinned graph  $G$  is pinned  $d$ -rigid, we have  $\text{rank } \mathcal{R}(\tilde{G}, q) = d|I|$ , and we get  $\dot{q} = (\mathcal{R}(\tilde{G}, q))^{-1} L(t)$ . Therefore, we can compute  $\dot{q}$  analytically using  $q(0)$  and  $p_j(0)$ 's via  $q(1) = q(0) + (\mathcal{R}(\tilde{G}, q(0)))^{-1} L(0) \cdot dt, q(2) = q(1) + \mathcal{R}(\tilde{G}, q(1))^{-1} L(1) \cdot dt$  for  $t = \{0, 1, 2, \dots\}$ . This method assumes no shape change, even if two different embeddings are close enough. This method works  $\dot{p}_i \neq 0$  for  $p \in P$  and  $\dot{q}_i \neq 0$  for  $q \in I$  if all  $\dot{p}_i$ 's are known. In that case, we get  $\mathcal{R}(\tilde{G}, q)\dot{q} + \mathcal{R}(\tilde{G}, p)\dot{p} = L(t)$  where  $\mathcal{R}(\tilde{G}, p)$  implies  $d|P| \times |E'|$  rigidity matrix. Since we have  $\frac{d}{dt} \sum_{i,j} (\sum_k (q_i^k(t) - p_j^k(t))^2 - l_{i,j}(t)^2) = 2 \sum_{i,j} \sum_k (q_i^k(t) - p_j^k(t)) (\dot{q}_i^k(t) - \dot{p}_j^k(t)) - 2 \sum_{i,j} l_{i,j}(t) \dot{l}_{i,j}(t) = 0$ , first term  $(q_i^k(t) - p_j^k(t)) (\dot{q}_i^k(t))$  corresponds with  $\mathcal{R}(\tilde{G}, q)\dot{q}$  and second term  $(q_i^k(t) - p_j^k(t)) (\dot{p}_j^k(t))$  corresponds with  $\mathcal{R}(\tilde{G}, p)\dot{p}$ . Note that this matrix  $\mathcal{R}(\tilde{G}, p)$  does not have to be invertible because we know  $\dot{p}$ . If  $G$  is pinned  $d$ -rigid, then  $\mathcal{R}(\tilde{G}, q)$  will be a full rank. Thus, we can compute  $\dot{q}$  using  $\dot{q} = (\mathcal{R}(\tilde{G}, q))^{-1} \{L(t) - \mathcal{R}(\tilde{G}, p)\dot{p}\}$ . These approaches require more information than our assumption (length of edges), but it is analytically easier considering time-varying objects, which may require more computation than the static one. We want to note that if two different embeddings are close enough to jump from one to another, there would be some failures in estimating the shape from the given information. If a graph  $G$  is globally rigid, and we want to predict the final shape, we do not have to compute length along the time, and this method may not be advantageous. However, this approach will be useful if  $|V| = n$  is not big and we require one-time computation (not point-to-point computations as previous methods).

### 3.3 Discussions for computational methods

We have introduced several methods in section 3.2.1 to compute solutions from given polynomials. Before we present algorithms, we will briefly discuss their limits. The resultant matrix is very versatile for applying any kind of polynomial equation. However, matrix sizes become bigger when we add more variables, so it is not simple to compute multiple

equations (for example, distance functions with points  $> 100$ ) [125]. Homotopy continuation allows accurate and fast computations. It is also available in various computational software (Maple, Macaulay2, Sage Math, ...). When we tested with a package in Julia, it did not handle greater than 10 points (30 variables). Lastly, we can recover the position matrix by computing the Gram matrix from the Euclidean distance matrix, which works nicely. However, we assume we do not have all the distance information between any two vertices, so we cannot eliminate some variables  $d_{ij}$  from a lack of information. For example, it is known that the low-dimensional Euclidean distance matrix completion problem is NP-hard [47]. Therefore, this section will discuss trilateration, linear matrix, and optimization methods. These are relatively fast and straightforward algorithms and can be used with points  $> 100$ , which does not require higher computing power. Computations and simulations have taken on the R platform [92] using system Intel i5-7300U 2.6GHz with 8GB RAM.

### 3.3.1 Trilateration

For the trilateration method, we have used an algorithm commonly used for the satellite system, as shown below. If there are 3d position vectors  $p_1, p_2, p_3$  with corresponding Euclidean length  $r_1, r_2, r_3$  defined by  $d(p_i, x) = r_i$  for unknown  $x$ , we can get  $x$  position as:

---

**Algorithm 3:** Trilateration

---

**Result:** Solution 1(ans1), Solution 2(ans2)

$$e_x = (p_1 - p_2)/|p_1 - p_2|;$$

$$i = \text{dot}(e_x, p_3 - p_1);$$

$$t = (p_3 - p_1 - e_x \cdot i);$$

$$e_y = t/|t|;$$

$$e_z = \text{cross}(e_x, e_y);$$

$$d = |p_2 - p_1|;$$

$$j = \text{dot}(e_y, p_3 - p_1);$$

$$x = (r_1^2 - r_2^2 + d^2)/(2 \cdot d);$$

$$y = (r_1^2 - r_3^2 - 2 \cdot i \cdot x + i^2 + j^2)/(2 \cdot j);$$

$$z = \sqrt{r_1^2 - x^2 - y^2};$$

$$\text{ans1} = p_1 + x \cdot e_x + y \cdot e_y + z \cdot e_z;$$

$$\text{ans2} = p_1 + x \cdot e_x + y \cdot e_y - z \cdot e_z;$$

---

Note that  $|\cdot|$  implies Euclidean distance function,  $\text{dot}(\cdot)$  and  $\text{cross}(\cdot)$  stand for inner product and cross product, respectively. For the trilateration method, because computation is done by vector calculation, it is done fast ( $< 1$  second per calculation). However, trilateration has two potential problems.

1. Number of solutions increases along with iteration.
2. Error inflation.

The first problem arises from computational methods. Because trilateration generates 2 solutions per time, this could occupy CPU resources and memory capacity if we would like to keep all possible results, though some are not true. There should be a reviewing procedure to check which solutions are correct. For example, one can implement an algorithm to compute the same loop starting from different points and compare each other. Also, employing a length checking algorithm may help to eliminate some unwanted candidates. Thus, to reduce computational power and resources, the best strategy will be to apply an algorithm

to choose a solution out of 2. However, it may not be easy if we do not have concrete criteria for selecting results. Error from the wrong choice of solutions may cause a considerable error. Trilateration uses linear vector computation, and errors can be added up and become more significant. The below figure shows the error test for reconstructing some fluctuating surfaces.

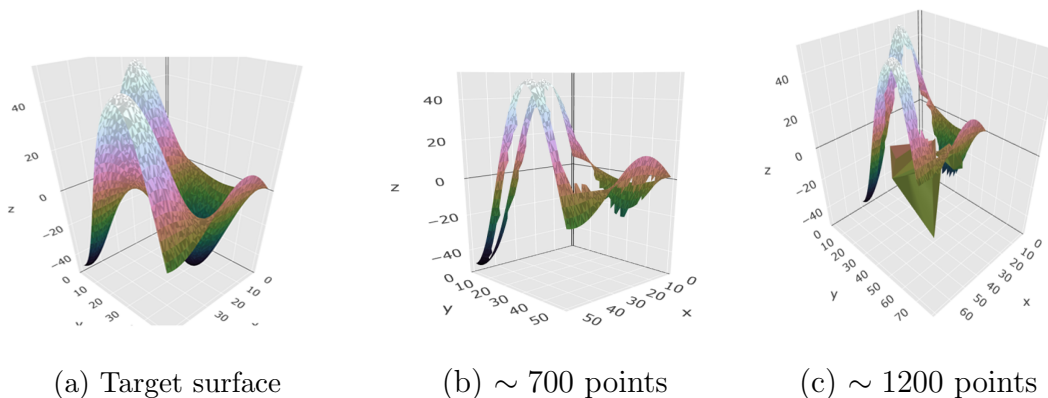


Figure 3.10: An example of error inflation.

For target surface (a), (b) shows  $\sim 700$  reconstructed points from the boundary. In (c), we see that error grows  $\sim 1200$ , and some position vectors have the wrong values. This problem comes from sequential computation, so if we have more pinned points, such as  $|P| \sim 3|I|$  (in general position with inner vertex connected to these), the computation can be done with more accuracy. However, if we add more and more points to the same loop, the angle between neighboring position vectors gets narrower, and it will cause error increases. That can be thought of as local positions having a rack of linear independence. For example, position vectors  $(0, 0, 0)$  and  $(0, 0, 0.000001)$  in  $\mathbb{R}^3$  are mathematically different points, but it may become similar values if we don't require enough accuracy. Let us consider an extreme case. With given pinned points  $p_1 = (0.000001, 0, 0)$ ,  $p_2 = (0, 0.000001, 0)$ ,  $p_3 = (0, 0, 0)$ , if we compare results between a set of lengths  $d(x, p_1) = 4, d(x, p_2) = 4, d(x, p_3) = 4$  and another set of length  $d(x, p_1) = 4, d(x, p_2) = 4.000001, d(x, p_3) = 4.000001$  via trilateration method, we will get  $x = (5.00e^{-7}, 5.00e^{-7}, 4), (5.00e^{-7}, 5.00e^{-7}, -4)$  and  $x = (0.40, 5.00e^{-7}, 3.98), (0.40, 5.00e^{-7}, -3.98)$  (rounded to 2 decimal places). Both sets have

approximately correct edge lengths, although  $x$  positions are not closed to each other. Thus, we may fail to obtain the correct solution sets by missing one digit. Moreover, this trade-off is also related to geometrical properties (local curvature, density of points, and global curvature).

### 3.3.2 Linear matrix

We have implemented the linear matrix method as follows. If we have 3d position vectors  $p_1, p_2, p_3, p_4$  with corresponding Euclidean length  $r_1, r_2, r_3, r_4$  defined by  $d(p_i, x) = r_i$  for unknown  $x$ , we can solve for  $x$  position as

---

**Algorithm 4:** Linear Matrix

---

**Result:** Solution for  $Ax = B$

$$b1 = r_1^2 - r_4^2 - p_{1x}^2 - p_{1y}^2 - p_{1z}^2 + p_{4x}^2 + p_{4y}^2 + p_{4z}^2;$$

$$b2 = r_2^2 - r_4^2 - p_{2x}^2 - p_{2y}^2 - p_{2z}^2 + p_{4x}^2 + p_{4y}^2 + p_{4z}^2;$$

$$b3 = r_3^2 - r_4^2 - p_{3x}^2 - p_{3y}^2 - p_{3z}^2 + p_{4x}^2 + p_{4y}^2 + p_{4z}^2;$$

$$a_{1x} = p_{4x} - p_{1x};$$

$$a_{1y} = p_{4y} - p_{1y};$$

$$a_{1z} = p_{4z} - p_{1z};$$

$$a_{2x} = p_{4x} - p_{2x};$$

$$a_{2y} = p_{4y} - p_{2y};$$

$$a_{2z} = p_{4z} - p_{2z};$$

$$a_{3x} = p_{4x} - p_{3x};$$

$$a_{3y} = p_{4y} - p_{3y};$$

$$a_{3z} = p_{4z} - p_{3z};$$

Define  $B$  as a column matrix  $B = \{b1; b2; b3\}$ ;

Define  $A$  as a  $3 \times 3$  matrix  $A = \{\{a_{1x}, a_{1y}, a_{1z}\}, \{a_{2x}, a_{2y}, a_{2z}\}, \{a_{3x}, a_{3y}, a_{3z}\}\}$ ;

Solve  $Ax = B$ ;

---

For the linear matrix, the computation can be done sequentially or once. We can get a solution for the point if we use  $Ax = b$  for each unknown vertex. We could also construct

one big matrix using all points if symbolic computation is available. The second method requires a complicated procedure because it requires feedback (the result of the previous calculation). However, one can construct a partial feedback algorithm instead of a full giant matrix. Linear matrix also has an error inflation problem as trilateration since it uses sequential computation. As shown below, we have implemented multiple discrete annulus structures to test potential issues for many points.

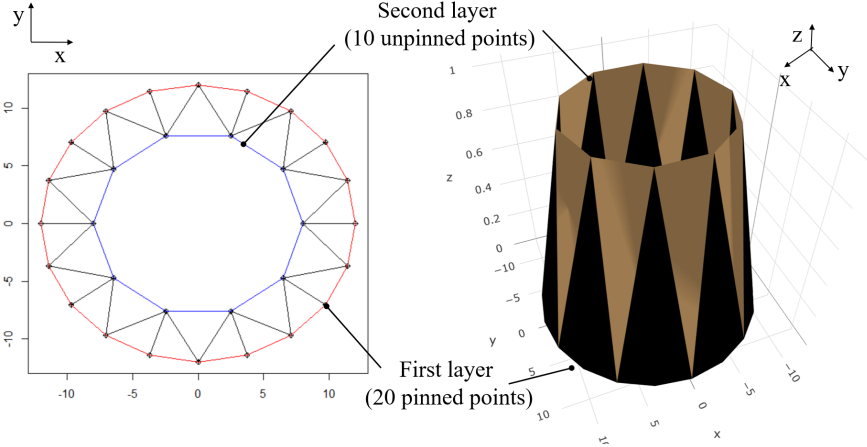


Figure 3.11: An example of discrete annulus.

Figure 3.11 represents a simple discrete annulus structure with no-crossing edges. Note that we have required a network to have  $2n$  pinned points to estimate  $n$  unpinned vertices to satisfy the non-crossing policy. As represented in figure 3.12, multiple discrete annuli can be stacked by taking unpinned points of the lower annulus as pinned vertices for the upper annulus. We could see the number of vertices of each layer decrease by 2 if we strictly require non-crossing edges. The following figure shows an evaluation for error inflation based on multiple discrete annulus structures. Each inner vertex has four neighboring position vectors, and the first point is computed using the trilateration method. We have assumed that we know which first solution is correct; otherwise, we will get a set of solutions with the opposite orientation because that is not the aim of this test. From the second point of the inner polygon, we have used the previous point as one of the input parameters (pinned

points) such that computation can be done sequentially.

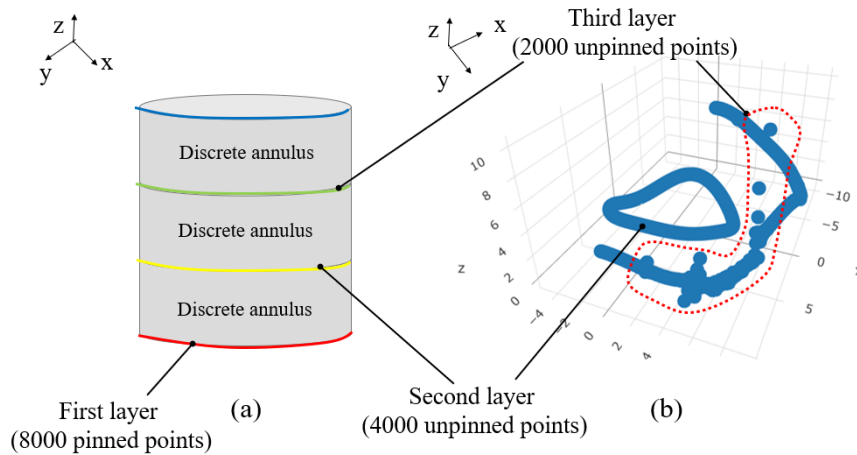


Figure 3.12: (a) Structure of test surface and (b) scatter plots of reconstructed surface.

(a) shows the structure of the test surface and (b) plots of the reconstructed surface. We can check that error increases drastically around 5000-th point (red circled points). The main reason for error inflation in the linear matrix is that the angle of the triangle gets narrower as we add more points to the boundary. From our test, we have observed error grows typically  $\sim 10^1 - 10^5$  times per layer based on the geometry. Boundary points can be constructed as zigzag types to reduce errors, as shown in the figure below.

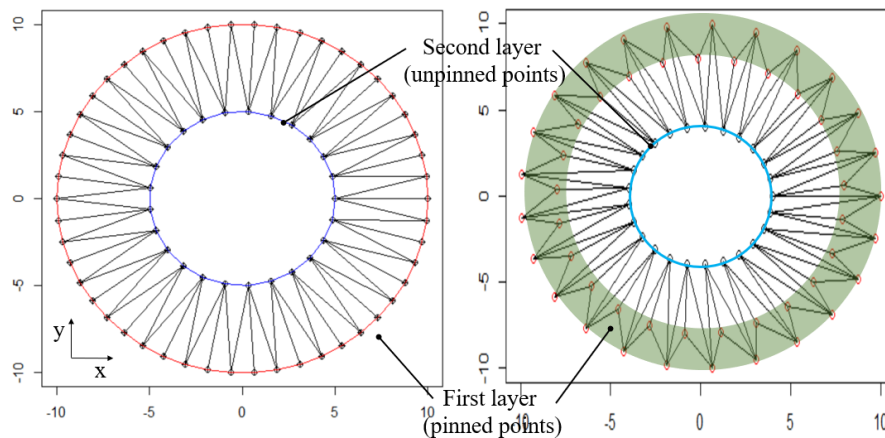
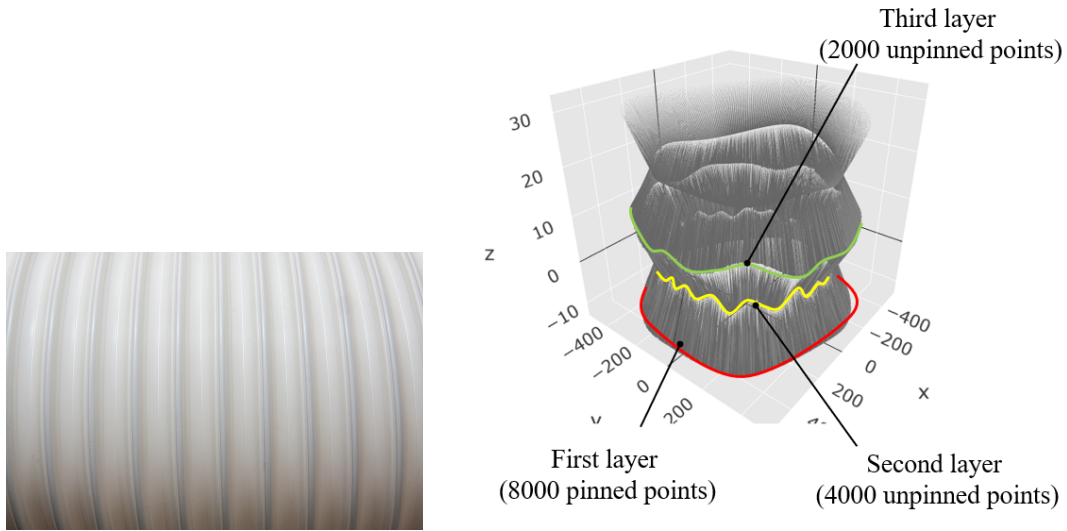


Figure 3.13: (a) circular type and (b) zigzag type of boundaries.



(a) Exhaust pipe. [110]

(b) Test structure.

Figure 3.14: Test structure for error inflation inspired by an exhaust pipe.

Error	Layer#1	Layer#2	Layer#3
Total points	8000	4000	2000
$(p_t - p_r)$ at first point	N/A	1.5e-12	1.9e-12
$\max(p_t - p_r)$	N/A	8.5e-7	1.5e-3

Table 3.1: Accumulated error for each layer.

The above image shows a test for error inflation with a zigzag type boundary, and we can see the error grows  $\sim 10^4$  times in this case (table 3.1). Notice that there was a slight improvement in error inflation compared to the previous figure ( $\sim 6000$  points). Error is estimated by  $\max(p_t - p_r)$  where  $p_t$  is the target position vector and  $p_r$  is the reconstructed one. However, as shown below, one can implement more steps to suppress the error. (a) displays discrete annulus for this example. (b) and (c) represent ways to compensate for error inflation using multiple-step calculation. (b) uses various starting points and (c) adopts different computing directions for sequential computation.

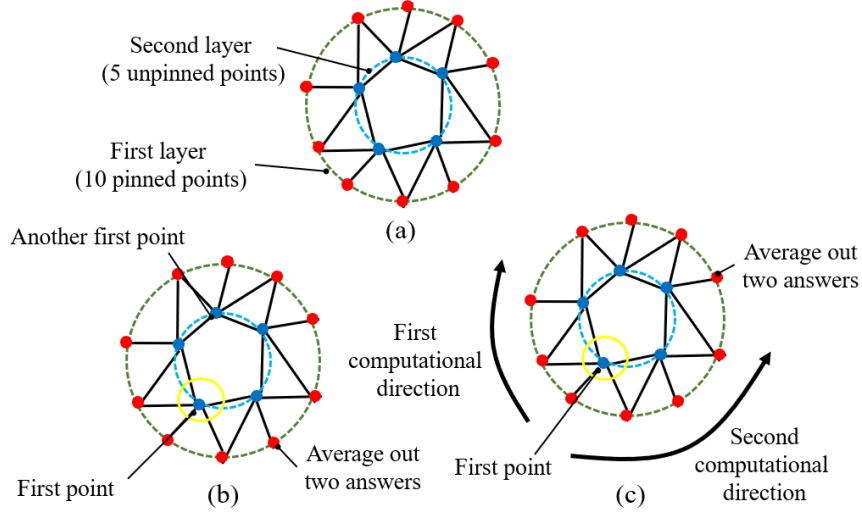


Figure 3.15: An example of (a) discrete annuli, (b) taking multiple starting points, and (c) computing solutions using two directions.

Since error inflation mainly comes from the density of vertices with computational limit (floating point digit limit as we examined before), there are several ways to improve error inflation, such as expanding digits for floating points or adding extra pinned points. If we have more pinned points  $|P| \sim 4|I|$  (for points locally, not co-planar) and suppose these points have enough angles/densities, error inflation would not be a problem since we do not need sequential computing. If we allow crossing edges, we do not have to keep  $2n$  at the boundary, improving the error. Moreover, the structure can be constructed using tetrahedrons instead of triangles.

### 3.3.3 Optimization

Finally, we will talk about the optimization method. The positive part of this method is that sequential computation is unnecessary. It has more flexibility than previous methods, such as it can be easily embedded inside machine learning algorithms, and there are many choices for optimization algorithms and functions ( $g, g^2, g^3, g^n$  as we discussed in the previous section). It is useful for any globally rigid framework with a fair number of pinned points. Also, once the algorithm finds a correct set of solutions, the error is not huge (in our test, the

coordinate error was  $< 1$ ). That is, it would not have error inflation. We have used `optimx` library in R [92], and this library provides a variety of optimization methods such as Nelder-Mead, conjugate gradients, limited-memory modification of the BFGS quasi-Newton method, Nonlinear minimization, and other methods. We've chosen conjugate gradient option to minimize  $\sum_{i,j}(d(q_i, q_j)^2 - l_{ij}^2)^2$ . For illustration, the figure below pictures an example of this method. (a) and (b) represent a two-dimensional diagram and plot for the target system (c) projected on the  $xy$ -plane. We have used a zigzag type arrangement of pinned points. (d) shows a reconstructed graph applying energy minimization and  $\max(p_t - p_r) \sim 0.160$  for all  $t, r$ .

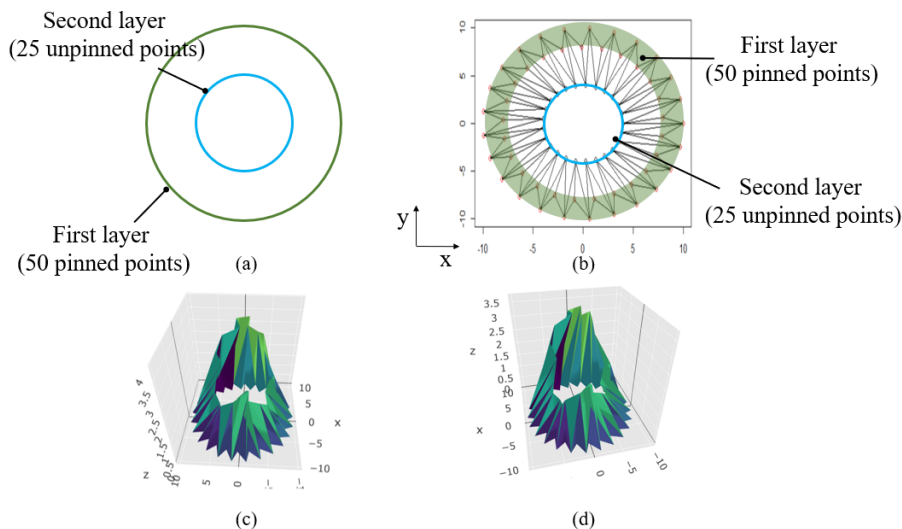


Figure 3.16: An example of the optimization method.

We have observed error variations between different geometrical objects with the same initial parameters.

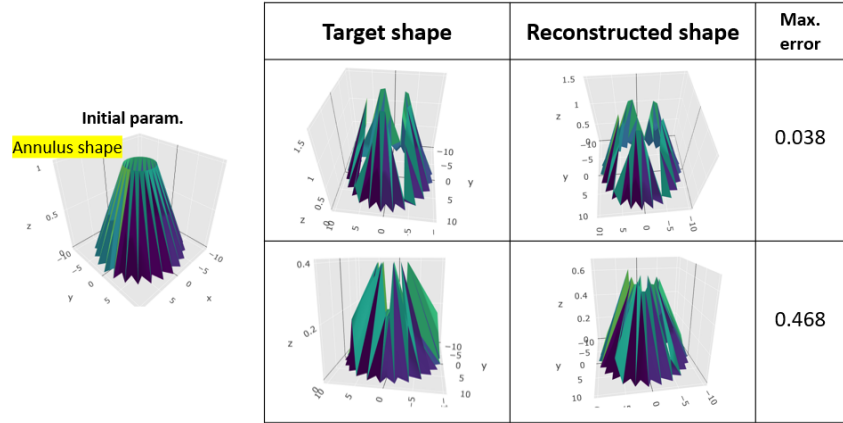


Figure 3.17: Error depends on geometrical structures.

There is more possibility of having the wrong set of solutions since the algorithm may stop at the local minimum instead of the global one. That will strongly depend on the selected function and optimization method. To overcome this issue, we could implement an algorithm to use reasonable input (for example, the result of a linear matrix as input for optimization) to improve computation failure from the local minimum.

### 3.3.4 Merging different methods

Finally, we will introduce how we can connect previous methods with natural shapes. The figure below shows our test design. (c) represents layer construction. The first layer is constructed discrete loop structure with 104 pinned points, the second one has 52 unpinned points with a petal shape, and the third one is a layer with 26 unpinned vertices. Since we've constructed  $|P| = 2|I|$  for every layer, we have to compute the first point of each layer by trilateration. Note that 50% of triangles are drawn for (b) to show third layer triangulation. By assuming we know which solution is correct among two possible solutions, we've obtained error  $\max(p_t - p_r) \sim 3.1e^{-12}$  for second layer computation and  $\max(p_t - p_r) \sim 1.7e^{-11}$  for third layer reconstruction for all  $t, r$  where  $p_t$  is target position vector and  $p_r$  is reconstructed one.

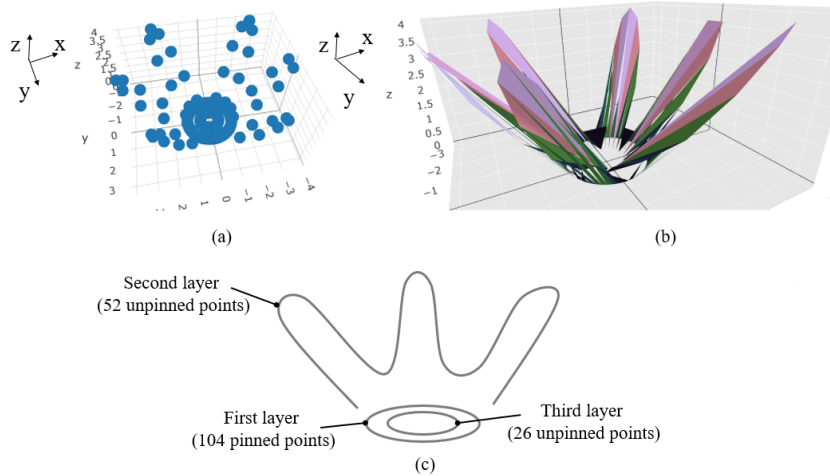


Figure 3.18: (a) Scatter plot, (b) triangulated plot, and (c) structure of the surface.

The figure below shows another test for combining optimization and linear matrix method to overcome minimization failure. (a) shows the target shape constructed with the first and second layer from the previous figure, (b) is the plot using the result from the linear matrix, and (c) shows the effect of optimization using (b) as an input. If we use a random unit vector as initial parameters, we get (d), which does not look like a target graph. Therefore, combining multiple methods may help reduce errors.

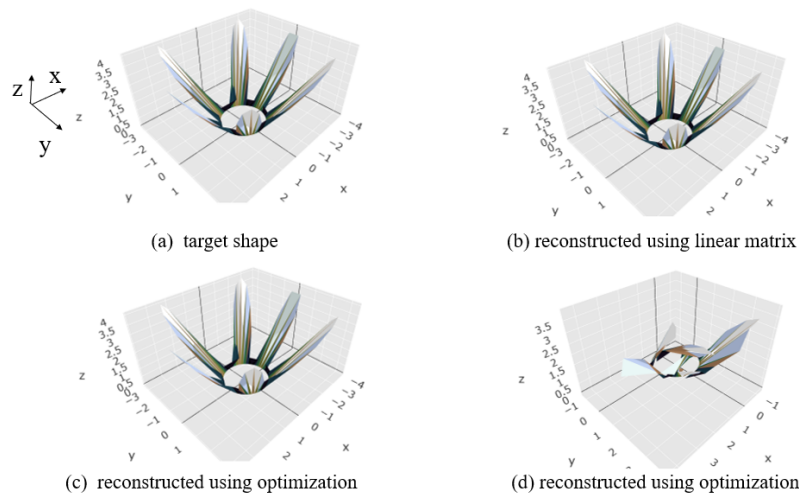


Figure 3.19: Comparison between different computational methods.

We have implemented a design inspired by calla lily for the next illustration. This structure can be constructed in multiple ways, as shown below. Figure 3.20 (a) presents

an illustration for sharing the first layer for two different second layers and (b) shows the sharing of the second layer to reconstruct two different third layers. (c) represents bottom to top construction for computing position vectors, which will get the largest noise. We have chosen (c) to present how error grows. The figure 3.21 (a) displays target triangulated surface for 3.20 (c). Figure 3.21 (b) is a 3d scatter plot which shows all vertices of each layer.

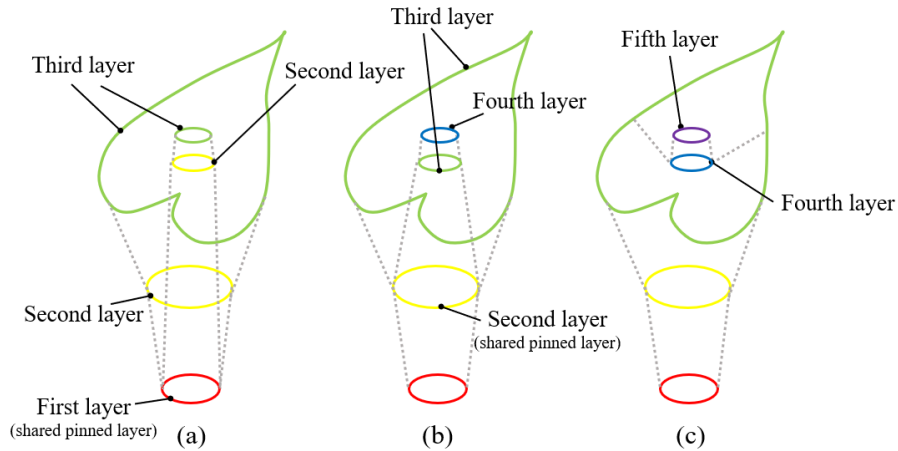


Figure 3.20: Demonstrations of different layer constructions.

Following figure shows (a) triangulated plot and (b) scatter plot of figure 3.20 (c).

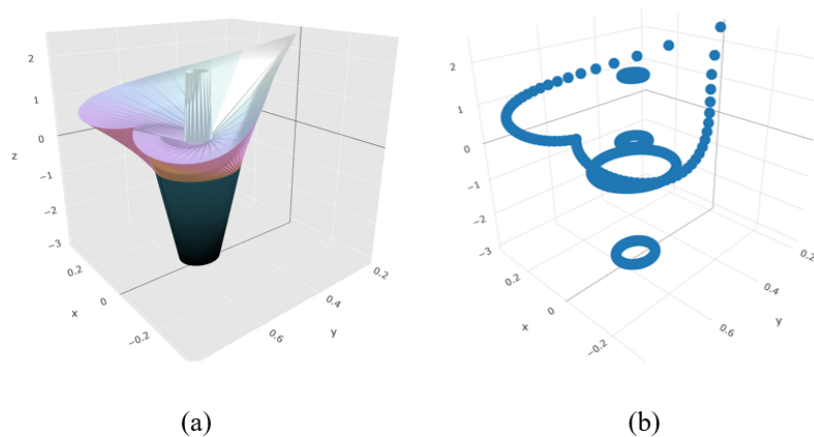


Figure 3.21: 3-dimensional (a) triangulated plot and (b) scatter plot of figure 3.20 (c)

Accumulated error for each layer can be seen in table 3.2. Notice that for this test

structure, error grows by  $1e^2 \sim 1e^4$  every layer. Figure 3.22 (a) shows the reconstructed

Error	Layer#1	Layer#2	Layer#3	Layer#4	Layer#5
$\max(p_t - p_r)$	N/A	2.40e-10	3.04e-07	4.07e-05	1.09e-1

Table 3.2: Accumulated error for each layer.

surface for 3.21 (a). We can see that the shape of the fifth layer does not perfectly match the original shape. As discussed earlier, optimization methods can compute each layer to reduce error. 3.22 (b) represents recomputed the fifth layer using optimization methods using results of (a) as an initial parameter, and we can see the reconstructed shape is slightly improved. However, by considering the error tolerance of optimization methods, we can conclude that the best way is minimizing layers to be reconstructed.

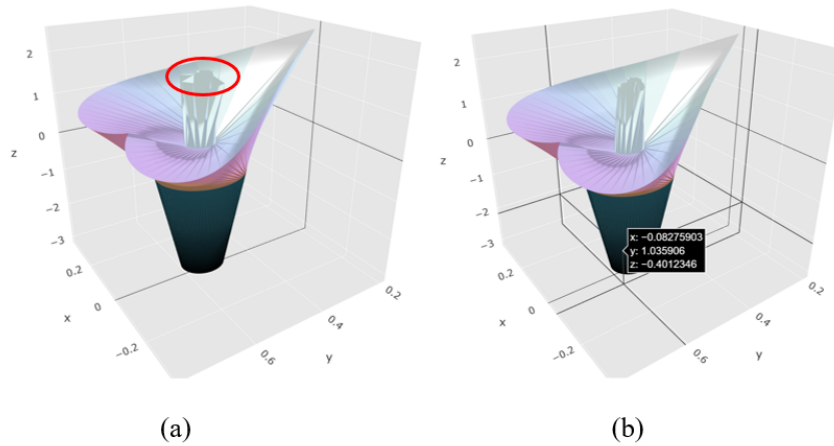


Figure 3.22: (a) reconstructed surface for 3.21 (b) reprocessed fifth layer using optimization methods.

# Chapter 4

## *n*-dimensional extension of Euler's elastica with constitutive relations

### 4.1 Mylar balloon and Euler's elastica

Mylar Balloon - an in-extensible balloon is one example of Euler's elastica, which were solved partially by Bernoulli and wholly by Euler. Besides the original derivation, there are various versions of proofs for Euler's elastica, including [52]. In this section, we are introducing a simple method using the Euler-Lagrange equation. Before we develop a formulation of a Mylar balloon with various masses connected to Euler's elastica later, we will start by deriving a Mathematical model of the Mylar balloon introduced in Paulsen's paper [64]. Next, we will briefly review parametrization methods in [57] and [33]. Next, we will use Paulsen's method to derive equations for the Mylar balloon with various masses (or perpendicular forces). Finally, we will briefly explain the connection between the Mylar balloon and Euler's elastica.

#### 4.1.1 History of Euler's elastica

First, we will briefly explain the history of the problem from [104] and [72], then we will follow the derivation of Euler's elastica from Euler's book appendix 1[24] and partially from

[72]. James Bernoulli posed the problem in 1691 that a uniform thickness string supported from point  $O$  has a weight that applies perpendicular force.

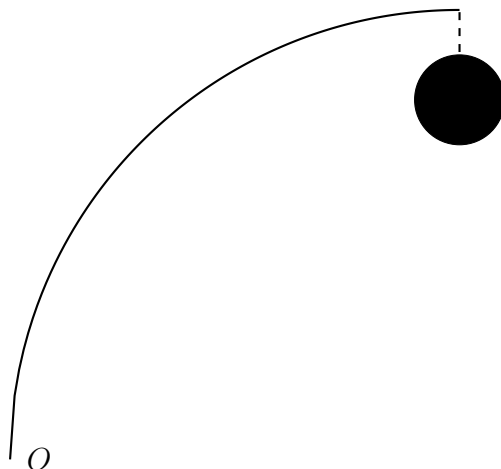


Figure 4.1: A problem posed by James Bernoulli.

According to Daniel Bernoulli, this can be solved

$$\min \left( \int \kappa(s)^2 ds = \int \frac{ds}{R^2} \right)$$

If the length, endpoints, and slopes at endpoints are fixed. We will start from scratch for readers with no background.  $\kappa$  can be represented using the Whewell equation (or Whewell parametrization) of curvature. That is defined by  $\kappa = \frac{d\varphi}{ds}$  for angle  $\varphi$  and arc length  $s$ , which is the change of the tangent angle from infinitesimal arc length variation. If we change this to Cartesian coordinates, we have  $ds = \sqrt{dx^2 + dy^2}$ . Since  $\varphi = \arctan\left(\frac{dy}{dx}\right)$ ,  $\frac{d^2y}{dx^2} = \frac{dx}{d\varphi} \sec^2(\varphi) = \frac{dx}{d\varphi} \left(1 + \left(\frac{dy}{dx}\right)^2\right)$ , we can represent  $\kappa$  in Cartesian coordinates.

$$\kappa = \frac{d\varphi}{ds} = \frac{dx}{ds} \frac{d\varphi}{dx} = \frac{1}{\left(1 + \left(\frac{dy}{dx}\right)^2\right)^{1/2}} \frac{\frac{d^2y}{dx^2}}{1 + \left(\frac{dy}{dx}\right)^2} = \frac{\frac{d^2y}{dx^2}}{\left(1 + \left(\frac{dy}{dx}\right)^2\right)^{3/2}}$$

Therefore, we have

$$\int \frac{ds}{R^2} = \int \frac{\left(\frac{d^2y}{dx^2}\right)^2}{\left(1 + \left(\frac{dy}{dx}\right)^2\right)^{5/2}} dx = \int \frac{q^2}{(1+p^2)^{5/2}} dx = \int Z dx$$

where  $p = \frac{dy}{dx}$ ,  $q = \frac{d^2y}{dx^2}$ . By solving the above using fixed arc length constraint, we get

$$dy = \frac{(\alpha x^2 + \beta x + \gamma) dx}{\sqrt{a^4 - (\alpha x^2 + \beta x + \gamma)^2}}$$

$$ds = \frac{a^2 dx}{\sqrt{a^4 - (\alpha x^2 + \beta x + \gamma)^2}}$$

See appendix C.2 for Euler's solution. More details about this problem can be found in [24] and [72]. Thus, Euler's elastica can be expressed as:

**Theorem 4.1** (Theorem 9[52]).

$$\begin{cases} Z(s) &= X(s) + Y(s)i \\ Y(s) &= \int^X \frac{\alpha X^2 + \beta X + \gamma}{\sqrt{\lambda^4 - (\alpha X^2 + \beta X + \gamma)^2}} dX \\ s &= \int^X \frac{\lambda^2}{\sqrt{\lambda^4 - (\alpha X^2 + \beta X + \gamma)^2}} dX \end{cases} \quad (4.1)$$

We can find proof of this equation from a modern point of view in [52].

### 4.1.2 Formation of Mylar balloon

A Mylar balloon is constructed by two disks with radius  $a$  glued along the edge. The mathematical model of the Mylar balloon was first introduced in Paulsen's paper [64]. As we mentioned earlier, we will repeat Paulsen's arguments and apply this method in a later section. Mylar balloon has the following assumptions.

- There is no stretch of this arc length  $a$ .
- Surface is formed to achieve maximal volume  $V$ .
- This surface is axis-symmetric (surface of revolution).

Note that a sphere is a surface that encloses a maximal volume for a given surface area. A Mylar balloon maximizes volume for a given arc length. Suppose the initial radius is defined by  $a$  and the final radius is set to  $R$ . By the first assumption and  $ds = \sqrt{dx^2 + dz^2} = \sqrt{1 + (dz/dx)^2}dx$ , we have

$$\int_0^R \sqrt{1 + z'(x)^2} dx = a$$

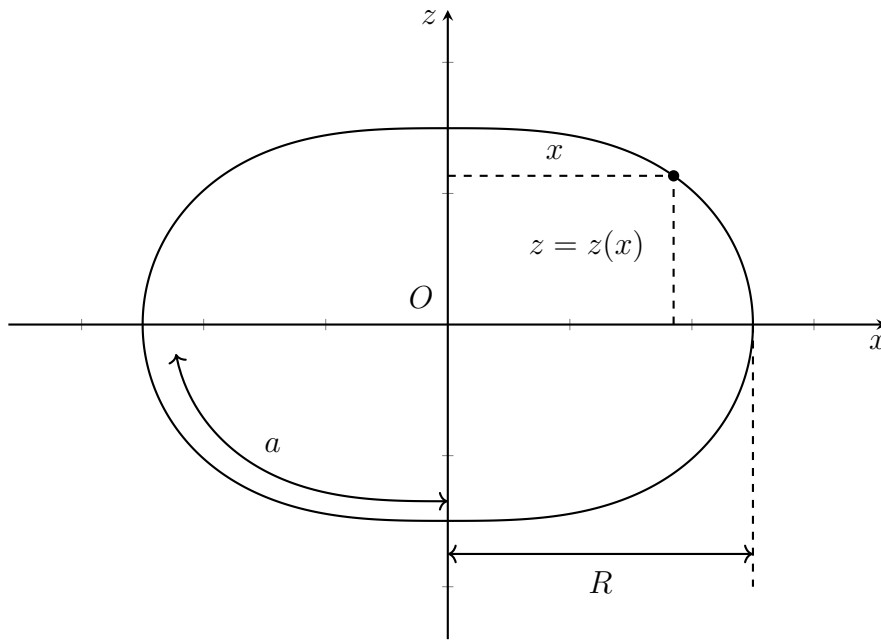


Figure 4.2: Geometry of the Mylar balloon.

We can compute volume via the following equation

$$V = 4\pi \int_0^R xz(x)dx.$$

Let  $F(x, z(x), z'(x))$ . If we apply Euler-Lagrange equation  $\frac{d}{dx}(\frac{\partial F}{\partial z'}) - \frac{\partial F}{\partial z} = 0$  with Lagrange Multiplier, then we get

$$\frac{d}{dx} \left( \frac{\lambda z'(x)}{\sqrt{1 + z'(x)^2}} \right) - 4\pi x = 0.$$

Integrate both sides, we will have

$$\frac{\lambda z'(x)}{\sqrt{1+z'(x)^2}} - 2\pi x^2 = C.$$

Since we know  $z'(0) = 0$  (flatness of top), we get  $C = 0$ . Notice that  $\lim_{x \rightarrow R^-} z'(x) = -\infty$  (considering the profile of balloon edges), so we need  $2\pi/\lambda$  to be gradually changing negative value. This will let us set  $2\pi/\lambda = -\frac{1}{m^2}$  and we can rewrite as:

$$\frac{z'(x)}{\sqrt{1+z'(x)^2}} = -\frac{x^2}{m^2}.$$

By manipulating this,

$$\begin{aligned} \frac{m^2 z'(x)}{\sqrt{1+z'(x)^2}} &= -x^2 \\ m^2 z'(x) &= -\sqrt{1+z'(x)^2} x^2 \\ m^4 z'(x)^2 &= (1+z'(x)^2) x^4 \\ m^4 z'(x)^2 - x^4 z'(x)^2 &= x^4 \\ (m^4 - x^4) z'(x)^2 &= x^4 \\ z'(x)^2 &= \frac{x^4}{m^4 - x^4} \\ z'(x) &= -\frac{x^2}{\sqrt{m^4 - x^4}}. \end{aligned}$$

Recall that we have a condition  $z(R) = 0$ . Therefore, we get  $z(x) = \int_x^R \frac{t^2}{\sqrt{m^4 - t^4}} dt$ . Recall  $\lim_{x \rightarrow R^-} z'(x) = -\infty$ , thus we get  $m = R$ . We can solve this integral using the elliptic function. Parametrization and geometrical properties were analyzed and visually presented in the series of Mladenov and Oprea's papers [57][58][33][56][69]. First, we will consider a method introduced in [57] and [33], then use a different approach in later sections. Suppose

we have an equation

$$\dot{z} = -\frac{\lambda x^2}{2}$$

where  $\dot{z}(0) = 0$ . That can be derived using different coordinates of Mylar balloon, and details can be found in [33]. We can easily assume  $\dot{x} = \cos \theta$ ,  $\dot{z} = -\sin \theta$ , and  $x(\theta) = \sqrt{\frac{2\sin \theta}{\lambda}}$ . By manipulating previous equations, we will have

$$z(\theta) = -\frac{1}{\sqrt{2\lambda}} \int \sqrt{\sin \theta} d\theta$$

Suppose  $\sin \theta = \xi^2$  for  $0 \leq \xi \leq 1$ . By manipulating variables, we can get

$$d\theta = \frac{2\xi d\xi}{\sqrt{1-\xi^4}}$$

$$\int \sqrt{\sin \theta} d\theta = 2 \int \frac{\xi^2 d\xi}{\sqrt{1-\xi^4}} = 2 \int \left[ \frac{\sqrt{1+\xi^2}}{\sqrt{1-\xi^2}} - \frac{1}{\sqrt{1-\xi^4}} \right] d\xi \quad (4.2)$$

Last equation is elliptic integral E and F. (See appendix C.3) However, we will have  $k = i$  if we directly convert equation 4.2 using elliptic integrals. To prevent this issue, we can apply a change of variables  $\xi = \text{cn}(t, k)$  with  $d\xi = -\text{sn}(t, k) \text{dn}(t, k) dt$  for  $0 \leq t \leq K(k)$ . With choice of  $k = \frac{1}{\sqrt{2}}$ , we get

$$2 \int \left[ \frac{\sqrt{1+\xi^2}}{\sqrt{1-\xi^2}} - \frac{1}{\sqrt{1-\xi^4}} \right] d\xi = 2 \left[ -\sqrt{2} E(\text{am}(t, k), k) + \frac{1}{\sqrt{2}} F(\text{am}(t, k), k) \right]$$

Since,  $\text{am}(t, k) = \arccos(\xi) = \arccos \sqrt{\sin \theta}$ , we can get

$$\begin{aligned} z(\theta) &= -\frac{1}{\sqrt{2\lambda}} \int \sqrt{\sin \theta} d\theta \\ &= \frac{2}{\sqrt{\lambda}} \left[ E(\arccos \sqrt{\sin \theta}, k) - \frac{1}{2} F(\arccos \sqrt{\sin \theta}, k) \right] \end{aligned}$$

Going back to the equation

$$z(x) = \int_x^R \frac{t^2}{\sqrt{R^4 - t^4}} dt$$

Solving this one is similar as before, we can set  $t = R \operatorname{cn}(x, k)$  with  $k = 1/\sqrt{2}$  and deduce

$$\begin{aligned} z(x) &= \frac{R}{\sqrt{2}} \int_0^x \operatorname{cn}^2 \left( \tilde{x}, \frac{1}{\sqrt{2}} \right) d\tilde{x} \\ &= \frac{R}{\sqrt{2}} \left[ 2 \operatorname{E} \left( \operatorname{sn} \left( x, \frac{1}{\sqrt{2}} \right), \frac{1}{\sqrt{2}} \right) - \operatorname{F} \left( \operatorname{sn} \left( x, \frac{1}{\sqrt{2}} \right), \frac{1}{\sqrt{2}} \right) \right] \end{aligned}$$

We can find details in [57]. Thus, we can get the parametrization of the Mylar balloon.

**Theorem 4.2** (Theorem 5.2 [57]). The surface of revolution  $S$  that models the Mylar balloon is parametrized by

$\mathbf{x} = \mathbf{x}(u, v) = (x(u, v), y(u, v), z(u, v))$  for  $u$  in  $[-K(1/\sqrt{2}), K(1/\sqrt{2})]$  and  $v$  in  $[0, 2\pi]$

$$\begin{aligned} x(u, v) &= R \operatorname{cn} \left( u, \frac{1}{\sqrt{2}} \right) \cos v \\ y(u, v) &= R \operatorname{cn} \left( u, \frac{1}{\sqrt{2}} \right) \sin v \\ z(u, v) &= R\sqrt{2} \left[ \operatorname{E} \left( \operatorname{sn} \left( u, \frac{1}{\sqrt{2}} \right), \frac{1}{\sqrt{2}} \right) - \frac{1}{2} \operatorname{F} \left( \operatorname{sn} \left( u, \frac{1}{\sqrt{2}} \right), \frac{1}{\sqrt{2}} \right) \right]. \end{aligned}$$

Using the relation  $\operatorname{dn}^2(u, k) + k^2 \operatorname{sn}^2(u, k) = 1$  and choosing  $k = \frac{1}{\sqrt{2}}$ , coefficient of the first and second fundamental forms can be derived as follows (see appendix C.3 and C.4). Now we will use results from paper [57].

$$E = \frac{R^2}{2}, F = 0, G = R^2 \operatorname{cn}^2 \left( u, \frac{1}{\sqrt{2}} \right), L = R \operatorname{cn} \left( u, \frac{1}{\sqrt{2}} \right), M = 0, N = R \operatorname{cn}^3 \left( u, \frac{1}{\sqrt{2}} \right).$$

Notice  $E, F$  are parameters related to the first fundamental form. We can compute Gaussian and mean curvatures as shown below

$$K = \frac{LN}{EG} = \frac{2cn^2(u, \frac{1}{\sqrt{2}})}{R^2}, \quad (4.3)$$

$$H = \frac{1}{2} \left( \frac{L}{E} + \frac{N}{G} \right) = \frac{3 \operatorname{cn}(u, \frac{1}{\sqrt{2}})}{2R} \quad (4.4)$$

By solving  $k^2 - 2kH + K = 0$ , we get  $k_\mu = 2k_\pi = \frac{2 \operatorname{cn}(u, \frac{1}{\sqrt{2}})}{R}$ . From these relations, we get principal curvatures have a ratio of 2 : 1. There could be several ways to compute the ratio between final radius  $R$  and initial radius  $a$ . Mladenov and Oprea's papers have used Elliptic integrals and Jacobi elliptic functions. However, Paulsen computed this integral using the Gamma function in [64]. This ratio can be computed from  $\int_0^R \sqrt{1 + z'(x)^2} dx = \int_0^R \frac{R^2}{\sqrt{R^4 - x^4}} dx = a$ . By plugging in  $x = at^{1/4}$ , we can get

$$\frac{R}{4} \int_0^1 t^{-3/4} (1-t)^{-1/2} dt = a \quad (4.5)$$

The solution in [64] is  $R = \frac{4a\sqrt{2\pi}}{\Gamma(1/4)^2} \simeq 0.7627a$ . Physical interpretation of this result can be shown below.

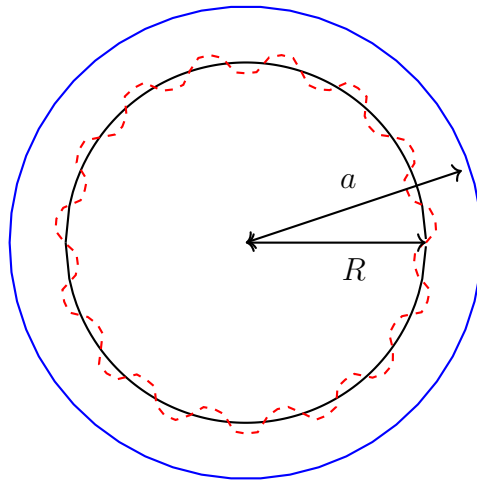


Figure 4.3: Top profile of Mylar balloon. The blue line represents the initial radius, the red dashed line shows wrinkles caused by the non-stretchable property, and the black line represents the final mean radius.

Since the perimeter of (initial state) disk will be fixed (if we assume gluing) to  $a$ , we can estimate that sides will be wrinkled to maintain their original perimeter and fulfill the requirement of new radius  $R$ . The azimuthal profile of a Mylar balloon can be solved using bending energy minimization with length constraints  $(2\pi a, 2\pi R)$ . Suppose we minimize for curvature  $\kappa(s)^2$  (or equivalently one-dimensional bending energy along azimuthal direction). In that case, this problem will be the same as Euler's elastica problem.

### 4.1.3 Mylar balloon with point mass

In this section, using a similar method as above, we will add masses and estimate the profile of the Mylar balloon. Suppose there is a point mass at  $x = 0$ , potential energy can be described by  $E_p = mgz(0)$ . We can rewrite this as  $\int_{-\infty}^{\infty} mg\delta(x)z(x)dx$ . Consider potential energy as

$$E_p = pV - mgz(0)$$

where  $p$  is the pressure and  $V$  is the volume of the membrane. We can assume that  $mgz(0)$  has a relatively smaller impact on total energy than energy from pressure. Therefore, if we apply the same assumptions (maximizing energy and maintaining arc length) from the geometry shown below, we get

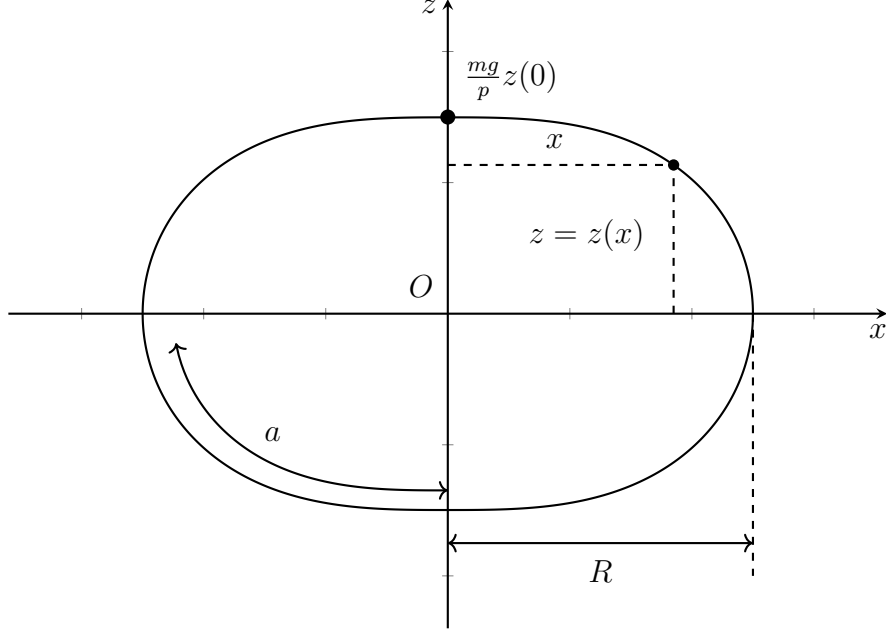


Figure 4.4: A geometry of Mylar balloon with point mass.

$$\text{maximize}(V - \frac{mg}{p} z(0)), \int_0^R \sqrt{1 + z'(x)^2} dx = a$$

First and second equation can be rewritten as  $V - \frac{mg}{p} z(0), \lambda \int_0^R \sqrt{1 + z'(x)^2} dx$ . By manipulating these equations as shown below

$$\begin{aligned} & 4\pi \int_0^R xz(x)dx - \frac{mg}{p} \int_{-\infty}^{\infty} \delta(x)z(x)dx + \lambda \int_0^R \sqrt{1 + z'(x)^2} dx \\ &= 4\pi \int_0^R xz(x)dx - \frac{mg}{p} \int_0^R \delta(x)z(x)dx + \lambda \int_0^R \sqrt{1 + z'(x)^2} dx \\ &= \int_0^R \left( 4\pi xz(x) - \frac{mg}{p} \delta(x)z(x) + \lambda \sqrt{1 + z'(x)^2} \right) dx \end{aligned}$$

If we apply the Euler-Lagrange equation with the Lagrange multiplier, we get

$$\frac{d}{dx} \left( \frac{\lambda z'(x)}{\sqrt{1 + z'(x)^2}} \right) - \left( 4\pi x - \frac{mg}{p} \delta(x) \right) = 0$$

Integrating both sides, we have

$$\frac{z'(x)}{\sqrt{1+z'(x)^2}} = \frac{2\pi}{\lambda}x^2 - \frac{mg}{p\lambda} + C$$

Note that  $z'(0) \neq 0$  in this case, so we are assuming case  $m = 0$  and get  $C = 0$  from  $z'(0) = 0$ .

Using same argument as above, we can set  $2\pi/\lambda = -\frac{1}{n^2}$  and define  $\frac{mg}{p\lambda} = \frac{mg}{-2\pi pn^2} = -c$ . Now we have

$$\frac{z'(x)}{\sqrt{1+z'(x)^2}} = -\frac{1}{n^2}x^2 + c$$

By manipulating the above equation again,

$$\begin{aligned} \frac{n^2 z'(x)}{\sqrt{1+z'(x)^2}} &= -x^2 + cn^2 \\ n^2 z'(x) &= -\sqrt{1+z'(x)^2}(x^2 - cn^2) \\ n^4 z'(x)^2 &= (1+z'(x)^2)(x^2 - cn^2)^2 \\ n^4 z'(x)^2 - (x^2 - cn^2)^2 z'(x)^2 &= (x^2 - cn^2)^2 \\ (n^4 - (x^2 - cn^2)^2) z'(x)^2 &= (x^2 - cn^2)^2 \\ z'(x)^2 &= \frac{(x^2 - cn^2)^2}{n^4 - (x^2 - cn^2)^2} \\ z'(x) &= -\frac{(x^2 - cn^2)}{\sqrt{n^4 - (x^2 - cn^2)^2}} \end{aligned}$$

We want to set  $z(R) = 0$  and  $\lim_{x \rightarrow R^-} z'(x) = -\infty$ . That will give us  $n^4 - (R^2 - cn^2)^2 = 0$ .

Thus, we get  $n^2 = \pm(R^2 - cn^2)$  and  $n = \sqrt{\frac{R^2}{c-1}}, \sqrt{\frac{R^2}{c+1}}$ . Both solutions will have  $n = R$  for

$n = 0, c = 0$ . Let  $\frac{mg}{2\pi p} = \eta$ . Plugging  $\eta$  into  $c = \frac{mg}{2\pi pn^2} = \frac{\eta}{n^2}$  and  $n^2 = \pm(R^2 - cn^2)$ , then

we get  $n^2 = \pm(R^2 - \eta)$  and  $c = \frac{\eta}{\pm(R^2 - \eta)}$ . Since we want  $\eta$  to be smaller than  $R^2$  ( $n$  will

be always real), we can take  $n = \sqrt{R^2 - \eta}$ . Following figure shows a comparison between

Mylar balloon ( $c = 0$ ) with cases  $c = 0.04/0.14$ .

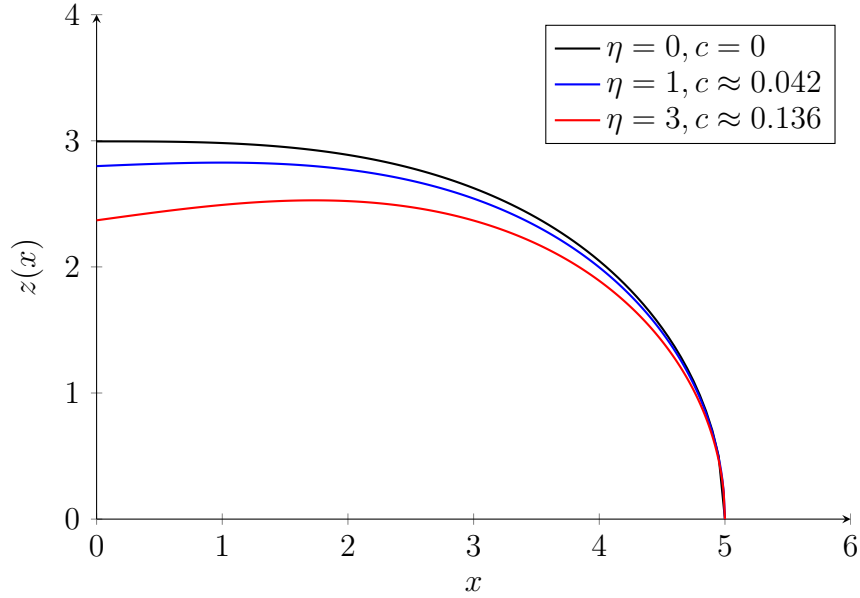


Figure 4.5: Profiles from different ratio of pressure and point mass defined by  $\eta = \frac{mg}{2\pi p}$ .

#### 4.1.4 Mylar balloon with cylindrical mass

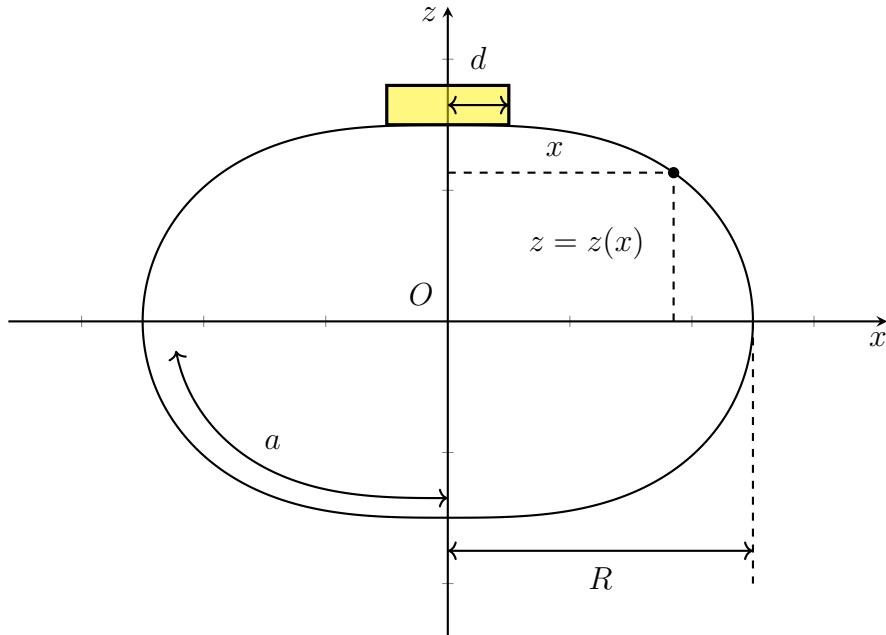


Figure 4.6: A geometry of Mylar balloon with cylindrical mass.

Suppose there is a cylindrical mass at  $x = 0$ , the same as a point mass. Since contact area of weight to surface is disk shape with radius  $d$ , we will apply mean height along  $x$  axis  $\frac{1}{N} \sum_{x_i \in X} z(x_i)$  for  $|X| = N$ . (one can use pressure  $p' = \frac{mg}{\pi d^2}$  instead of  $mgz$ , however, we

will use mean height for representing constant force in perpendicular direction.) Previous equation can be written as  $\frac{1}{d} \int_0^d z(x) dx$  for continuous case. From energy relations, we have  $\frac{E}{p} = V - \frac{mg}{pd} \int_0^d z(x) dx$ . Thus, we have the following conditions.

$$\text{maximize} \left( V - \frac{mg}{pd} \int_0^d z(x) dx, \int_0^R \sqrt{1 + z'(x)^2} dx = a \right)$$

$$\begin{aligned} & 4\pi \int_0^R xz(x) dx - \frac{mg}{pd} \int_0^R z(x)\theta(d-x) dx + \lambda \int_0^R \sqrt{1 + z'(x)^2} dx \\ &= \int_0^R \left( 4\pi xz(x) - \frac{mg}{pd} z(x)\theta(d-x) + \lambda \sqrt{1 + z'(x)^2} \right) dx \end{aligned}$$

Notice that  $\frac{mg}{pd} \int_0^d z(x) dx$  can be rewritten using Heaviside function  $\theta(x)$  and we have  $\frac{mg}{pd} \int_0^R z(x)\theta(d-x) dx$ . If we apply the Euler-Lagrange equation with the Lagrange multiplier, we get

$$\frac{d}{dx} \left( \frac{\lambda z'(x)}{\sqrt{1 + z'(x)^2}} \right) - \left( 4\pi x - \frac{mg}{pd} \theta(d-x) \right) = 0$$

Integrating both sides, we have

$$\frac{z'(x)}{\sqrt{1 + z'(x)^2}} = \frac{2\pi}{\lambda} x^2 - \frac{mg}{pd\lambda} \left( (d-x)\theta(x-d) + x \right) + C$$

Note that the above equation holds for  $d \neq 0$ . Since  $z'(0) \neq 0$  in this case, we are assuming case  $m = 0$  and get  $C = 0$  from  $z'(0) = 0$ . Using same argument as above, we can set  $2\pi/\lambda = -\frac{1}{n^2}$  and define  $\frac{mg}{pd\lambda} = \frac{mg}{-2\pi pdn^2} = -c$ . By setting  $f(x) = ((d-x)\theta(x-d) + x)$ , we

have

$$\begin{aligned}
\frac{z'(x)}{\sqrt{1+z'(x)^2}} &= -\frac{1}{n^2}x^2 + c\left((d-x)\theta(x-d)+x\right) \\
\frac{n^2 z'(x)}{\sqrt{1+z'(x)^2}} &= -x^2 + cn^2 f(x) \\
n^2 z'(x) &= -\sqrt{1+z'(x)^2}(x^2 - cn^2 f(x)) \\
n^4 z'(x)^2 &= (1+z'(x)^2)(x^2 - cn^2 f(x))^2 \\
n^4 z'(x)^2 - (x^2 - cn^2 f(x))^2 z'(x)^2 &= (x^2 - cn^2 f(x))^2 \\
(n^4 - (x^2 - cn^2 f(x))^2) z'(x)^2 &= (x^2 - cn^2 f(x))^2 \\
z'(x)^2 &= \frac{(x^2 - cn^2 f(x))^2}{n^4 - (x^2 - cn^2 f(x))^2} \\
z'(x) &= -\frac{(x^2 - cn^2 f(x))}{\sqrt{n^4 - (x^2 - cn^2 f(x))^2}}
\end{aligned}$$

Thus, we get  $z'(x) = -\frac{(x^2 - cn^2 f(x))}{\sqrt{n^4 - (x^2 - cn^2 f(x))^2}} = -\frac{(x^2 - cn^2((d-x)\theta(x-d)+x))}{\sqrt{n^4 - (x^2 - cn^2((d-x)\theta(x-d)+x))^2}}$ . Like before, by solving  $n^4 - (R^2 - cn^2((d-R)\theta(R-d)+R))^2 = 0$ , we get  $n^2 = \pm(R^2 - \eta)$  and  $c = \frac{\eta}{\pm(R^2 - \eta)d}$  where  $\frac{mg}{2\pi p} = \eta$ . Notice that potential energy is described by mass, so  $n$  does not have any effects from  $d$ . Finally, we get an expression for  $z(x)$  as below.

$$z(x) = \int_x^R \frac{(t^2 - cn^2((d-t)\theta(t-d)+t))}{\sqrt{n^4 - (t^2 - cn^2((d-t)\theta(t-d)+t))^2}} dt$$

The following graph compares some  $\eta$  and  $d$  values.

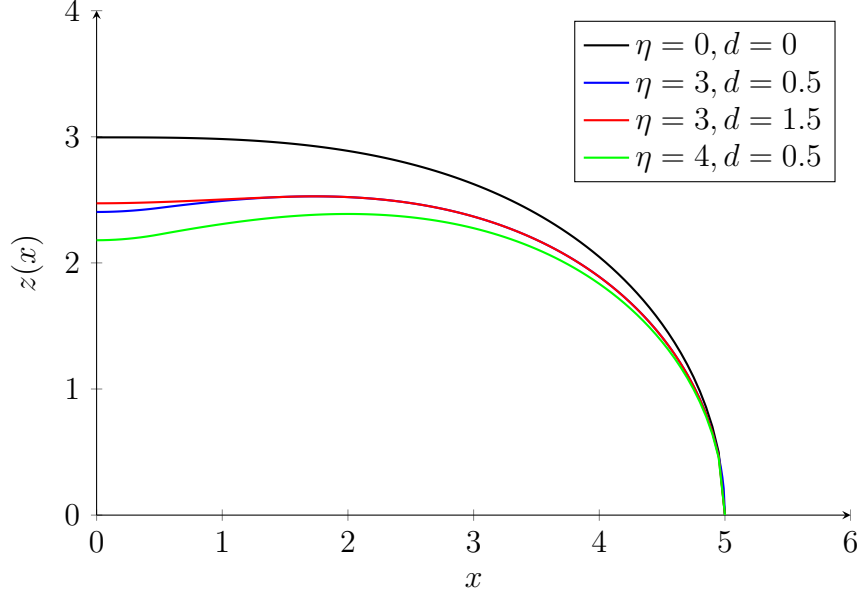


Figure 4.7: Profiles from different radius  $d$  of masses and  $\eta = \frac{mg}{2\pi p}$ .

#### 4.1.5 Mylar ballon with perpendicular forces

If we assume  $d \geq R$ , we can eliminate a Heaviside function.

$$z(x) = \int_x^R \frac{t^2}{\sqrt{n^4 - t^4}} dt \quad (4.6)$$

$$z(x) = \int_x^R \frac{(t^2 - cn^2)}{\sqrt{n^4 - (t^2 - cn^2)^2}} dt \quad (4.7)$$

$$z(x) = \int_x^R \frac{(t^2 - cn^2t)}{\sqrt{n^4 - (t^2 - cn^2t)^2}} dt \quad (4.8)$$

where equation 1 comes from section 4.1.2 and 2,3 come from sections 4.1.3,4.1.4 respectively.

Note that  $n, c$  vary from the shape/configuration of masses. We can generalize the above as

$$z(x) = \int_x^R \frac{\alpha t^2 - \beta t - \gamma}{\sqrt{n^4 - (\alpha t^2 - \beta t - \gamma)^2}} dt \quad (\alpha \neq 0). \quad (4.9)$$

This can be thought as optimizing  $\frac{E}{2\pi p} = 2 \int_0^R xz(x)dx - \frac{F}{2\pi p} \int_0^R z(x)dx - \frac{f}{2\pi p} \int_0^R z(x)\delta(x)dx$  with fixed arc length for  $z'(0) \neq 0$  where  $F, f, p$  represent uniform perpendicular force, point force at the center, and pressure. Notice that  $\lambda$  will be added from the length constraint,

and the value of  $\lambda$  can be chosen from boundary conditions as we did in previous sections. If we recall from the previous section, this is the same problem statement as Euler's elastica. Using condition  $z(R^-)' = -\infty$ , we get  $n^2 = \pm(\alpha R^2 - \beta R - \gamma)$ .

$$z(x) = \int_x^R \frac{\alpha t^2 - \beta t - \gamma}{\sqrt{(\alpha R^2 - \beta R - \gamma)^2 - (\alpha t^2 - \beta t - \gamma)^2}} dt \quad (\alpha \neq 0). \quad (4.10)$$

Since  $n$  is determined by  $\alpha, \beta, \gamma$  in this case, the ratio between these parameters will decide to shape of the curve.

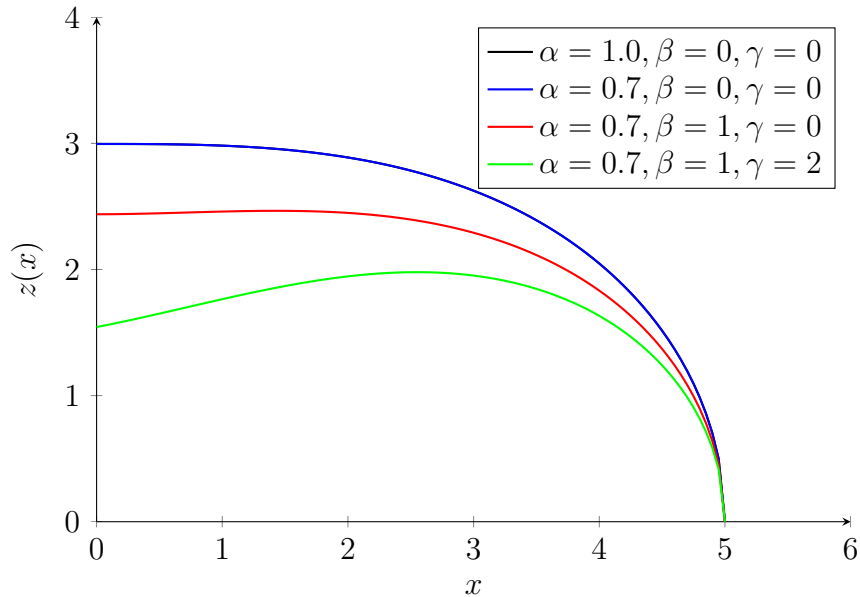


Figure 4.8: Profiles from different  $\alpha, \beta, \gamma$  where  $\alpha = \frac{1}{\lambda}, \beta = \frac{F}{2\pi p \lambda}$ , and  $\gamma = \frac{f}{\lambda 2\pi p}$ .

As we can expect, if  $\beta = \gamma = 0$ , we get a Mylar balloon. We will get exact results if we maintain the same ratio between parameters as presented in figure 4.9. Mylar balloon is symmetric at  $z = 0$ , so we get (reflected) lower part of surface for  $\alpha < 0$ . The sign of  $\beta, \gamma$  determines the direction of applied forces relative to pressure for an inflated surface.

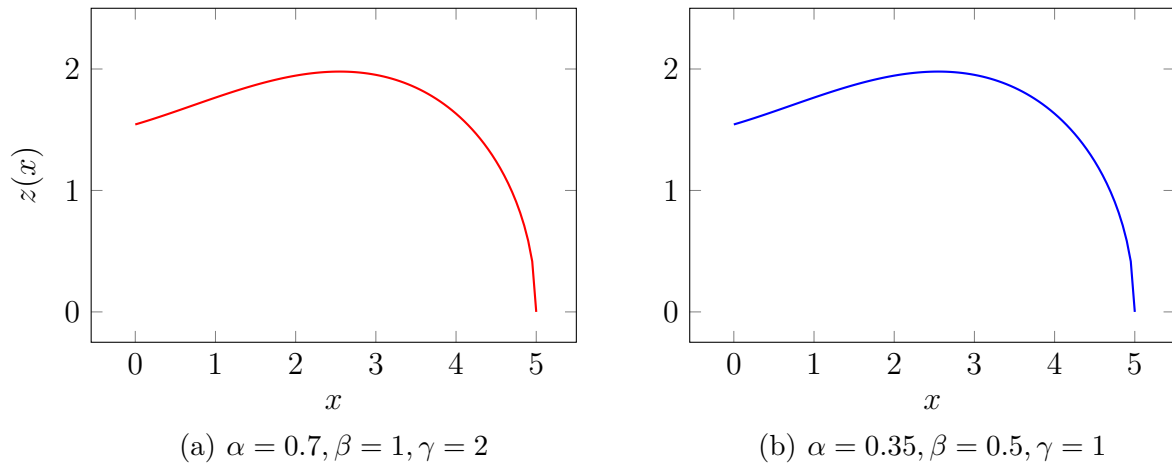


Figure 4.9: Different values of  $\alpha$  with a same ratio of  $\frac{\alpha}{\beta} = 0.7, \frac{\alpha}{\gamma} = 0.35$  show identical profile.

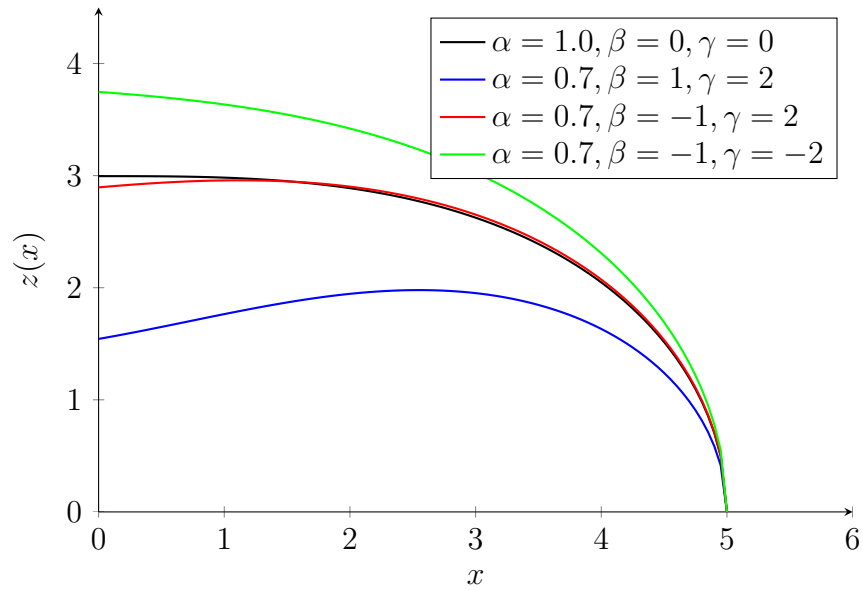


Figure 4.10: Profile comparison of forces with different directions for  $\gamma \neq 0$ .

We can draw similar plots for  $|\beta| = 1, \gamma = 0$ .

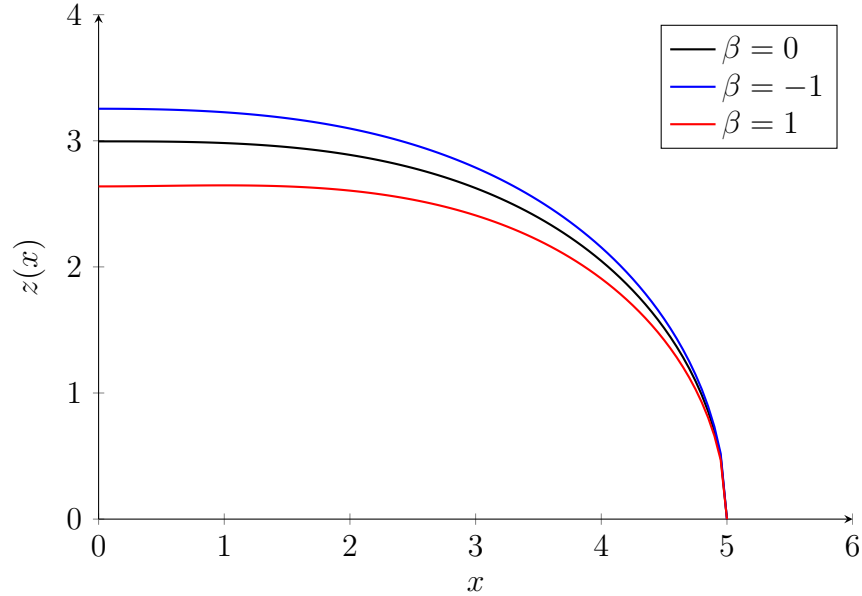


Figure 4.11: Profile comparison of forces with different directions for  $\gamma = 0$ .

We can observe the amount of deformation in  $z(x)$  from the same perpendicular forces with different directions is not symmetric. Notice that Euler-Lagrange assumes arc length is a constant. Thus, physically, various forces with the same arc length will have different radii, so all of them can have the same arc length. One can get radius by solving an arc length equation similar to Paulsen's paper [64].

#### 4.1.6 Mylar balloon with applied force

We already know that a Mylar balloon with applied force from previous sections is just Euler's elastica. This result comes from symmetric geometry in the azimuthal direction, and we can reduce the three-dimensional problem (or surface in  $\mathbb{R}^2$ ) to two-dimensional (or curve in  $\mathbb{R}$ ). Notice that Euler's elastica problem has assumptions.

- Endpoints are fixed.
- One side slope is fixed.

So far, we have considered the transversality condition for Mylar balloons  $z(R_-) = -\infty$ . We will show a different case in later sections. We can find various studies, methods, and tools

to parameterize Euler's elastica using elliptic and trigonometric functions. For example, [55] introduced parametrization methods of Euler's elastica. [2], and [1] showed a process to solve this problem using boundary conditions. This section will introduce a direct computational approach that will be used later.

$$z(x) = \int_x^R \frac{\alpha t^2 + \beta t + \gamma}{\sqrt{\lambda^4 - (\alpha t^2 + \beta t + \gamma)^2}} dt.$$

If we don't require  $z(R) = 0$ , we can change the range of  $t$ , and we have

$$\begin{aligned} z(x) &= \int_0^x \frac{\alpha t^2 + \beta t + \gamma}{\sqrt{(\lambda^2 - \alpha t^2 - \beta t - \gamma)(\lambda^2 + \alpha t^2 + \beta t + \gamma)}} dt \\ &= \int_0^x \frac{1}{2} \left[ \frac{\sqrt{(\lambda^2 + \alpha t^2 + \beta t + \gamma)}}{\sqrt{(\lambda^2 - \alpha t^2 - \beta t - \gamma)}} - \frac{\sqrt{(\lambda^2 - \alpha t^2 - \beta t - \gamma)}}{\sqrt{(\lambda^2 + \alpha t^2 + \beta t + \gamma)}} \right] dt. \end{aligned}$$

$$\begin{aligned} z(x) &= \int_0^x \frac{\alpha t^2 + \beta t + \gamma}{\sqrt{(\lambda^2 - \alpha t^2 - \beta t - \gamma)(\lambda^2 + \alpha t^2 + \beta t + \gamma)}} dt \\ &= \int_0^x \frac{1}{2} \left[ \frac{\sqrt{(\lambda^2 + \alpha t^2 + \beta t + \gamma)}}{\sqrt{(\lambda^2 - \alpha t^2 - \beta t - \gamma)}} - \frac{\sqrt{(\lambda^2 - \alpha t^2 - \beta t - \gamma)}}{\sqrt{(\lambda^2 + \alpha t^2 + \beta t + \gamma)}} \right] dt. \end{aligned}$$

Suppose  $F(t), G(t)$  be indefinite integral defined by

$$F(t) = \frac{1}{2} \int_0^x \left[ \frac{\sqrt{(\lambda^2 + \alpha t^2 + \beta t + \gamma)}}{\sqrt{(\lambda^2 - \alpha t^2 - \beta t - \gamma)}} \right] dt, \quad G(t) = \frac{1}{2} \int_0^x \left[ \frac{\sqrt{(\lambda^2 - \alpha t^2 - \beta t - \gamma)}}{\sqrt{(\lambda^2 + \alpha t^2 + \beta t + \gamma)}} \right] dt$$

Let us consider a more straightforward case

$$\int_0^x \frac{\sqrt{(\alpha(t + \beta)^2 + \gamma_1)}}{\sqrt{(\alpha(t + \beta)^2 + \gamma_2)}} dt.$$

Therefore, we can rewrite the following equation using an elliptic integral

$$\int_0^x \sqrt{\frac{\gamma_1}{\gamma_2}} \frac{\sqrt{(\alpha(t + \beta)^2/\gamma_1 + 1)}}{\sqrt{(\alpha(t + \beta)^2/\gamma_2 + 1)}} dt.$$

Then we can apply a change of variable  $t' = \sqrt{-\alpha/\gamma_2}(t + \beta)$

$$\int_0^{\sqrt{-\alpha/\gamma_2}(x+\beta)} \sqrt{\frac{\gamma_1}{-\alpha} \frac{\sqrt{(-\gamma_2/\gamma_1 t'^2 + 1)}}{\sqrt{(-t'^2 + 1)}}} dt'$$

Finally, we can apply C.2 and get  $k = \sqrt{\frac{\gamma_2}{\gamma_1}}$ ,  $\phi = \arcsin(\sqrt{-\alpha/\gamma_2}(t' + \beta))$ , and  $\sqrt{\frac{\gamma_1}{-\alpha}} \mathbb{E}[\arcsin(\sqrt{-\alpha/\gamma_2}(t' + \beta)), \sqrt{\frac{\gamma_2}{\gamma_1}}] + C$  ( $C$  is constant). Thus, we can compute the solution in the following

$$\int_0^x \frac{\sqrt{(\lambda^2 + \alpha t^2 + \beta t + \gamma)}}{\sqrt{(\lambda^2 - \alpha t^2 - \beta t - \gamma)}} dt.$$

By using Mathematica v12.1[96], the solution will be as shown below:

$$\frac{\sqrt{-\frac{\alpha}{m}n(x)(n(x) + 2\lambda^2)} \mathbb{E}[\arcsin[\frac{\beta+2\alpha x}{\sqrt{m}}, \frac{m}{m-8\alpha\lambda^2}]] + C}{\frac{2\alpha}{\sqrt{m}} \sqrt{n(x) \frac{\alpha(n(x)+2\lambda^2)}{m-8\alpha\lambda^2}}}$$

where  $m = \beta^2 + 4\alpha(-\gamma + \lambda^2)$ ,  $n(x) = \gamma + \lambda^2 + x(\beta + \alpha x)$ , and  $C$  is constant. Note that Mathematica uses  $k^2$  instead of  $k$ .

$$\mathbb{E}(\phi, k) = \int_0^{\sin \phi} \frac{\sqrt{1 - kt^2}}{\sqrt{1 - t^2}} dt. \quad (4.11)$$

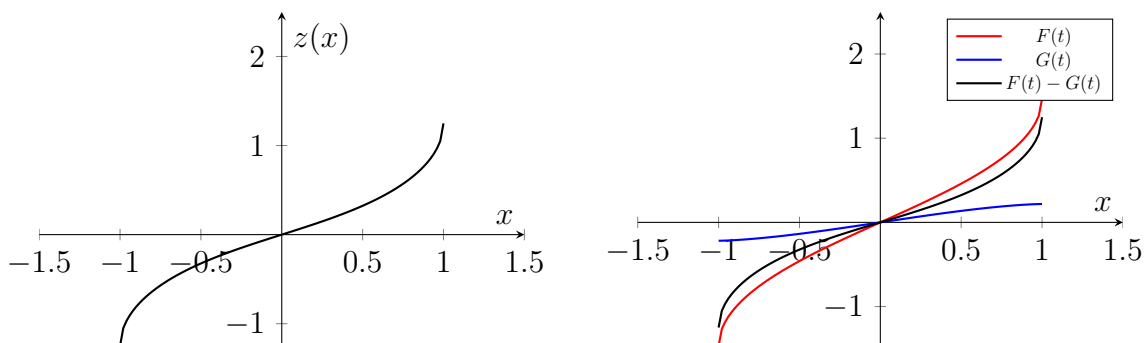
Therefore, we can get desired results from  $F(t) - G(t)$  using the boundary conditions. Notice that if  $k < 0$ , then we get  $\mathbb{E}(\phi, ia)$  and  $k = ia$  for  $a \in \mathbb{R}$ . If we do not want to work with imaginary values, we need to start by assuming  $x$  as we have already seen in section 4.1.2. As presented in [2], Euler's elastica can have multiple solutions on the boundary conditions. However, in the next section, we will expand to the  $n$ -dimensional case. There might not be known solutions to work out these integrals. Thus, the easier way will be to expand complex space and employ complex numbers for the real functions. Recall that from the previous

section, we have

$$\begin{cases} Z(s) &= X(s) + Y(s)i \\ Y(s) &= \int^X \frac{\alpha X^2 + \beta X + \gamma}{\sqrt{\lambda^4 - (\alpha X^2 + \beta X + \gamma)^2}} dX \\ s &= \int^X \frac{\lambda^2}{\sqrt{\lambda^4 - (\alpha X^2 + \beta X + \gamma)^2}} dX \end{cases} \quad (4.12)$$

where  $Z(s) \in \mathbb{C}$ ,  $X(s) \in \mathbb{R}$ . We generally require  $Y(s) \in \mathbb{R}$ . For some reflective/symmetric case, we may need to compute integral separately for  $Y(s) = a + ib$  and  $a, b \in \mathbb{R}$  such that combination  $\Re(Y(s))$  and  $\Im(Y(s))$  can be used to represent curves/surfaces. The following figure shows an example for comparing numerical and symbolic integration results.

$$z(x) = \int_x^R \frac{t^2 + 1}{\sqrt{2 - (t^2 + 1)^2}} dt. \quad (4.13)$$



(a) Numerical integration

(b) Symbolic integration

Figure 4.12: Comparison of numerical and symbolic integration results for equation 4.13.

Notice that Numeric integration and symbolic results agree. Going back to the following equation again,

$$z(x) = \int_0^x \frac{\alpha t^2 + \beta t + \gamma}{\sqrt{\lambda^4 - (\alpha t^2 + \beta t + \gamma)^2}} dt.$$

Above equation can be represented as (by Bernoulli and Euler)

$$z(x) = \int_0^x \frac{a^2 - c^2 + t^2}{\sqrt{(c^2 - t^2)(2a^2 - c^2 + t^2)}} dt \quad (4.14)$$

By setting  $\lambda = \frac{a^2}{2c^2}$ , we can observe how graph changes for  $0.25 < \lambda < \infty$ , and  $-1 \leq x \leq 1$ . Below plot shows results for various  $\lambda$ . More specific values and visualizations could be found in [104].

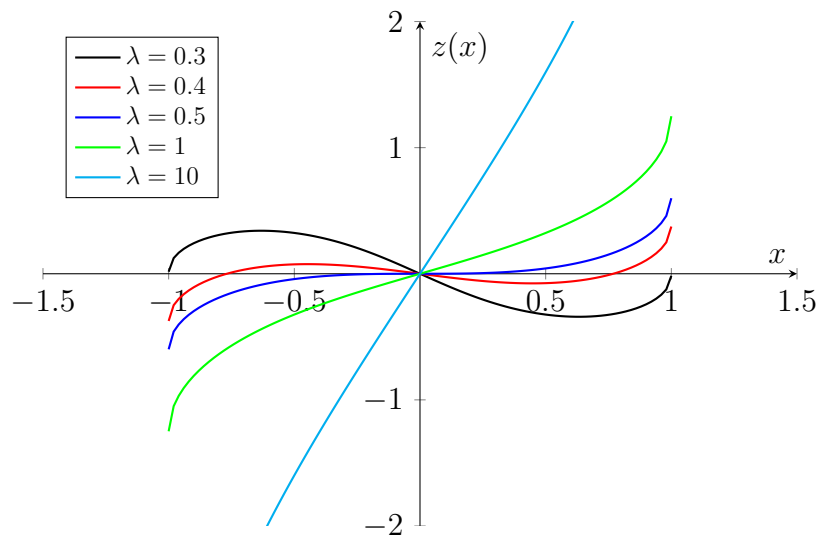


Figure 4.13: Various profiles of equation 4.14 for  $0.3 \leq \lambda \leq 10$ .

For  $\lambda \leq 0.25$ , a separate calculation is required. Please check [72] for more details.

## 4.2 Euler's elastica for $n$ -dimensional implementation

In this section, we will first use Paulsen's arguments to derive an equation for a spherical balloon. Then, we will develop  $n$ -dimensional Euler's elastica using previous results, which we can expand to more complicated structures for polynomials, multiple boundary conditions, and multiple volumes.

### 4.2.1 Spherical balloon with perpendicular forces

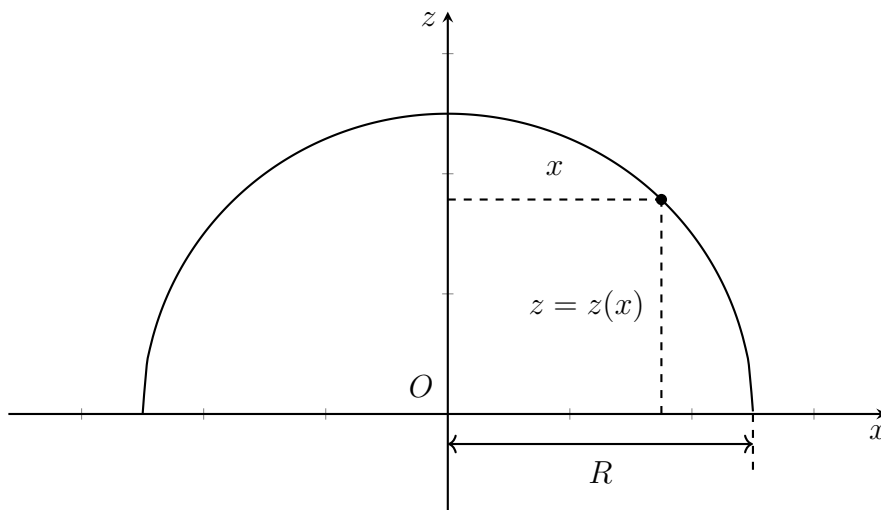


Figure 4.14: Geometry of spherical balloon.

We can write similar equations for a spherical balloon.

$$V = 4\pi \int_0^R xz(x)dx, \quad S = 4\pi \int_0^R x\sqrt{1 + z'(x)^2}dx$$

Notice that the first equation is the same as the volume equation of the Mylar balloon, we have used  $z(x)$ , and eventually,  $z(x)$  will be used to plot  $z$  coordinate in  $\mathbb{R}^3$  along  $x$  (radial direction). Let  $F(x, z(x), z'(x)) = 4\pi xz(x) + \lambda 4\pi x\sqrt{1 + z'(x)^2}$ . Since  $F(x, z(x), z'(x))$  contains both  $x$  and  $z(x)$ , we can apply usual Euler-Lagrange equation  $\frac{d}{dx}\left(\frac{\partial F}{\partial z'}\right) - \frac{\partial F}{\partial z} = 0$  same as Mylar balloon case, then we get

$$\begin{aligned} \frac{d}{dx} \left( \frac{\lambda 4\pi x z'(x)}{\sqrt{1 + z'(x)^2}} \right) - 4\pi x &= 0 \\ \int \frac{d}{dx} \left( \frac{\lambda x z'(x)}{\sqrt{1 + z'(x)^2}} \right) dx &= \int x dx \\ \frac{\lambda x z'(x)}{\sqrt{1 + z'(x)^2}} &= \frac{1}{2}x^2 + C. \end{aligned}$$

Using  $x = 0$  and  $z'(0) = 0$ , we get  $C = 0$ . We can continue manipulating equations as follows,

$$\begin{aligned}\frac{xz'(x)}{\sqrt{1+z'(x)^2}} &= \frac{1}{2\lambda}x^2 \\ \frac{z'(x)}{\sqrt{1+z'(x)^2}} &= \frac{1}{2\lambda}x \\ 4\lambda^2 z'(x)^2 &= (1+z'(x)^2)x^2 \\ z'(x)^2(4\lambda^2 - x^2) &= x^2 \\ z'(x)^2 &= \frac{x^2}{4\lambda^2 - x^2} \\ z'(x) &= -\frac{x}{\sqrt{4\lambda^2 - x^2}}.\end{aligned}$$

Notice that we have chosen a negative solution like the Mylar Balloon case. By requiring  $z'(R_-) = -\infty$ , we get  $4\lambda^2 = R^2$  and  $2\lambda = R$ . By integrating both sides,

$$\begin{aligned}\int dz &= -\int \frac{x}{\sqrt{R^2 - x^2}} dx \\ z &= \sqrt{R^2 - x^2}.\end{aligned}$$

Therefore, we finally have  $z^2 = R^2 - x^2$  as expected.

We can consider generalized cases discussed in section 4.1.5 starting from the following equation for a spherical balloon with forces.

$$\frac{xz'(x)}{\sqrt{1+z'(x)^2}} = \frac{1}{2\lambda}x^2$$

Let us consider

$$\frac{xz'(x)}{\sqrt{1+z'(x)^2}} = ax^2 + bx + c \quad (a, b, c \text{ constant})$$

Note that we are working on  $x, z$  in real space (and  $a, b, c, R \in \mathbb{R}$ ). Rewriting in terms of  $z(x)'$ , we have

$$\begin{aligned}
\frac{xz'(x)}{\sqrt{1+z'(x)^2}} &= ax^2 + bx + c \\
\frac{x^2z'(x)^2}{1+z'(x)^2} &= (ax^2 + bx + c)^2 \\
x^2z'(x)^2 &= (1+z'(x)^2)(ax^2 + bx + c)^2 \\
(x^2 - (ax^2 + bx + c)^2)z'(x)^2 &= (ax^2 + bx + c)^2 \\
z'(x)^2 &= \frac{(ax^2 + bx + c)^2}{x^2 - (ax^2 + bx + c)^2} \\
z'(x) &= -\frac{ax^2 + bx + c}{\sqrt{x^2 - (ax^2 + bx + c)^2}}
\end{aligned}$$

Thus, we can get

$$z(x) = \int_x^R \frac{at^2 + bt + c}{\sqrt{t^2 - (at^2 + bt + c)^2}} dt \quad (4.15)$$

where  $a, b, c \in \mathbb{R}$  have the following relation  $aR^2 + bR + c = \pm R$  from transversality condition  $z'(R_-) = -\infty$ . The above equation can be easily rewritten as

$$\begin{aligned}
z(x) &= \int_x^R \frac{mat^2 + mbt + mc}{\sqrt{(mt)^2 - (mat^2 + mbt + mc)^2}} dt \\
&= \int_x^R \frac{\alpha t^2 + \beta t + \gamma}{\sqrt{(mt)^2 - (\alpha t^2 + \beta t + \gamma)^2}} dt
\end{aligned} \quad (4.16)$$

The figure below shows plots for  $0 < x \leq R$ .

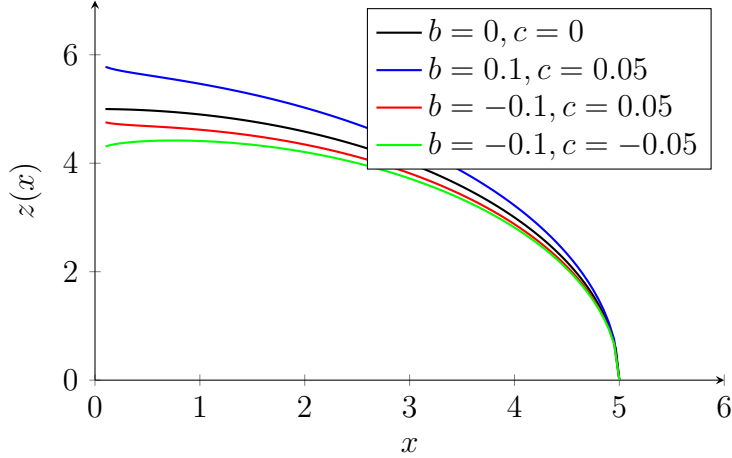


Figure 4.15: Profiles of spherical balloon with different  $b, c$  values (where  $a = \frac{R-bR-c}{R^2}$ ).

Notice that if  $c = 0$ , the equation can be easily computed, and we have

$$z(x) = \frac{\sqrt{x^2(1 - (ax + b)^2)}}{ax} = \frac{\sqrt{1 - (ax + b)^2}}{a}$$

for  $a, b \in \mathbb{R}$  satisfies  $aR^2 + bR = \pm R$ . If  $b = c = 0$ , we get  $a = \frac{1}{R}$  and  $z(x) = \sqrt{R^2 - x^2}$  as expected.

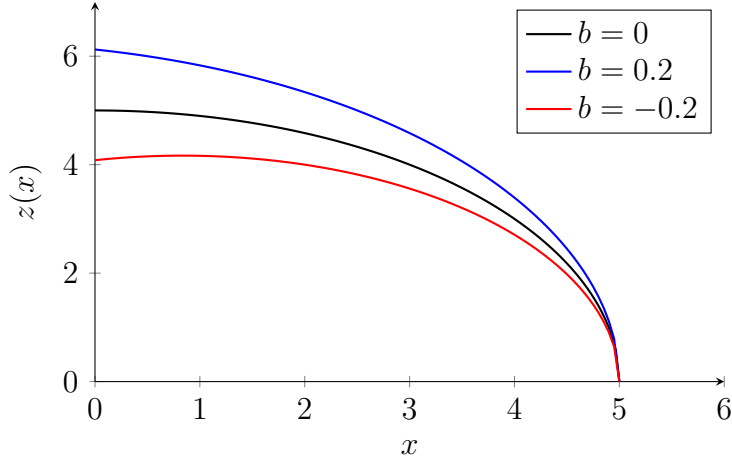


Figure 4.16: Profile comparison of a spherical balloon for positive and negative  $b$  values (where  $c = 0$ ).

The above figure represents a comparison between positive and negative  $b$  values. Going back to equation 4.16, if we take  $\Re(z(x))$  and consider higher forces that are pressing down to the plane, the surface will look like donuts, as shown below. (technically, it is not a torus because the inner radius has a different value with a maximum  $z(x)$ .)

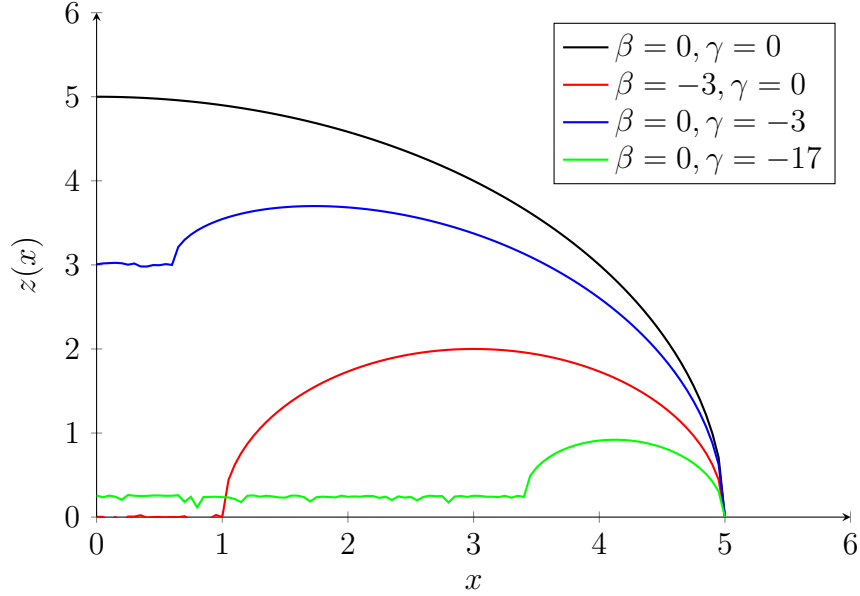


Figure 4.17: Profile of a spherical balloon with higher forces for  $\alpha = 1$ .

where  $\alpha = 1$  and  $m$  is chosen for a condition  $z'(R_-) = -\infty$ . Because of imaginary values, there is a precision problem in this graph. Notice that the effect of  $\beta$  (radial, perpendicular force-related parameter) and  $\gamma$  (point force-related parameter) are different. Varying  $\beta$  will change radius (inner horizontal radius), but changing  $\gamma$  will have an intermediate angle between a spherical balloon and donuts based on its values. That will be easier to understand if we consider poking spherical balloons with force.

## 4.2.2 $n$ -dimensional implementation

Recall that we have

$$z(x) = \int_x^R \frac{\alpha t^2 + \beta t + \gamma}{\sqrt{n^4 - (\alpha t^2 + \beta t + \gamma)^2}} dt \quad (\text{Mylar balloon/Euler elastica}) \quad (4.17)$$

$$z(x) = \int_x^R \frac{\alpha t^2 + \beta t + \gamma}{\sqrt{t^2 - (\alpha t^2 + \beta t + \gamma)^2}} dt \quad (\text{Spherical balloon}) \quad (4.18)$$

As we inspect in the previous section, the first equations agree with Euler elastica. The second one disagrees because it is optimized from the surface (not the arc length). Thus, we

can integrate both equations into single one as

$$z(x) = \int_x^R \frac{\alpha t^2 + \beta t + \gamma}{\sqrt{\lambda^2 t^{2n} - (\alpha t^2 + \beta t + \gamma)^2}} dt \quad (t \in \mathbb{R} \setminus \{0\}). \quad (4.19)$$

We can define this type of structure where  $n$  is the power for additional optimization parameter  $\int x^n \sqrt{1 + z'(x)^2}$  besides the volume equation in  $3d$  ( $n = 0$  for arc,  $n = 1$  for surface). Note that Euler's elastica is an equation for a curve, so we can think of this one for describing a one-dimensional curve optimized using area and length-related constraints  $\int x^n \sqrt{1 + z'(x)^2}$ . Consider the following case for  $n = -1, \lambda = 1$ .

$$z(x) = \int_x^R \frac{\alpha t^2 + \beta t + \gamma}{\sqrt{t^{-2} - (\alpha t^2 + \beta t + \gamma)^2}} dt \quad (t \in \mathbb{R})$$

Constraint is  $\int x^{-1} \sqrt{1 + z'(x)^2} dx = a$ . This can be thought as in terms of  $\int x^{-1} (\sqrt{1 + z'(x)^2} - 1) dx = a'$ . Notice that  $a'$  is fixed for  $0 < t \leq R$  if  $a$  is a fixed value. To expand this idea, we can rewrite equation 4.19 as

$$z(x) = \int_x^R \frac{\alpha t^{2-n} - \beta t^{1-n} + \gamma t^{-n}}{\sqrt{\lambda^2 - (\alpha t^{2-n} + \beta t^{1-n} + \gamma t^{-n})^2}} dt \quad (t \in \mathbb{R} \setminus \{0\} \quad n \in \mathbb{Z}) \quad (4.20)$$

Note that  $\lambda^2 = (\alpha R^{2-n} + \beta R^{1-n} + \gamma R^{-n})^2$  at  $t = R$  is not required for general case, but we need  $\lambda^2 \geq (\alpha t^{2-n} + \beta t^{1-n} + \gamma t^{-n})^2$  for real solution. That also implies one can use  $z'(R_-) \neq -\infty$  based on boundary condition (which depends on the slope of one end). If we expand this equation to complex space ( $\mathbb{C} \setminus \{0\}$  and  $\mathbb{C}$  depends on constraints in general), we will get

$$\begin{cases} Z(s) &= X(s) + Y(s)i \\ Y(s) &= \int^X \frac{\alpha t^{2-n} + \beta t^{1-n} + \gamma t^{-n}}{\sqrt{\lambda^2 - (\alpha t^{2-n} + \beta t^{1-n} + \gamma t^{-n})^2}} dt \quad (n \in \mathbb{Z}) \\ s &= \int^X \frac{\lambda}{\sqrt{\lambda^2 - (\alpha t^{2-n} + \beta t^{1-n} + \gamma t^{-n})^2}} dt \quad (n \in \mathbb{Z}). \end{cases} \quad (4.21)$$

Therefore, this is  $n$ -dimensional Euler's elastica curve and can be expanded to axis-symmetric surfaces or symmetric space. Notice that this equation can be obtained by changing  $\alpha t^2 + \beta t^1 + \gamma t^0$  to  $\alpha t^{2-n} + \beta t^{1-n} + \gamma t^{-n}$  from Euler's equation. Moreover, we have used  $\lambda^2$  instead of  $\lambda^4$  compared to Euler's equation because  $\lambda$  comes from the Lagrange multiplier of  $\int x^n \sqrt{1 + z'(x)^2} dx$ . Also,  $\lambda^2 \geq (\alpha t^{2-n} + \beta t^{1-n} + \gamma t^{-n})^2$  is required if solution have to be real. As we've discussed in the previous section, we can use  $\Re(Y(s)) + \Im(Y(s))$  or  $\Re(Y(s)) - \Im(Y(s))$  based on the condition. For example, if we revisit figure 4.17 in section 4.2.1, we may use  $\Re(Y(s)) - \Im(Y(s))$  instead of  $\Re(Y(s))$  as shown below.

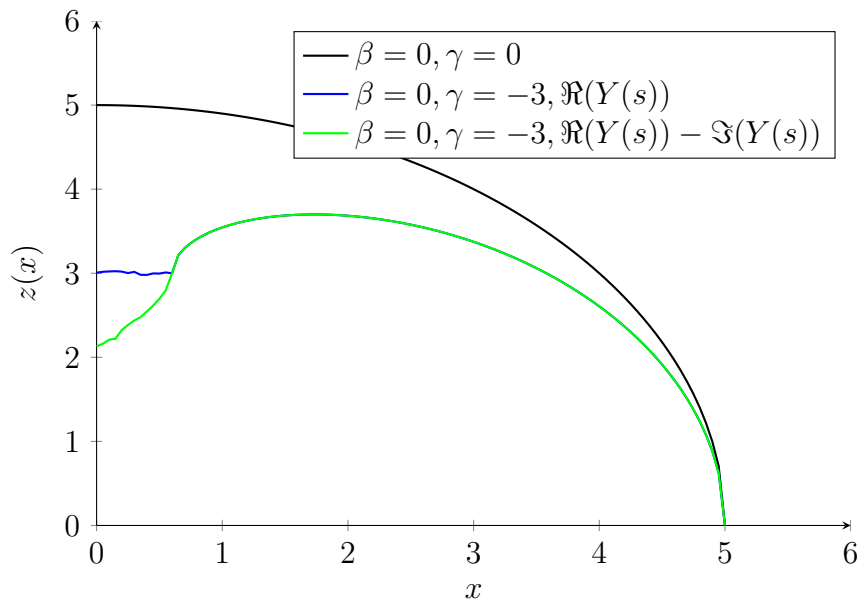


Figure 4.18: Profiles of figure 4.17 for  $x \leq 0.6$ ,  $z(x) \in \mathbb{C}$ .

Notice that there are precision issues in  $x \leq 0.6$  because of singularity and complex integration. This could be solved if we separate integral instead of taking  $\Re(Y(s)), \Im(Y(s))$ . Let's

consider a condition  $ax^2 + bx + c > \lambda$

$$\frac{\lambda z'(x)}{\sqrt{1 + z'(x)^2}} = ax^2 + bx + c$$

$$\frac{\lambda^2 z'(x)^2}{1 + z'(x)^2} = \lambda^2 + d(x) \quad \text{where } d(x) > 0 \text{ for some } x$$

$$\lambda^2 z'(x)^2 = (1 + z'(x)^2)(\lambda^2 + d(x))$$

$$\lambda^2 z'(x)^2 = z'(x)^2(\lambda^2 + d(x)) + (\lambda^2 + d(x))$$

$$z'(x)^2 d(x) = -(\lambda^2 + d(x))$$

$$z'(x)^2 = -\frac{(\lambda^2 + d(x))}{d(x)}$$

Since  $z'(x)^2$  is positive definite, it is difficult to eliminate  $i$  for  $d(x) > 0$  in this case. However, figure 4.18 could be solved by choosing different coordinates and boundary conditions. By setting a coordinate  $(\tilde{x}, \tilde{z}(\tilde{x}))$  for  $0 \leq x \leq 0.6$ , we can solve separately for each  $V, \tilde{V}$  as shown below.

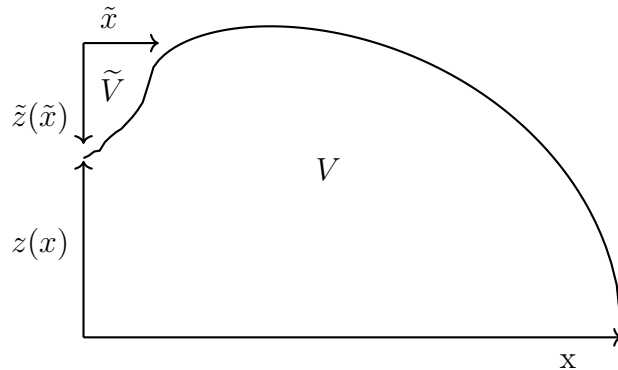


Figure 4.19: An example of coordinate settings for  $z(x) \in \mathbb{C}$ .

Notice that the resulted surface may not be convex. Since we are minimizing energy, if we divide the surface with several volumes, it will maintain minimum energy globally. However,

we may need to optimize using different methods to make it “as rounded as possible”. We will discuss more details in the conclusion section. There might not be a physical model out of  $n = 0, 1$  for the 4.21, but we can combine these different  $n$  values to represent non-linear behavior which we will discuss in the next section. The figure below shows a profile of different  $n$  values when it is added to Euler’s elastica.

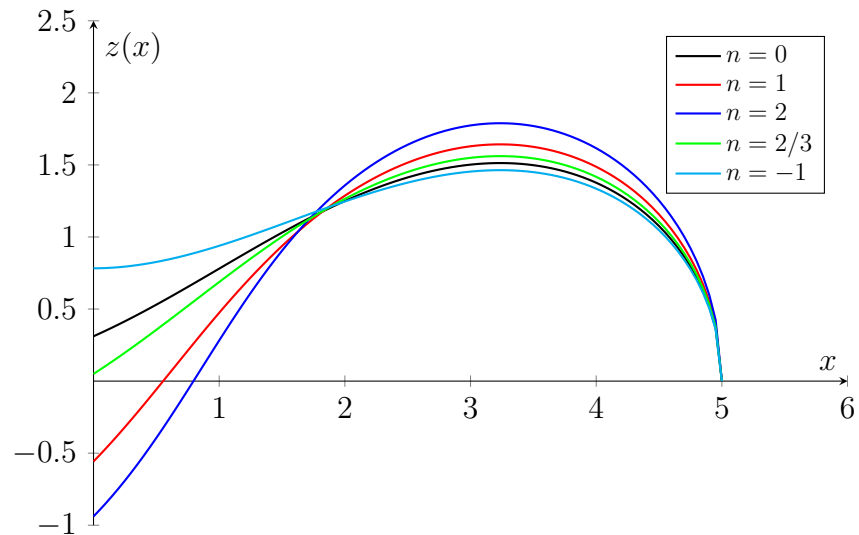


Figure 4.20: Profiles of  $f(x) = mt^n + \lambda$  for various  $m, n$ .

$$z(x) = \int_x^R \frac{\alpha(t + \beta)^2 + \gamma}{\sqrt{f(x)^2 - (\alpha(t + \beta)^2 + \gamma)^2}} dt$$

where  $\alpha = 1, \beta = -1, \gamma = -5$ , and

$$\begin{aligned} n = 0: f(x) &= \lambda \\ n = \frac{2}{3}: f(x) &= t^{\frac{2}{3}} + \lambda \\ n = 1: f(x) &= t + \lambda \\ n = 2: f(x) &= 0.2t^2 + \lambda \\ n = -1: f(x) &= 10t^{-1} + \lambda \end{aligned}$$

Note that  $\lambda$  is a constant defined by condition  $z(R) = 0, z'(R_-) = -\infty$ . Based on the boundary condition, we can take  $z'(R_-) = c_z$  ( $c_z \in \mathbb{R} \setminus \{-\infty, \infty\}$ ) other than  $z'(R_-) = -\infty$

and this will generate a different profile nearby  $x = R$ . For example, we can consider the following equation

$$z(x) = \int_x^R \frac{t^2 + t}{\sqrt{(m + \delta)^2 - (t^2 + t)^2}} dt$$

where  $\delta$  is a constant to adjust  $z'(R)$ .

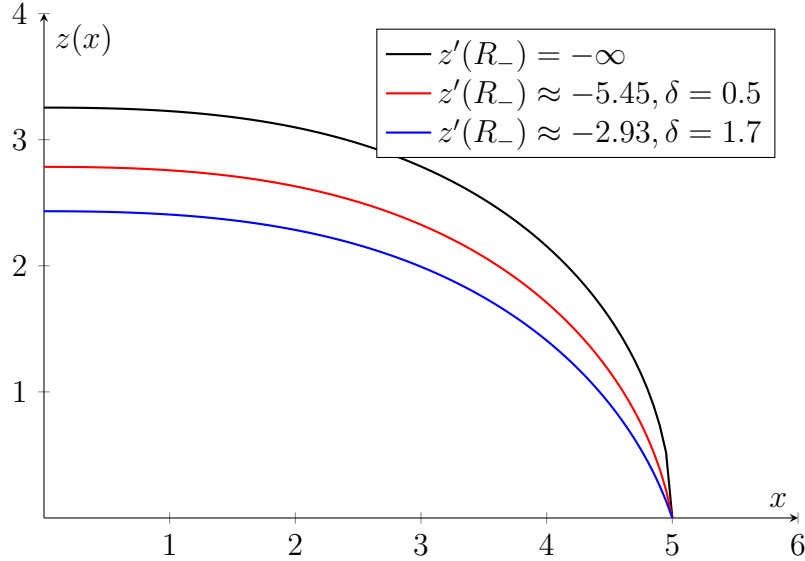


Figure 4.21: Profile changes from different slope  $z'(R_-)$ .

### 4.2.3 Generalized implementation

Consider one-dimensional curve describe with polynomials  $f(x) = \sum_I a_i x^i$  ( $a_i$ 's are constants) where  $f(x)$  is a function related to the arc length for  $i \in I$  where power of  $x$  doesn't have to be integer (Puiseux series). Using constraint  $\int^X f(x) \sqrt{1 + z'(x)^2} dx = a$  (or  $\int^X (\sum_I a_i x^i) (\sqrt{1 + z'(x)^2} - 1) dx = a'$ ) in finite,

bounded interval (at least one side), we will have

$$\begin{aligned}
\frac{(\sum_I a_i x^i) z'(x)}{\sqrt{1 + z'(x)^2}} &= ax^2 + bx + c \\
\frac{(\sum_I a_i x^i)^2 z'(x)^2}{1 + z'(x)^2} &= (ax^2 + bx + c)^2 \\
(\sum_I a_i x^i)^2 z'(x)^2 &= (1 + z'(x)^2)(ax^2 + bx + c)^2 \\
\left( (\sum_I a_i x^i)^2 - (ax^2 + bx + c)^2 \right) z'(x)^2 &= (ax^2 + bx + c)^2 \\
z'(x)^2 &= \frac{(ax^2 + bx + c)^2}{(\sum_I a_i x^i)^2 - (ax^2 + bx + c)^2} \\
z'(x) &= -\frac{ax^2 + bx + c}{\sqrt{(\sum_I a_i x^i)^2 - (ax^2 + bx + c)^2}}.
\end{aligned}$$

Note that we used  $a, b, c$  instead of  $\alpha, \beta, \gamma$ . Thus, we can get

$$Z(s) = X(s) + Y(s)i \tag{4.22}$$

$$Y(s) = \int^X \frac{ax^2 + bx + c}{\sqrt{(\sum_I a_i x^i)^2 - (ax^2 + bx + c)^2}} dx \tag{4.23}$$

$$s = \int^X \frac{(\sum_I a_i x^i)}{\sqrt{(\sum_I a_i x^i)^2 - (ax^2 + bx + c)^2}} dx. \tag{4.24}$$

This approach allows us to use a polynomial approximation for a function  $f(x) \sim \sum_I a_i x^i$  satisfying  $\int^X f(x) \sqrt{1 + z'(x)^2} dx = a$  where  $a$  is a constant. If we go back to  $x, z$  plane with  $(x, z(x))$ , special case of this will be  $f(x) \sim x^n(a_2 x^2 + a_1 x + a_0)$  for reasonably small  $n$  (because of computational complexity)  $-\infty < n < \infty, n \in \mathbb{Z}$ . As we have shown in section

4.1.6, we can manipulate

$$\begin{aligned}
z(x) &= \int \frac{ax^2 + bx + c}{\sqrt{(x^n(a_2x^2 + a_1x + a_0))^2 - (ax^2 + bx + c)^2}} dx \\
&= \int \frac{ax^2 + bx + c}{\sqrt{(x^n(a_2x^2 + a_1x + a_0) - (ax^2 + bx + c))(x^n(a_2x^2 + a_1x + a_0) + (ax^2 + bx + c))}} dx \\
&= \int \frac{1}{2} \left[ \frac{\sqrt{x^n(a_2x^2 + a_1x + a_0) + (ax^2 + bx + c)}}{\sqrt{x^n(a_2x^2 + a_1x + a_0) - (ax^2 + bx + c)}} \right. \\
&\quad \left. - \frac{\sqrt{x^n(a_2x^2 + a_1x + a_0) - (ax^2 + bx + c)}}{\sqrt{x^n(a_2x^2 + a_1x + a_0) + (ax^2 + bx + c)}} \right] dx.
\end{aligned}$$

The solution for  $z(x)$  can be solved by integrating each component separately

$$\begin{aligned}
F(x) &= \int \frac{1}{2} \frac{\sqrt{x^n(a_2x^2 + a_1x + a_0) + (ax^2 + bx + c)}}{\sqrt{x^n(a_2x^2 + a_1x + a_0) - (ax^2 + bx + c)}} dx \\
G(x) &= \int \frac{1}{2} \frac{\sqrt{x^n(a_2x^2 + a_1x + a_0) - (ax^2 + bx + c)}}{\sqrt{x^n(a_2x^2 + a_1x + a_0) + (ax^2 + bx + c)}} dx.
\end{aligned}$$

Notice that we can simplify the above equation for  $n = 0$

$$\begin{aligned}
F(x) &= \int \frac{1}{2} \frac{\sqrt{(b_2x^2 + b_1x + b_0)}}{\sqrt{(c_2x^2 + c_1x + c_0)}} dx \\
G(x) &= \int \frac{1}{2} \frac{\sqrt{(c_2x^2 + c_1x + c_0)}}{\sqrt{(b_2x^2 + b_1x + b_0)}} dx
\end{aligned}$$

where  $b_2 = a_2 + a, b_1 = a_1 + b, b_0 = a_0 + c, c_2 = a_2 - a, c_1 = a_1 - b, c_0 = a_0 - c$  respectively.

Thus, we have  $z(x) = F(x) - G(x)$ . As we have shown in the previous section, we can solve these equations from manipulating variables using trigonometric, elliptic, or hypergeometric functions. For  $n \neq 0$  with some coefficients, there may not be solutions for indefinite integration methods. However, numerical computation can be used instead. Note that coefficients have to be carefully chosen using boundary conditions to get proper results. Thus, we can represent above to more general expression as  $\int^X f(x)\sqrt{1 + z'(x)^2}dx = a$  where  $a$  is

a constant,  $\frac{\partial}{\partial z(x)}f(x) = 0$ , and  $\frac{\partial}{\partial z'(x)}f(x) = 0$ .

$$\begin{cases} Z(s) &= X(s) + Y(s)i \\ Y(s) &= \int^X \frac{\alpha x^2 + \beta x + \gamma}{\sqrt{f(x)^2 - (\alpha x^2 + \beta x + \gamma)^2}} dx \\ s &= \int^X \frac{f(x)}{\sqrt{f(x)^2 - (\alpha x^2 + \beta x + \gamma)^2}} dx. \end{cases} \quad (4.25)$$

For applications, one can use (non-)linear polynomial fit  $f(x) = \sum_I a_i x^i$  for surface/curve satisfies this condition and do analytical simulation. One example will be generating a table of  $x^n \sqrt{1 + z'(x)^2}$  of different  $n$  values and run linear fit using original curve to find out coefficients  $a_i$ 's for  $f(x)$  when we have information about  $\alpha, \beta, \gamma$ . Another example could be a surface described with multiple functions. We will see a demonstration of the second case. Suppose there is a spherical balloon with some area  $b \leq x \leq b + d$  (axis-symmetric) has high stiffness such that we have a constraint  $\int^X [f(x)] \sqrt{1 + z'(x)^2} dx = \int^X [x - \lambda(\theta(x - b) - \theta(x - b - d))] \sqrt{1 + z'(x)^2} dx = a$ . The following figure presents a plot described by an equation below.

$$\int_x^R \frac{(\frac{1}{2}t^2 - t)}{\sqrt{(mt + \lambda(\theta(t - 1) - \theta(t - 1 - d)))^2 - (\frac{1}{2}t^2 - t)^2}} dt$$

for  $m = \frac{1}{2}R - 1$

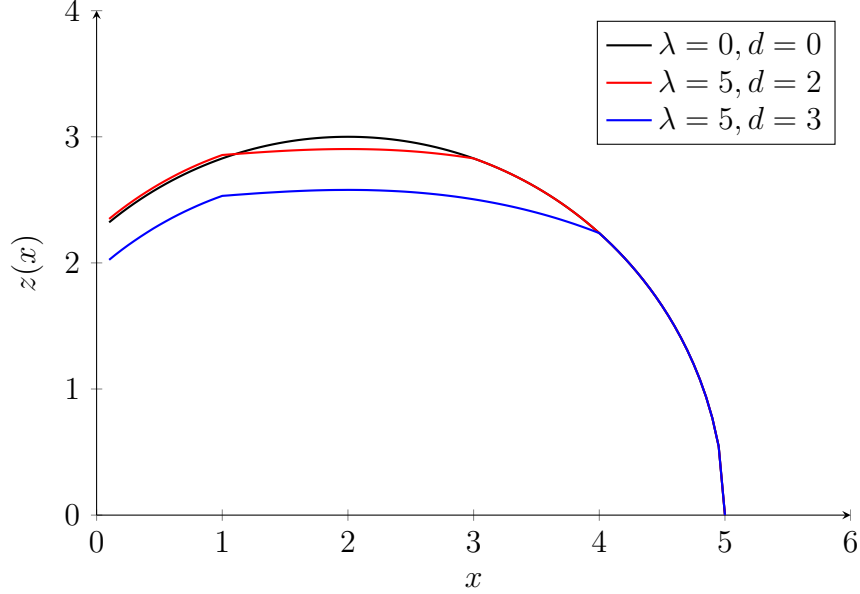


Figure 4.22: A surface constructed with high and low stiffness regions.

Note that computed values nearby Heaviside functions may not be close enough because of precision errors. However, we can still observe the effect of local stiffness changes on the structure. Notice that  $(ax^2 + bx + c)$  can be generalized to  $g(x)$  if we are maximizing other than  $\int xz(x)dx$ . Therefore, finally, we can get an equation below

$$\begin{cases} Z(s) &= X(s) + Y(s)i \\ Y(s) &= \int^X \frac{\lambda g(x)}{\sqrt{f(x)^2 - \lambda^2 g(x)^2}} dx \\ s &= \int^X \frac{f(x)}{\sqrt{f(x)^2 - \lambda^2 g(x)^2}} dx \end{cases} \quad (4.26)$$

where above equation is optimized from  $\int^X g'(x)z(x)dx$  with constraint  $\int^X f(x)\sqrt{1 + z'(x)^2}dx$  for  $\frac{\partial}{\partial z(x)}f(x) = \frac{\partial}{\partial z'(x)}f(x) = \frac{\partial}{\partial z(x)}g(x) = \frac{\partial}{\partial z'(x)}g(x) = 0$ . We will show simple a example for  $g(x)$ . Let us consider inflating surface having some clutch or band that cannot be inflated more than  $z(x) = z_0$  for some range of  $x$ . Let us say  $0 \leq x \leq d$ . In that case, we can write

$g'(x)$  as  $g'(x) = xz(x)[\theta(x) - \theta(x - d)]$  and apply to the equation below.

$$z(x) = \int^X \frac{\lambda g(x)}{\sqrt{f(x)^2 - \lambda^2 g(x)^2}} dx$$

The following figure shows a demonstration of the surface described by an equation

$$z(x) = \int_x^R \frac{(\alpha(t^2 - d^2)\theta(t - d) + \beta t + \gamma)}{\sqrt{(mt)^2 - (\alpha(t^2 - d^2)\theta(t - d) + \beta t + \gamma)^2}} dt$$

where  $\alpha = 1, \beta = -0.5, \gamma = 0, d = 2$ , and  $m$  is chosen for satisfying  $z'(R_-) = -\infty$ .

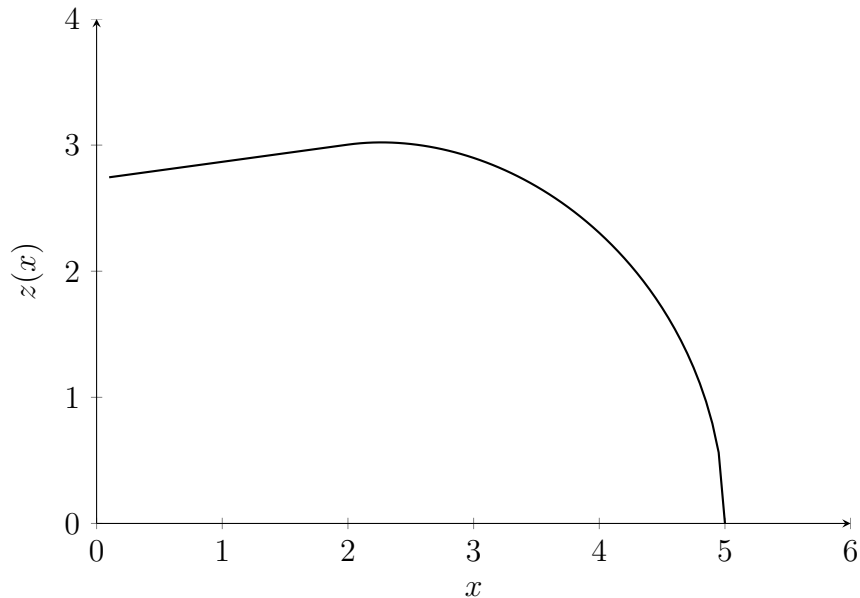


Figure 4.23: A surface having a fixed volume region for  $x \leq 2$ .

Note that polynomial fit of  $g'(x)$  can be applied if it satisfies conditions to use equation 4.26 with proper boundary condition. As discussed in the [1][2], for Euler's elastica, there are a finite number of solutions if two ends are fixed and one side slope is known as shown in [1], or [2]. We can apply the same thing for equation 4.26. If two sides are fixed, shape (frequency) is set, and one side's slope is defined, we will have a single up to isometric transformation in general for equation 4.20 or a finite number of solutions for 4.26.

## 4.2.4 Generalized case with multiple boundary conditions

Consider the equation 4.26. Suppose we are constructing a surface

- A surface or a curve can be described with multiple parts having different constraints.
- A patch with different constraints is added to a surface or a curve.
- A surface or a curve can be interpreted as a combination of multiple curves or surfaces.

We will explain each case using one example. Let us consider

$$\begin{aligned}
 V &= 2\pi \int_0^R xz(x)dx, \\
 S &= 2\pi \left[ \int_0^1 \sqrt{1+z'(x)^2}dx + \lambda' \int_1^3 x\sqrt{1+z'(x)^2}dx + \int_3^R \sqrt{1+z'(x)^2}dx \right] \\
 &= 2\pi \int_0^R \left[ (\theta(x) - \theta(x-1) + \theta(x-3)) + \lambda'x(\theta(x-1) - \theta(x-3)) \right] \sqrt{1+z'(x)^2}dx.
 \end{aligned}$$

Then we get,

$$z(x) = \int_x^R \frac{\alpha t^2 + \beta t + \gamma}{\sqrt{\lambda^2 \left[ (\theta(x) - \theta(x-1) + \theta(x-3)) + \lambda'x(\theta(x-1) - \theta(x-3)) \right]^2 - (\alpha t^2 + \beta t + \gamma)^2}} dt$$

where  $\lambda$  is a constant for the Lagrange multiplier, and  $\lambda'$  is a parameter from a constitutive relation. That could be the case for gluing materials having different stiffness. Other cases will be

$$\begin{aligned}
 V &= 2\pi \int_0^R xz(x)dx, \\
 S &= 2\pi \left[ \int_0^R x\sqrt{1+z'(x)^2}dx + \lambda' \int_1^3 \sqrt{1+z'(x)^2}dx \right] \\
 &= 2\pi \int_0^R \left[ x + \lambda'(\theta(x-1) - \theta(x-3)) \right] \sqrt{1+z'(x)^2}dx.
 \end{aligned}$$

Therefore, we can write as

$$z(x) = \int_x^R \frac{\alpha t^2 + \beta t + \gamma}{\sqrt{f(x)^2 - (\alpha t^2 + \beta t + \gamma)^2}} dt$$

$$f(x) = \left[ \lambda_1 f_1(x) + \lambda_2 f_2(x) \right]$$

where  $f_1(x), f_2(x)$  are different constraints related to the surface. For example, we can imagine patches with different stiffness attached to the surface or gluing each other. Let flexible membrane (F type) be the surface constrained to area and non-flexible (NF type) be the one constrained to arc length. Then, we can think about three different cases.

- Non-flexible patch is attached to the flexible membrane. (F type + NF patch)
- Flexible patch is attached to the non-flexible membrane. (NF type + F patch)
- A membrane is formed by gluing several non-flexible and flexible patches. (Glued)

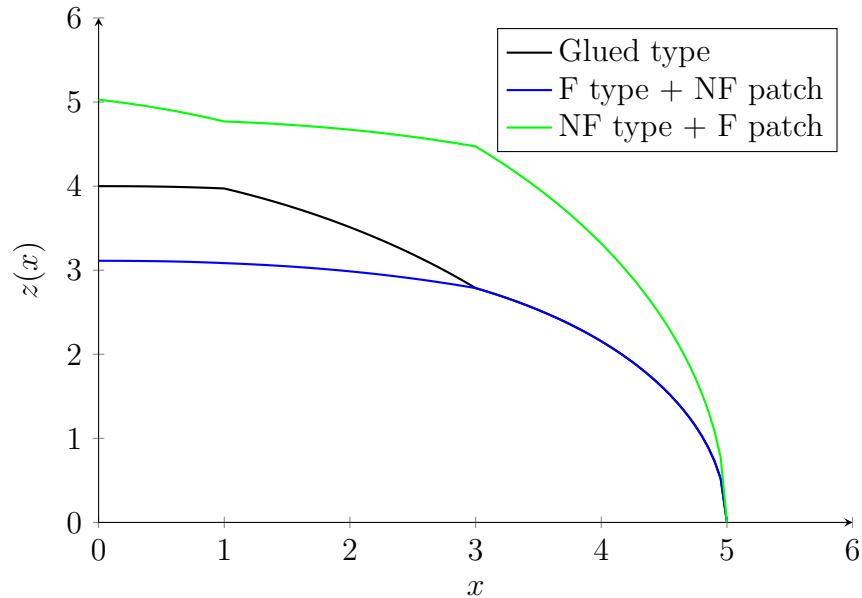


Figure 4.24: Profile differences of high and low stiffness surfaces from different gluing methods.

The above figure shows a graph for the following equation

$$z(x) = \int_x^5 \frac{t^2 + t}{\sqrt{f(x)^2 - (t^2 + t)^2}} dt$$

$$f(x) = \left[ \lambda_1 f_1(x) + \lambda_2 f_2(x) \right].$$

Notice that  $f_1(x) = 1$  and  $f_2(x) = x$  with Heaviside function  $\theta(x - 1) - \theta(x - 3)$ .  $\lambda_1, \lambda_2$  are constants chosen to satisfy  $z(R) = 0$  for each  $f_1(x), f_2(x)$ . As we can expect, the blue graph implies that a flexible patch attached to a non-flexible surface does not have much impact on the profile of the curve. The following picture shows how glued type can be computed from two different curves. For example, we can think about adding volume to the membrane.

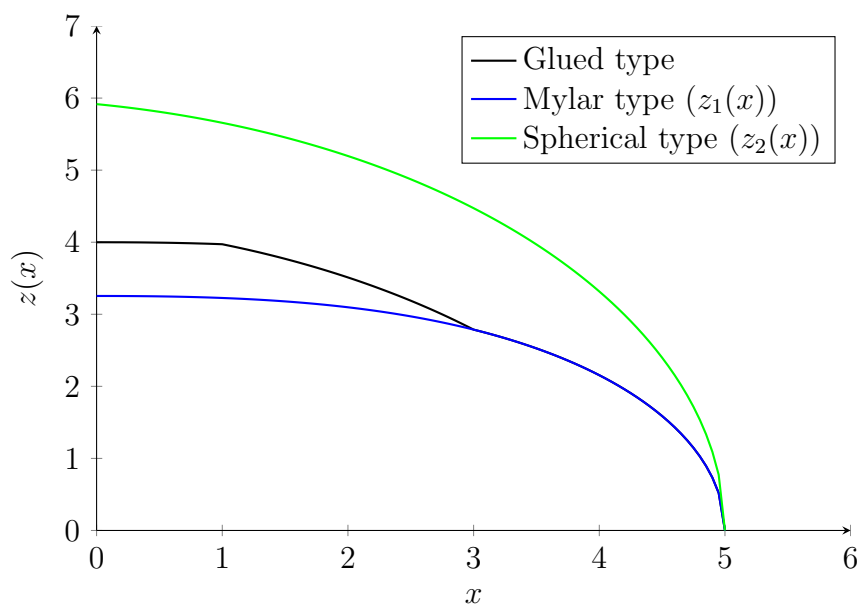


Figure 4.25: Glued type of surface can be composed by adding two different surfaces.

$z_1(x), z_2(x)$  are as follows

$$z_1(x) = \int_x^5 \frac{t^2 + t}{\sqrt{30^2 - (t^2 + t)^2}} dt$$

$$z_2(x) = \int_x^5 \frac{t^2 + t}{\sqrt{(6x)^2 - (t^2 + t)^2}} dt$$

Glued type is a combination of  $z_1(x)$  and  $z_2(x)$ . One may notice that glue type graph is almost flat nearby  $x = 1, 3$  although it is rounder in real-life examples. That comes from non-uniform forces because of the different stiffness of nearby edges. (Notice that Euler assumes uniform perpendicular forces.) We could solve this by adding more boundary conditions. However, the following equations cannot have multiple boundary conditions except endpoints and slopes.

$$z(x) = \int_x^5 \frac{t^2 + t}{\sqrt{f(x)^2 - (t^2 + t)^2}} dt$$

Instead, one can think about solving for additional volume/energy  $V'$  in  $1 \leq x \leq 3$ . This method interprets non-uniform force as uniform (additional) pressure applied to some part of surfaces. Let us consider adding extra volume to the Mylar-type surface, as shown below so that the  $V'$  part is more flexible and inflated.

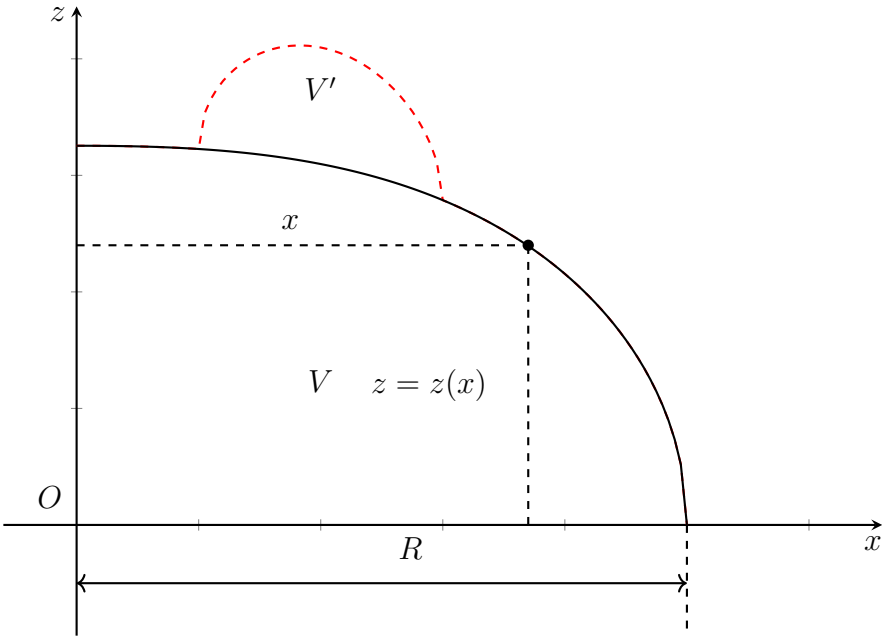


Figure 4.26: Geometry for the multiple volume method

Then, we can solve separate sets of  $\{V, S\}$  and  $\{V', S'\}$  and combine two  $z(x)$ 's. For example, suppose the membrane is more inflated for  $1 \leq x \leq 3$  amount of  $\delta$  constrained like a spherical

balloon. Then, we can add extra volume, as shown below.

$$z(x) = \int_x^5 \frac{t^2 + t}{\sqrt{f(x)^2 - (t^2 + t)^2}} dt + \delta \sqrt{1 - (x - 2)^2} (\theta(x - 1) - \theta(x - 3)) \quad (4.27)$$

Note that one can count on uniform pressure applied on surface normal, but we have considered a simpler case here (uniform pressure on the plane). For the first case (pressure applied on surface normal), one can apply a method in section 4.3. Normal vectors can be computed using this method, and we can add additional surface easily if it is not located near the boundary (surface edges). Figure shows a comparison between glued type with additional volume for  $\delta = 0.2$  using 4.27.

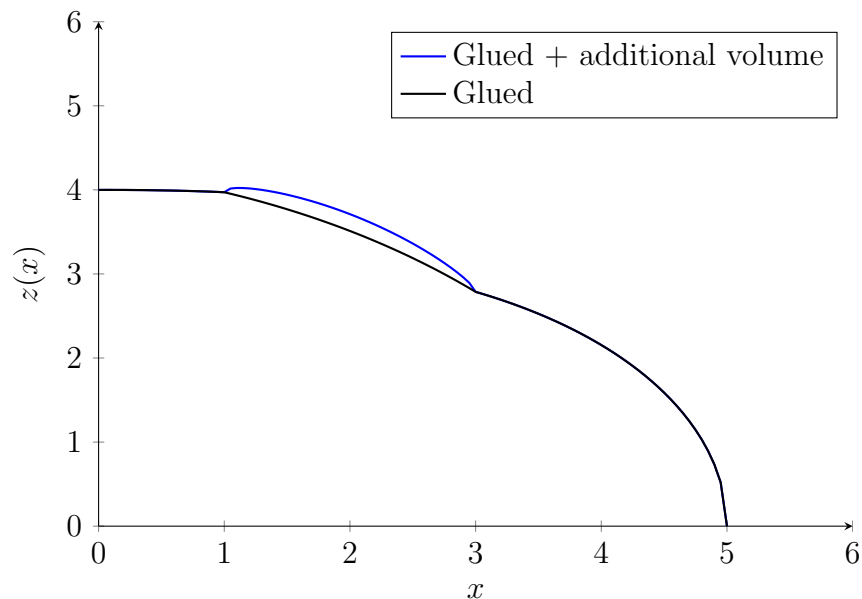


Figure 4.27: One way to simulate non-uniform perpendicular force can be done by adding extra volume to the surface.

So far, we have considered a membrane with a fixed radius. However, we can apply different radii if we consider the surface as a collection of curves. The following figure shows an example of these types of surfaces. The left plot shows a surface glued with different stiffness materials and inflated together. The right one is a structure that can be made by the following process:

- The non-stretchable membrane is inflated.

- Attaching stiff material to the surface, such as metal wires to maintain boundary before cutting out (this contains both material border and radial boundary  $z(R) = 0$ ).
- The surface is deflated and cut out along the boundary.
- The stretchable material is attached and inflated together.

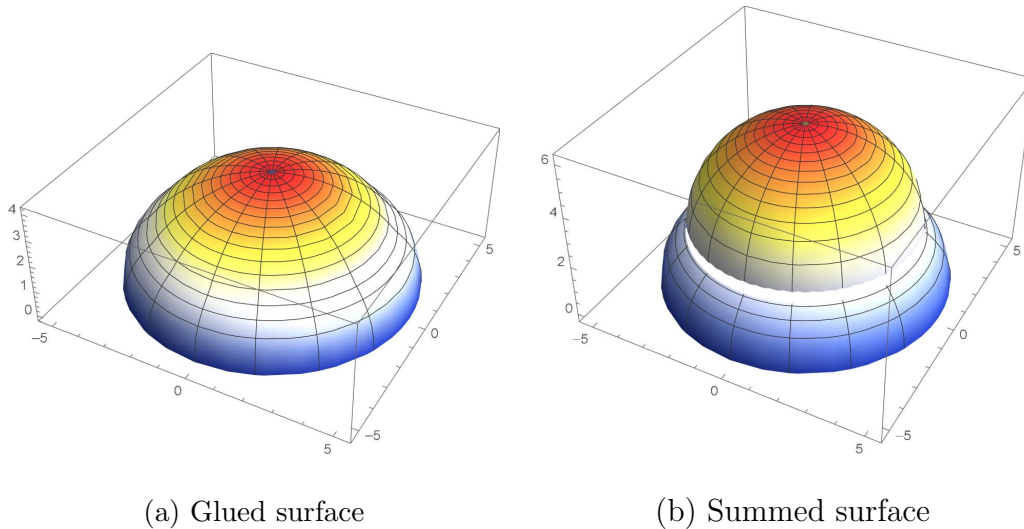


Figure 4.28: An example to show a difference between gluing and summing method.

Notice that the left one has less volume than the right one because a non-stretchable surface constrains the outer part, but the right one is proportional to adding a volume of two different structures. Following graph represents  $x, z(x)$  for each case.

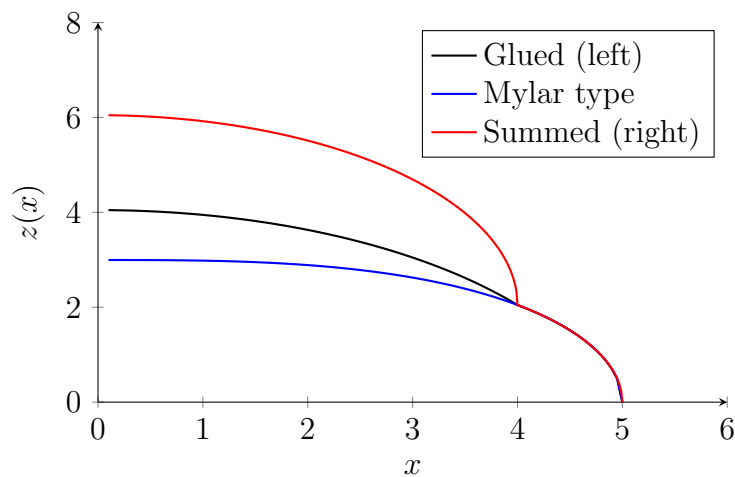


Figure 4.29: Vertical profiles of figure 4.28.

We can describe these two cases using the following equations

$$\text{Glued surface: } z(x) = \int_x^5 \frac{t^2}{\sqrt{(m_1x(\theta(x) - \theta(x-4)) + m_2\theta(x-4))^2 - t^4}} dt$$

$$\text{Summed surface: } z(x) = z_1(x) + z_2(x)$$

$$z_1(x) = \theta(x-4) \int_x^5 \frac{t^2}{\sqrt{m_2^2 - t^4}} dt$$

$$z_2(x) = \Re(\sqrt{4^2 - x^2} + z_1(4))(\theta(x) - \theta(x-4))$$

where  $m_1, m_2$  are constants satisfying  $z'(R_-) = -\infty$  as before. One can use the same equation for both left and right plots by substituting  $m_1$  satisfying  $z'(4_-) = -\infty$  instead of  $z'(R_-) = -\infty$ . That might work for rough estimations but may fail to get enough numerical precision since  $z(x)$  can easily become a complex function if the inside square root becomes negative. Last, we can write this for the general case as follows:

For a surface/curve satisfies a set  $X$  consists of optimizer and constraints pairs

$$X = \{(V_1, S_1), (V_2, S_2), \dots, (V_n, S_n)\}$$

$$\left\{ \begin{array}{l} V_1 = \int_a^b g'_1(x)z(x)dx, \quad \text{for } \int g'_1(x)dx = g_1(x) \\ S_1 = \int_a^b f_1(x)\sqrt{1 + z'(x)^2}dx \\ V_2 = \int_c^d g'_2(x)z(x)dx, \quad \text{for } \int g'_2(x)dx = g_2(x) \\ S_2 = \int_c^d f_2(x)\sqrt{1 + z'(x)^2}dx \\ \vdots \\ V_n = \int_v^w g'_n(x)z(x)dx, \quad \text{for } \int g'_n(x)dx = g_n(x) \\ S_n = \int_v^w f_n(x)\sqrt{1 + z'(x)^2}dx \end{array} \right. \quad (4.28)$$

where  $[a, b]$ ,  $[c, d]$ , and  $[v, w]$  are finite intervals may not contain  $\{0\}$ .

### 4.2.5 Application for non axis-symmetric surface

By using these results, we can apply to a non-axis-symmetric dome-type surface for the following applications. The idea is simple. By setting

$$\left\{ \begin{array}{l} x(r, \theta) = r \cos \theta \\ y(r, \theta) = r \sin \theta \\ z(r, \theta) = \int^r \frac{g(r, \theta)}{\sqrt{(f(r, \theta))^2 - (\lambda g(r, \theta))^2}} dt + C(\theta) \\ \frac{\partial}{\partial z(r, \theta)} f(r, \theta) = 0, \frac{\partial}{\partial z'(r, \theta)} f(r, \theta) = 0, \quad (x, y, z) \in \mathbb{R}^3 \\ (r \text{ could be a function of } \theta \text{ or other variables}). \end{array} \right. \quad (4.29)$$

Note that parametrization of  $x, y$  are chosen for easier computation, which does not mean that these are the only possible solutions. One can take other parametrization such as Jacobi elliptic functions (for example  $\text{cn}(u, k)$ ) or other trigonometric functions. The above approach will work for

- Surfaces/structures can be interpreted as a collection of curves/surfaces satisfying equation 4.29 where parameters of individual curves could differ, but these are continuous along  $\theta$  and boundaries.
- For any  $\theta_1, \theta_2 \in \theta, r_0 \in r$ , we can assume  $z(r_0, \theta_1) \approx z(r_0, \theta_2)$ .

From analytical perspectives, we can rewrite this as

- Axis-symmetric surface
- Analyzing the distribution of horizontal force when the azimuthal direction of forces/deformations are negligible.
- Surfaces could be interpreted as a collection of curves
- Surfaces could be interpreted as a collection of (fractional) axis-symmetric surfaces

- Parametrizing noisy dome-shaped membrane which is closer to axis-symmetric surface.

Then, one can solve these equations along boundary conditions for a fixed center (not applicable for fixed dome edge if no solutions exist to satisfy both conditions). Notice that  $b(\theta), c(\theta)$  are related to constant force over the surface and at the center. Also extended version of equation 4.28 over  $\theta$  can be used. For the second approach, one can use a reconstructed surface to estimate curvatures. Consider a surface described with the following equation.

$$z(x, \theta) = \int_x^5 \frac{t^2 + b(\theta)t}{\sqrt{m(\theta)^2 - (t^2 + b(\theta)t)^2}} dt \quad (4.30)$$

$$b(\theta) = \cos(4\theta)$$

$$m(\theta) = 5^2 + b(\theta)5$$

Notice that  $b(\theta)$  is a parameter related to uniform perpendicular force along the radial direction. Below shows a graph of  $b(\theta)$  and  $-1 \leq b(\theta) \leq 1$  for this example.

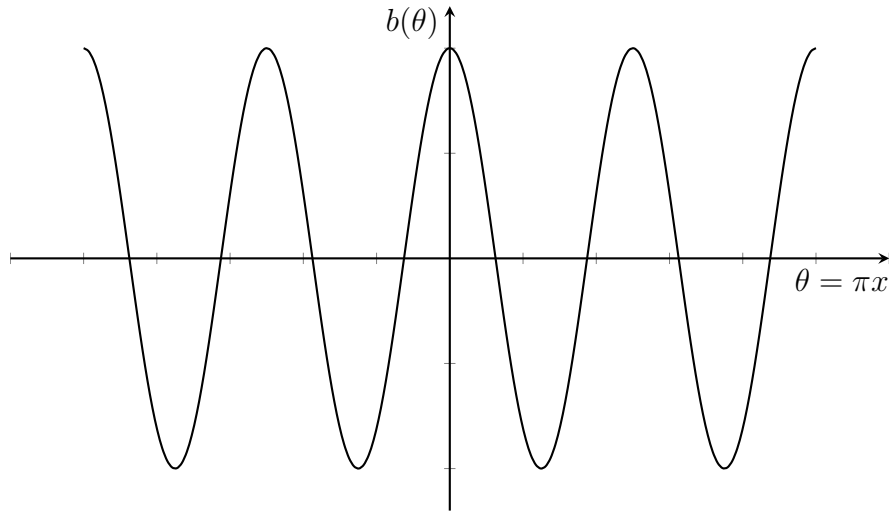


Figure 4.30: Graph of  $b(\theta) = \cos(4\theta)$ .

As we know, minimum and maximum of  $b(\theta)$  are  $-1, 1$ . These can be plotted as shown below.

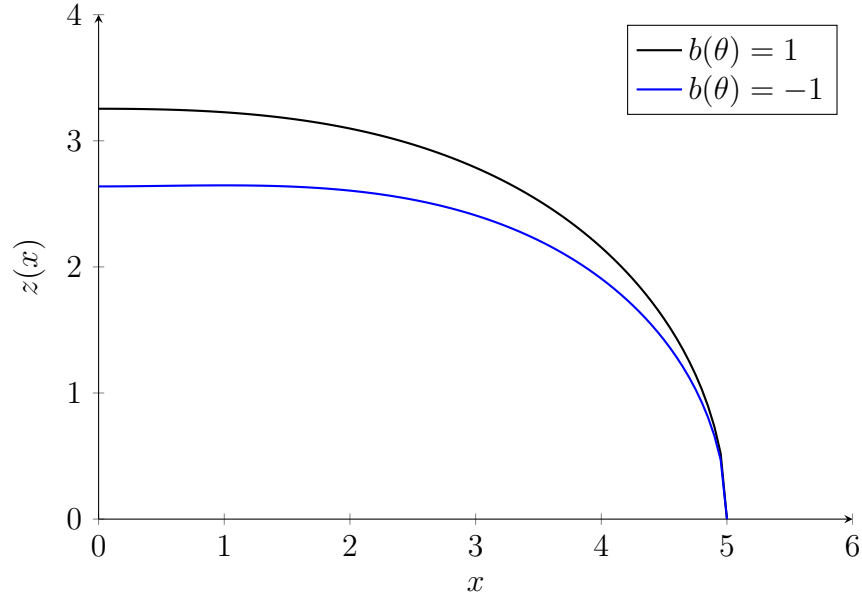


Figure 4.31: Profiles of  $b(\theta) = -1, 1$  for  $z(5_-) = -\infty$ .

Since other parameters are fixed for some  $\theta$ , we can let  $z(x, \theta) = \int_x^5 \frac{t^2 + b(\theta)t}{\sqrt{m(\theta)^2 - (t^2 + b(\theta)t)^2}} dt + C(\theta)$  for constant  $C(\theta)$ . Therefore, we can set either  $z(R, \theta)$  or  $z(0, \theta)$  to be the same. These surfaces can be plotted as shown below.

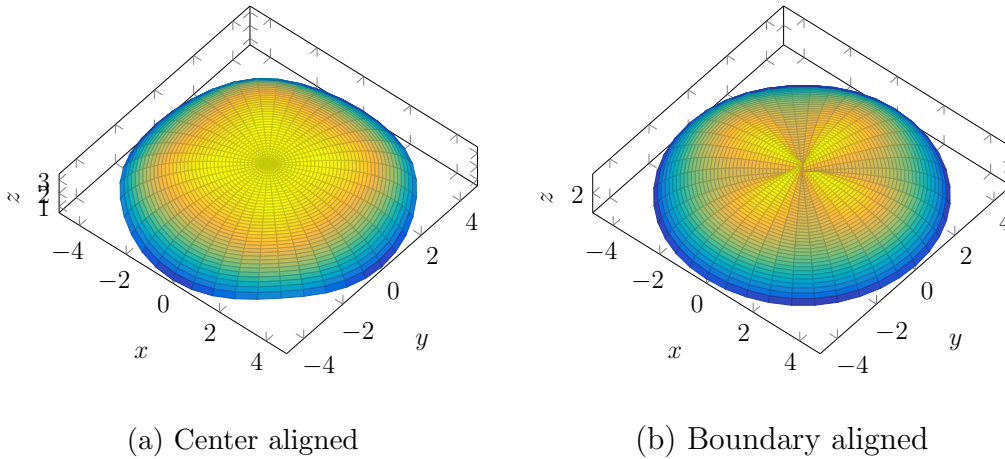


Figure 4.32: Equation 4.30 with different aligning methods.

Left plot shows center aligned ( $z(0, \theta_1) = z(0, \theta_2)$ ) and right plot shows boundary aligned

$(z(5, \theta_1) = z(5, \theta_2))$ . Next, we will consider

$$z(x, \theta) = \int_x^{R(\theta)} \frac{t^2 + t}{\sqrt{m^2 - (t^2 + t)^2}} dt \quad (4.31)$$

$$R(\theta) = 5 + \cos \theta$$

$$m = R^2 + R.$$

Notice that the radius varies from 4 to 6. That could be an example of surfaces as a collection of different curves.

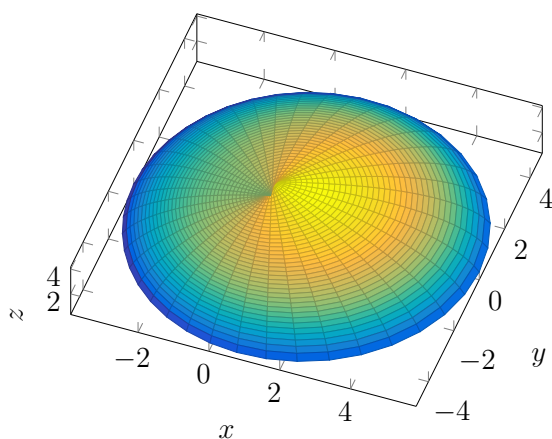


Figure 4.33: 3-dimensional plot of equation 4.31.

Next, we will consider the non-axis-symmetric glued (joint) type of surfaces. We can think of that as solving multiple  $(V, S)$  pairs where  $V$  is energy (volume) related parameter to be optimized, and  $S$  is constraints. This approach assumes that a fraction of  $V$  has the same property as the whole  $V$ . If we take a half of each  $V, V'$  and gluing together, the outcome can be same as solving with  $(\frac{1}{2}V, S)$  and  $(\frac{1}{2}V', S')$ . Notice that  $S, S'$  need to be adjusted based on the boundary conditions. Let us consider the following picture, which shows the top view of the surface. The dashed line represents two non-stretchable strings crossing each other where the length of each one is the same as twice of Mylar balloon's arc length with the same radius. The other parts will be stretchable materials.

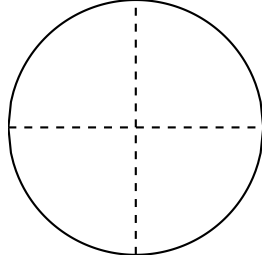


Figure 4.34: Top view of a surface.

In that case, we can solve this problem by combining two different membranes. Since the Mylar type cannot be stretched (fixed length), this will fix both ends of curves. Thus, we can solve for  $a$  satisfies  $z_1(0) = z_2(0)$ .

$$\begin{aligned} z_1(x) &= \int_x^R \frac{t^2}{\sqrt{(m_1)^2 - t^4}} dt \\ z_2(x) &= \int_x^R \frac{t^2 + at}{\sqrt{(m_2 t)^2 - (t^2 + at)^2}} dt. \end{aligned} \tag{4.32}$$

This plot represents the profile of Mylar and spherical type with  $a = -1.62$ .

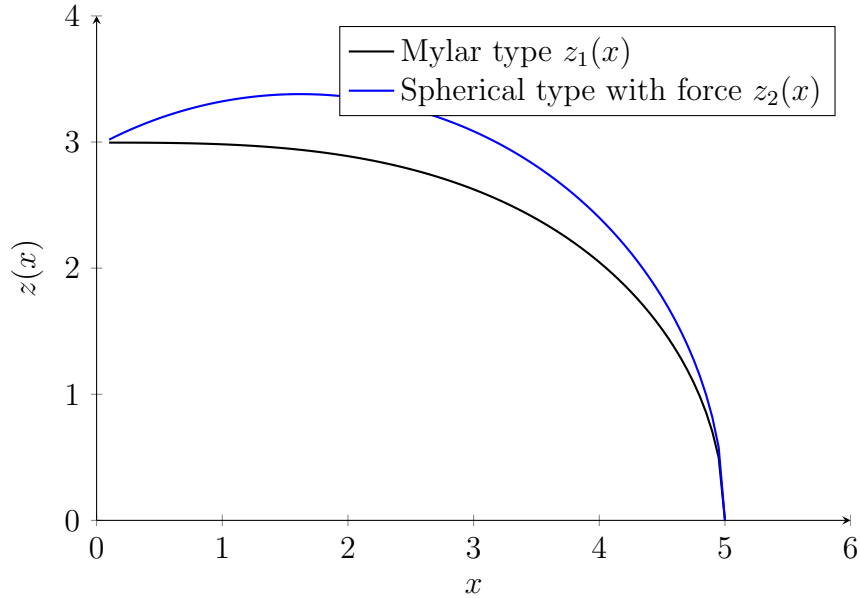


Figure 4.35: Vertical slices of a surface.

If we want to plot this surface in 3d, since we are assuming this surface is continuous, we need more information in the azimuthal direction. Suppose at  $\theta = 0$ , surface can be described

by  $z_1(x)$  and  $z_2(x)$  for  $\theta = \frac{\pi}{2}$ . If there are constraints for azimuthal directional forces, one can set an equation using these constraints. (For example,  $z(x, \theta) = (\frac{1}{2} \cos(4\theta) + \frac{1}{2})z_1(x) + (\frac{1}{2} \sin(4\theta) + \frac{1}{2})z_2(x)$ ) Following plot represent a demonstration of  $z_1(x)$  for  $\theta = 0, \frac{\pi}{2}, \pi, \frac{3\pi}{2}$  and  $z_2(x)$  for everywhere else.

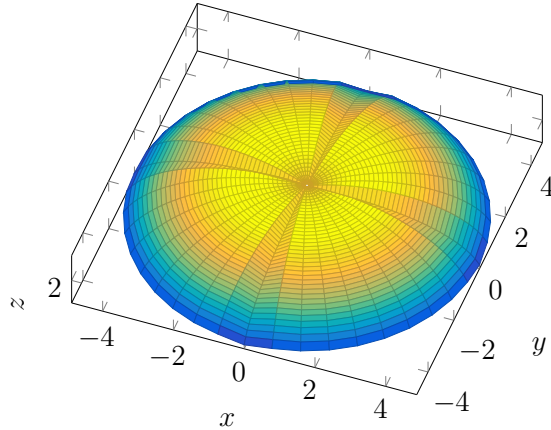


Figure 4.36: three-dimensional representation of a joint surface for eq. 4.32.

This graph shows plot of  $z(x) = |\sin(2\theta)| \cdot z_1(x) + |\cos(2\theta)| \cdot z_2(x)$ .

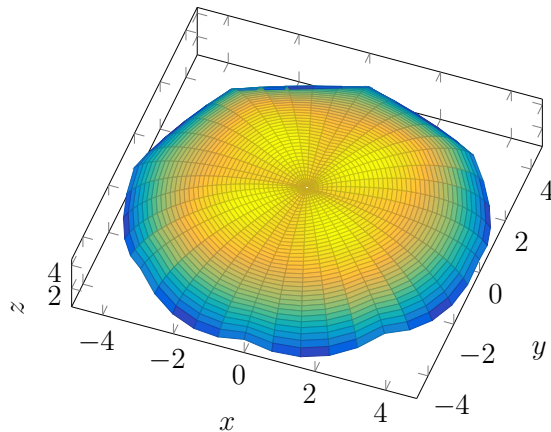


Figure 4.37: three-dimensional representation of a smooth surface for eq. 4.32.

Notice that this one is center aligned. Although both  $z_1(x)$  and  $z_2(x)$  have the same endpoints, intermediate values can have a different center or boundary edges. (We can solve this by applying weight than using trigonometric functions). However, the better way will be to apply the model in the azimuthal direction instead of using arbitrary functions (or one can use a slope of one end to fix this issue which we will discuss next). Notice that this

approach assumes perpendicular force, so it may not be enough for the surface to inflate using pressurized air. If the surface is inflated more than the above demonstrations, one can apply additional volume methods and add spherical balloons patches with a smaller radius (such as  $\frac{R}{2}$ ).

So far, we have considered fixing one endpoint for different  $z(x)$ 's. Recall that Euler's elastica has the following boundary condition. Two endpoints and one slope are fixed. Thus, if we fix two endpoints by varying slope for a non-axis-symmetric case assuming perpendicular force is uniformly applied, we can get the same two endpoints for different  $z(x)$ 's. Consider the following case

$$\begin{aligned}
 z(x, \theta) &= \int_x^{R(\theta)} \frac{t^2}{\sqrt{((R(\theta) + d)t)^2 - (t^2)^2}} dt & (4.33) \\
 &= \sqrt{(R(\theta) + d)^2 - x^2} - \sqrt{d^2 + 2R(\theta)d} \\
 R(\theta) &= 5 + \cos \theta, \quad 0 \leq x \leq R(\theta) \\
 d &= \frac{1}{8}(R(\theta) - 4)^2.
 \end{aligned}$$

The plot below presents a spherical balloon with a different radius and the same endpoints.

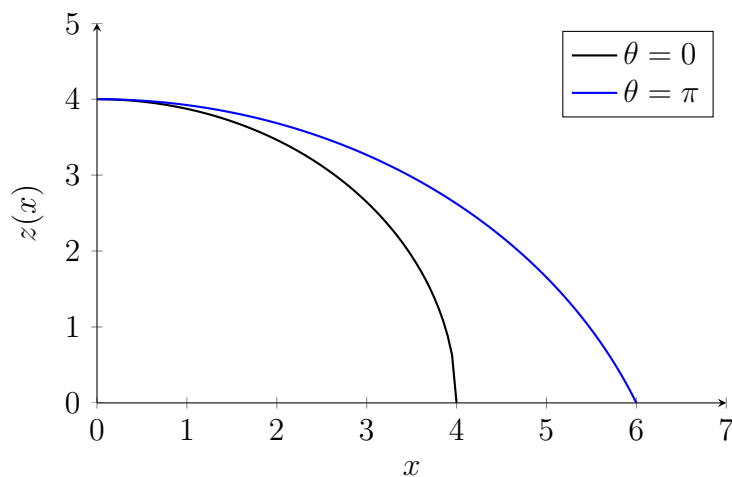
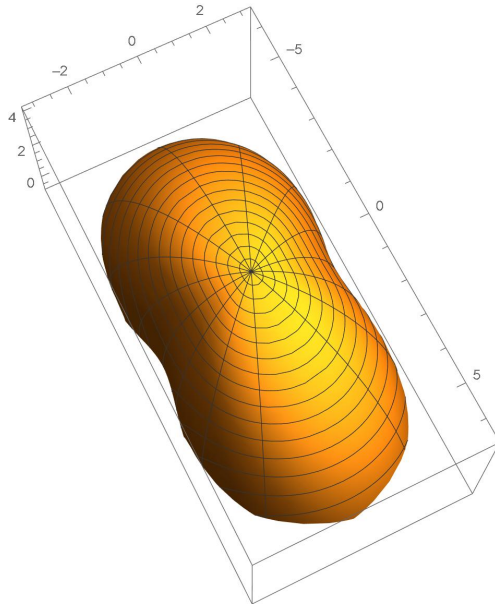


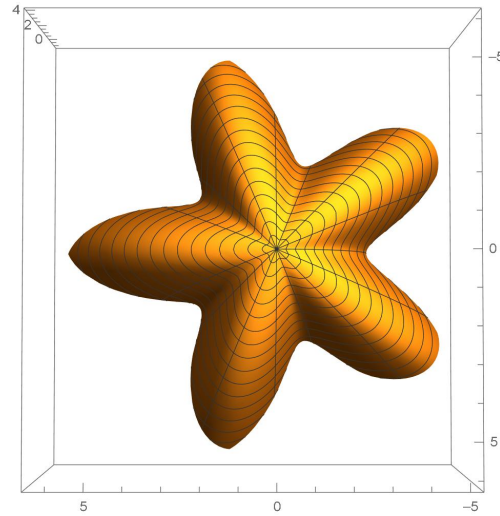
Figure 4.38: Profiles of eq. 4.33 for  $\theta = 0, \pi$ .

Notice that we can repeat these kinds of structures along the azimuthal direction. We can

plot in 3d as shown below



(a)  $R(\theta) = 5 + \cos(2\theta)$



(b)  $R(\theta) = 5 + \cos(5\theta)$

Figure 4.39: Examples of  $R(\theta) = 5 + \cos(n\theta)$  for  $n = 2, 5$ .

If we apply slightly different parametrization of  $(x(r, \theta), y(r, \theta), z(r, \theta)) \in \mathbb{R}^3$  for  $-R(\theta) \leq r \leq R(\theta)$  as represented below, we can get 4.40.

$$\begin{aligned}
 x(r, \theta) &= \frac{(r - 7)R(\theta)}{6 \cos \theta} \\
 y(r, \theta) &= \frac{(r - 7)R(\theta)}{6 \sin \theta} \\
 z(r, \theta) &= \int_r^{R(\theta)} \frac{t^2}{\sqrt{((R(\theta) + d)t)^2 - (t^2)^2}} dt \\
 &= \sqrt{(R(\theta) + d)^2 - r^2} - \sqrt{d^2 + 2R(\theta)d} \\
 R(\theta) &= 5 + \cos \theta \\
 d &= \frac{1}{8}(R(\theta) - 4)^2
 \end{aligned}$$

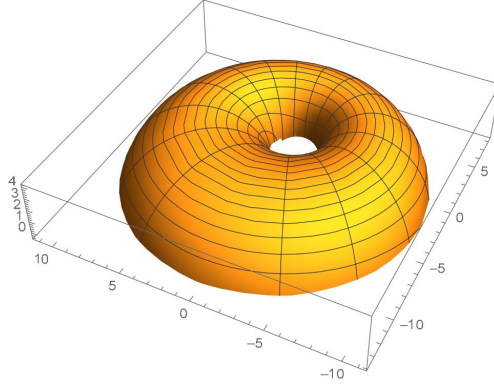


Figure 4.40: An example of a surface with genus 1.

### 4.3 Analytical approximation of $n$ -dimensional Euler's elastica

We already have parametrization for  $n$ -dimensional Euler's elastica in  $\mathbb{R}^3$  from the preceding section. That is simply  $(x, y, z) = (r \cos \theta, r \sin \theta, z(r, \theta))$  for  $(x, y, z) \in \mathbb{R}^3$ . However, considering solutions for  $z(x)$  from the early section requires a high computational ability to compute curvature (a derivative of elliptic functions). For some  $n$ , there may not be suitable functions to solve integral. In this section, we will introduce a simple parametrization approach to estimate  $z(x)$  and approximate curvatures, which does not require special functions. Write that we are limiting this application to be a real function that never goes negative inside the square root. Moreover, we will apply this approach to the equation 4.20 in section 4.2.2. However, this approach can be applied to the equation 4.20 for  $n \in \mathbb{Q}$  and 4.22 by dividing  $\sum_I a_i x^i$ . Indicating that the latter case may not be easier to integrate or not integrable symbolically based on the choice. Suppose we can represent the whole surface with separate equations satisfying eq. 4.20 applied for specific intervals and continuous along boundaries of intervals. This approach could be applied for each non-overlapping interval and could be merged, which can be described with eq. 4.28.

### 4.3.1 Parametrization method

Consider the following equation

$$z(x) = \int_x^R \frac{\alpha t^{2-n} - \beta t^{1-n} + \gamma t^{-n}}{\sqrt{\lambda^2 - (\alpha t^{2-n} + \beta t^{1-n} + \gamma t^{-n})^2}} dt \quad (t \in \mathbb{R} \setminus \{0\} \quad n \in \mathbb{Z}). \quad (4.34)$$

By setting  $f(t) = \alpha t^{2-n} - \beta t^{1-n} + \gamma t^{-n}$ , we get

$$z(x) = \int_x^R \frac{f(t)}{\sqrt{\lambda^2 - f(t)^2}} dt \quad (t \in \mathbb{R} \setminus \{0\} \quad n \in \mathbb{Z}) \quad (4.35)$$

For real function, we require  $\lambda^2 \geq (\alpha t^{2-n} + \beta t^{1-n} + \gamma t^{-n})^2$  and we have  $\lambda^2 \geq f(t)^2$ . This condition is unnecessary for binomial expansion unless it does not have  $\frac{1}{0}$  or infinity in the interval. Since we have  $\frac{1}{\sqrt{\lambda^2 - f(t)^2}} = (\lambda^2 - f(t)^2)^{-\frac{1}{2}}$ , we can expand as shown below.

$$z'(x) = \frac{f(t)}{\lambda} \left(1 - \frac{f(t)^2}{\lambda^2}\right)^{-\frac{1}{2}} \quad (4.36)$$

$$\approx \frac{f(t)}{\lambda} \left(1 + \frac{1}{2} \frac{f(t)^2}{\lambda^2} + \mathcal{O}(n)\right) \quad (4.37)$$

$$(t \in \mathbb{R} \setminus \{0\} \quad n \in \mathbb{Z}). \quad (4.38)$$

Once it is expanded for some  $n$ , we can plug in  $f(t)$  and compute the resulting polynomials. This function  $z'(x)$  can directly integrate because it can be represented a series of polynomials for a single variable  $t$ . That is  $z(x) = \int \sum_I a_i t^i dt$ . Since binomial approximation is suitable for small  $f(t)$ , we can expect the approximated value near the center will be much closer than the boundary (edge).

### 4.3.2 Curvature estimation of Mylar and spherical balloon

We will discuss the binomial approximation method using Mylar and spherical balloon. Note that we will use  $R = 5$  for all examples in this section. Let's start from  $z(x) = \int_x^R \frac{t^2}{\sqrt{m^4 - t^4}} dt$ .

Consider indefinite integral

$$z(t) = \int \frac{t^2}{\sqrt{m^4 - t^4}} dt$$

$$z(t) = \int \frac{t^2}{m^2} \left(1 - \frac{t^4}{m^4}\right)^{-\frac{1}{2}} dt$$

$$z(t) = \int \frac{t^2}{m^2} \left(1 + \frac{1}{2} \left(\frac{t^4}{m^4}\right) + \frac{3}{8} \left(\frac{t^4}{m^4}\right)^2 \cdots + \mathcal{O}(n)\right) dt.$$

Suppose if we take up to the highest term  $n$ , then  $z(t)$  can be represented as a finite sum of polynomials  $z(t) = \int \sum a_i t^i dt$ . Using boundary conditions, we can evaluate the integral and get  $z(t)$ . Let  $f(t) = t^2, \lambda = 5^2$ , then we have  $z(t) = \int \frac{f(t)}{\sqrt{\lambda^2 - f(t)^2}} dt$ . Following figure shows a comparison between numerical integration and indefinite integration  $\sqrt{1 - \frac{f(t)^2}{m^2}}$  using binomial expansion up to  $n \sim 10$ .

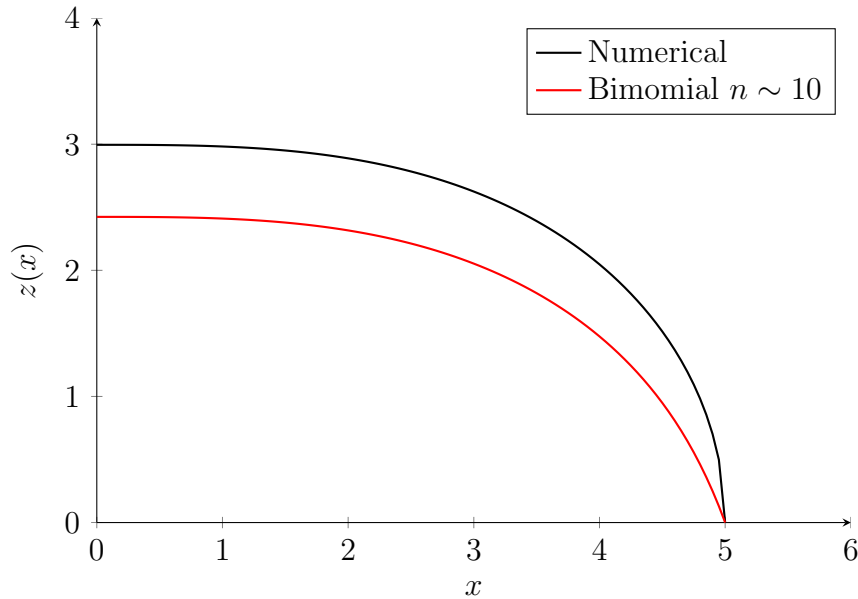


Figure 4.41: Profiles of Mylar balloon from numerical integration and binomial expansion for  $n \sim 10$ .

Notice that the central part's shape (or slope) is almost the same, but nearby  $R = 5$  has a big difference. If we increase  $n$  and get more terms, we can get close values near the boundary around  $n = 100 \sim 150$ . However, large  $n$  is unnecessary for central curvature estimation. For Mylar balloon without forces, we can use known parametrization from various papers or

solve indefinite integral directly using computational software.

$$\begin{aligned}
z(t) &= \int \frac{t^2}{\sqrt{R^4 - t^4}} dt \\
&= \int \left[ \frac{t^2}{R^2} \left( \frac{1}{\sqrt{1 - \frac{t^4}{R^4}}} - {}_2F_1 \left[ \frac{1}{2}, \frac{3}{4}, \frac{7}{4}; \frac{t^4}{R^4} \right] \right) + \frac{t^2}{R^2} {}_2F_1 \left[ \frac{1}{2}, \frac{3}{4}, \frac{7}{4}; \frac{t^4}{R^4} \right] \right] dt \\
&= \frac{1}{3} \frac{t^3}{R^2} {}_2F_1 \left[ \frac{1}{2}, \frac{3}{4}, \frac{7}{4}; \frac{t^4}{R^4} \right].
\end{aligned}$$

Note that the above computation is done using Mathematica v12.1. By applying 4.36 up to  $n \sim 10$  and let  $f(t) = \frac{t^2}{R^2}$ ,

$$z(t) = \int \frac{f(t)}{\sqrt{1 - f(t)^2}} dt \quad (4.39)$$

$$\approx \int f(t) \left( 1 + \frac{1}{2} f(t)^2 + \frac{3}{8} f(t)^4 + \frac{5}{16} f(t)^6 + \frac{35}{128} f(t)^8 + \frac{63}{256} f(t)^{10} \right) dt. \quad (4.40)$$

Then we can plug in  $f(t) = \frac{t^2}{R^2}$  and integrate by hand or using symbolic computational tools.

Next, we will write the parametrization of the surface as:

$$f_{uv} = (u \cos v, u \sin v, z(u)) \quad (\text{or } z(R) - z(u)).$$

We can take partial derivatives with respect  $u, v$  and find Gaussian/mean curvatures. Let  $K(u, v), H(u, v)$  to be Gaussian and mean curvatures, respectively. We have used parametrizations from [57] and [111] to compare results. Recall that we have equation 4.3 from [57].

$$x(u, v) = R \operatorname{cn} \left( u, \frac{1}{\sqrt{2}} \right) \cos v$$

$$K(u, v) = \frac{2}{R^2} \operatorname{cn}^2 \left( u, \frac{1}{\sqrt{2}} \right)$$

$$H(u, v) = \frac{3}{2R} \operatorname{cn} \left( u, \frac{1}{\sqrt{2}} \right)$$

$$\text{where } 0 \leq u \leq K \left( \frac{1}{\sqrt{2}} \right)$$

$K$  is a complete elliptic integral of the first kind, and  $R$  is the radius of a Mylar balloon. By taking  $v = 0$ , we have  $(x, K) = \left( R \operatorname{cn} \left( u, \frac{1}{\sqrt{2}} \right), \frac{2}{R^2} \operatorname{cn}^2 \left( u, \frac{1}{\sqrt{2}} \right) \right)$  and  $(x, H) = \left( R \operatorname{cn} \left( u, \frac{1}{\sqrt{2}} \right), \frac{3}{2R} \operatorname{cn} \left( u, \frac{1}{\sqrt{2}} \right) \right)$ . Also, given parametrization from [111], we can compute principal curvatures  $k_1, k_2$  as

$$x(u, v) = R \frac{\cos v}{\sqrt{\cosh(2u)}}$$

$$k_1(u, v) = \frac{2}{R} \operatorname{sech}(u) \sqrt{\frac{1}{1 + \tanh(u)^2}}$$

$$k_2(u, v) = \frac{1}{R} \operatorname{sech}(u) \sqrt{\frac{1}{1 + \tanh(u)^2}}$$

where  $0 \leq u \leq 8$

Then, we get  $(x, K) = \left( \frac{R}{\sqrt{\cosh(2u)}}, (k_1 \cdot k_2) \right)$  and  $(x, H) = \left( \frac{R}{\sqrt{\cosh(2u)}}, \frac{1}{2}(k_1 + k_2) \right)$  for  $v = 0$ . The figures below compare parametrizations from two resources, approximated function and direct integration (hypergeometric function).

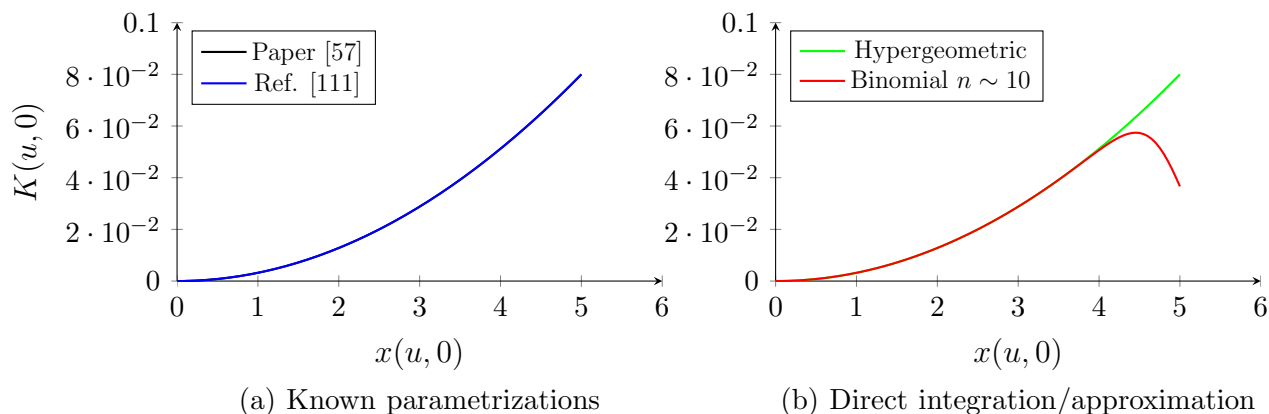


Figure 4.42: Gaussian curvature of Mylar balloon from different parametrization methods.

Notice that values from binomial approximation have sudden drops near the boundary, which a lack of terms can cause. That can be easily solved by increasing  $n$ , and then one can assume the true function by comparing several  $n$  as shown below.

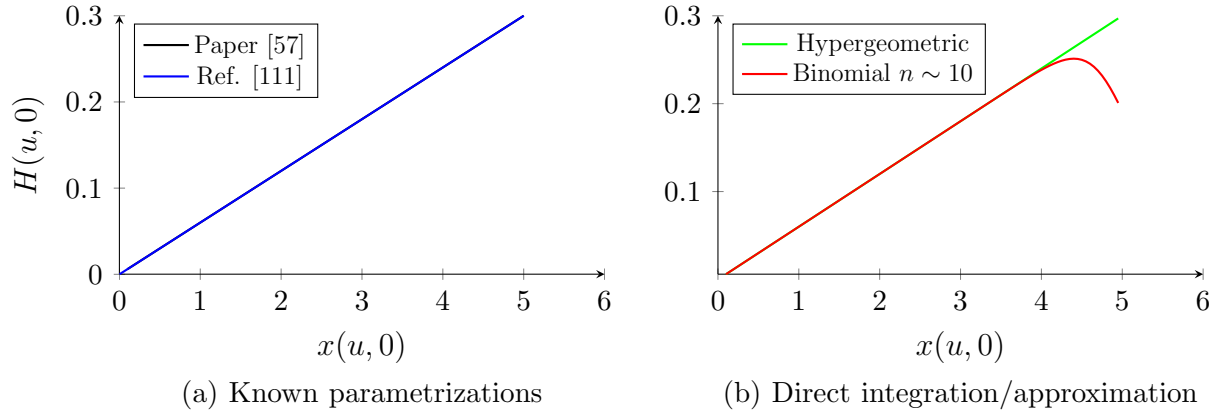


Figure 4.43: Mean curvature of Mylar balloon from different parametrization methods.

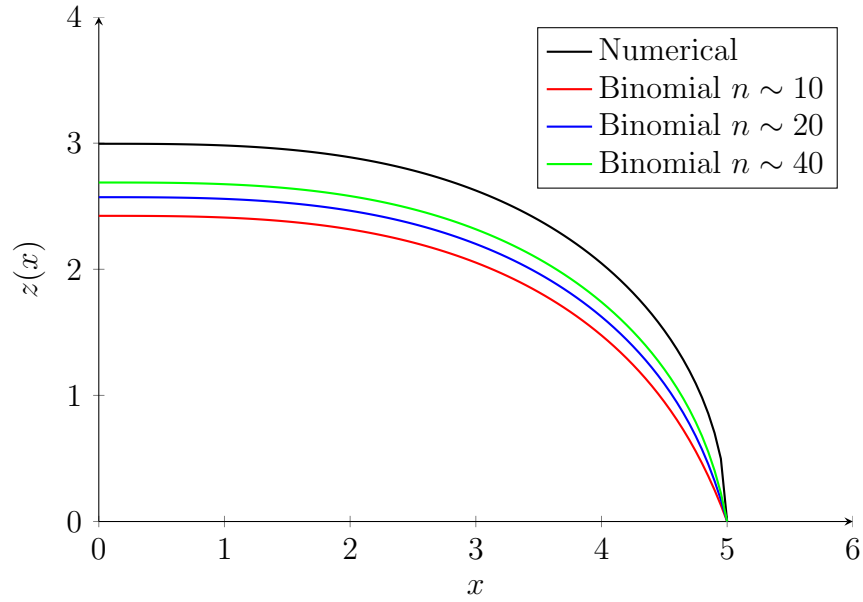


Figure 4.44: Profiles of Mylar balloon for various  $n$ .

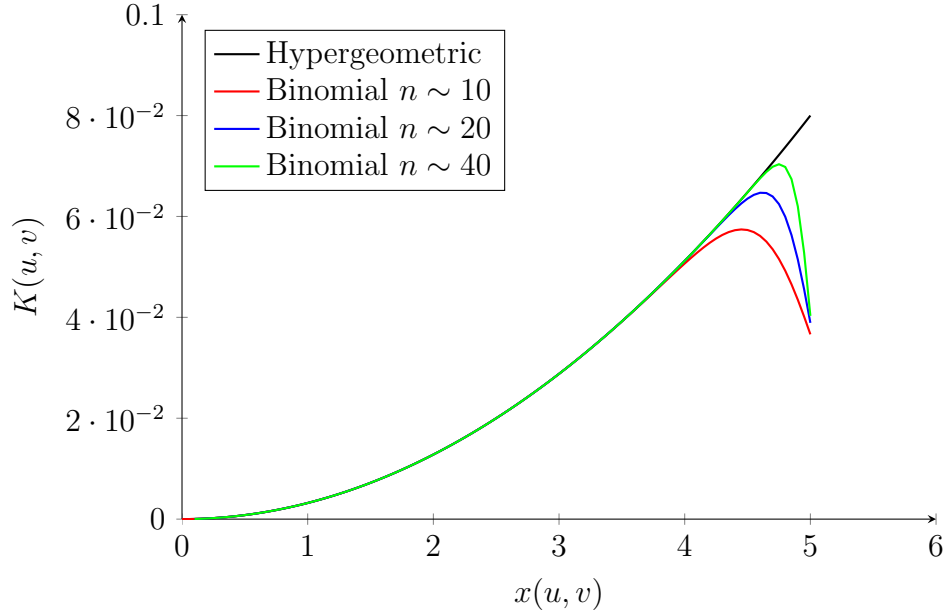


Figure 4.45: Gaussian curvature of Mylar balloon for various  $n$ .

Notice that for  $z(x)$ , we require higher  $n$ , but we do not need larger  $n$  to estimate  $K, H$  because we will be able to guess values from several  $n$ . ( $z(x)$  varies slowly along  $x$ ) For a spherical balloon, going back to equation 4.39, let  $f(x) = \frac{x}{R}$ , then we have

$$\text{Direct integration: } z(x) = -\sqrt{R^2 - x^2}$$

$$\begin{aligned} \text{Binomial approx. } n \sim 10: \quad z(x) &= \int f(x) \left( 1 + \frac{f(x)^2}{2} + \frac{3f(x)^4}{2^3} + \frac{5f(x)^6}{2^4} + \frac{35f(x)^8}{2^7} + \frac{63f(x)^{10}}{2^8} \right) dx \\ &= \frac{x^2}{2R} + \frac{x^4}{2^3 R^3} + \frac{x^6}{2^4 R^5} + \frac{5x^8}{2^7 R^7} + \frac{7x^{10}}{2^8 R^9} + \frac{21x^{12}}{2^{10} R^{11}} \end{aligned}$$

As expected, the below figure represents values obtained using binomial approximation and shows differences near the boundary.

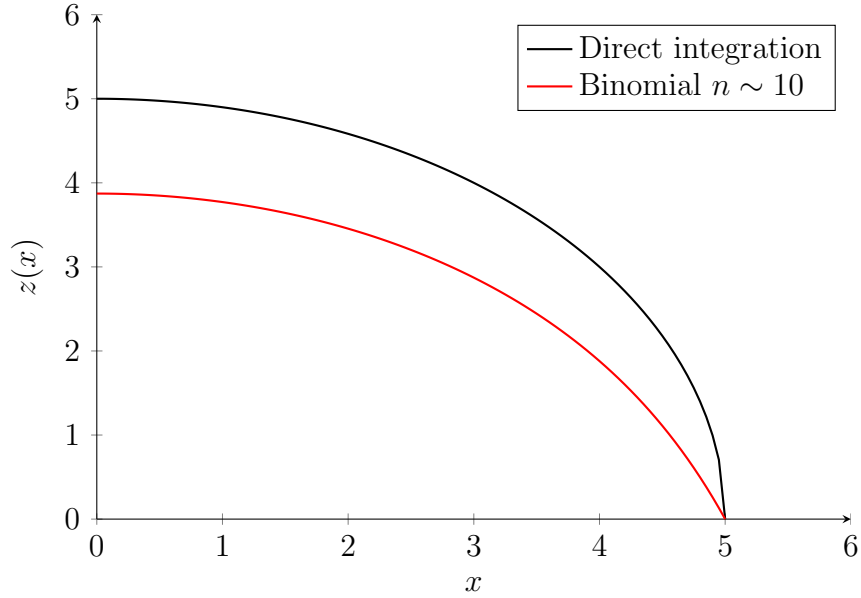


Figure 4.46: Profiles of a spherical balloon for  $n \sim 10$ .

We can apply the same method using a Mylar balloon case and get the following plots.

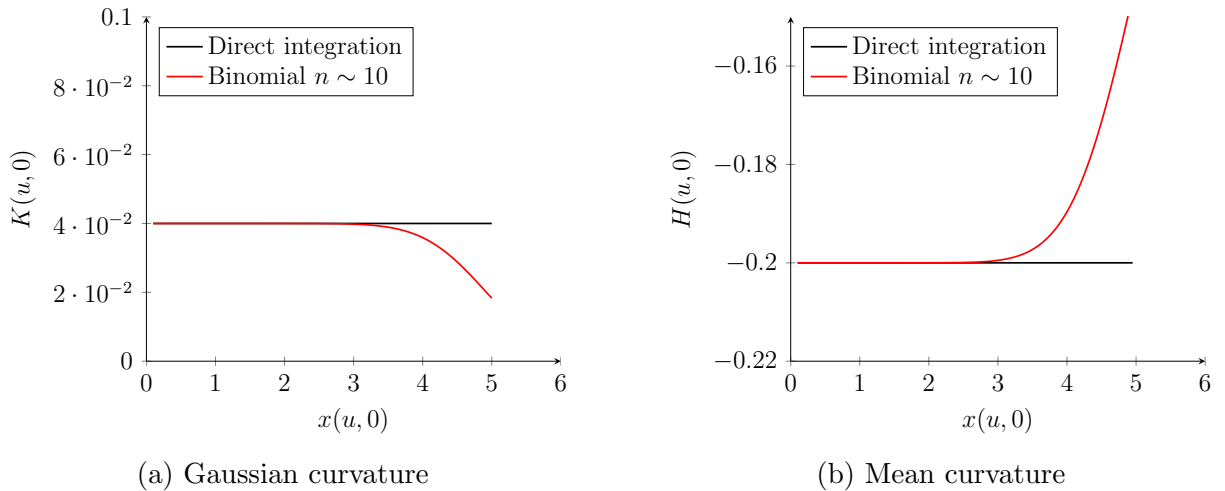


Figure 4.47: Gaussian and mean curvatures of a spherical balloon for  $n \sim 10$ .

### 4.3.3 Curvature estimation of $n$ -dimensional Euler's elastica

From the earlier section, we know Mylar balloon with force can be regarded as Euler's elastica. For Euler's elastica, there are known parametrization methods from various papers, so

one can derive curvatures using these. However, we do not have generalized parameterization methods for a spherical balloon with force. Thus, we will go over an example related to this one. Let us start with the following equation

$$\begin{aligned}
 z(t) &= \int \frac{\alpha t^2 + \beta t + \gamma}{\sqrt{(\lambda t)^2 - (\alpha t^2 + \beta t + \gamma)^2}} dt \quad (t \in \mathbb{R} \setminus \{0\} \quad n \in \mathbb{Z}) \\
 z(t) &= \int \frac{\alpha t^1 + \beta + \gamma t^{-1}}{\sqrt{\lambda^2 - (\alpha t^1 + \beta + \gamma t^{-1})^2}} dt \quad (t \in \mathbb{R} \setminus \{0\} \quad n \in \mathbb{Z}) \\
 &= \int \frac{f(t)}{\sqrt{1 - f(t)^2}} dt
 \end{aligned} \tag{4.41}$$

where  $f(t) = (\alpha t^1 - \beta + \gamma t^{-1})/\lambda$ . Then we can apply equation 4.39 and integrate as shown in the previous section. Parametrization of this surface will be the same as:

$$f_{uv} = (u \cos v, u \sin v, z(u)) \quad (\text{or } z(R) - z(u)).$$

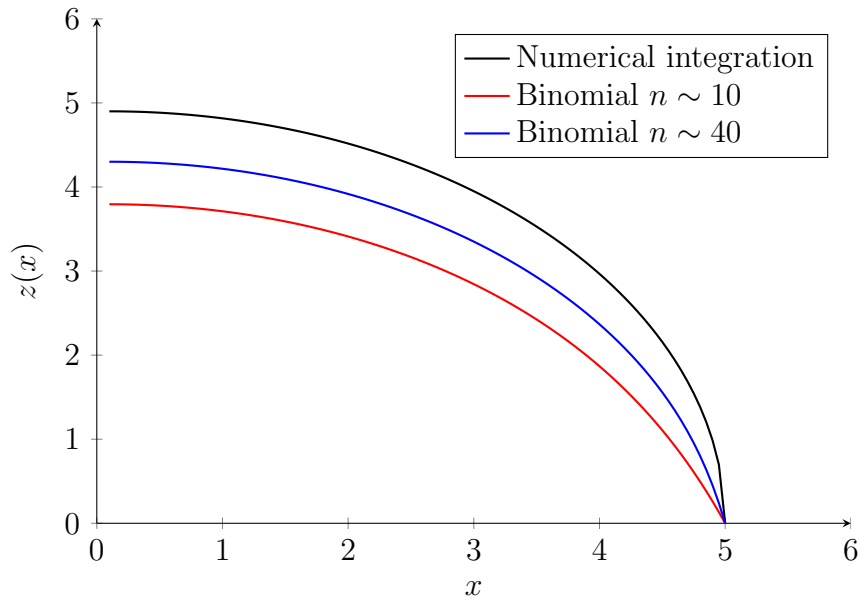


Figure 4.48: Profiles of eq. 4.41 from the binomial approximation for  $n \sim 10, 40$ .

Below plots are an approximation for  $\alpha = 1, \beta = -0.1, \gamma = 0$ .

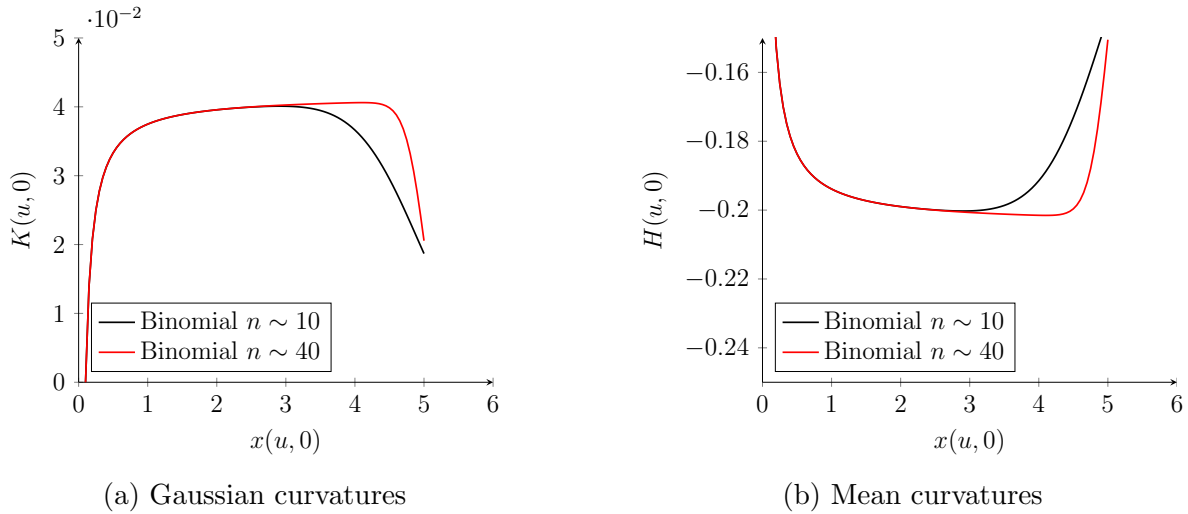


Figure 4.49: Gaussian and mean curvatures of eq. 4.41 from the binomial approximation for  $n \sim 10$ .

### 4.3.4 Curvature estimation of a surface with multiple functions

This section will briefly explain how this approach can be applied to the combined case. We are limiting application to be

- Generally, a case satisfying equation 4.20 (There could be possible cases without satisfying equation 4.20.)
- A continuous and bounded curve or surface where each interval satisfies 4.20.
- Curvature information near the boundary (farthest from the center) is less important than the central part.

We will see an example for the second case. Let us consider a curve consisting of the following equations.

$$z_1(x) = \int_x^R \frac{t^2 + 2t}{\sqrt{(\lambda_1 t)^2 - (t^2 + 2t)^2}} dt$$

$$z_2(x) = \int_x^R \frac{t^2 + 2t}{\sqrt{(\lambda_2 t)^2 - (t^2 + 2t)^2}} dt$$

$$z(x) = z_1(x) + h_1 \quad \text{for } (0 \leq x \leq 1)$$

$$z(x) = z_2(x) + h_2 \quad \text{for } (1 \leq x \leq 3)$$

$$z(x) = z_1(x) \quad \text{for } (3 \leq x \leq 5)$$

where  $\lambda_1, \lambda_2$  are constants satisfying  $z_1(R) = 0, z_2(R) = 0$  and  $h_1, h_2$  are defined by  $h_1 = z_2(3) - z_2(1), h_2 = z_1(3) - z_2(3)$ . Following figure shows plots described from  $z_1(x), z_2(x)$ , and  $z(x)$ .

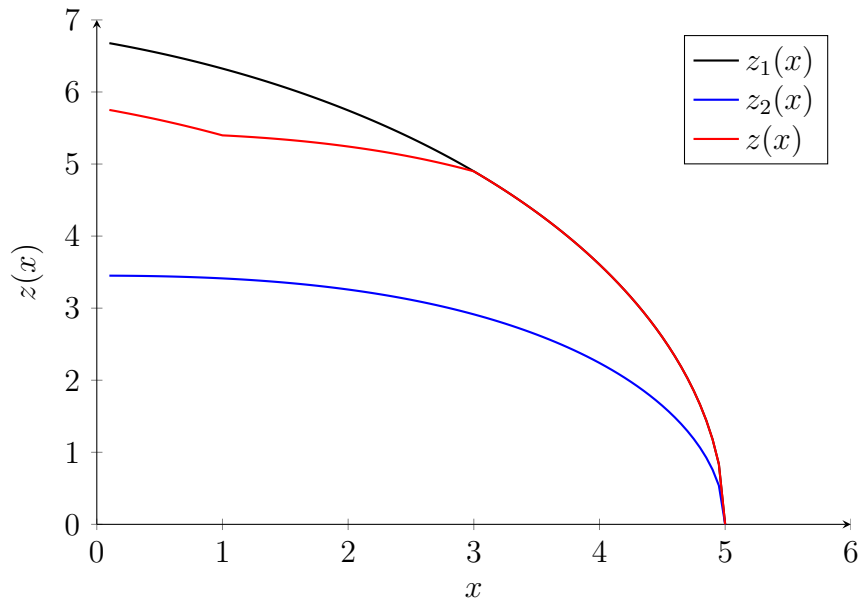


Figure 4.50: Profiles of  $z_1(x), z_2(x)$ , and a surface  $z(x)$  constructed using  $z_1(x)$  and  $z_2(x)$ .

We can apply the binomial expansion for  $n \sim 10$  and calculate curvatures.

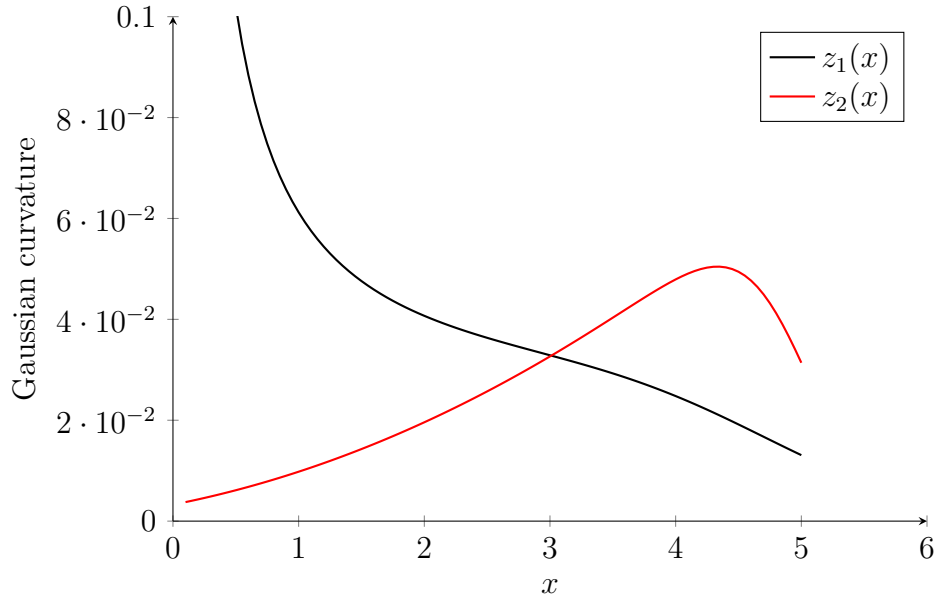


Figure 4.51: Gaussian curvatures of  $z_1(x)$  and  $z_2(x)$  from the binomial approximation  $n \sim 10$ .

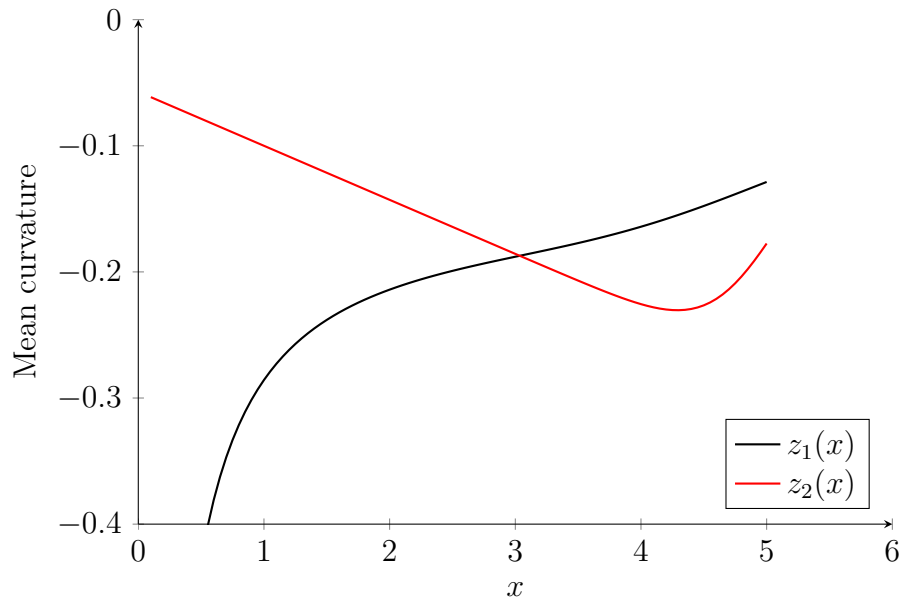


Figure 4.52: Mean curvatures of  $z_1(x)$  and  $z_2(x)$  from the binomial approximation  $n \sim 10$ .

We can represent a curvature of  $z(x)$  from the combinations of  $z_1(x)$  and  $z_2(x)$ . Notice that there should be a gap  $h_2$  for  $z_2(x)$  because  $z(x) = z_2(x) + h_2$  at  $x = 1$ . One can apply binomial expansion for  $z_2(x) + h_2$ . However,  $h_2$  is a constant, which implies it does not affect curvature. Thus, we can combine two different curves as shown below.

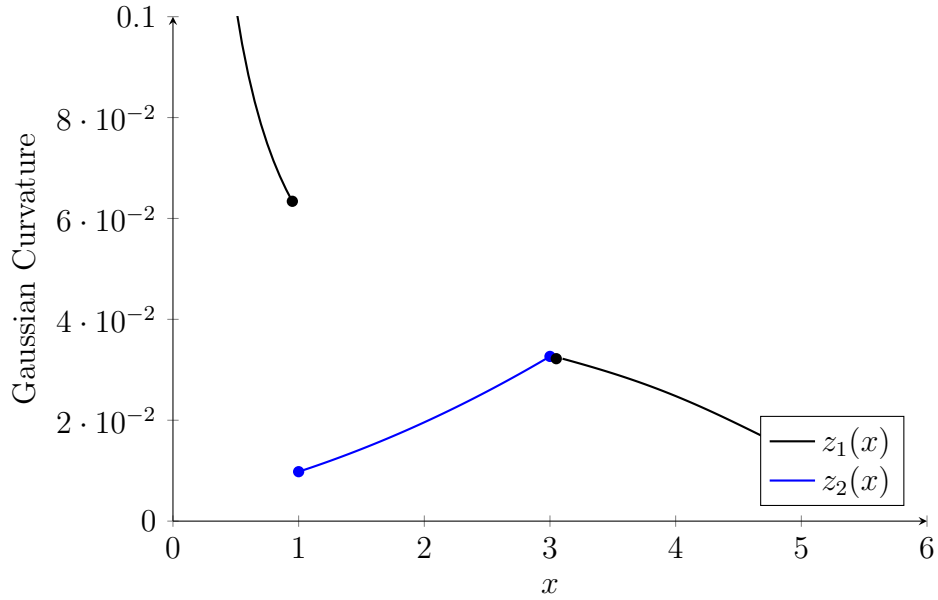


Figure 4.53: Approximated Gaussian curvature of  $z(x)$ .

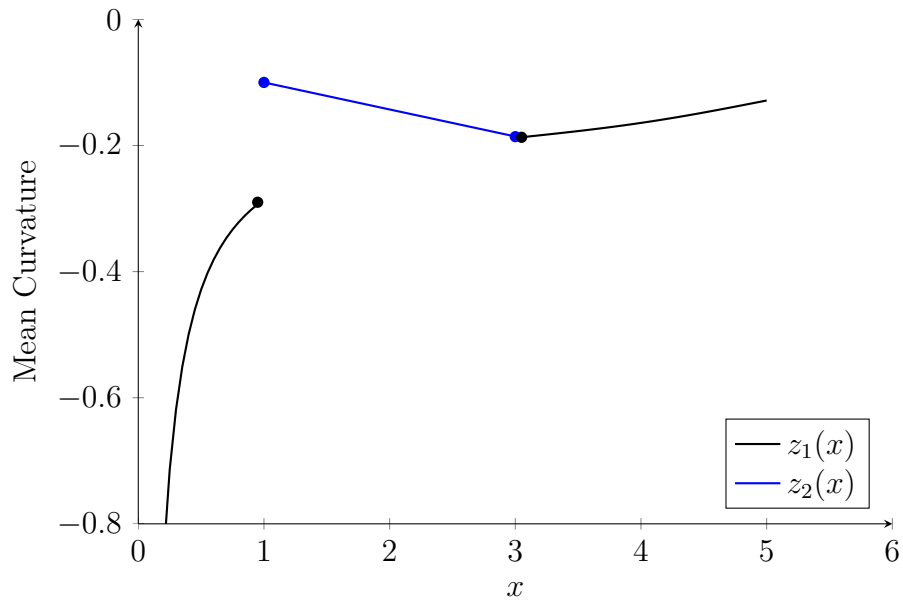


Figure 4.54: Approximated mean curvature of  $z(x)$ .

Note that we cannot define curvatures at  $x = 1, 3$  from this method.

### 4.3.5 Curvature estimation of generalized case

So far, we have considered stretchable and non-stretchable types of surfaces. In this section, we will cover a general case that can be described by equation 4.20. We note that there

would be possible cases in 4.26 or 4.29 which does not satisfy 4.20. However, we can still use this approach if the equation satisfies conditions to apply binomial expansion and take partial derivatives. Compared to section 4.3.1, this approach allows integrating first than computing summation. Recall that we have

$$z(t) = \int_t^R \frac{\alpha x^{2-n} - \beta x^{1-n} + \gamma x^{-n}}{\sqrt{\lambda^2 - (\alpha x^{2-n} + \beta x^{1-n} + \gamma x^{-n})^2}} dx \quad (x \in \mathbb{R} \setminus \{0\} \quad n \in \mathbb{Z})$$

$$z^*(t) = \int \frac{f(t)}{\sqrt{1-f(t)^2}} dt$$

$$z(x) = z^*(R) - z^*(x)$$

where  $f(t) = \frac{\alpha t^{2-n} + \beta t^{1-n} + \gamma t^{-n}}{\lambda}$  and  $f(t)^2 \leq 1$ . Let  $2-n = m$ , then we can write  $f(t) = \frac{\alpha}{\lambda} t^m + \frac{\beta}{\lambda} t^{m-1} + \frac{\gamma}{\lambda} t^{m-2} = at^{m-2}((t+b)^2 + c)$ . Notice that  $a, b, c$  are corresponding constants satisfying above relation. By applying binomial theorem, we get  $\frac{f(t)}{\sqrt{1-f(t)^2}} = f(t)(1-f(t)^2)^{-\frac{1}{2}} = f(t) \sum_{k=0}^{\infty} \binom{-\frac{1}{2}}{k} (-f(t)^2)^k = \sum_{k=0}^{\infty} \left(-\frac{1}{4}\right)^k \binom{2k}{k} (-1)^k (f(t))^{2k+1}$  (See appendix C.5 for proof).

$$z^*(t) = \int \sum_{k=0}^{\infty} \left(-\frac{1}{4}\right)^k \binom{2k}{k} (-1)^k (f(t))^{2k+1} dt$$

$$z^*(t) = \sum_{k=0}^{\infty} \left(-\frac{1}{4}\right)^k \binom{2k}{k} (-1)^k \int (f(t))^{2k+1} dt$$

$$z^*(t) = \sum_{k=0}^{\infty} \left(-\frac{1}{4}\right)^k \binom{2k}{k} (-1)^k \int (at^{m-2}((t+b)^2 + c))^{2k+1} dt$$

We can solve the last equation using computational software. The solution from Mathematica is

$$z^*(t) = \sum_{k=0}^{\infty} \left(-\frac{1}{4}\right)^k \binom{2k}{k} (-1)^k \left[ at^m \left(\frac{b - \sqrt{-c} + t}{b - \sqrt{-c}}\right)^{-2k} \left(\frac{b + \sqrt{-c} + t}{b + \sqrt{-c}}\right)^{-2k} (at^{m-2}((t+b)^2 + c))^{2k} \right. \\ \left. \left[ \frac{\left( (b^2 + c)F_1(2k(m-2) + m - 1; -2k, -2k, 2k(m-2) + m; -\frac{t}{b+\sqrt{-c}}, \frac{t}{\sqrt{-c}-b}) \right)}{t(2k(m-2) + m - 1)} \right. \right. \\ \left. \left. + \frac{2bF_1(2k(m-2) + m; -2k, -2k, 2k(m-2) + m + 1; -\frac{t}{b+\sqrt{-c}}, \frac{t}{\sqrt{-c}-b})}{2k(m-2) + m} \right. \right. \\ \left. \left. + \frac{\left( tF_1(2k(m-2) + m + 1; -2k, -2k, 2k(m-2) + m + 2; -\frac{t}{b+\sqrt{-c}}, \frac{t}{\sqrt{-c}-b}) \right)}{(2k(m-2) + m + 1)} \right] + C \right].$$

Note that  $C$  is constant and  $F_1(a; b_1; b_2; c; x; y)$  is the Appell hypergeometric function [114]. We will compare plots in section 4.3.2 to check both results are identical. First, we will start with a Mylar balloon. Recall that we have

$$z^*(t) = \sum_{k=0}^{\infty} \left(-\frac{1}{4}\right)^k \binom{2k}{k} (-1)^k \int (f(t))^{2k+1} dt \\ z(x) = z^*(R) - z^*(x).$$

For Mylar balloon, we can rewrite and solve

$$\begin{aligned}
 z^*(t) &= \sum_{k=0}^{\infty} \left(-\frac{1}{4}\right)^k \binom{2k}{k} (-1)^k \int \left(\frac{t^2}{R^2}\right)^{2k+1} dt \\
 &= \sum_{k=0}^{\infty} \left(-\frac{1}{4}\right)^k \binom{2k}{k} (-1)^k \int \left(\frac{t}{R}\right)^{4k+2} dt \\
 &= \sum_{k=0}^{\infty} \left(-\frac{1}{4}\right)^k \binom{2k}{k} (-1)^k \left(\frac{1}{4k+3} \frac{t^{4k+3}}{R^{4k+2}}\right) \\
 &= \frac{1}{3} \frac{t^3}{R^2} {}_2F_1\left[\frac{1}{2}, \frac{3}{4}, \frac{7}{4}; \frac{t^4}{R^4}\right] \\
 &\quad - \frac{1}{4n+7} 4^{-n-1} R^{-4n-6} t^{4n+7} \binom{2(n+1)}{n+1} {}_pF_q\left[\left\{1, n + \frac{3}{2}, n + \frac{7}{2}\right\}, \left\{n + 2, n + \frac{11}{4}\right\}; \frac{t^4}{R^4}\right] \\
 &= \frac{1}{3} \frac{t^3}{R^2} {}_2F_1\left[\frac{1}{2}, \frac{3}{4}, \frac{7}{4}; \frac{t^4}{R^4}\right] - c(t)
 \end{aligned}$$

where  $c(t) = \frac{1}{4n+7} 4^{-n-1} 5^{-4n-6} t^{4n+7} \binom{2(n+1)}{n+1} {}_pF_q\left[\left\{1, n + \frac{3}{2}, n + \frac{7}{2}\right\}, \left\{n + 2, n + \frac{11}{4}\right\}; \frac{t^4}{R^4}\right]$ . Notice that  $c(t)$  is excess term added to the true solution. The last two equations can be obtained from Mathematica. The above equation can be drawn with different  $n$  values. This graph agrees with one in section 4.3.2.

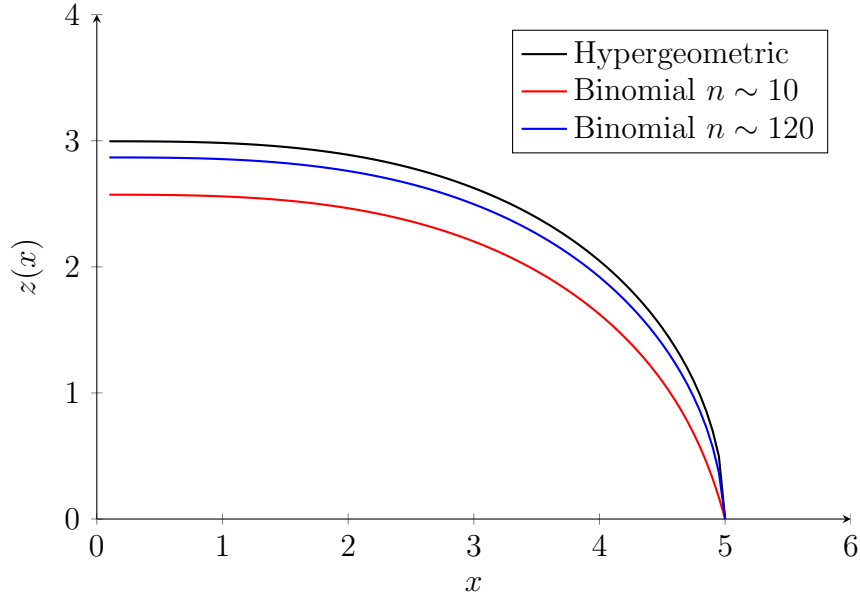


Figure 4.55: Profiles of Mylar balloon from binomial approximation for  $n \sim 10, 120$ .

Notice that  $c(t)$  converges to zero if  $n$  goes to infinity. Following figure shows  $c(t)$  with

different  $n$  values.

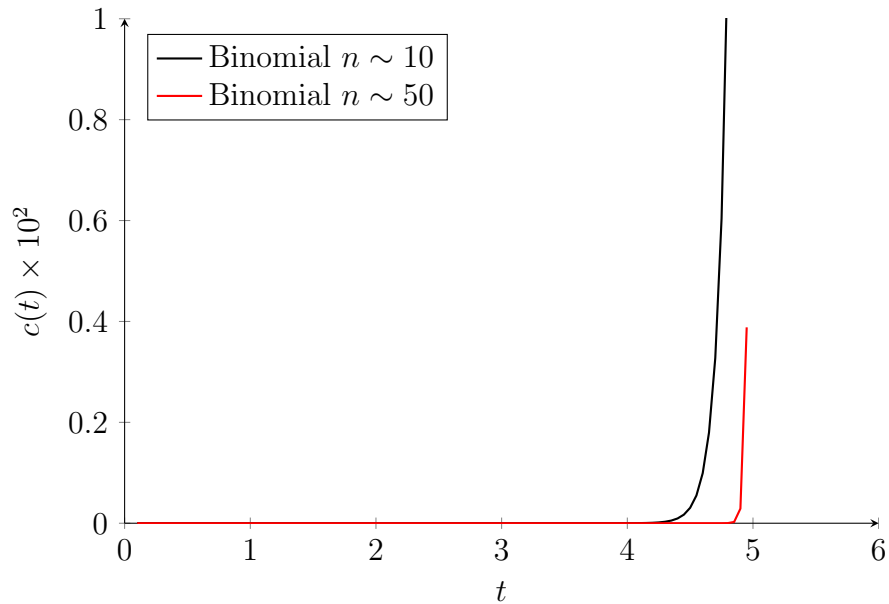


Figure 4.56: Profiles of excess term  $c(t)$  for  $n \sim 10, 50$ .

As we already know  $\frac{\partial}{\partial x}z(x)$  shows pretty good agreement for relatively smaller  $n$  than  $z(x)$ .

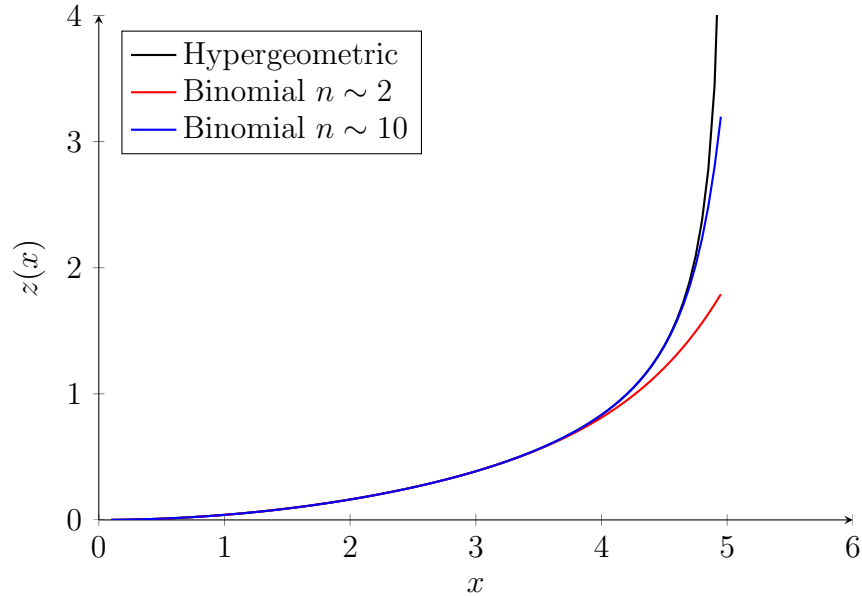


Figure 4.57: Profiles of  $\frac{\partial}{\partial x}z(x)$  (partial derivative of Mylar balloon along  $x$ ) from binomial approximation for  $n \sim 2, 10$ .

For a spherical balloon, we can write and solve

$$\begin{aligned}
 z^*(t) &= \sum_{k=0}^{\infty} \left(-\frac{1}{4}\right)^k \binom{2k}{k} (-1)^k \int \left(\frac{t}{R}\right)^{2k+1} dt \\
 &= \sum_{k=0}^{\infty} \left(-\frac{1}{4}\right)^k \binom{2k}{k} (-1)^k \int \left(\frac{t}{R}\right)^{2k+1} dt \\
 &= \sum_{k=0}^{\infty} \left(-\frac{1}{4}\right)^k \binom{2k}{k} (-1)^k \left(\frac{1}{2k+2} \frac{t^{2k+2}}{R^{2k+1}}\right) \\
 &= R - \sqrt{R^2 - t^2} - \frac{1}{n+2} 2R^{-2n-3} t^{2n+4} \binom{2(n+1)}{n+1} {}_2F_1\left[1, n + \frac{3}{2}, n + 3; \frac{t^2}{R^2}\right]
 \end{aligned}$$

which will be the same as figure 4.47 as shown below:

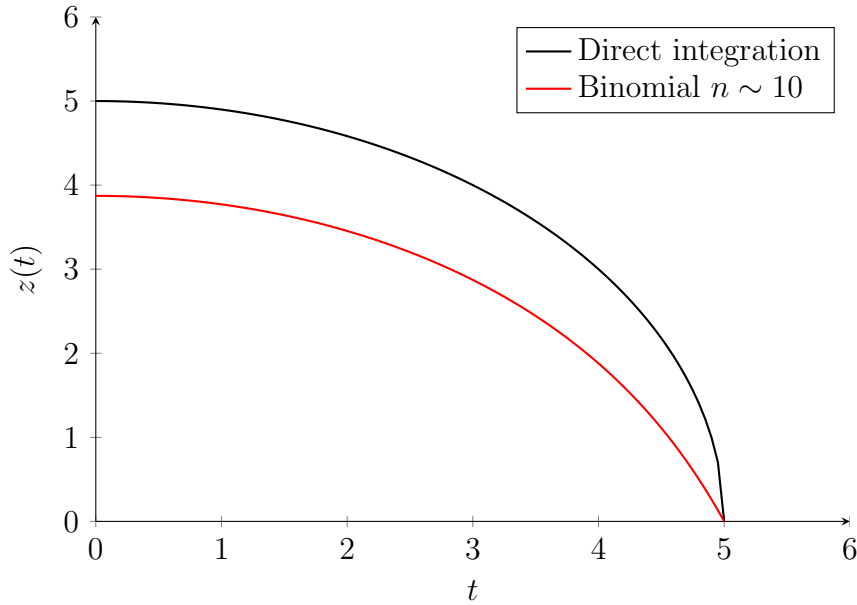


Figure 4.58: Profiles of a spherical balloon from binomial approximation for  $n \sim 10$ .

In section 4.3.1, we first applied binomial expansion, then evaluated integration. We have also shown in this section that the opposite case will work. Let's call integration operation for a function  $f$  as  $I(f)$  and summation as  $S(f)$ . Specifically, these operations can be defined as  $I(f) = \int f(x)dx$  and  $S(f) = \sum_{k=0}^{\infty} c^k \binom{dk}{ek} f(x)$  (where  $c, d, e$  are constants) for this case. Then we can think  $I \cdot S(f) = S \cdot I(f)$  when  $f$  doesn't depend on  $k$ . However, these are not commutes when  $f$  relates to  $k$  because additional singularity can be caused by  $k$ . We will show an example for  $I \cdot S(f(x)^{ak+b}) \neq S \cdot I(f(x)^{ak+b})$  for constants  $a, b$ . Let us go back to

the example in section 4.2.1 described by

$$z(x) = \int_x^R \frac{t^2 - 3}{\sqrt{\left(\frac{22}{5}t\right)^2 - (t^2 - 3)^2}} dt.$$

We can apply the binomial expansion as follows.

$$\begin{aligned} z^*(t) &= \sum_{k=0}^{\infty} \left(-\frac{1}{4}\right)^k \binom{2k}{k} (-1)^k \int \left(\frac{5}{22}\left(t - \frac{3}{t}\right)\right)^{2k+1} dt \\ &= \sum_{k=0}^{\infty} \left(-\frac{1}{4}\right)^k \binom{2k}{k} (-1)^k \left(\frac{5}{22}\right)^{2k+1} \int \left(t - \frac{3}{t}\right)^{2k+1} dt \\ &= \sum_{k=0}^{\infty} \left[ \left(-\frac{1}{4}\right)^k \binom{2k}{k} (-1)^k \left(\frac{5}{22}\right)^{2k+1} \left[ \frac{3}{2k} \left(t - \frac{3}{t}\right)^{2k} \left(1 - \frac{t^2}{3}\right)^{-2k} {}_2F_1\left[-2k - 1, -k, -k + 1; \frac{t^2}{3}\right] \right] \right]. \end{aligned}$$

Notice that this series goes to infinity because of  $\frac{3}{2k}$ . However, we can still apply binomial expansion. We have

$$\begin{aligned} z^*(t) &= \int \sum_{k=0}^{\infty} \left(-\frac{1}{4}\right)^k \binom{2k}{k} (-1)^k \left(\frac{5}{22}\left(t - \frac{3}{t}\right)\right)^{2k+1} dt \\ &\simeq \int \left( \frac{5(t^2 - 3)}{22t} + \frac{125(t^2 - 3)^3}{21296t^3} + \frac{9375(t^2 - 3)^5}{41229056t^5} + \dots \right) dt \\ &= \frac{5}{21296} \left( -2229 \log(t) + \frac{675}{2t^2} + \frac{743t^2}{2} + \frac{25t^2}{4} + \dots \right). \end{aligned}$$

This  $z^*(t)$  has a singularity at  $x = 0$ , but there is no singularity related to  $k$ . The below figure shows plots with different  $n$  and numerical integration.

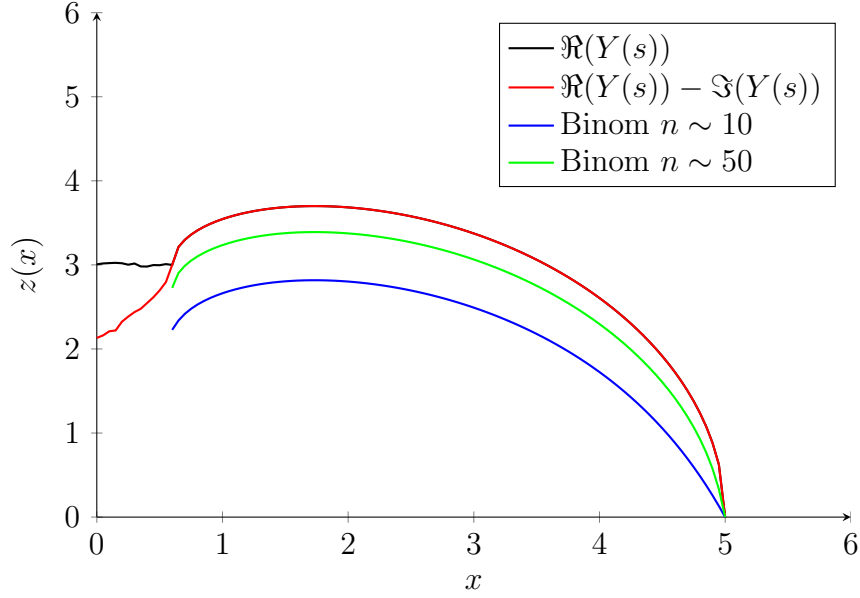


Figure 4.59: Profiles of figure 4.18 approximated from binomial expansion for  $n \sim 10, 50$ .

Note that  $x < 0.6$  is not plotted in the above picture because of the scaling issue (significant drop nearby  $x \sim 0.6$ ).

So far, we have considered  $z(x)$  for the axis-symmetric case. If we think of the non-axis-symmetric surface with an azimuthal angle as a variable, we can start from

$$\begin{aligned}
z(x, \theta) &= \int_x^R \frac{\alpha(\theta)t^{2-n} + \beta(\theta)t^{1-n} + \gamma(\theta)t^{-n}}{\sqrt{\lambda(\theta)^2 - (\alpha(\theta)t^{2-n} + \beta(\theta)t^{1-n} + \gamma(\theta)t^{-n})^2}} dt \quad (t \in \mathbb{R} \setminus \{0\} \quad n \in \mathbb{Z}) \\
&= \int_x^R \frac{\alpha(\theta)t^m + \beta(\theta)t^{m-1} + \gamma(\theta)t^{m-2}}{\sqrt{\lambda(\theta)^2 - (\alpha(\theta)t^m + \beta(\theta)t^{m-1} + \gamma(\theta)t^{m-2})^2}} dt \\
&= \int_x^R \frac{a(\theta)t^{m-2} \left( (t + b(\theta))^2 + c(\theta) \right)}{\sqrt{1 - \left( a(\theta)t^{m-2} \left( (t + b(\theta))^2 + c(\theta) \right) \right)^2}} dt.
\end{aligned}$$

Since  $\theta$  does not involve the integration process, we can apply the same method.

$$\begin{aligned}
z^*(t, \theta) &= \int \sum_{k=0}^{\infty} \left(-\frac{1}{4}\right)^k \binom{2k}{k} (-1)^k (f(t, \theta))^{2k+1} dt \\
&= \sum_{k=0}^{\infty} \left(-\frac{1}{4}\right)^k \binom{2k}{k} (-1)^k \int (f(t, \theta))^{2k+1} dt \\
&= \sum_{k=0}^{\infty} \left(-\frac{1}{4}\right)^k \binom{2k}{k} (-1)^k \int \left[ a(\theta) t^{m-2} \left( (t + b(\theta))^2 + c(\theta) \right) \right]^{2k+1} dt
\end{aligned}$$

If  $\lambda$  does not have  $\theta$  dependency, computation will be more straightforward. Extended version of equation 4.28 (by adding  $\theta$ ) will work same way if the choice of  $f_i(x, \theta)$  and  $g_i(x, \theta)$  satisfies conditions to apply binomial expansion and do symbolic integration. Let us consider an example in section 4.2.5 can be described as

$$z(x, \theta) = \int_x^{R(\theta)} \frac{t^2 + t}{\sqrt{m^2 - (t^2 + t)^2}} dt \quad (4.42)$$

$$R(\theta) = 5 + \cos \theta$$

$$m = R(\theta)^2 + R(\theta).$$

Therefore, we can get

$$\begin{aligned}
z^*(t, \theta) &= \sum_{k=0}^{\infty} \left(-\frac{1}{4}\right)^k \binom{2k}{k} (-1)^k \int \left( \frac{t^2 + t}{30 + 11 \cos(\theta) + \cos(\theta)^2} \right)^{2k+1} dt \\
&= \sum_{k=0}^{\infty} \left[ \left(-\frac{1}{4}\right)^k \binom{2k}{k} (-1)^k \right. \\
&\quad \left. \left[ \frac{t(t+1)^{-2k-1}}{2k+2} \left( \frac{t^2 + t}{30 + 11 \cos(\theta) + \cos(\theta)^2} \right)^{2k+1} {}_2F_1[-2k-1, 2k+2, 2k+3; -x] \right] \right]
\end{aligned}$$

$$z(x, \theta) = z^*(R(\theta), \theta) - z^*(x, \theta).$$

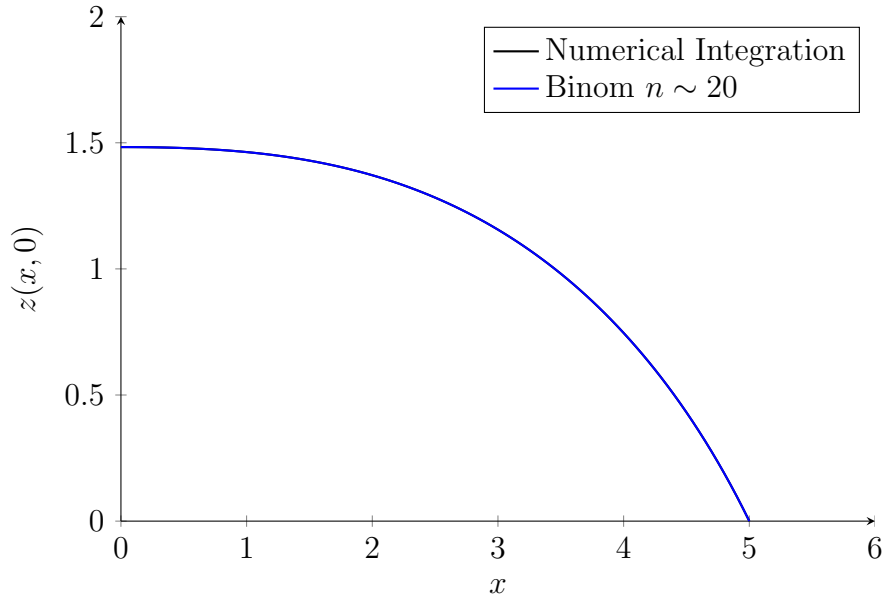


Figure 4.60: Profiles of eq. 4.42 at  $\theta = 0$  approximated from binomial expansion for  $n \sim 20$ .

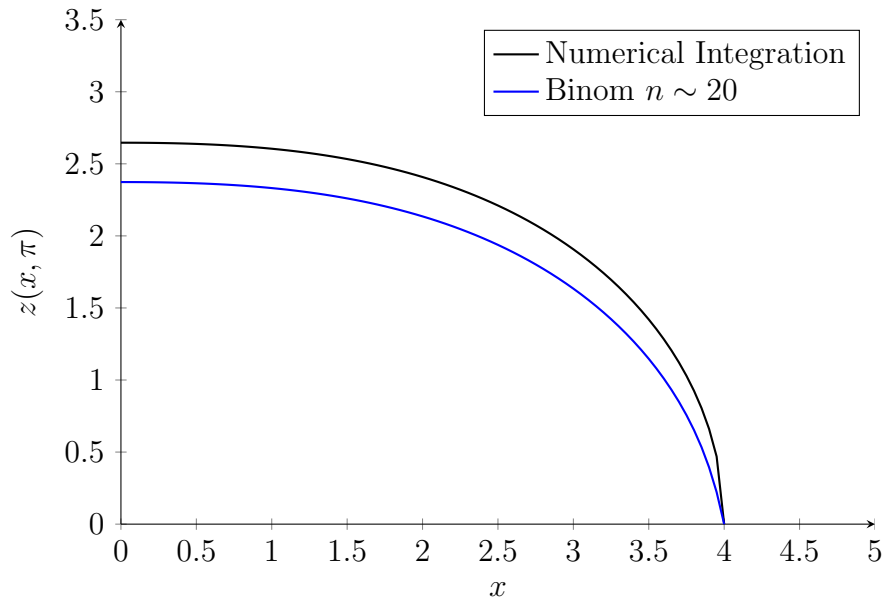


Figure 4.61: Profiles of eq. 4.42 at  $\theta = \pi$  approximated from binomial expansion for  $n \sim 20$ .

As we can observe in the first graph, if  $\max(z(x, \theta))$  is smaller, binomial expansion shows a pretty good agreement with relatively small  $n$ .

# Chapter 5

## Conclusion

### 5.1 Conditions and constructions of a pinned rigid graph

We have presented bounds for the number of embeddings for pinned rigid graphs, which is  $2^{|I|} \leq N(G) \leq 4^{|I|}$  using Bezout's Theorem (where  $|I|$  is the number of inner vertices of pinned rigid graph). This result comes from simple counting rules adopting intersection points of circles related to the Euclidean distance functions. Next, we demonstrated how to construct a pinned rigid graph with a finite number of embeddings. Using a set of vertices (or sub-graph  $H$ ) built up from one inner vertex  $v_i$  and its neighboring points satisfying to be in the general position (Definition A.1.3), we have performed the way to construct a graph for a finite number of embeddings. Although we've focused on discrete annulus and strips, we can apply these results to the general pinned graphs. Moreover, we have shown that we can merge these rigid structures. If it is glued to the rigid face, it will maintain rigidity. We can gauge the maximum possible realizations using the number of embeddings from each graph. Last, we have presented methods that uses vector and matrix operations to reconstruct position vectors from the given Euclidean distance functions. There are many ways to solve this problem. For example, we have introduced the resultant matrix or homotopy continuation method. They are precise and work well with polynomials. However, it requires more computing power when we add more points. Our method works fast and handles points

$> 10$ . Because it employs sequential computation, an error inflation problem arises and can work best with points  $< 1000$ . We have shown that our approach can be worked with optimization techniques to reduce error inflation. We have demonstrated examples of flower and calla lily shapes. Still, errors are  $10^{-1} \sim 10^{-3}$ . Therefore, a potential extension for this project will be testing structures with other methods. For example, the surface can be reconstructed with a combination of our method and a resultant matrix or a Gram matrix to reduce errors. Following figure 5.1 is an illustration of this. We can compute distance

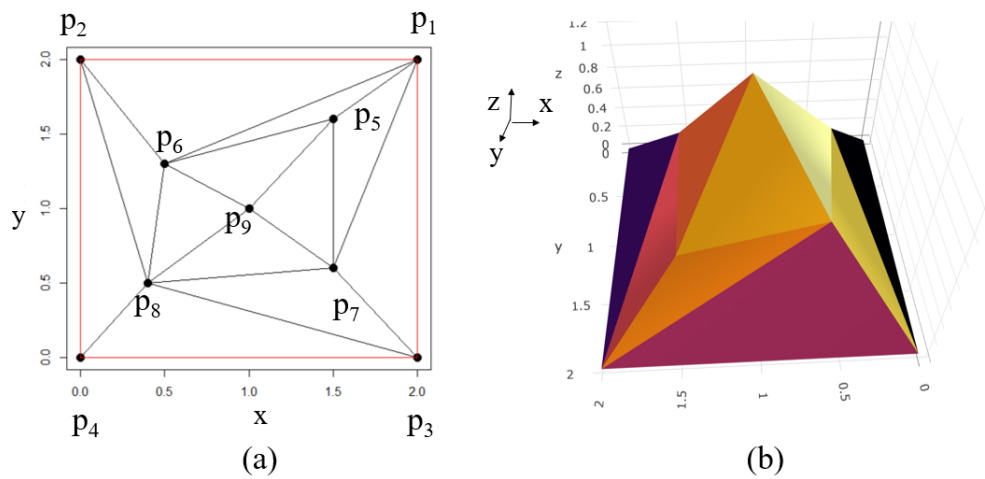


Figure 5.1: A graph with  $N_G = 2$ .



## 5.2 $n$ -dimensional extension of Euler's elastica with constitutive relations

Starting from an isoperimetric problem, we have derived Euler's elastica using Paulsen's formulation for the Mylar balloon. The approach is based on the Euler-Lagrange equation to achieve maximum volume or minimum energy. The solution will be unique if we fix two ends and one side slope and can be multiple with fixed two ends. Next, we develop  $n$ -dimensional extension applying the same mathematical formulation. We have demonstrated that this technique can be extended to the surface with different constraints. Thus, this can simulate the shapes of surfaces made from different materials. Because these solutions from this approach are in integral form, we have presented an analytical approach based on a binomial approximation. We can use this approach to estimate curvature and derivatives for analytical purposes. However, it does not have a good agreement at the boundary. Because there is an additional term generated from series expansion, and it is drastically increasing function at the border to almost zero everywhere, that will cause an error at the boundary. We have demonstrated that the binomial approach shows good agreement  $n \geq 10$  for derivatives and  $n \geq 100$  for the original equation if we exclude results near the boundary. Figure 5.2 shows three-dimensional structure generated from a perpendicular force for  $n = 1$  and  $n = 2$  (recall that constraints of  $x^n \sqrt{1 + z'(x)}$ ).

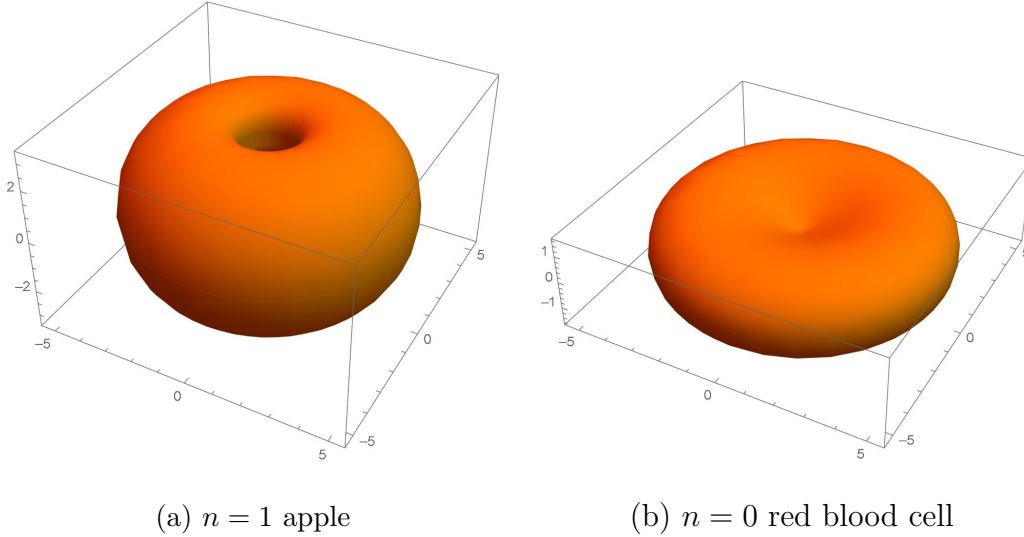


Figure 5.2: Plots drawn using  $n$ -dimensional Euler's elastica similar to nature structures.

The left plot resembles a shape of an apple, and the right one looks like a red blood cell. The body of red blood cells is determined by minimizing bending energy with internal negative pressure [15]. Apple is grown up uniformly except for the central part. We want to note that none of them are convex. Since we minimize energy (not volume), it is still at minimum energy even if we compute using different patches of  $(V, S)$ . However, if the integral has imaginary values, we can make it smoother by applying optimization methods. We can

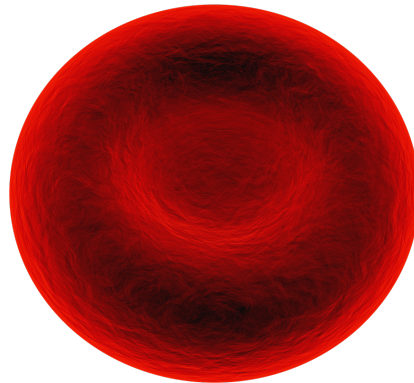


Figure 5.3: Image of red blood cell [108].

extend these structures to Willmore surfaces via conformal mapping. We know that Euler's elastica satisfies  $\min(\int \frac{ds}{R^2})$ . If we apply  $x^n \sqrt{1+z'(x)} = x^n \sqrt{1+p^2}$  rather than  $\sqrt{1+p^2}$ , we will have  $\frac{d^2Q}{dx^2} - \frac{dP}{dx} + \gamma \frac{d}{dx} \frac{x^n p}{\sqrt{1+p^2}} = 0$ . Then we get,

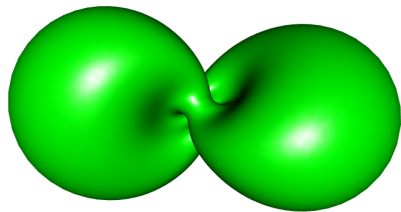
$$dx = \frac{dp}{(1+p^2)^{5/4} \sqrt{\gamma' x^n \sqrt{1+p^2} + \beta' p + \alpha'}}$$

$$dy = \frac{p dp}{(1+p^2)^{5/4} \sqrt{\gamma' x^n \sqrt{1+p^2} + \beta' p + \alpha'}}$$

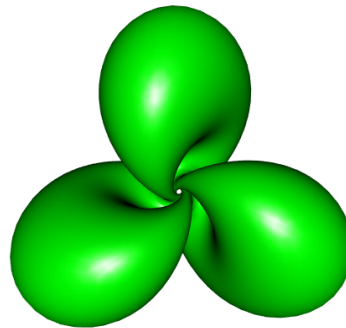
Since  $d^2 \frac{\sqrt{\gamma' x^n \sqrt{1+p^2} + \beta' p + \alpha'}}{(1+p^2)^{1/4}} = \frac{dp(\beta' - \alpha' p)}{(1+p^2)^{5/4} \sqrt{\gamma' x^n \sqrt{1+p^2} + \beta' p + \alpha'}} + dx f(x, p)$ , we have an extra term  $dx f(x, p)$ . Depending on  $f(x, p)$ , the surface may not be in a minimum bending energy. [77] shows a red blood cell applying area constraints from the sphere obtained from Willmore flow. Thus, the relation between the Willmore surface and  $n$ -dimensional extension can be a subject of a future project. As shown in Appendix D.3, Hopf torus is an interesting geometrical object related to Willmore energy. Hopf torus is Willmore surface, which can be created via a simple elastic curve on the sphere [100]. The figure below represents Hopf tori with 2-Lobe and 3-Lobe.



Figure 5.4: Image of apple [109].



(a) 2-Lobe



(b) 3-Lobe

Figure 5.5: Hopf torus plotted using R with codes in [102].

Recall that figure 4.20 illustrates a curve obtained from adding a term (higher dimension) to Euler's elastica. Hopf torus using these curves may not be Willmore surfaces, but it would be interesting to examine how these curves change the geometrical structures and energies of Hopf torus. Another possible application will be Constrained Willmore Hopf torus. Figure 5.6 shows Constrained Willmore Hopf torus. This surface can be obtained via Willmore flow using constraints [35]. Moreover, we can apply  $p$ -Willmore flow for any surfaces to discover how they morph based on given constraints. For example, cow mesh can be optimized using 2-Willmore flow with the conformal penalty and becomes a sphere after several steps. Similarly, an animal face can be morphed into a red blood cell shape [32]. Finally, we conclude that one can study related analyses for Willmore flow or constrained Willmore surfaces connected to  $n$ -dimensional extension of Euler's elastica to examine energy variations.

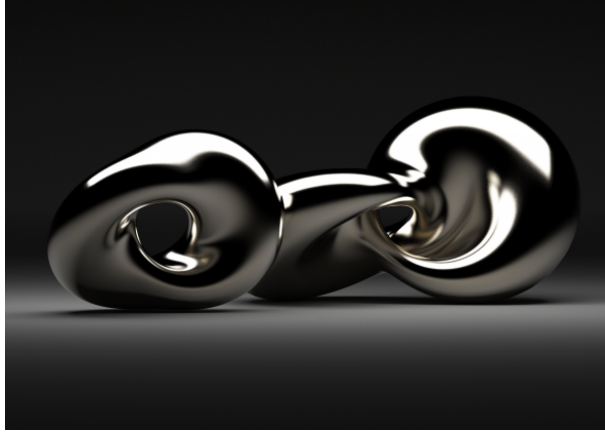


Figure 5.6: Constrained Willmore Hopf torus by GeometrieWerkstatt in [94] under License CC BY-NC-SA 3.0.

# Appendices

# Appendix A

## Mathematical backgrounds for isometric embeddings

### A.1 Properties of isometric mappings

**Definition A.1.1** (Definition 2.5 [71][106][116])). A mapping  $f: A \rightarrow B$  between two metric spaces is said to preserve equality of distance if there exists a function  $\rho$  whose domain and range is the real interval  $[0, \infty)$  such that for  $x, y \in A$  and  $f(x), f(y) \in B$ , we have  $\rho(x, y) = \rho(f(x), f(y))$ .

**Definition A.1.2** ([91]). An isometry is a bijective map between two metric spaces that preserve the equality of distances. For an isometry of  $\mathbb{R}^n$  is a function  $f: \mathbb{R}^n \rightarrow \mathbb{R}^n$  such that  $|f(v) - f(w)| = |v - w|$  where  $|(x_1, \dots, x_n)| = \sqrt{x_1^2 + \dots + x_n^2}$  for all  $v, w \in \mathbb{R}^n$ .

**Definition A.1.3** ([91]). A set of  $(n + 1)$  points  $(p_0, p_1, \dots, p_n)$  for  $p_i \in \mathbb{R}^n$  is said to be in the general position if they don't all lie in a hyperplane.

### A.2 $C^k$ isometric embeddings

**Theorem A.2.1** (Theorem 1[60]). Any closed Riemannian  $n$ -manifold has a  $C^1$  isometric embedding in  $E^{2n}$ .

**Theorem A.2.2** (Theorem 2[60]). Any Riemannian  $n$ -manifold has a  $C^1$  isometric immersion in  $E^{2n}$  and an isometric embedding in  $E^{2n+1}$ .

**Theorem A.2.3** (Nash-Kuiper[60][48]). If a compact  $C^1$ -Riemannian  $C^1$ -manifold with boundary of dimension  $n$  has a  $C^1$ -embedding in the Euclidean  $N$ -space  $E^N$   $N \geq n + 1$ , then it has a  $C^1$ -isometric embedding in  $E^N$ .

**Theorem A.2.4** (Theorem 2[61]). A compact  $n$ -manifold with a  $C^k$  positive metric has a  $C^k$  isometric embedding in any small volume of the Euclidean  $(n/2)(3n+11)$ -space, provided  $3 \leq k \leq \infty$ .

**Theorem A.2.5** (Theorem 3[61]). Any Riemannian  $n$ -manifold with a  $C^k$  positive metric, where  $3 \leq k \leq \infty$ , has a  $C^k$  isometric embedding in  $(\frac{n^3}{2} + 7n^2 + \frac{5}{2}n)$ , in fact, in any small portion of this space.

### A.3 Isoperimetric problems

Let  $\Omega$  be a bounded open set in  $\mathbb{R}^m$  and  $u: \bar{\Omega} \rightarrow \mathbb{R}^n$  is a function of class  $C^1$ . We will refer this as  $C^1(\bar{\Omega}, \mathbb{R}^n)$ . Solutions of isoperimetric problems have conditions for local extrema  $u \in C^1(\bar{\Omega}, \mathbb{R}^n)$  of variational integrals  $\mathcal{F}(u) := \int_{\Omega} F(x, u, Du)dx$ , where  $Du$  denotes the first derivative of  $u$ . In addition to the boundary conditions on  $\partial\Omega$ , there is a subsidiary condition  $\mathcal{G}(u) = c$ , with some constant  $c$  and  $\mathcal{G}(u)$  has a form of  $\mathcal{G}(u) = \int_{\Omega} G(x, u, Du)dx$ .

**Definition A.3.1** ([27][107]). Let  $\mathcal{U}$  be an open set in  $\mathbb{R}^m \times \mathbb{R}^n \times \mathbb{R}^{mn}$  containing  $\{(x, u(x), Du(x)): x \in \bar{\Omega}, u \in C^1(\bar{\Omega}, \mathbb{R}^n)\}$ .  $\mathcal{G}$  satisfies  $\mathcal{G}(u) := \int_{\Omega} G(x, u, Du)dx$  and  $\mathcal{G}(u) = c$ . Isoperimetric problem reduces to the Lagrange problem when  $\dot{H} = G(x, u, Du)$  with boundary conditions  $H(x_1) = 0, H(x_2) = c$  for  $\Omega$  with a range  $[x_1, x_2]$ .

Note that the solution to the isoperimetric problem must be convex. Otherwise, the dent part can be flipped to increase the area, which has the same constraints [27][122]. Next, we

will briefly include a theorem related to the Lagrange multiplier, which will be connected to Chapter 3.

**Definition A.3.2** ([27]).  $\mathcal{J}$  has the variational property  $\mathcal{V}$  if  $\mathcal{J}$  is a class of mappings  $v \in C^1(\bar{\Omega}, \mathbb{R}^n)$  such that, for every  $v$  in  $\mathcal{J}$  and for every pair of functions  $\varphi, \psi \in C_c^\infty(\Omega, \mathbb{R}^n)$ , there exist numbers  $\epsilon_0 > 0, t_0 > 0$  such that  $v + \epsilon\varphi + t\psi \in \mathcal{J}$  for  $|\epsilon| < \epsilon_0, |t| < t_0$ .

Note that  $C_c^k$  implies compact support of the  $C^k$  function in  $\Omega$ .

**Remark A.3.0.1** (Remark [25]). An admissible function is the set of functions satisfying the constraints of a given variational problem.

**Remark A.3.0.2** (Remark [27]). If a set  $\mathcal{J}$  of admissible functions has the property  $(\mathcal{V})$ , then  $\mathcal{J}$  is, in a weak sense, open.

**Theorem A.3.1** (Theorem 1 [27]). Suppose that  $u$  furnishes a weak extremum of the functional  $\mathcal{F}$  in the class  $\mathcal{J}_c := \mathcal{J} \cap \{v: \mathcal{G}(v) = c\}$ . Then there exists a real number  $\lambda$ , called the Lagrange multiplier, such that  $\delta\mathcal{F}(u, \varphi) + \lambda\delta\mathcal{G}(u, \varphi) = 0$  for all  $\varphi \in C_c^\infty(\Omega, \mathbb{R}^n)$  holds, provided that  $\delta\mathcal{G}(u, \varphi)$  does not vanish for all  $\varphi \in C_c^\infty(\Omega, \mathbb{R}^n)$ .

Proof of the above theorem can be found in various textbooks, including [27].

# Appendix B

## Mathematical backgrounds for rigidity theory

### B.1 Rings and matrices

This section includes basic results from abstract and linear algebra. We will first introduce rings and free modules.

**Definition B.1.1** (Chapter A-3[42]). A **field**  $F$  is a commutative ring in which  $1 \neq 0$  and every nonzero element  $a$  is a unit; that is, there is  $a^{-1} \in F$  with  $a^{-1}a = 1$ .

**Definition B.1.2** (Chapter III-1[38]). A commutative ring  $R$  with identity  $1 \neq 0$  and no zero divisors is called an **integral domain**. A ring  $D$  with identity  $1 \neq 0$  in which every nonzero element is a unit is called a **division ring**. A **field** is a commutative division ring.

**Definition B.1.3** (Chapter B-1[42]). A **ring**  $R$  is a set with two binary operations, addition, and multiplication, such that

- (i)  $R$  is an abelian group under addition,
- (ii)  $a(bc) = (ab)c$  for every  $a, b, c \in R$ ,
- (iii) there is an element  $1 \in R$  with  $1a = a = a1$  for every  $a \in R$ ,
- (iv)  $a(b + c) = ab + ac$  and  $(b + c)a = ba + ca$  for every  $a, b, c \in R$ .

A ring  $R$  is **commutative** if  $ab = ba$  for all  $a, b \in R$ .

**Definition B.1.4** (Chapter B-1[42]). Let  $R$  be a ring. A **left  $R$ -module** is an additive abelian group  $M$  equipped with a **scalar multiplication**  $R \times M \rightarrow M$ , denoted by

$$(r, m) \mapsto rm, \tag{B.1}$$

such that the following axioms hold for all  $m, m' \in M$  and all  $r, r', 1 \in R$ :

- (i)  $r(m + m') = rm + rm'$ .
- (ii)  $(r + r')m = rm + r'm$ .
- (iii)  $(rr')m = r(r'm)$ .
- (iv)  $1m = m$ .

**Definition B.1.5** (Chapter III-2[38]). A nonempty subset  $I$  of a ring  $R$  is a left ideal if and only if for all  $a, b \in I$  and  $r \in R$ :

- (i)  $a, b \in I \rightarrow a - b \in I$ ; and
- (ii)  $a \in I, r \in R \rightarrow ra \in I$ .

**Definition B.1.6** (Chapter B-2[42]). If  $R$  is a ring, then a **free left  $R$ -module**  $F$  is a direct sum of copies of  $R$ , where each summand  $R$  is views as a left  $R$ -module.

Next, we will introduce results from linear algebra, which will be used in a later section. Proofs of the following theorems can be easily found in [38][42]. For the rest of this paper, we define  $R$  as a ring with identity.

**Theorem B.1.1** (Theorem 1.2[38]). Let  $E$  be a free left  $R$ -module with a finite basis of  $n$  elements and  $F$  a free left  $R$ -module with a finite basis of  $m$  elements. Let  $M$  be the left  $R$ -module of all  $n \times m$  matrices over  $R$ . Then there is an isomorphism of abelian groups:

$$\text{Hom}_R(E, F) \cong M \tag{B.2}$$

If  $R$  is commutative, this is an isomorphism of left  $R$ -modules.

**Theorem B.1.2** (Theorem 1.6[38]). Let  $E$  and  $F$  be free left  $R$ -modules with finite bases  $U$  and  $V$  respectively such that  $|U| = n$ ,  $|V| = m$ . Let  $f \in \text{Hom}_R(E, F)$  have  $n \times m$  matrices  $A$  relative to  $U$  and  $V$ . Then  $f$  has  $n \times m$  matrix  $B$  relative to another pair of ordered bases of  $E$  and  $F$  if and only if  $B = PAQ$  for some invertible matrices  $P$  and  $Q$ .

**Definition B.1.7** (Definition 1.8[38]). Two  $n \times m$  matrices  $C, D$  are said to be **equivalent** if there exist invertible matrices  $P$  and  $Q$  such that  $D = PCQ$ .

**Definition B.1.8** (Chapter VII-2[38]). For a division ring  $D$ ,  $E_r^{n,m}$  is defined as  $n \times m$  matrix whose first  $r$  rows are the standard basis vectors  $\epsilon_1, \dots, \epsilon_r$  of  $D^m$  and zero elsewhere.

**Theorem B.1.3** (Theorem 2.6[38]). Let  $M$  be the set of all  $n \times m$  matrices over a division ring  $D$  and let  $A, B \in M$

- (i)  $A$  is equivalent to  $E_r^{n,m}$  if and only if  $\text{rank } A = r$
- (ii)  $A$  is equivalent to  $B$  if and only if  $\text{rank } A = \text{rank } B$
- (iii) The matrices  $E_r^{n,m}$  ( $r = 1, 2, \dots, \min(n, m)$ ) constitute a set of canonical forms for the relation of equivalence on  $M$ .

**Definition B.1.9** (Chapter B-3[42]). If  $A$  is an  $r \times r$  matrix and  $B$  is an  $s \times s$  matrix, then their **direct sum**  $A \oplus B$  is the  $(r + s) \times (r + s)$  matrix

$$A \oplus B = \begin{bmatrix} A & 0 \\ 0 & B \end{bmatrix} \quad (\text{B.3})$$

Note that we will use same definition for non-square matrices  $A$  and  $B$  where  $A$  is  $m \times n$  matrix,  $B$  is  $r \times s$  matrix, and  $A \oplus B$  is  $(m + r) \times (n + s)$  matrix.

**Lemma B.1.1.** If  $A$  is an  $r \times r$  matrix,  $B$  is an  $s \times s$  matrix,  $C$  an  $r \times s$  matrix, and  $D$   $s \times r$  matrix, then

$$(i) \text{rank}(A \oplus B) = \text{rank} A + \text{rank} B.$$

$$(ii) \text{rank} \begin{bmatrix} A & 0 \\ C & B \end{bmatrix} \geq \text{rank} A + \text{rank} B.$$

$$(iii) \text{rank} \begin{bmatrix} A & D \\ 0 & B \end{bmatrix} \geq \text{rank} A + \text{rank} B.$$

*Proof.* (i) Suppose  $\text{rank} A = a$  and  $\text{rank} B = b$ . Let  $P, Q$  be  $r \times r$  matrices and  $P', Q'$  be  $s \times s$  matrices,  $\tilde{P} = P \oplus P'$ , and  $\tilde{Q} = Q \oplus Q'$ . From theorem B.1.2 and B.1.3, there exist  $A = PE_a^{r,r}Q$  and  $B = P'E_b^{s,s}Q'$ . We have  $A \oplus B = \begin{bmatrix} PE_a^{r,r}Q & 0 \\ 0 & P'E_b^{s,s}Q' \end{bmatrix} = \begin{bmatrix} P & 0 \\ 0 & P' \end{bmatrix} \begin{bmatrix} E_a^{r,r} & 0 \\ 0 & E_b^{s,s} \end{bmatrix} \begin{bmatrix} Q & 0 \\ 0 & Q' \end{bmatrix} = \tilde{P} \begin{bmatrix} E_a^{r,r} & 0 \\ 0 & E_b^{s,s} \end{bmatrix} \tilde{Q} = \tilde{P}(E_a^{r,r} \oplus E_b^{s,s})\tilde{Q}$ . Let  $E_a^{r,r} \oplus E_b^{s,s} = E$ . Since  $E_a^{r,r}$  is a matrix whose first  $r$  rows are the standard basis vectors  $\epsilon_1, \dots, \epsilon_a$  and  $E_b^{s,s}$  is a matrix whose first  $s$  rows are the standard basis vectors  $\epsilon_1, \dots, \epsilon_b$  which is  $\epsilon_{r+1}, \dots, \epsilon_{r+b}$  inside  $E$ . Thus,  $\text{rank} E = a + b$  and  $A \oplus B = \tilde{P}E\tilde{Q}$ . By theorem B.1.3(i),  $\text{rank} E = \text{rank}(A \oplus B) = \text{rank} A + \text{rank} B$ .

(ii) Take  $A = 0$ ,  $B = 0$ , and  $C \neq 0$ . Because the rank of any matrix is greater than and equal to 0, we get the desired result.

(iii) Take  $A = 0$ ,  $B = 0$ , and  $D \neq 0$ . Rests are equivalent to (ii).

□

**Lemma B.1.2.** If  $A$  is an  $m \times n$  matrix,  $B$  is an  $r \times s$  matrix,  $C$  an  $m \times s$  matrix, and  $D$   $r \times n$  matrix, then

$$(i) \text{rank}(A \oplus B) = \text{rank} A + \text{rank} B.$$

$$(ii) \text{rank} \begin{bmatrix} A & 0 \\ C & B \end{bmatrix} \geq \text{rank} A + \text{rank} B.$$

$$(iii) \text{ rank } \begin{bmatrix} A & D \\ 0 & B \end{bmatrix} \geq \text{rank } A + \text{rank } B.$$

*Proof.* Same as B.1.1 □

## B.2 Matroid and ring theory

A graph  $G(V, E)$  is denoted as a finite, labeled, and undirected graph without loops or multiple edges. Let  $V(G)$  be a vertex set and  $E(G)$  be edge set, and  $f_p$  be a positioning function for a graph where  $f_p$  maps graph  $G$  to real space in  $d$ -dimension  $f_p: G \rightarrow \mathbb{R}^d / J$  (where  $J$  is rigid motions), then graph  $G(V, E)$  satisfies

- (i) For any edge  $e \in E$  and vertex  $v \in V$ ,  $V(e_i) \neq \{v_j, v_j\}$  for all  $i, j$ .
- (ii) If  $e_i \neq e_j$ , then  $V(e_i) \neq V(e_j)$  for all  $i, j$ .
- (iii)  $G$  is equivalent with  $G'$  if  $E(G) = E(G')$ ,  $V(G) = V(G')$ , and  $f_p(G) \neq f_p(G')$ .
- (iv)  $G$  is congruent with  $G'$  if  $E(G) = E(G')$ ,  $V(G) = V(G')$ , and  $f_p(G) = f_p(G') / J$  (congruent up to rigid motion).

From now, we will consider graph  $G$  with known edge lengths and satisfies the following property.

**Definition B.2.1.** We define **labeled** graph  $G$  with known edge length for every  $e_k \in E$  and  $e_k = \{v_i, v_j\}$  such that a set of vertex  $v_i$  and  $v_j$  is connected to  $e_k$ .

**Definition B.2.2.** Euclidean distance function (simply length function) between vertex  $v_i$  and  $v_j$  is defined as  $d(v_i, v_j) = d(e_k)$  for vertex  $v_i, v_j$  and corresponding edge  $e_k$ . If we know positions of these vertices, then it can be derived as  $d(v_i, v_j) = \sqrt{\sum_{l=1}^d (v_i^l - v_j^l)^2} = d(e_k)$  of tuple  $v_i = (x_i^1, \dots, x_i^d)$  and  $v_j = (x_j^1, \dots, x_j^d)$  in  $d$ -dimension.

We assume that we know edge lengths, but we do not have information about the position vector of each vertex in  $\mathbf{R}^d$  unless we have a function  $f_p$  for graph  $G$ . We will look at abstract structure next, which is related to finding  $f_p$ . Let  $k$  be a field and  $k[X] = k[x_1, \dots, x_n]$  be polynomial ring over  $k$  with  $n$  number of indeterminate.

**Definition B.2.3.** Let  $g_p$  be a function which maps graph  $G$  to affine algebraic set as  $g_p: G \rightarrow X \subset k[X]$  where  $X$  is algebraic set defined by relations  $d(x_i, x_j)^2 - l_{ij}^2 = 0$  for all  $i, j$  for  $V$  and  $l_{ij}$  is the length of edge (real value) connected with vertex set  $v_i$  and  $v_j$  of  $G$ . Thus,  $g_p(v_i) = x_i$  with relations  $d(x_i, x_j)^2 - l_{ij}^2 = 0$  for all  $i, j$ .

**Definition B.2.4.** We define **labeled, unpositioned** vertex as an indeterminate  $x_i \in k[X]$  for  $n = d \cdot |V|$  such that  $h_p: X \subset k[X] \rightarrow \mathbb{R}^d$ ,  $h_p(x_i)$  is a position vector in  $\mathbb{R}^d$  with relations  $d(h_p(x_i), h_p(x_j))^2 = l_{ij}^2$ , and original edge length of  $G$  is preserved.

So far, we have the following diagram commutes.

$$\begin{array}{ccc} G & \xrightarrow{g_p} & X \\ & \searrow f_p & \downarrow h_p \\ & & \mathbb{R}^d / J \end{array}$$

Therefore,  $f_p = h_p \cdot g_p$  and this will allow us to find  $f_p$ . Equivalently  $f_p(G)$  represent realization (or embedding) of the graph in  $\mathbf{R}^d$ . Therefore, we can define the followings.

- (i) Graph  $G$  embedded in  $\mathbb{R}^d$ :  $f_p: G \rightarrow \mathbb{R}^d$  where  $f_p$  is a function which maps vertices to points  $\in \mathbb{R}^d / J$
- (ii)  $X \subset k[X]$  is constructed with relations  $d(x_i, x_j)^2 = l_{ij}^2$ . Since the intersection of these relations (roots of polynomials) constructs space  $X$ , thus  $X$  is a set of finite points if  $\dim X = 0$ .
- (iii) Counting number of embeddings ( $N_G$ ): Given a graph  $G$ , determine the maximum number of embeddings in  $\mathbb{R}^d / J$  ( $J$  is rigid motions).  $N_G = \infty$  if  $\dim X > 0$ .

We will define rigidity matroid without defining matroid. More details about matroid theory can be found in [39][83][31].

**Definition B.2.5.** For a framework  $G(V, E)$ , we define rigidity matroid of  $G(V, E)$  is the  $|E| \times d|V|$  matrix with variable  $x_i \in k[X]$  as shown below.

$$\mathcal{R}(G) = \begin{bmatrix} \ddots & & & \vdots & & & & \ddots \\ \cdots & 0 & (x_i - x_j) & 0 & \cdots & 0 & (x_j - x_i) & 0 & \cdots \\ \vdots & & & \vdots & & & & & \vdots \\ \cdots & 0 & (x_i - x_k) & 0 & \cdots & 0 & 0 & (x_k - x_i) & \cdots \\ \ddots & & & \vdots & & & & & \ddots \end{bmatrix} \text{ where } i, j, k\text{'s are la-}$$

bels for  $V$ . Recall  $x_i$  is an indeterminate represented as  $x_i = (x_i^1, \dots, x_i^d)$  in  $d$ -dimension.

**Definition B.2.6.** For a framework  $G(V, E)$ , we define a rigidity matrix of  $G(V, E)$  is the  $|E| \times d|V|$  matrix with variable  $f_p(v_i) = q_i \in \mathbb{R}^d$  as shown below.

$$\mathcal{R}(G, q) = \begin{bmatrix} \ddots & & & \vdots & & & & \ddots \\ \cdots & 0 & (q_i - q_j) & 0 & \cdots & 0 & (q_j - q_i) & 0 & \cdots \\ \vdots & & & \vdots & & & & & \vdots \\ \cdots & 0 & (q_i - q_k) & 0 & \cdots & 0 & 0 & (q_k - q_i) & \cdots \\ \ddots & & & \vdots & & & & & \ddots \end{bmatrix} \text{ where } i, j, k\text{'s are la-}$$

bels for  $V$  and  $q_i$  is a  $d$ -dimensional vector such that  $q_i = (q_i^1, \dots, q_i^k, \dots, q_i^d)$ . Note that  $q_i$  is not a variable and we have  $\text{rank } \mathcal{R}(G, q) \leq \text{rank } \mathcal{R}(G)$ .

**Definition B.2.7** (Section 2.1 [31]). Let  $V$  be the fixed  $n$ -element set and let  $K$  be the collection of all unordered pairs of elements of  $V$ . Then  $(V, K)$  is a complete graph.

We will refer  $K$  as a complete graph from now.

**Lemma B.2.1** (Lemma 1.1[39]). Let  $(G, q)$  be a framework in  $\mathbb{R}^d$ . Then the  $\text{rank}$  of  $\mathcal{R}(G, q)$

is at most  $S(n, d)$ , where  $n = |V(G)|$  and

$$S(n, d) = \begin{cases} nd - \binom{d+1}{2}, & \text{if } n \geq d + 2, \\ \binom{n}{2}, & \text{if } n \leq d + 1. \end{cases} \quad (\text{B.4})$$

Notice that if  $d \leq n \leq d + 1$ ,  $nd - \binom{d+1}{2} = \binom{n}{2}$  and if  $n < d$ , then  $G$  is not rigid unless  $G$  is a complete graph.

**Definition B.2.8** (Section 2.1 [31]). The set  $V(E)$  is the support of  $E$  if  $V(E) = \{i | \exists j \in V \text{ with } (i, j) \in E \text{ or } (j, i) \in E\}$  for any edge set  $E \subseteq K$ .

**Definition B.2.9** ([31]). For a framework  $(G, q)$ , the collection of an element  $s$  in the set of functions from  $E$  into real space  $s \in \mathbb{R}^{|E|}$  satisfies that each  $v \in V$  the sum  $\sum s(i, j)(q_i - q_j)$  is a zero vector. We will denote this space as  $\mathcal{S}$ .

**Theorem B.2.1** (Maxwell, 1864[31]). Let  $(G, q)$  be a framework in  $d$ -space, then

$$\dim(\mathcal{S}) \geq |E| - S(n, d)$$

with equality if and only if the framework is infinitesimally rigid.

**Definition B.2.10** ([31]). Let  $|V| = n$ ,  $p$  mapping  $V$  into  $\mathbb{R}^d$  be given.  $u \in (\mathbb{R}^d)^V$  is an infinitesimal motion of  $(G, q)$  if

$$(u_i - u_j) * (q_i - q_j) = 0, \text{ for all } (i, j) \text{ in } E,$$

where  $*$  denotes the inner product in  $\mathbb{R}^d$ . We will denote this space of infinitesimal motions of  $E$  by  $\mathcal{V}(E)$ . Note that  $(\mathbb{R}^d)^V$  represents the space of functions from  $V$  into  $\mathbb{R}^d$ . In fact, we have a natural isomorphism  $I: (\mathbb{R}^d)^V \rightarrow \mathbb{R}^{nd}$  given by  $I(q) = (q_1, \dots, q_n)$ .

$u \in (\mathbb{R}^d)^V$  can be identified with the  $n$ -tuple of vectors  $(u_1, \dots, u_n)$ . Here, we have

$$(u_1, \dots, u_n) * (0, \dots, 0, q_i - q_j, 0, \dots, 0, q_j - q_i, 0, \dots, 0) = 0,$$

where  $*$  denotes inner product in  $\mathbb{R}^{nd}$ .

**Corollary B.2.1.1** (Corollary 2.3.1[31]). Let  $V$ , the embedding  $q$  of  $V$  into  $\mathbb{R}^d$  ( $q: V \rightarrow \mathbb{R}^d$ ) and the edge set  $E \subseteq K$  be given, then

$$\dim(\mathcal{V}(E)) = nd - |E| + \dim(\mathcal{S}(E)).$$

where  $\mathcal{S}(E)$  denotes the space of resolvable stresses for  $E$ .

**Lemma B.2.1** (Lemma 2.3.1[31]). Given  $V$ , the embedding  $q$  of  $V$  into  $\mathbb{R}^d$  and the edge set  $E \subseteq K$ ; the space  $\mathcal{D}(E) = \mathcal{V}(K(V(E)))$  is a subspace of  $\mathcal{V}(E)$ .

**Definition B.2.11** ([31]). The framework  $(G, q)$  is infinitesimally rigid if  $\mathcal{V}(E) = \mathcal{D}(E)$  and infinitesimal motion in  $\mathcal{V}(E) - \mathcal{D}(E)$  and infinitesimal flex of  $E$ .

**Theorem B.2.2** (Theorem 2.4.1[31]). Let  $V$ , the general embedding  $q$  of  $V$  into  $\mathbb{R}^d$  and  $E \subseteq K$  be given with  $|V(E)| = n$ ,

- (i)  $\dim(\mathcal{S}(E)) \geq 0$ , with equality if and only if  $E$  is independent.
- (ii)  $\dim(\mathcal{V}(E) - \mathcal{D}(E)) \geq 0$ , with equality if and only if  $E$  is rigid.
- (iii) If  $n \geq d$ , then  $|E| = S(n, d) + \dim(\mathcal{S}(E)) - \dim(\mathcal{V}(E) - \mathcal{D}(E))$ .
- (iv) If  $n \leq d + 1$ , then  $\dim(\mathcal{S}(E)) = 0$  and  $\dim(\mathcal{V}(E) - \mathcal{D}(E)) = S(n, d) - |E|$ .

with equality if and only if the framework is infinitesimally rigid.

**Theorem B.2.3** (Theorem 2.1[73]). A framework  $(G, p)$  in  $\mathbb{R}^d$  is infinitesimally rigid if and only if either  $\text{rank } \mathcal{R}(G, q) = S(n, d)$  or  $G$  is a complete graph  $K_n$  and the points  $f_p(v_i), v_i \in V(G)$ , are affinely independent.

Since a graph  $G$  is rigid if it is infinitesimally rigid,  $G(V, E)$  is rigid in  $\mathbb{R}^d$  if  $\text{rank}\mathcal{R}(G, q) = S(n, d)$ . By regarding [39] in sub-graph structure  $H \subseteq G$ , we obtain following lemma.

**Definition B.2.12** (Section 11.1[83]). The framework  $(G, q)$  is  $d$ -independent if its edge set is independent in  $\text{rank}\mathcal{R}(G, q)$ .

**Theorem B.2.4** (Theorem 2.2[73]). For a  $d$ -dimensional realization  $(G, q)$  of a graph  $G$  with  $|V(G)| \geq$ , the following are equivalent.

- (i)  $(G, q)$  is isostatic.
- (ii)  $(G, q)$  is infinitesimally rigid, and  $|E(G)| = d|V(G)| - \binom{d+1}{2}$ .
- (iii)  $(G, q)$  is independent, and  $|E(G)| = d|V(G)| - \binom{d+1}{2}$ .

**Lemma B.2.1** (Lemma 11.1.1/Lemma 2.2[83][39]). Given a graph  $G = (V, E)$ , a vertex  $d$ -addition of 0 is the addition of one new vertex,  $q_0$ , and  $d$  new edges  $\{q_0, q_{i1}\}, \dots, \{q_0, q_{id}\}$  creating the graph  $G' = (V', E')$ . Given a framework  $(G, q)$  and a vertex  $d$ -addition of 0 creating  $G'$ , the framework  $(G', q_0, q)$ , with  $q_0, q_{i1}, \dots, q_{id}$  in the general position in  $d$ -space, then

- (i)  $(G', q, q_0)$  is  $d$ -independent if and only if  $(G, q)$  is  $d$ -independent.
- (ii)  $\text{rank}\mathcal{R}(G, q_0, q) = \text{rank}\mathcal{R}(G, q) + d$ .
- (iii) For  $v \in V$  with  $|E(V)| \leq d$ ,  $G$  is  $d$ -independent in  $\mathbb{R}^d$  if and only if  $G - v$  is  $d$ -independent in  $\mathbb{R}^d$ .

**Lemma B.2.2** (Lemma 11.1.9/Lemma 2.1[83][39]). Suppose  $G = G_1 \cup G_2$ .

- (i) If  $|V(G_1) \cap V(G_2)| \geq d$  and  $G_1, G_2$  are rigid in  $\mathbb{R}^d$  then  $G$  is rigid in  $\mathbb{R}^d$ .
- (ii) If  $E_1$  and  $E_2$  are generically  $d$ -independent and  $E_1 \cap E_2$  is generically  $d$ -rigid, then set  $E_1 \cup E_2$  is generically  $d$ -independent.

**Definition B.2.13** (Section 3.1[75]). A pinned graph  $G(I, P, E_I)$  is a graph with pinned vertices that has a fixed position where  $I$  is the set of inner vertices,  $P$  is the set of pinned vertices,  $E_I \subseteq E$  is the set of edges, and each edge  $e \in E_I$  has at least one endpoint in  $I$ .

**Definition B.2.14** (Section 3.1[75]). For a graph  $G(V, E)$  in  $\mathbb{R}^d$ , we can define a pinned rigid graph  $G(I, P, E_I) = (\tilde{G}, q)$ .  $P$  can be defined by rigid graph  $H \subset G$  via  $V(H) = P$ , and  $E_P$  is a set of edges connecting these vertices.  $G(I, P, E_I) = G(V, E) \setminus E_P$  where  $E_P$  is set of edges connecting points  $p \in P$ .

$$\mathbf{R}(\tilde{G}, q) = \begin{bmatrix} \ddots & & & \vdots & & & & \ddots \\ \cdots & 0 & (q_i - q_j) & 0 & \cdots & 0 & (q_j - q_i) & 0 & \cdots \\ \vdots & & & \vdots & & & & \vdots & \\ \cdots & 0 & (q_i - q_k) & 0 & \cdots & 0 & 0 & 0 & \cdots \\ \ddots & & & \vdots & & & & \ddots \end{bmatrix} \text{ where } q_i, q_j \in I, q_k \in P, \text{ and}$$

$q_i$  is a  $d$ -dimensional vector such that  $q_i = (q_i^1, \dots, q_i^d)$ .

**Definition B.2.15** (Section 3.1[75]). A framework  $(\tilde{G}, q)$  is pinned  $d$ -rigid if the only infinitesimal motion is the zero motion or equivalently, if pinned rigidity matrix  $(\tilde{G}, q)$  has full rank  $d|I|$ .

**Definition B.2.16.** Suppose  $G(I, P, E)$  has the relation  $|P| = a|I|$  for  $0 < a < d$  where  $a \in \mathbb{N}^+$ . We will refer  $G$  as a symmetric graph when  $G$  is projected to  $d - 1$  dimension, there exists an unlabeled sub-graph  $H \subset G$  consisting of some vertices, edges, and half-cut edges such that  $G$  can be decomposed with a sum of non-overlapping  $b$  copies of  $H$  for  $b \in \mathbb{N}^+$ .

**Definition B.2.17.** We can define rank preserving graph  $G'$  by moving edges and vertices for graph  $G$  such that  $G \rightarrow G'$  satisfies  $rank \mathcal{R}(G, q) = rank \mathcal{R}(G', q)$  and  $|E(G)| = |E(G')|$ .

Now we will rewrite Lemma B.2.2 for a pinned graph.

**Lemma B.2.3.** Suppose  $G = G_1 \cup G_2$ .

- (i) If  $G_1(V_1, E_1)$  is rigid,  $G_2(V_2, E_2) = G_2(I_2, P_2, E_2)$  is pinned rigid for  $|P_2| \geq d$ ,  $V(G_1) \cap V(G_2) = P_2$ , and  $E_1 \cap E_2 = \emptyset$  in  $\mathbb{R}^d$  then  $G$  is rigid in  $\mathbb{R}^d$ .
- (ii) If  $E_1$  is generically  $d$ -independent,  $E_2$  is edges of pinned rigid for graph  $G_2$  satisfies generically  $d$ -independent, and  $E_1 \cap E_2 = \emptyset$ , then set  $E_1 \cup E_2$  is generically  $d$ -independent.
- (iii) If  $G_1(V_1, E_1)$  is rigid in  $\mathbb{R}^{d-1}$ ,  $G_2(V_2, E_2) = G_2(I_2, P_2, E_2)$  is pinned rigid in  $\mathbb{R}^d$ , and  $V(G_1) = P_2$ , then at least  $|E_2| = d \cdot |I_2| + |P_2| - d$  to be infinitesimally rigid in  $\mathbb{R}^d$ .
- (iv) Any pinned rigid graph  $G_1(V_1, E_1) = G_1(I_1, P_1, E_1)$  can be embedded in rigid graph  $G$  by adding rigid graph  $G_2(V_2, E_2)$  with same dimension such that  $V(G_1) \cap V(G_2) = P_2$  for  $|P_2| \geq d$ .

*Proof.* (i) Since edges connecting unpinned points are not overlapping, we can think of a direct sum of two rigidity matrices. From Lemma B.1.2 (ii), we have  $\text{rank } \mathcal{R}(G, q) \geq \text{rank } \mathcal{R}(G_1, q) + \text{rank } \mathcal{R}(\widetilde{G}_2, q) = d \cdot |V(G_1)| - \binom{d+1}{2} + d \cdot |V(G_2)| = d \cdot |V(G)| - \binom{d+1}{2}$ . Since  $\text{rank } \mathcal{R}(G, q) \leq S(n, d) = d \cdot |V(G)| - \binom{d+1}{2}$ . By Squeeze Theorem, we get  $\text{rank } \mathcal{R}(G, q) = d \cdot |V(G)| - \binom{d+1}{2}$ .

(ii) Same as above

(iii) From Theorem B.2.4, we require  $|E(G)| = d|V(G)| - \binom{d+1}{2}$ . We know that  $\text{rank } \mathcal{R}(G_1, q) = (d-1) \cdot |P_2| - \binom{d}{2}$  and  $\text{rank } \mathcal{R}(\widetilde{G}_2, q) = d \cdot |I_2|$ . Since from Lemma B.1.2, we have  $\text{rank } \mathcal{R}(G, q) \geq \text{rank } \mathcal{R}(G_1, q) + \text{rank } \mathcal{R}(\widetilde{G}_2, q)$  and  $(d-1) \cdot |P_2| + d \cdot |I_2| - \binom{d}{2} = d \cdot |V(G)| - \binom{d+1}{2} - |P_2| + d$ , so we get  $d \cdot |V(G)| - \binom{d+1}{2} - |P_2| + d \leq \text{rank } \mathcal{R}(G, q) \leq d|V(G)| - \binom{d+1}{2}$ . Therefore, to be rigid graph,  $|E_2| = d \cdot |I_2|$  is not sufficient, and we require at least  $|P_2| - d$  additional edges.

(iv) Same as (i)

□

Finally, we will define a globally rigid framework.

**Definition B.2.18** ([29]). If  $(G, q)$  is **globally rigid**, then  $(G, q)$  is congruent to every realization  $(G, q')$  in  $\mathbb{R}^d$  of  $G$  with the same edge lengths.

Compared with Definition B.2.4 (iii),  $N_G$  for globally rigid framework is 2 (up to rigid motion) since it counts reflection.

**Definition B.2.19** ([29]). A framework  $(G, q)$  in  $\mathbb{R}^d$  is called **universally rigid framework** for which every other realization  $(G, q')$  in  $\mathbb{R}^d$  of  $G$  with the same edge lengths as in  $(G, q)$  is congruent to  $(G, q')$ .

**Theorem B.2.5** (Theorem 63.1.4[29]). For a graph  $G$  on at least  $d + 2$  vertices and a fixed dimension  $d$ , the following are equivalent:

- (i) A graph  $G$  is generically globally rigid in  $\mathbb{R}^d$
- (ii) A graph is weakly generically universally rigid in  $\mathbb{R}^d$
- (iii) There exists a generic framework  $(G, q')$  in  $\mathbb{R}^d$  which is universally rigid.
- (iv) There exists a generic framework  $(G, q)$  in  $\mathbb{R}^d$  which is globally rigid.
- (v) There exists a generic framework  $(G, q)$  in  $\mathbb{R}^d$  with a stress matrix  $\mathcal{S}$  which has rank  $n - d - 1$ .
- (vi) There exists a generic framework  $(G, q')$  in  $\mathbb{R}^d$  with positive semi-definite stress matrix  $\mathcal{S}$  which has rank  $n - d - 1$ .

The following theorem is gluing lemma (Lemma B.2.2) for a globally rigid graph.

**Theorem B.2.6** (Theorem 63.2.4[29]). If  $G_1 = (V_1; E_1)$  and  $G_2 = (V_2, E_2)$  are globally rigid graphs in  $\mathbb{R}^d$  sharing at least  $d + 1$  vertices, then  $G = (V_1 \cup V_2, E_1 \cup E_2 - G_1[V_1 \cap V_2])$  is globally rigid in  $\mathbb{R}^d$ . If  $G_1 = (V_1; E_1)$  and  $G_2 = (V_2, E_2)$  are globally rigid graphs in  $\mathbb{R}^d$  sharing exactly  $d + 1$  vertices and some edge  $e$ , then  $G = (V_1 \cup V_2, E_1 \cup E_2 - e)$  is globally rigid in  $\mathbb{R}^d$ .

## B.3 Algebraic geometry and distance geometry

Let  $k$  be a field and  $k[X] = k[x_1, \dots, x_n]$  be polynomial ring over  $k$  with  $n$  number of indeterminate.

**Definition B.3.1** ([17]). Affine  $n$ -space over  $k$  is defined by  $\mathbb{A}^n = \{(a_1, \dots, a_n) | a_1, \dots, a_n \in k\}$  such that a point  $p = (a_1, \dots, a_n) \in \mathbb{A}^n$ .

**Definition B.3.2** ([17]). The zeros of a regular function  $f \in k[X] = k[x_1, \dots, x_n] = k[\mathbb{A}^n]$  are  $Z(f) = \{p \in \mathbb{A}^n | f(p) = 0\}$  and if  $T \subset k[X]$  is a subset, then  $Z(T)$  is the set of common zeros for  $T$  such that  $Z(T) = \{p \in X | f(p) = 0 \text{ for all } f \in T\}$ .

**Proposition B.3.0.1** (Proposition 2.1[17]). Suppose that  $I_1, I_2, \{I_\alpha\}_{\alpha \in S}$  are ideals in  $k[X] = k[\mathbb{A}^n]$  then

$$(i) \quad Z(I_1 I_2) = Z(I_1) Z(I_2)$$

$$(ii) \quad Z(\sum_{\alpha} I_{\alpha}) = \cap_{\alpha} Z(I_{\alpha})$$

$$(iii) \quad Z(k[X]) = \emptyset$$

$$(iv) \quad \mathbb{A}^n = Z(0)$$

**Lemma B.3.1** (Lemma[74]). Let  $f \in k[x, y]$  an irreducible polynomial, and  $g \in k[x, y]$  an arbitrary polynomial. If  $g$  is not divisible by  $f$ , then the system of equations  $f(x, y) = g(x, y) = 0$  has only a finite number of solutions.

**Definition B.3.3** ([36]). Two nonzero points in  $\bar{k}^3$  are equivalent if each is a scalar multiple of the other, and the equivalence class of this is the projective plane  $\mathbb{P}^2$ .

We will introduce Bézout's Theorem in  $\mathbb{P}^2$ .

**Theorem B.3.1** (Theorem 1[36]). Let  $A, B \in k[x, y, z]$  be homogeneous of degrees  $m, n$  respectively, with no nonconstant common factor. Then the two curves  $A = 0$  and  $B = 0$  in  $\mathbb{P}^2$  in exactly  $mn$  points, counting multiplicities.

The following theorem is more generalized Bézout's Theorem.

**Theorem B.3.2** (Theorem[74]). Let  $X$  and  $Y$  be projective curves, with  $X$  nonsingular and not contained in  $Y$ . Then the sum of the multiplicities of the intersection of  $X$  and  $Y$  at all points of  $X \cap Y$  equals the product of the degrees of  $X$  and  $Y$ .

**Definition B.3.4** ([118]). Cayley-Menger determinants are defined by distances between sets of points such that

$$CM(A_0, \dots, A_n) = \begin{vmatrix} 0 & d_{01}^2 & d_{02}^2 & \cdots & d_{0n}^2 & 1 \\ 0 & d_{01}^2 & d_{02}^2 & \cdots & d_{0n}^2 & 1 \\ d_{01}^2 & 0 & d_{12}^2 & \cdots & d_{1n}^2 & 1 \\ \vdots & \vdots & \vdots & \ddots & \vdots & \vdots \\ d_{0n}^2 & d_{1n}^2 & d_{2n}^2 & \cdots & 0 & 1 \\ 1 & 1 & 1 & \cdots & 1 & 0 \end{vmatrix}$$

where  $A_0, \dots, A_n$  are points in  $k$ -dimensional Euclidean space (or  $\mathbb{R}^k$ ) for  $k \geq n$  and  $d_{ij}$ 's are Euclidean distances between vertices  $A_i$  and  $A_j$ .

It has a nice property that  $n$ -dimensional volume of the simplex  $v_n$  satisfies

$$\text{Vol}_n(v_n)^2 = \frac{(-1)^{n+1}}{(n!)^2 2^n} CM(A_0, \dots, A_n).$$

**Definition B.3.5** (Definition 2.1[11]). The complex Cayley-Menger Variety  $CM^{2,n}(\mathbb{C}) = CM_{2n-4}(\mathbb{C})$  is defined as the Zariski-closure of the image of the configuration space  $C_n(\mathbb{R}^2)$  in  $\mathbb{P}_{\binom{n}{2}-1}(\mathbb{C})$ .

Note that we have a natural map  $C_n(\mathbb{R}^2) \rightarrow \mathbb{P}_{\binom{n}{2}-1}(\mathbb{C})$  defined by  $p_i \mapsto d_{ij} = |p_i - p_j|^2$ . That can be thought of as retaining only the mutual distances between points and getting the same projective coordinates for equivalent configurations as explained in [11]. Now, we

will introduce several theorems related to rigidity theory. Since proofs can be easily founded in [11][10] related to these subjects, we will not include in here.

**Corollary B.3.2.1** (Corollary 2.4[11]). The complex Cayley-Menger variety  $CM_{2n-4}(\mathbb{C}) \subset \mathbb{P}_{\binom{n}{2}-1}(\mathbb{C})$  is an irreducible projective subvariety of complex dimension  $2n - 4$  and degree  $D^{2,n} = \deg(CM_{2n-4}(\mathbb{C})) = \frac{1}{2} \binom{2n-4}{n-2}$  is swept-out by an  $(n - 2)$ -parameter family of linear subspaces  $\mathbb{P}_{n-2}(\mathbb{C})$  corresponding th the two  $\mathbb{P}_{n-2}(\mathbb{C})$  fibrations of  $(\mathbb{P}_{n-2}(\mathbb{C}))^2$

**Theorem B.3.3** (Theorem 4.3[11]). The complex dimension of  $CM^{d,n}(\mathbb{C})$  is  $dn - \binom{d+1}{2} - 1$  and its degree for  $d \leq n-2$  is given by the formula  $D^{d,n} = \deg(CM^{d,n}(\mathbb{C})) = \prod_{k=0}^{n-d-2} \frac{\binom{n-1+k}{n-d-1-k}}{\binom{2k+1}{k}}$

**Theorem B.3.4** (Theorem 1.3[10]). Let  $d$  be a given dimension. Let  $\mathcal{G}$  be a class of connected graphs with  $n \geq d + 1$  vertices and  $m = dn - \binom{d+1}{2}$  edges such that each graph allows an infinitesimally rigid realization in  $\mathbb{R}^d$ . Then, for a generic choice of edge lengths, each graph in  $\mathcal{G}$  has a finite number of embeddings in  $\mathbb{R}^d$ . Then, for a generic choice of edge lengths, each graph in  $\mathcal{G}$  has a finite number of embeddings in  $\mathbb{R}^d$ , and this number is bounded from above by  $2D^{d,n}$ . For  $d$  constant and  $n$  sufficiently large,  $D^{d,n} \simeq 2^{dn}$ .

# Appendix C

## Mathematical backgrounds for Euler's elastica and binomial expansion

### C.1 Elements of the calculus of variations

First, we will introduce definitions and derivations from [14] with modern notations. Then, we will briefly show Euler's notations used for deriving equations in section C.2. These principles can be found in his book [24].

For fixed endpoints variational problem in vector space  $C^2[x_1, x_2]$ , consider  $J: C^2[x_1, x_2] \rightarrow \mathbb{R}$  be a functional of the form.

$$J(u) = \int_{x_1}^{x_2} F(x, u, Du) dx.$$

We assume  $u$  is a function of  $x$  such that  $u(x)$ . Given two values  $u_1, u_2 \in \mathbb{R}$ , the problem comprises determining the functions  $u \in C^2[x_1, x_2]$  such that  $u(x_1) = u_1, u(x_2) = u_2$  and  $J$

has a local extremum in  $S$  at  $u \in S$ . Defined by

$$S = \{u \in C^2[x_1, x_2]: u(x_1) = u_1, u(x_2) = u_2\}$$

$$H = \{\eta \in C^2[x_1, x_2]: \eta(x_1) = \eta(x_2) = 0\}.$$

If  $J$  has a local maximum at  $u$ , then there is an  $\epsilon > 0$  such that  $J(\hat{u}) - J(u) \leq 0$  for all  $\hat{u} \in S$  such that  $\|\hat{u} - u\| < \epsilon$ . Using Taylor's theorem for small  $\eta$  and  $\hat{u} = u + \epsilon\eta$ , we can get

$$F(x, \hat{u}, D\hat{u}) = F(x, u, Du) + \epsilon \left\{ \eta \frac{\partial F}{\partial u} + \eta' \frac{\partial F}{\partial Du} \right\} + \mathcal{O}(\epsilon^2).$$

Then we have

$$J(\hat{u}) - J(u) = \epsilon \int_{x_1}^{x_2} \left( \eta \frac{\partial F}{\partial u} + \eta' \frac{\partial F}{\partial Du} \right) dx + \mathcal{O}(\epsilon^2)$$

$$= \epsilon \delta J(\eta, u) + \mathcal{O}(\epsilon^2).$$

If  $J(u)$  is a local maximum, then

$$\delta J(\eta, u) = \int_{x_1}^{x_2} \left( \eta \frac{\partial F}{\partial u} + \eta' \frac{\partial F}{\partial Du} \right) dx = 0.$$

That can be written as

$$\delta J(\eta, u) = \int_{x_1}^{x_2} \left( \eta \frac{\partial F}{\partial u} + \eta' \frac{\partial F}{\partial Du} \right) dx$$

$$= \int_{x_1}^{x_2} \eta \frac{\partial F}{\partial u} dx - \int_{x_1}^{x_2} \eta \frac{d}{dx} \left( \frac{\partial F}{\partial Du} \right) dx = 0 \quad \text{for all } \eta \in H.$$

Therefore, we get the following equation

$$E(x) = \frac{\partial F}{\partial u} - \frac{d}{dx} \left( \frac{\partial F}{\partial Du} \right)$$

If the function contains higher-order derivatives, we have

$$E(x) = (-1)^n \frac{d^n}{dx^n} \left( \frac{\partial F}{\partial u^n} \right) + (-1)^{n-1} \frac{d^{n-1}}{dx^{n-1}} \left( \frac{\partial F}{\partial u^{n-1}} \right) + \cdots + \frac{\partial F}{\partial u}$$

for  $J(u) = \int_{x_1}^{x_2} F(x, u, u', \dots, u^n) dx$ . Notice that we use  $u'$  instead of  $Du$  for clarification. If we use notations  $P = \frac{\partial F}{\partial u'}$  and  $Q = \frac{\partial F}{\partial u''}$  for  $u \in C^4[x_1, x_2]$ , then we get

$$E(x) = \frac{d^2 Q}{dx^2} - \frac{dP}{dx} + \frac{\partial F}{\partial u}.$$

Moreover, if we apply the Lagrange multiplier from Theorem A.3.1, we have

$$E(x) = \frac{d^2 Q}{dx^2} - \frac{dP}{dx} + \frac{\partial F}{\partial u} - \lambda \left( \frac{d^2 Q'}{dx^2} - \frac{dP'}{dx} + \frac{\partial G}{\partial u} \right)$$

where  $P' = \frac{\partial G}{\partial u'}$  and  $Q' = \frac{\partial G}{\partial u''}$ . If  $\frac{\partial F}{\partial u} = 0$ ,  $\frac{\partial G}{\partial u} = 0$ ,  $Q' = 0$ , we can get following Euler-Lagrange differential equation.

$$\frac{d^2 Q}{dx^2} - \frac{dP}{dx} + \lambda \left( \frac{dP'}{dx} \right) = 0 \tag{C.1}$$

## C.2 Original proof of Euler's elastica

We will follow Euler's original proof in his book appendix 1[24]. Recall that we have

$$\int \frac{ds}{R^2} = \int \frac{\left(\frac{d^2 y}{dx^2}\right)^2}{\left(1 + \left(\frac{dy}{dx}\right)^2\right)^{5/2}} dx = \int \frac{q^2}{(1+p^2)^{5/2}} dx = \int Z dx,$$

where  $p = \frac{dy}{dx}$ ,  $q = \frac{d^2 y}{dx^2}$ . Euler wrote in [24] about the problem as follows

Primum ergo quia curvae, ex quibus quaefita erui debet, ifoperimetrae ftauuntur, habebitur ifta expreffio confideranda  $\int dx \sqrt{1+p^2}$ . quae cum generali  $\int Z dx$  comparete hunc praebet valorem differentialem  $\frac{d}{dx} \frac{p}{\sqrt{1+p^2}}$ .

With rough English translation, this can be written as:

Therefore, because the curves from which the questions ought to be deduced and the perimeters are fixed, we shall have to consider this expression  $\int dx \sqrt{1+p^2}$ .

By comparing  $\int Zdx$ , will provide a differential value of  $\frac{d}{dx} \frac{p}{\sqrt{1+p^2}}$ .

Euler used following relation  $dZ = Mdx + Ndy + Pdp + Qdq$  where  $M = N = 0$ ,  $P = \frac{-5pq^2}{(1+p^2)^{7/2}}$ , and  $Q = \frac{2q}{(1+p^2)^{5/2}}$ . Please check appendix C.1 for derivations. He wrote as follows

Valor ergo differentialis ex hac formula  $\int \frac{q^2}{(1+p^2)^{5/2}} dx$  oriundus, erit  $-\frac{dP}{dx} + \frac{d^2Q}{dx^2}$ .

Again, translation will be

Therefore, the differential value derived from this formula  $\int \frac{q^2}{(1+p^2)^{5/2}} dx$  will be  $-\frac{dP}{dx} + \frac{d^2Q}{dx^2}$ .

Thus, Euler solved the differential equation as

$$\begin{aligned} \frac{d^2Q}{dx^2} - \frac{dP}{dx} + \gamma \frac{d}{dx} \frac{p}{\sqrt{1+p^2}} &= 0 \quad (\text{equation C.1}) \\ \frac{dQ}{dx} - P + \gamma \frac{p}{\sqrt{1+p^2}} + \beta &= 0 \\ qdQ - Pdp + \gamma \frac{pdp}{\sqrt{1+p^2}} + \beta dp &= 0 \quad (q = \frac{dp}{dx}) \\ qdQ - dZ + Qdq + \gamma \frac{pdp}{\sqrt{1+p^2}} + \beta dp &= 0 \quad (dZ = Pdp + Qdq) \\ qQ - Z + \gamma \sqrt{1+p^2} + \beta p + \alpha &= 0 \quad (d(qQ) = qdQ + Qdq), \end{aligned}$$

and we have

$$\gamma \sqrt{1+p^2} + \beta p + \alpha = \frac{-q^2}{(1+p^2)^{5/2}}.$$

Euler assumed

sumantur confiantes arbitrarie  $\alpha$ ,  $\beta$ , &  $\gamma$  negative.

(Suppose the arbitrary constants  $\alpha$ ,  $\beta$ , &  $\gamma$  are negative.)

Then, we get

$$\begin{aligned}\sqrt{-\gamma\sqrt{1+p^2}-\beta p-\alpha} &= \frac{q}{(1+p^2)^{5/4}} \\ (1+p^2)^{5/4}\sqrt{\gamma'\sqrt{1+p^2}+\beta'p+\alpha'} &= q = \frac{dp}{dx},\end{aligned}$$

where  $-\alpha = \alpha'$ ,  $-\beta = \beta'$ ,  $-\gamma = \gamma'$ . Using  $dy = p dx$ , we have

$$\begin{aligned}dx &= \frac{dp}{(1+p^2)^{5/4}\sqrt{\gamma'\sqrt{1+p^2}+\beta'p+\alpha'}} \\ dy &= \frac{p dp}{(1+p^2)^{5/4}\sqrt{\gamma'\sqrt{1+p^2}+\beta'p+\alpha'}}\end{aligned}$$

Although there is no known formula for these equations, Euler figured out a way as

Harum formularum hic in genere spectatarum neutra est integrabilis; combinari autem certo quodam modo possunt, ut aggregatum integrationem admittat. Cum enim fit  $d\frac{2\sqrt{\gamma'\sqrt{1+p^2}+\beta'p+\alpha'}}{(1+p^2)^{1/4}} = \frac{dp(\beta'-\alpha'p)}{(1+p^2)^{5/4}\sqrt{\gamma'\sqrt{1+p^2}+\beta'p+\alpha'}}$  erit  $\frac{2\sqrt{\gamma'\sqrt{1+p^2}+\beta'p+\alpha'}}{(1+p^2)^{1/4}} = \beta'x - \alpha'y + \delta$ .

Again, a rough translation will be

Neither of these formulas can be integrated into the known class but can be combined in a certain way to allow aggregate integration. When it becomes  $d\frac{2\sqrt{\gamma'\sqrt{1+p^2}+\beta'p+\alpha'}}{(1+p^2)^{1/4}} = \frac{dp(\beta'-\alpha'p)}{(1+p^2)^{5/4}\sqrt{\gamma'\sqrt{1+p^2}+\beta'p+\alpha'}}$  it will be  $\frac{2\sqrt{\gamma'\sqrt{1+p^2}+\beta'p+\alpha'}}{(1+p^2)^{1/4}} = \beta'x - \alpha'y + \delta$ .

Also, Euler set some constants to be zero and simplified the equation.

Quoniam axis positio est arbitraria, constant  $\delta$  sine defectu amplitudinis omitti potest. Deinde vero etiam axis ita mutari potest ut fiat  $\frac{\beta'x-\alpha'y}{\sqrt{\beta'\beta'+\alpha'\alpha'}}$  abscissa, eritque

applicata  $\frac{\alpha'x+\beta'y}{\sqrt{\beta'\beta'+\alpha'\alpha'}}$ ; hinc etiam tuto  $\alpha'$  nihilo aequalis poni poteft, quia nihil impedit, quoinus illa nova abfciffa per  $x$  exprimatur.

Since the position of the axis is arbitrary, the constant  $\delta$  at the end of the amplitude can be omitted by default. Then, even the axis can be changed so that the abscissa  $\frac{\beta'x-\alpha'y}{\sqrt{\beta'\beta'+\alpha'\alpha'}}$  can be changed and  $\frac{\alpha'x+\beta'y}{\sqrt{\beta'\beta'+\alpha'\alpha'}}$  will be applied; hence also  $\alpha'$  can be safely placed equal to zero, because nothing prevents the new abscissa from being expressed by  $x$ .

By assuming  $\delta = \alpha' = 0$  as Euler did and letting  $\gamma' = \frac{4m}{a^2}, \beta' = \frac{4n}{a^2}$ , we can get

$$\begin{aligned} \frac{2\sqrt{\gamma'\sqrt{1+p^2} + \beta'p}}{(1+p^2)^{1/4}} &= \beta'x \\ 4\gamma'\sqrt{1+p^2} + 4\beta'p &= \beta'^2x^2\sqrt{1+p^2} \\ na^2p &= (n^2x^2 - ma^2)\sqrt{1+p^2} \\ n^2a^4p^2 &= (n^2x^2 - ma^2)^2(1+p^2) \\ p^2 &= \frac{(n^2x^2 - ma^2)^2}{n^2a^4 - (n^2x^2 - ma^2)^2} \\ \frac{dy}{dx} &= \frac{(n^2x^2 - ma^2)}{\sqrt{n^2a^4 - (n^2x^2 - ma^2)^2}}. \end{aligned}$$

If we assume  $\frac{dy}{dx}$  to be a decreasing function for  $0 \leq x \leq R$ , we will have

$$\begin{aligned} y(x) &= \int_x^R \frac{(t^2 - \frac{ma^2}{n^2})}{\sqrt{\frac{a^4}{n^4} - (t^2 - \frac{ma^2}{n^2})^2}} dt \\ y(x) &= \int_x^R \frac{(t^2 - \frac{ma^2}{n^2})}{\sqrt{(\frac{a^4}{n^4} + \frac{ma^2}{n^2} - t^2)(\frac{a^4}{n^4} - \frac{ma^2}{n^2} + t^2)}} dt \\ y(x) &= \int_x^R \frac{a'^2 - c'^2 + t^2}{\sqrt{(c'^2 - t^2)(2a'^2 - c'^2 + t^2)}} dt. \end{aligned}$$

The last equation is obtained by setting  $a' = \frac{a^4}{n^4}$ ,  $c' = \frac{a^4}{n^4} + \frac{ma^2}{n^2}$ . For an increasing function  $\frac{dy}{dx}$ , we get

$$y(x) = \int_0^x \frac{a'^2 - c'^2 + t^2}{\sqrt{(c'^2 - t^2)(2a'^2 - c'^2 + t^2)}} dt.$$

This is an equation 4.14.

### C.3 Elliptic integrals and functions

We will introduce general definitions from [34]. Then, we show typical notations of Elliptic functions, which can be easily found in [34][93][119].

**Definition C.3.1** ([34]). Let  $R(z) = C_0z^n + C_1z^{n-1} + \dots + C_n$ . For  $n = 3, 4$ , the integral  $\int \frac{f(z)}{\sqrt{R(z)}} dz$  is an elliptic integral.

where  $f(z)$  is the rational function and may be written

$$f(z) = G(z) + \sum_i \frac{A_{\lambda_i}}{(z - bi)^{\lambda_i}} \quad (A_{\lambda_i} \text{ constants}).$$

Thus,

$$\int \frac{f(z)}{\sqrt{R(z)}} dz = \int \frac{G(z)}{\sqrt{R(z)}} dz + \sum_i A_{\lambda_i} \int \frac{dz}{(z - bi)^{\lambda_i} \sqrt{R(z)}}$$

$G(z)$  may be resolved into a number of polynomials  $z^k$ . Therefore, we have two general types of integrals to consider

**Definition C.3.2** ([34]).

$$I_k = \int \frac{z^k}{\sqrt{R(z)}} dz$$

$$H_k = \int \frac{dz}{(z - b)^k \sqrt{R(z)}}$$

$I_1$  reduces to elementary integrals, so we call

- $I_0 = \int \frac{dz}{\sqrt{R(z)}}$  : an elliptic integral of the first kind
- $I_2 = \int \frac{z^2 dz}{\sqrt{R(z)}}$  : an elliptic integral of the second kind
- $H_1 = \int \frac{dz}{(z-b)\sqrt{R(z)}}$  : an elliptic integral of the third kind

These functions have explicit forms with names  $E, F, \Pi$  as represented below.

$$\begin{aligned}
 F(\phi, k) &= \int_0^{\sin \phi} \frac{1}{\sqrt{(1-t^2)(1-k^2t^2)}} dt \quad (\text{first kind}) \\
 E(\phi, k) &= \int_0^{\sin \phi} \frac{\sqrt{1-k^2t^2}}{\sqrt{1-t^2}} dt \quad (\text{second kind}) \\
 \Pi(\phi, n, k) &= \int_0^{\sin \phi} \frac{1}{(1+nt)^2 \sqrt{(1-t^2)(1-k^2t^2)}} dt \quad (\text{third kind}),
 \end{aligned} \tag{C.2}$$

where  $0 \leq k^2 \leq 1$ . The complete elliptic integral of the first kind  $K$  is defined as

$$K(k) = F\left(\frac{\pi}{2}, k\right) = \int_0^1 \frac{1}{\sqrt{(1-t^2)(1-k^2t^2)}} dt.$$

Jacobi amplitude is defined by  $\text{am}(u) = \text{am}(u, m = k^2) = \phi$  and there are corresponding trigonometric functions.

$$\text{sn}(u, m) = \sin \text{am}(u, m)$$

$$\text{cn}(u, m) = \cos \text{am}(u, m)$$

$$\text{dn}(u, m) = \frac{d}{du} \text{am}(u, m)$$

where  $u$  is

$$u = \int_0^\phi \frac{d\theta}{\sqrt{1-k^2 \sin^2 \theta}}.$$

The following two relations are addition theorems.

$$\begin{aligned}\operatorname{sn}^2(u, m) + \operatorname{cn}^2(u, m) &= 1 \\ \operatorname{dn}^2(u, m) + k^2 \operatorname{sn}^2(u, m) &= 1\end{aligned}$$

More relations and details about these functions can be found in [34][123].

## C.4 Coefficients of first and second fundamental forms

Suppose  $\mathbf{x}: D \rightarrow \mathbb{R}^3$  and  $\mathbf{x}(u, v) \rightarrow (x^1(u, v), x^2(u, v), x^3(u, v))$  denote a mapping of  $D$  in  $\mathbb{R}^2$ [89].

**Definition C.4.1** ([99][90]). Let  $M \subseteq \mathbb{R}^3$  be a surface with a unit normal vector field  $U$ . If  $p \in M$ , for each  $v_p \in TpM$  defined  $S(v_p) = -\nabla_{v_p} U$  where  $S$  denote the shape operator of  $M$  at  $p$ .

Note that with respect to  $u, v$  the Shape Operator has the associated matrix  $\begin{bmatrix} k_1(p) & 0 \\ 0 & k_2(p) \end{bmatrix}$ .

**Definition C.4.2** ([99][90]). The Gaussian curvature of  $M$  at  $p \in M$  is defined to be  $K(p) = \det(S_p) = k_1(p)k_2(p)$ . The mean curvature of  $M$  at  $p \in M$  is defined to be  $H(p) = \frac{1}{2} \operatorname{trace}(S_p) = \frac{1}{2}(k_1(p) + k_2(p))$ .

Consider Gauss map  $G: M \rightarrow S^2$  and  $\mathbf{x}_u = (\frac{\partial x^1}{\partial u}, \frac{\partial x^2}{\partial u}, \frac{\partial x^3}{\partial u})$  and  $\mathbf{x}_v = (\frac{\partial x^1}{\partial v}, \frac{\partial x^2}{\partial v}, \frac{\partial x^3}{\partial v})$ . To compute  $K$  and  $H$ , we use the first and second fundamental forms defined as [97]:

$$Edu^2 + 2Fdudv + Gdv^2, Ldu^2 + 2Mdudv + Ndv^2$$

$$E = \mathbf{x}_u \cdot \mathbf{x}_u, F = \mathbf{x}_u \cdot \mathbf{x}_v, G = \mathbf{x}_v \cdot \mathbf{x}_v,$$

$$L = S(\mathbf{x}_u) \cdot \mathbf{x}_u, M = S(\mathbf{x}_v) \cdot \mathbf{x}_u, N = S(\mathbf{x}_v) \cdot \mathbf{x}_v,$$

where  $S(\mathbf{x}_u)$  and  $S(\mathbf{x}_v)$  are tangent vectors. Using  $S = M_1^{-1}M_2$ ,  $M_1 = \begin{bmatrix} E & F \\ F & G \end{bmatrix}$  and

$$M_2 = \begin{bmatrix} L & M \\ M & N \end{bmatrix}, \text{ we get}$$

$$K = \frac{LN - M^2}{EG - F^2}, H = \frac{1}{2} \frac{LG - 2MF + NE}{EG - F^2}.$$

If  $F = M = 0$ , we have

$$K = \frac{LN}{EG}, H = \frac{1}{2} \frac{LG + NE}{EG} = \frac{1}{2} \left( \frac{L}{E} + \frac{N}{G} \right)$$

Similarly, principal curvatures  $k_1$  and  $k_2$  can be easily found using  $k^2 - 2Hk + K = 0$  where  $k_1$  and  $k_2$  are two roots. More details can be found in [99][90][97][89].

## C.5 Fractional binomial theorem

We will briefly explain how to derive equality of  $\sum_{k=0}^{\infty} \binom{-\frac{1}{2}}{k} x^k = \sum_{k=0}^{\infty} \left(-\frac{1}{4}\right)^k \binom{2k}{k} x^k$  using the properties of factorial function and derivations from [87]. First, we will define the following equality:

$$\begin{aligned} (2k)! &= (2k) \cdots 2 \cdot 1 \\ &= ((2k-1) \cdots 3 \cdot 1) \cdot (2k \cdots 2) \quad (\text{separation of even and odd parts}) \\ &= ((2k-1) \cdots 3 \cdot 1) \cdot (2^k) \cdot (k!). \end{aligned} \tag{C.3}$$

Since  $k$  is a positive integer, we have

$$\begin{aligned}
& \sum_{k=0}^{\infty} \binom{-\frac{1}{2}}{k} x^k \\
&= \sum_{k=0}^{\infty} \frac{(-\frac{1}{2}) \cdots (-\frac{2k-1}{2})}{k!} x^k \\
&= \sum_{k=0}^{\infty} \frac{(-1) \cdots (-2k+1)}{2^k \cdot k!} x^k \\
&= \sum_{k=0}^{\infty} (-1)^k \frac{(2k-1) \cdots 1}{2^k \cdot k!} x^k \\
&= \sum_{k=0}^{\infty} (-1)^k \frac{(2k)!}{(2^k) \cdot (k!) \cdot (2^k \cdot k!)} x^k \quad (\text{equation C.3}) \\
&= \sum_{k=0}^{\infty} (-1)^k \frac{(2k)!}{(2^k \cdot k!)^2} x^k \\
&= \sum_{k=0}^{\infty} (-1)^k (2^{-2k}) \frac{(2k)!}{(k!)^2} x^k \\
&= \sum_{k=0}^{\infty} \left(-\frac{1}{4}\right)^k \frac{(2k)!}{(k!)^2} x^k \\
&= \sum_{k=0}^{\infty} \left(-\frac{1}{4}\right)^k \binom{2k}{k} x^k.
\end{aligned}$$

# Appendix D

## Willmore energy and Willmore surfaces

**Definition D.0.1.** For every compact surface  $\Sigma \subset \mathbb{R}^3$ , Willmore energy is defined by

$$W(\Sigma) = \int_{\Sigma} H^2 d\mu = \int_{\Sigma} \left( \frac{k_1 + k_2}{2} \right)^2 d\mu.$$

For immersed closed surface  $n \geq 3$ , we can write above as

**Definition D.0.2** ([53]). For immersed closed surface  $f: \Sigma \subset \mathbb{R}^n$ , Willmore energy is defined by

$$W(f) = \int_{\Sigma} \frac{1}{2} |\vec{H}|^2 d\mu_g$$

where  $g = f^*g_{euc}$  denotes the pull-back metric of the Euclidean metric under  $f$ . We define  $g_{ij} := \langle \partial_i f, \partial_j f \rangle$ ,  $A_{ij} := (\partial_{ij} f)^\perp$ , and  $\vec{H} = g^{ij} A_{ij}$ .

We can easily guess the lower bound of Willmore energy from the sphere, which is

$$\begin{aligned} W(f) &= \int_{\Sigma} H^2 dA \\ &= \int_{\Sigma} \frac{1}{R^2} dA \\ &= \frac{1}{R^2} 4\pi R^2 = 4\pi. \end{aligned}$$

Because  $H^2 - K = \frac{(k_1+k_2)^2}{2} - k_1k_2 = \frac{(k_1-k_2)^2}{2} \geq 0$ , we get following inequality in  $\mathbb{R}^3$  (for a smooth immersion of a compact, orientable surface of dimension two).

$$\begin{aligned}\tilde{W}(f) &= \int_{\Sigma} (H^2 - K)dA \geq 0 \\ W(f) &= \int_{\Sigma} H^2 dA \geq \int_{\Sigma} K dA \geq 4\pi.\end{aligned}$$

Notice that the last term can also be obtained from Gauss-Bonnet Theorem  $\int_{\Sigma} K dA = 2\pi\chi(\Sigma)$  where  $\chi(\Sigma)$  is the Euler characteristic of the surface  $\Sigma$ . Note that the above definition can be changed depending on the space. For example,  $W(f) = \int_{\Sigma} H^2 + 1dA$  for the surface projected into  $S^3$  [80].

**Proposition D.0.0.1** (Proposition 1.1.1[53]). For any embedding  $f: \Sigma \rightarrow \mathbb{R}^3$  of a closed surface  $\Sigma$ , we have

$$W(f) \geq 4\pi$$

More detailed explanations can be found in [53][5].

## D.1 Willmore conjectures

In 1965, Willmore found it is difficult to find examples of energy close to  $4\pi$  for genus  $g = 1$  surfaces. All the known examples of tori embedded in  $\mathbb{R}^3$  have energies always greater than  $2\pi^2$  [84].

**Conjecture D.1.1** ([51]). Every compact surface  $\Sigma$  of genus one in  $f: \Sigma \rightarrow \mathbb{R}^3$  must satisfy

$$W(f) \geq 2\pi^2.$$

**Theorem D.1.1** ([51]). Every embedded compact surface  $\Sigma$  in  $f: \Sigma \rightarrow \mathbb{R}^3$  with positive

genus satisfies

$$W(f) \geq 2\pi^2$$

up to rigid motions, the equality holds only for stereographic projections of the Clifford torus.

Therefore, it turns out Willmore's conjecture holds. Moreover, Li and Yau showed  $W(f) \geq \text{area}(k \text{ great spheres}) = 4\pi k$  [51]. Next, we will introduce the upper and lower limits of Willmore energy. Defining  $\beta_p^n$  as [53]

$$\beta_p^n := \inf\{W(f) | f: \Sigma \rightarrow \mathbb{R}^n, \text{genus}(\Sigma) = p, \Sigma \text{ orientable}\}$$

**Theorem D.1.2** (Theorem 8.1.1 [53]).

$$\lim_{p \rightarrow \infty} \beta_p^n = 8\pi.$$

In summary, we have  $4\pi < \beta_p^n < 8\pi$  for  $p \geq 1$  [53]. Li-Yau inequality implies that an immersion of a closed surface in  $\mathbb{R}^n$  with  $W(f) < 8\pi$  has to be embedded [84][51][50].

## D.2 Willmore surfaces and Willmore flow

For a given topological space, the Willmore surfaces are the critical points of the function  $W(f) = \int_{\Sigma} H^2 dA$  for the embedding of the sphere in  $\mathbb{R}^3$  [126]. The process is defined in [67].

For a given abstract surface  $W(M^2)$  and  $f: M^2 \rightarrow \mathbb{R}^3$ ,

- Determine  $W(M^2) := \inf W(f)$  over all immersions  $f: M^2 \rightarrow \mathbb{R}^3$ .
- Classify all  $f$  for which  $W(f)$  equals the minimal value  $W(M^2)$ .
- Determine all critical points  $f$  of  $W$  and the corresponding values  $W(f)$ .

Critical points of  $W$  are characterized by the Euler equation.

$$\Delta H + 2H(H^2 - K) = 0$$

where  $\Delta$  is the Laplace–Beltrami operator. There is also  $p$ -Willmore energy which is simply

$$W^p(f) = \int_{\Sigma} H^p dA, p \in \mathbb{Z}_{\geq 0},$$

Furthermore, there are corresponding  $p$ -Willmore surfaces and flow. Willmore surfaces have a nice property that it is invariant under the conformal change of metric.

**Proposition D.2.0.1** ([53]). For an immersion  $f: \Sigma \rightarrow M$  of a closed surface  $\Sigma$  into an  $n$ -dimensional manifolds  $M$  with metric  $g$ , we define the Willmore functional

$$W(f) = W(f, g) := \int_{\Sigma} \left( \frac{1}{4} |\vec{H}|^2 + K_M^{\Sigma} \right) d\mu_g,$$

where  $K_{\Sigma}$  is a Gaussian curvature of  $\Sigma$  and  $K_M^{\Sigma}$  is the sectional curvature of  $M$  regarding the tangent space of  $\Sigma$ . The Willmore functional is invariant under conformal changes of the metric, that is

$$W(f, \bar{g}) = W(f)$$

for any conformal metric  $\bar{g} = e^{2u}g$ .

The Willmore flow is the  $l^2$ -gradient flow corresponding to the Generalized Willmore energy related to the conformal invariances [3]. The Generalized Willmore energy for a smooth immersed surface in  $\mathbf{R}^3$  is defined by [79]

$$W(f) = \int_{\Sigma} (aH^2 + b) dA$$

$$W(f) = \int_{\Sigma} (H^2 + \epsilon) dA,$$

where  $a = 2k_c$ ,  $\epsilon = b/a$ ,  $k_c$  is the bending rigidity and  $b$  represents surface tension coefficient. Then, the corresponding Euler-Lagrange equation becomes

$$\Delta H + 2H(H^2 - K - \epsilon) = 0$$

[7] shows a discrete version of Willmore flow. Finally, we will briefly introduce Constrained Willmore surfaces

**Definition D.2.1** ([8]). An immersion  $f: M \rightarrow \mathbb{R}^3$  of a Riemann surface  $M$  is a constrained Willmore surface if it is critical for  $W(f)$  under compactly supported infinitesimal conformal variations of  $f$ .

These are a Möbius invariant class of surfaces related to the theory of integrable systems [8].

### D.3 Hopf tori and Willmore Hopf tori

Heinz Hopf discovered Hopf fibration (or Hopf map) in 1931, which describes a 3-sphere ( $S^3$ ) in terms of circles  $S^1$  and an ordinary sphere  $S^2$  [121].

$$S^1 \hookrightarrow S^3 \xrightarrow{p} S^2.$$

Then the inverse image of any closed curve  $\gamma: \mathbb{R} \rightarrow S^2$  will be an immersed torus in  $S^3$  which will be called a Hopf torus [100][68]. It was shown that there are infinitely many simple closed curves on  $S^2$  that are critical points for Willmore energy in  $S^3$  by Langer and Singer (recall that  $W(f) = \int_{\Sigma} 1 + H^2 dA$  in  $S^3$ ). The embedded Willmore tori in  $\mathbb{R}^3$  is the stereographic projection of this tori [68]. If these are defined by a closed constrained elastic curve, then we call constrained Willmore Hopf torus [100]. Visual images of Hopf tori, Willmore Hopf tori, and Constrained Willmore tori can be found in [112]. [35] shows pictures and processes of constrained Willmore Hopf tori with different constraints.

# Bibliography

- [1] Andrei Ardentov. “Multiple Solutions in Euler’s Elastic Problem”. In: *Automation and Remote Control* 79 (July 2018), pp. 1191–1206. DOI: 10.1134/S0005117918070020.
- [2] Josu Arroyo, Oscar Garay, and Alvaro Pampano. “Boundary Value Problems for Euler-Bernoulli Planar Elastica. A Solution Construction Procedure”. In: *Journal of Elasticity* 139 (Nov. 2019). DOI: 10.1007/s10659-019-09755-7.
- [3] Eugenio Aulisa et al. “New Developments on the p-Willmore Energy of Surfaces”. In: *Geometry Integrability and Quantization* 21 (Jan. 2020), pp. 57–65. DOI: 10.7546/giq-21-2020-57-65.
- [4] Evangelos Bartzos, Ioannis Z. Emiris, and Josef Schicho. *On the multihomogeneous Bézout bound on the number of embeddings of minimally rigid graphs*. 2020. DOI: 10.1007/s00200-020-00447-7. eprint: 2005.14485. URL: <https://doi.org/10.1007/s00200-020-00447-7>.
- [5] Yann Bernard. “Noether’s theorem and the Willmore functional”. In: *Advances in Calculus of Variations* 9.3 (2016), pp. 217–234. DOI: 10.1515/acv-2014-0033. URL: <https://doi.org/10.1515/acv-2014-0033>.
- [6] Aisa Biria and Eliot Fried. “Theoretical and experimental study of the stability of a soap film spanning a flexible loop”. In: *International Journal of Engineering Science* 94 (2015), pp. 86–102. ISSN: 0020-7225. DOI: <https://doi.org/10.1016/j.ijengsci.2015.05.002>. URL: <https://www.sciencedirect.com/science/article/pii/S0020722515000701>.

- [7] Alexander I. Bobenko and Peter Schröder. “Discrete Willmore Flow”. In: *Eurographics Symposium on Geometry Processing 2005*. Ed. by Mathieu Desbrun and Helmut Pottmann. The Eurographics Association, 2005. ISBN: 3-905673-24-X. DOI: 10.2312/SGP/SGP05/101-110.
- [8] Christoph Bohle, G. Paul Peters, and Ulrich Pinkall. “Constrained Willmore surfaces”. In: *Calculus of Variations and Partial Differential Equations* 32.2 (Jan. 2008), pp. 263–277. DOI: 10.1007/s00526-007-0142-5. URL: <https://doi.org/10.1007/2Fs00526-007-0142-5>.
- [9] Joran W. Booth et al. “OmniSkins: Robotic skins that turn inanimate objects into multifunctional robots”. In: *Science Robotics* 3.22 (2018). DOI: 10.1126/scirobotics.aat1853.
- [10] Ciprian Borcea and Ileana Streinu. “On the Number of Embeddings of Minimally Rigid Graphs”. In: *Proceedings of the Eighteenth Annual Symposium on Computational Geometry*. Association for Computing Machinery, 2002, pp. 25–32. ISBN: 1581135041. DOI: 10.1145/513400.513404.
- [11] Ciprian S. Borcea. “Point Configurations and Cayley-Menger Varieties”. In: (2002). DOI: 10.48550/ARXIV.MATH/0207110. URL: <https://arxiv.org/abs/math/0207110>.
- [12] Stephen Boyd and Lieven Vandenberghe. *Convex Optimization*. Cambridge University Press, 2004. ISBN: 0521833787.
- [13] Manuel Bronstein et al. *Solving Polynomial Equations*. Springer Berlin, Heidelberg, 2005. ISBN: 9783540243267. DOI: 10.1007/b138957.
- [14] Bruce van Brunt. *The Calculus of Variations*. Universitext. Springer New York, 2004. ISBN: 9780387402475. DOI: 10.1007/b97436.

- [15] P.B. Canham. “The minimum energy of bending as a possible explanation of the biconcave shape of the human red blood cell”. In: *Journal of Theoretical Biology* 26.1 (1970), pp. 61–81. ISSN: 0022-5193. DOI: 10.1016/S0022-5193(70)80032-7. URL: <https://www.sciencedirect.com/science/article/pii/S0022519370800327>.
- [16] Jose Capco et al. “The Number of Realizations of a Laman Graph”. In: *SIAM Journal on Applied Algebra and Geometry* 2.1 (Jan. 2018), pp. 94–125. ISSN: 2470-6566. DOI: 10.1137/17m1118312. URL: <http://dx.doi.org/10.1137/17M1118312>.
- [17] Steven Dale Cutkosky. *Introduction to Algebraic Geometry*. Graduate Studies in Mathematics. American Mathematical Society, 2018.
- [18] Jon Dattorro. *Convex Optimization & Euclidean Distance Geometry*. Meboo Publishing USA, 2005. ISBN: 9780578161402.
- [19] E. Efrati, E. Sharon, and R. Kupferman. “Elastic theory of unconstrained non-Euclidean plates”. In: *Journal of the Mechanics and Physics of Solids* 57.4 (2009), pp. 762–775. ISSN: 0022-5096. DOI: <https://doi.org/10.1016/j.jmps.2008.12.004>. URL: <https://www.sciencedirect.com/science/article/pii/S0022509608002160>.
- [20] Efi Efrati, Eran Sharon, and Raz Kupferman. “The metric description of elasticity in residually stressed soft materials”. In: *Soft Matter* 9 (34 2013), pp. 8187–8197. DOI: 10.1039/C3SM50660F. URL: <http://dx.doi.org/10.1039/C3SM50660F>.
- [21] Michael Eigensatz, Robert W. Sumner, and Mark Pauly. “Curvature-Domain Shape Processing”. In: *Computer Graphics Forum* 27.2 (2008), pp. 241–250. DOI: 10.1111/j.1467-8659.2008.01121.x.
- [22] Mohamed Elkadi and Bernard Mourrain. “Symbolic-numeric methods for solving polynomial equations and applications”. In: Jan. 2006, pp. 125–168. ISBN: 3540243267. DOI: 10.1007/3-540-27357-3\_3.

- [23] I. Emiris, E. Tsigaridas, and A. Varvitsiotis. “Mixed Volume and Distance Geometry Techniques for Counting Euclidean Embeddings of Rigid Graphs”. In: *Distance Geometry*. 2013.
- [24] Leonhard Euler. *Methodus inveniendi lineas curvas maximi minimive proprietate gaudentes, sive Solutio problematis isoperimetrici latissimo sensu accepti*. Lausannæ, Genevæ, apud Marcum-Michaellem Bousquet & socios, 1744, p. 322. DOI: <http://hdl.loc.gov/loc.rbc/General.28085.1>.
- [25] Izrail’ Moiseevitch Gel’fand, Sergei Vasil’evich Fomin, and Richard A. Silverman. *The Calculus of Variations*. Dover Books on Mathematics. Courier Corporation, 2000. ISBN: 9780486414485.
- [26] John Gemmer et al. “Isometric immersions, energy minimization and self-similar buckling in non-Euclidean elastic sheets”. In: *EPL (Europhysics Letters)* 114.2 (Apr. 2016), p. 24003. DOI: 10.1209/0295-5075/114/24003. URL: <https://doi.org/10.1209/0295-5075/114/24003>.
- [27] Mariano Giaquinta and Stefan Hildebrandt. *Calculus of Variations I*. Springer Berlin, Heidelberg, 2004. ISBN: 9783540506256. DOI: 10.1007/978-3-662-03278-7.
- [28] L. Giomi and L. Mahadevan. “Minimal surfaces bounded by elastic lines”. In: *Proceedings of the Royal Society A: Mathematical, Physical and Engineering Sciences* 468.2143 (2012), pp. 1851–1864. DOI: 10.1098/rspa.2011.0627. URL: <https://royalsocietypublishing.org/doi/abs/10.1098/rspa.2011.0627>.
- [29] Jacob E. Goodman and Joseph O’Rourke. *Handbook of Discrete and Computational Geometry*. CRC Press, Inc., 1997. ISBN: 0849385245.
- [30] Georg Grasegger, Christoph Koutschan, and Elias Tsigaridas. “Lower Bounds on the Number of Realizations of Rigid Graphs”. In: *Experimental Mathematics* 29.2 (Mar. 2018), pp. 125–136. ISSN: 1944-950X. DOI: 10.1080/10586458.2018.1437851. URL: <http://dx.doi.org/10.1080/10586458.2018.1437851>.

- [31] Jack Graver, Brigitte Servatius, and Herman Servatius. *Combinatorial Rigidity*. Graduate Studies in Mathematics. American Mathematical Society, 1993.
- [32] Anthony Gruber and Eugenio Aulisa. “Computational p-Willmore Flow with Conformal Penalty”. In: *ACM Transactions on Graphics* 39.5 (Sept. 2020), pp. 1–16. DOI: 10.1145/3369387. URL: <https://doi.org/10.1145/3369387>.
- [33] Mariana Hadzhilazova and Ivailo Mladenov. “Once More the Mylar Balloon”. In: *Comptes Rendus de l’Académie Bulgare des Sciences* 61 (Jan. 2008), pp. 847–856.
- [34] Harris Hancock. *Lectures on the theory of elliptic functions*. New York, J. Wiley & Sons, 1910.
- [35] Lynn Heller and Cheikh Birahim Ndiaye. “First explicit constrained Willmore minimizers of non-rectangular conformal class”. In: (2017). DOI: 10.48550/ARXIV.1710.00533. URL: <https://arxiv.org/abs/1710.00533>.
- [36] Jan Hilmar and Chris Smyth. “Euclid Meets Bézout: Intersecting Algebraic Plane Curves with the Euclidean Algorithm”. In: *The American Mathematical Monthly* 117.3 (2010), pp. 250–260. DOI: 10.4169/000298910x480090.
- [37] Ingrid Hotz and Hans Hagen. “Isometric Embedding for a Discrete Metric”. In: Jan. 2004, pp. 19–35. ISBN: 978-3-642-07263-5. DOI: 10.1007/978-3-662-07443-5\_2.
- [38] Thomas W. Hungerford. *Algebra*. Graduate Texts in Mathematics. Springer, 1974. ISBN: 0387905189.
- [39] Bill Jackson and Tibor Jordán. “The d-dimensional rigidity matroid of sparse graphs”. In: *Journal of Combinatorial Theory* B.95 (2005), pp. 118–133. DOI: 10.1016/j.jctb.2005.03.004.
- [40] Kavinda Jayawardana. *A Critical Study of Efrati et al.’s Elastic Theory of Unconstrained non-Euclidean Plates*. 2020. DOI: 10.48550/ARXIV.2012.13345. URL: <https://arxiv.org/abs/2012.13345>.

- [41] Tibor Jordán. “A note on generic rigidity of graphs in higher dimension”. In: *Discrete Applied Mathematics* 297 (2021), pp. 97–101. ISSN: 0166-218X. DOI: <https://doi.org/10.1016/j.dam.2021.03.003>. URL: <https://www.sciencedirect.com/science/article/pii/S0166218X21001050>.
- [42] Rotman Joseph J. *Advanced Modern Algebra*. Graduate Studies in Mathematics. American Mathematical Society, 2015. ISBN: 9781470415549.
- [43] Eiji Kaneda. “On the Gauss-Codazzi equations”. In: *Hokkaido Mathematical Journal* 19 (1990), pp. 189–213.
- [44] Jungwook Kim et al. “Designing Responsive Buckled Surfaces by Halftone Gel Lithography”. In: *Science* 335.6073 (2012), pp. 1201–1205. DOI: 10.1126/science.1215309. URL: <https://www.science.org/doi/abs/10.1126/science.1215309>.
- [45] Yael Klein, Efi Efrati, and Eran Sharon. “Shaping of Elastic Sheets by Prescription of Non-Euclidean Metrics”. In: *Science* 315 (2007), pp. 1116–1120.
- [46] Ousmane Kodio, Alain Goriely, and Dominic Vella. “Dynamic buckling of an inextensible elastic ring: Linear and nonlinear analyses”. In: *Phys. Rev. E* 101 (5 May 2020), p. 053002. DOI: 10.1103/PhysRevE.101.053002. URL: <https://link.aps.org/doi/10.1103/PhysRevE.101.053002>.
- [47] Nathan Krislock and Henry Wolkowicz. “Euclidean Distance Matrices and Applications”. In: *Handbook on Semidefnite, Conic and Polynomial Optimization*. Ed. by Miguel F. Anjos and Jean B. Lasserre. Springer US, 2012, pp. 879–914. ISBN: 9781461407690. DOI: 10.1007/978-1-4614-0769-0\_30. URL: [https://doi.org/10.1007/978-1-4614-0769-0\\_30](https://doi.org/10.1007/978-1-4614-0769-0_30).
- [48] Nicolaas H. Kuiper. “On  $C^1$ -isometric imbeddings. II”. In: 1955.
- [49] M. Marder and N. Papanicolaou. “Geometry and Elasticity of Strips and Flowers”. In: *Journal of Statistical Physics* 125.5 (2006), pp. 1065–1092. DOI: 10.1007/s10955-006-9087-x. URL: <https://doi.org/10.1007/s10955-006-9087-x>.

- [50] Fernando C. Marques and André Neves. “Min-Max theory and the Willmore conjecture”. In: *Annals of Mathematics* 179 (2014), pp. 683–782. DOI: 10.4007/annals.2014.179.2.6. URL: <https://doi.org/10.4007/annals.2014.179.2.6>.
- [51] Fernando C. Marques and André Neves. *The Willmore conjecture*. 2014. DOI: 10.48550/ARXIV.1409.7664. URL: <https://arxiv.org/abs/1409.7664>.
- [52] Shigeki Matsutani. “Euler’s elastica and beyond”. In: *Journal of Geometry and Symmetry in Physics* 17 (Jan. 2010).
- [53] Giuseppe Mingione, ed. *Topics in Modern Regularity Theory*. Publications of the Scuola Normale Superiore. Edizioni della Normale Pisa, 2012. ISBN: 9788876424267. DOI: 10.1007/978-88-7642-427-4.
- [54] Diego Misseroni, Ettore Barbieri, and Nicola Maria Pugno. “Extreme deformations of the cantilever Euler Elastica under transverse aerodynamic load”. In: *Extreme Mechanics Letters* 42 (2021), p. 101110. ISSN: 2352-4316. DOI: <https://doi.org/10.1016/j.eml.2020.101110>. URL: <https://www.sciencedirect.com/science/article/pii/S2352431620302856>.
- [55] I. M. Mladenov et al. “On the Whewell Parametrization of the Euler Elastica”. In: *AIP Conference Proceedings* 1191.1 (2009), pp. 133–140. DOI: 10.1063/1.3275585. eprint: <https://aip.scitation.org/doi/pdf/10.1063/1.3275585>. URL: <https://aip.scitation.org/doi/abs/10.1063/1.3275585>.
- [56] Ivaïlo Mladenov and John Oprea. “Balloons, domes and geometry”. In: *Geometry and Symmetry in Physics* 15 (2009), pp. 53–88.
- [57] Ivaïlo Mladenov and John Oprea. “The Mylar Balloon Revisited”. In: *American Mathematical Monthly* 110 (Nov. 2003), pp. 761–784. DOI: 10.2307/3647797.
- [58] Ivaïlo M. Mladenov. “New Geometrical Applications of the Elliptic Integrals: The Mylar Balloon”. In: *Journal of Nonlinear Mathematical Physics* 11 (Supplement 1

- 2004), pp. 55–65. ISSN: 1776-0852. DOI: 10.2991/jnmp.2004.11.s1.7. URL: <https://doi.org/10.2991/jnmp.2004.11.s1.7>.
- [59] Olaf Müller. *A note on closed isometric embeddings*. 2008. DOI: 10.48550/ARXIV.0805.4657. URL: <https://arxiv.org/abs/0805.4657>.
- [60] John Nash. “ $C^1$  Isometric Imbeddings”. In: *Annals of Mathematics* 60.3 (1954), pp. 383–396. ISSN: 0003486X. URL: <http://www.jstor.org/stable/1969840>.
- [61] John Nash. “The Imbedding Problem for Riemannian Manifolds”. In: *Annals of Mathematics* 63.1 (1956), pp. 20–63. ISSN: 0003486X. URL: <http://www.jstor.org/stable/1969989>.
- [62] Jorge Nocedal and Stephen J. Wright. *Numerical Optimization*. second. New York, NY, USA: Springer, 2006.
- [63] Joseph O’Rourke. *How to Fold It: The Mathematics of Linkages, Origami, and Polyhedra*. Cambridge University Press, 2011. DOI: 10.1017/CB09780511975028.
- [64] William Paulsen. “What Is the Shape of a Mylar Balloon?” In: *The American Mathematical Monthly* 101.10 (1994), pp. 953–958. ISSN: 00029890, 19300972. URL: <http://www.jstor.org/stable/2975161>.
- [65] Stefano Pigola and Giona Veronelli. *The smooth Riemannian extension problem*. 2016. DOI: 10.48550/ARXIV.1606.08320. URL: <https://arxiv.org/abs/1606.08320>.
- [66] Stefano Pigola and Giona Veronelli. *The smooth Riemannian extension problem: completeness*. 2016. DOI: 10.48550/ARXIV.1601.05075. URL: <https://arxiv.org/abs/1601.05075>.
- [67] U. Pinkall and I. Sterling. “Willmore Surfaces”. In: *The Mathematical Intelligencer* 9 (1987), pp. 38–43. DOI: 10.1007/BF03025897. URL: <https://doi.org/10.1007/BF03025897>.

- [68] Ulrich Pinkall. “Hopf tori in  $S^3$ ”. In: *Inventiones Mathematicae* 81 (Sept. 1985), p. 379. DOI: 10.1007/BF01389060.
- [69] Vladimir Pulov, Mariana Hadzhilazova, and Ivaïlo Mladenov. “The Mylar Balloon: An Alternative Description”. In: *Geometry, Integrability and Quantization* 16 (June 2015), pp. 256–269. DOI: 10.7546/giq-16-2015-256-269.
- [70] Charlotte Py et al. “Capillary Origami: Spontaneous Wrapping of a Droplet with an Elastic Sheet”. In: *Phys. Rev. Lett.* 98 (15 Apr. 2007), p. 156103. DOI: 10.1103/PhysRevLett.98.156103. URL: <https://link.aps.org/doi/10.1103/PhysRevLett.98.156103>.
- [71] Themistocles M. Rassias. “Properties of Isometric Mappings”. In: *Journal of Mathematical Analysis and Applications* 235.1 (1999), pp. 108–121. ISSN: 0022-247X. DOI: 10.1006/jmaa.1999.6363. URL: <https://www.sciencedirect.com/science/article/pii/S0022247X99963631>.
- [72] J. Ravetz. *The Rational Mechanics of Flexible or Elastic Bodies by C. Truesdell*. Vol. 53. University of Chicago Press, 1962, pp. 263–66. DOI: 10.1086/349580.
- [73] Bernd Schulze. “Symmetric Versions of Laman’s Theorem”. In: *Discrete and Computational Geometry* 44.4 (2010), pp. 946–972. DOI: 10.1007/s00454-009-9231-x.
- [74] Igor R. Shafarevich. *Basic Algebraic Geometry 1*. Springer, 2013.
- [75] Offer Shai, Adnan Sljoka, and Walter Whiteley. “Directed Graphs, Decompositions, and Spatial Linkages”. In: *Discrete Applied Mathematics* 161.18 (2013), pp. 3028–3047. DOI: 10.1016/j.dam.2013.06.004.
- [76] M. J. Sippl and H. A. Scheraga. “Solution of the embedding problem and decomposition of symmetric matrices”. In: *Proceedings of the National Academy of Sciences* 82.8 (1985), pp. 2197–2201. DOI: 10.1073/pnas.82.8.2197. eprint: <https://www.pnas.org/doi/pdf/10.1073/pnas.82.8.2197>. URL: <https://www.pnas.org/doi/abs/10.1073/pnas.82.8.2197>.

- [77] Yousuf Soliman et al. “Constrained Willmore Surfaces”. In: *ACM Trans. Graph.* 40.4 (July 2021). ISSN: 0730-0301. DOI: 10.1145/3450626.3459759. URL: <https://doi.org/10.1145/3450626.3459759>.
- [78] Reinhard Steffens and Thorsten Theobald. *Mixed Volume Techniques for Embeddings of Laman Graphs*. 2009. arXiv: 0805.4120 [math.CO].
- [79] Magdalena Toda et al. “New Advances in the Study of Generalized Willmore Surfaces and Flow”. In: *Seventeenth International Conference on Geometry, Integrability and Quantization* 17 (Jan. 2016), pp. 133–142. DOI: 10.7546/giq-17-2016-133-142.
- [80] Peter Topping. “Towards the Willmore conjecture”. In: *Calculus of Variations and Partial Differential Equations* 11 (2000), pp. 361–393. DOI: 10.1007/s005260000042. URL: <https://doi.org/10.1007/s005260000042>.
- [81] Nathan S. Usevitch et al. “An untethered isoperimetric soft robot”. In: *Science Robotics* 5.40 (2020). DOI: 10.1126/scirobotics.aaz0492.
- [82] Y. Wang, B. Liu, and Y. Tong. “Linear Surface Reconstruction from Discrete Fundamental Forms on Triangle Meshes”. In: *Computer Graphics Forum* 31.8 (2012), pp. 2277–2287. DOI: 10.1111/j.1467-8659.2012.03153.x.
- [83] Walter Whiteley. “Some matroids from discrete applied geometry”. In: *Contemporary Mathematics* 197 (1996), pp. 171–311. DOI: 10.1090/conm/197/02540.
- [84] Shing-Tung Yau. “On the Willmore Conjecture for Surfaces”. In: 2013.

## Other References

- [85] Erik Demaine et. al. *The 85 Foldings of the Latin Cross*. URL: <http://erikdemaine.org/aleksandrov/cross/>.
- [86] Michael Kelly Annie Pa. *Real-Time Balloon Simulation*. URL: <http://haelmichael.com/downloads/other/paper.pdf>.
- [87] Brilliant.org. *Fractional Binomial Theorem*. URL: <https://brilliant.org/wiki/fractional-binomial-theorem/>.
- [88] The Geometry Center. *1-Skeleton*. URL: <http://www.geom.uiuc.edu/docs/research/RP2-handle/Glossary/1-skeleton.html#:~:text=The%201%2Dskeleton%20of%20a,than%20or%20equal%20to%20n..>
- [89] Hunter S. Chase. *Fundamental forms of surfaces and the Gauss-Bonnet Theorem*. URL: <https://math.uchicago.edu/~may/REU2012/REUPapers/Chase.pdf>.
- [90] Mark Coleman. *Differential Geometry*. URL: <https://personalpages.manchester.ac.uk/staff/mark.coleman/Diff%20Geom/D%20G%20Chapter%204.pdf>.
- [91] Keith Conrad. *Isometries of  $\mathbb{R}^n$* . URL: <https://kconrad.math.uconn.edu/blurbs/grouptheory/isometryRn.pdf>.
- [92] CRAN. *The Comprehensive R Archive Network*. 2022. URL: <https://cran.r-project.org/>.
- [93] J. R. Culham. *Elliptic Functions*. URL: [http://www.mhtlab.uwaterloo.ca/courses/me755/web\\_chap3.pdf](http://www.mhtlab.uwaterloo.ca/courses/me755/web_chap3.pdf).

- [94] GeometrieWerkstatt. *Constrained Willmore Hopf torus*. URL: <https://www.imaginary.org/gallery/constrained-willmore-surfaces-in-3-space>.
- [95] Raju George. *Lecture Notes : Calculus of Variations*. URL: <https://www.iist.ac.in/sites/default/files/people/COVMain.pdf>.
- [96] Wolfram Research Inc. *Mathematica, Version 13.0.0*. Champaign, IL, 2021. URL: <https://www.wolfram.com/mathematica>.
- [97] Yan-Bin Jia. *Gaussian and Mean Curvatures*. URL: <https://faculty.sites.iastate.edu/jia/files/inline-files/gaussian-curvature.pdf>.
- [98] Yan-Bin Jia. *Roots of a Polynomial System*. URL: <https://faculty.sites.iastate.edu/jia/files/inline-files/polysystem.pdf>.
- [99] Ilya Kapovich. *Shape operator*. URL: <https://faculty.math.illinois.edu/~kapovich/423-15/shape.pdf>.
- [100] Martin Kilian. *Elastic curves and Willmore Hopf-Tori*. URL: <http://wpd.ugr.es/~geometry/seminar/files/talks/MKilian20130619.pdf>.
- [101] Christos Konaxis. *Distance Geometry-Matrix Completion*. URL: [https://cgi.di.uoa.gr/~ckonaxis/files/teach/mobio2010\\_slides.pdf](https://cgi.di.uoa.gr/~ckonaxis/files/teach/mobio2010_slides.pdf).
- [102] Stéphane Laurent. *Back to the parametric Hopf torus*. URL: <https://www.r-bloggers.com/2020/04/back-to-the-parametric-hopf-torus/>.
- [103] Nina Lebedeva and Anton Petrunin. *Alexandrov's embedding theorem*. URL: [http://mathcenter.spb.ru/nikaan/book/alexandrov\\_math.pdf](http://mathcenter.spb.ru/nikaan/book/alexandrov_math.pdf).
- [104] Raph Levien. *The elastica: a mathematical history*. Tech. rep. UCB/EECS-2008-103. EECS Department, University of California, Berkeley, Aug. 2008. URL: <http://www2.eecs.berkeley.edu/Pubs/TechRpts/2008/EECS-2008-103.html>.
- [105] Erik Mahieu. *Wolfram Demonstrations Project - Trilateration and the Intersection of Three Spheres*. 2015. URL: <http://demonstrations.wolfram.com/TrilaterationAndTheIntersectionOfThreeSpheres>.

- [106] Encyclopedia of Mathematics. *Isometric mapping*. URL: [http://encyclopediaofmath.org/index.php?title=Isometric\\_mapping&oldid=40182](http://encyclopediaofmath.org/index.php?title=Isometric_mapping&oldid=40182).
- [107] Encyclopedia of Mathematics. *Isoperimetric problem*. URL: [http://encyclopediaofmath.org/index.php?title=Isoperimetric\\_problem&oldid=52024](http://encyclopediaofmath.org/index.php?title=Isoperimetric_problem&oldid=52024).
- [108] Raman Oza in Pixabay. *Red blood cell*. 2016. URL: <https://pixabay.com/illustrations/red-blood-cell-rbc-erythrocyte-1861640/>.
- [109] Rob Owen-Wahl in Pixabay. *Apple*. 2016. URL: <https://pixabay.com/photos/apple-food-fresh-fruit-green-1239300/>.
- [110] stux in Pixabay. *Exhaust pipe structure*. 2013. URL: <https://pixabay.com/photos/exhaust-pipe-structure-fund-plastic-186946/>.
- [111] Wolfram Research. *EllipticE*. <https://reference.wolfram.com/language/ref/EllipticE.html>. 13.
- [112] Nick Schmitt. *Hopf Torus*. URL: <https://www.math.uni-tuebingen.de/user/nick/gallery/HopfTorus.html>.
- [113] StackExchange. *Intersection coordinates of two spheres*. URL: <https://mathematica.stackexchange.com/questions/121087/intersection-coordinates-of-two-spheres>.
- [114] Eric W. Weisstein. "*Appell Hypergeometric Function*." *From MathWorld—A Wolfram Web Resource*. URL: <https://mathworld.wolfram.com/AppellHypergeometricFunction.html>.
- [115] Eric W. Weisstein. "*Beltrami Identity*." *From MathWorld—A Wolfram Web Resource*. URL: <https://mathworld.wolfram.com/BeltramiIdentity.html>.
- [116] Eric W. Weisstein. "*Isometry*." *From MathWorld—A Wolfram Web Resource*. URL: <https://mathworld.wolfram.com/Isometry.html>.

- [117] Eric W. Weisstein. "*Laman Graph*." *From MathWorld—A Wolfram Web Resource*. URL: <https://mathworld.wolfram.com/LamanGraph.html>.
- [118] Wikipedia. *Distance geometry*. URL: [https://en.wikipedia.org/wiki/Distance\\_geometry](https://en.wikipedia.org/wiki/Distance_geometry).
- [119] Wikipedia. *Elliptic integral*. URL: [https://en.wikipedia.org/wiki/Elliptic\\_integral](https://en.wikipedia.org/wiki/Elliptic_integral).
- [120] Wikipedia. *Gram matrix*. URL: [https://en.wikipedia.org/wiki/Gram\\_matrix](https://en.wikipedia.org/wiki/Gram_matrix).
- [121] Wikipedia. *Hopf fibration*. URL: [https://en.wikipedia.org/wiki/Hopf\\_fibration](https://en.wikipedia.org/wiki/Hopf_fibration).
- [122] Wikipedia. *Isoperimetric inequality*. URL: [https://en.wikipedia.org/wiki/Isoperimetric\\_inequality](https://en.wikipedia.org/wiki/Isoperimetric_inequality).
- [123] Wikipedia. *Jacobi elliptic functions*. URL: [https://en.wikipedia.org/wiki/Jacobi\\_elliptic\\_functions](https://en.wikipedia.org/wiki/Jacobi_elliptic_functions).
- [124] Wikipedia. *Resultant*. URL: <https://en.wikipedia.org/wiki/Resultant>.
- [125] Wikipedia. *System of polynomial equations*. URL: [https://en.wikipedia.org/wiki/System\\_of\\_polynomial\\_equations](https://en.wikipedia.org/wiki/System_of_polynomial_equations).
- [126] Wikipedia. *Willmore energy*. URL: [https://en.wikipedia.org/wiki/Willmore\\_energy](https://en.wikipedia.org/wiki/Willmore_energy).
- [127] Henry Woody. *Polynomial Resultants*. URL: <http://buzzard.ups.edu/courses/2016spring/projects/woody-resultants-ups-434-2016.pdf>.

# VITA

**AUTHOR:** Kyung Eun Kim

**DEGREES AWARDED:**

- M.S. in Electronic & Computer Engineering, Hanyang University, Seoul, South Korea  
2010
- B. Eng. in Electronic & Electrical Engineering, Hongik University, Seoul, South Korea  
2004

**AWARDS:**

- Research Excellence Doctoral Funding (REDF) Fellowship, Syracuse University  
Fall 2019-Spring 2020
- Samsung Industrial Scholarship Student  
2009
- Academic Scholarship, Hongik University  
2000-2002

**RESEARCH EXPERIENCE:**

- 3-D surface control for object manipulation with stretchable materials (NSF EFRI 1935294)  
Summer 2020-Spring 2022
- LHCb Quarkonia Analysis  
Fall 2018-Fall 2019
- The LHCb Upstream Tracker Upgrade  
Summer 2017-Fall 2019
- Hardware chip against side-channel attacks using static current (Electronics and Telecommunications Research Institute)  
2009

**TEACHING EXPERIENCE:**

- Lab Instructor for PHY221  
Spring 2018

- Lab Instructor for PHY101 Fall 2017
- Lab Instructor for AST102 Spring 2017
- Lab Instructor for AST101 Fall 2016
- Instructor for Electronics Lab (for 3rd-4th year undergrads) Spring 2008
- Lab Instructor for Electrical & Computer Experiment IV Fall 2008

### **PUBLICATIONS:**

- R. Aaij et al. (LHCb Collaboration) First Observation of Excited  $\Omega_b^-$  States, LHCb-PAPER-2019-042, Phys. Rev. Lett. 124, 082002,[2001.00851] 2020
- Byong-Deok Choi, Kyung Eun Kim, Ki-Seok Chung, and Dong Kyue Kim. Symmetric Adiabatic Logic Circuits against Differential Power Analysis. ETRI Journal, Volume 32, pp.166-168. 2010

### **PRESENTATIONS:**

#### **Contributed Talks:**

- Discrete 4D printing, APS March Meeting 2021
- Contact force estimation from deformation of surface, APS March Meeting 2022

#### **Posters:**

- Gregory Campbell, Jessica Yin, and Kyungeun Kim. 3-D surface control for object manipulation with stretchable materials. EFRI All-Teams Workshop 2021
- Kyung Eun Kim, Byong-Deok Choi, and Dong Kyue Kim. Delayed-Input Differential Power Analysis of Symmetric Discharge Logic. Conference Proceedings MITA, pp.252-255. 2009